DarkSPIDER: A Tool to Constrain Parameter Space of Generic Dark Matter Models with Astrophysical Observations

Dissertation

zur Erlangung des Doktorgrades

an der Fakultät für

Mathematik, Informatik und Naturwissenschaften

Fachbereich Physik

der Universität Hamburg

Vorgelegt von

Chao Zhang

Hamburg

2020

Gutachter der Dissertation:	Prof.Dr. Dieter Horns Dr. Kai Schmidt-Hoberg
Gutachter der Disputation:	Prof. Dr. Dieter Horns Dr. Kai Schmidt-Hoberg Prof. Dr. Sven-Olaf Moch Prof. Dr. Roman Schnabel Dr. Andrei Lobanov
Datum der Disputation:	14/01/2020
Vorsitzender des Prüfunggsausschusses:	Prof. Dr. Roman Schnabel
Vorsitzender des Promotionsausschusses:	Prof. Dr. Günter Sigl
Leiter der Fachbereichs Physik:	Prof. Dr. Wolfgang Hansen
Dekan der Fakultät für Mathematik, Informatik und Naturwissenschaften:	Prof. Dr. Heinrich Graener

Kurzfassung

Das Thema dieser Doktorarbeit ist die Entwicklung des DarkSPIDER Programms für die Suche nach dunkler Materie (DM) mit allgemeinen Modellen sowie dessen Anwendung. Nach jahrzehntelanger Suche nach supersymmetrischen Teilchen, spezieller nach WIMPs (weakly interacting dark matter), konnten nur negative Resultate in indirekten, direkten und Beschleunigerexperimenten gefunden werden. Art und Eigenschaften der dunklen Materie bleiben rätselhaft. Im Rahmen der vorliegenden Arbeit wird versucht, möglichst viele allgemeine Modelle zu sammeln, um ein Gesamtbild des Feldes zu erlangen. Zusammen mit Daten neuerer Experimente werden komplementäre Einschränkungen berechnet, mit dem Ziel diejenigen Modelle zu finden, welche mit den experimentellen Daten kompatibel sind. Zur Berechnung des Wechselwirkungsquerschnittes der Annihilation wird eine mit einfachen Modellen ergänzte effektive Feldtheorie verwendet. Die Einschränkungen aus indirekten Experimenten werden, ausgehend von einer gegebenen Reliktdichte, berechnet. Koannihilation wird ebenfalls berücksichtigt, um den Effekt von mehreren Teilchen im dunklen Sektor zu untersuchen. Das Ergebnis dieser Arbeit ist der Ausschluss eines großen Teils des Parameterraumes. Lediglich kleine Regionen im Bereich 10 GeV und oberhalb von 10 TeV sind im Rahmen der getesteten Modelle erlaubt.

Vorherige Arbeiten konzentrierten sich auf s-Wellen Modelle für DM. Die Kopplung der dunklen Materie an Standardmodellteilchen ist in vielen p-Wellen Modelle unterdrückt und daher nicht für einen direkten Nachweis oder Beschleunigerexperimente zugänglich. Der Wechselwirkungsquerschnitt von p-Wellen DM-Kandidaten ist Geschwindigkeitsabhängig, und könnte durch "boost"-Faktoren verstärkt werden. Daher wurden auch Sommerfeld-verstärkte p-Wellen Annihilationsmodelle untersucht. Die Dynamik von DM-dominierten sphärischen Zwerggalaxien (dwarf spheroidals, dSphs) wurde durch Anwendung der Jeans-Gleichung auf allgemeine Modelle der Massendichte- und Anisotropieprofile untersucht. Hierbei wurde die PSO-Methode (particle swarm optimization method, Teilchenschwarmoptimierung) implementiert, um einen schnellen Scan des Parameterraumes zu ermöglichen. Die Ergebnisse erlauben eine neue Sicht auf das "core-cusp" Problem. Die Berechnung des effektiven Wechselwirkungsquerschnittes aus dSphs zeigt, dass die durch die Reliktdichte erlaubten Modelle keinen starken geschwindigkeitsabhängigen "boost"-Faktor der Sommerfeldverstärkung aufweisen. Schließlich wurde der isotrope Gammastrahlen-Hintergrund (IGRB) für den Fall der p-Wellen DM studiert. Der IGRB wurde zu den astrophysikalischen Objekten hinzugefügt, um dann eine neue Anpassung an FermiLAT IGRB Daten durchzuführen. Sowohl die prompte Emission, als auch Inverse Compton Streuung (IC) wurden hier berücksichtigt. Dies führte zum Ausschluss sehr kleiner Regionen im Bereich zwischen 1 und 50 GeV. Allerdings liefert dieses Modell im selben Massenbereich der DM und für mehrere Annihilationskanäle eine bessere Anpassung als ein Modell ohne Berücksichtigung der dunklen Materie.

Das DarkSPIDER Paket ist ein unabhängiges Fortran-Tool, welches auch auf weitere DM-Modelle erweitert, und auf weitere experimentelle Daten angewendet werden könnte.

Abstract

The topic of this thesis is the development and applications of the DarkSPIDER program for Dark Matter searches with generic models. After decades-long efforts in the searches for the Supersymmetric particle candidate namely the weakly interacting Dark Matter (WIMP), only null results have been found in the indirect, direct, and collider-based experiments. The nature and properties of Dark Matter remain puzzling to us.

This thesis tries to collect as many generic models as possible to make a global view of this field. Together with data from all the recent experiments, complementary constraints are obtained in order to find models which could not be excluded. For the annihilation cross section, the effective field theory supplemented with simplified models is applied in the analysis. With the requirement of the relic density, the constraints from indirect detection are computed. The case of coannihlation is also taken into account to see what it will change if there are multiple particles in the dark sector. It is found that most of the parameter space has been ruled out except some small regions around several GeV or above 10 TeV are still allowed in the models treated here.

However, most of the previous efforts have been done for the s-wave annihilating Dark Matter. Many p-wave models have parametrically suppressed couplings to the SM particles, they are not accessible in direct detection or collider-based experiments. The annihilation cross section of the p-wave Dark Matter candidates is velocity-dependent, and could be enhanced by several boost factors. So the Sommerfeld enhanced p-wave annihilating Dark Matter models have been investigated. The dynamics of the dark-matter-dominated dwarf spheroidal galaxies (dSphs) are studied using the Jeans equation with general models of mass density and anisotropy profiles. The particle swarm optimization (PSO) method is implemented to make a fast scan on the parameter space. The best fitting results provide an explanation on the "core-cusp" problem. The computation of the effective annihilation cross section in the dSphs shows the models allowed by the relic density does not have large boost factor of the Sommerfeld enhancement with the volocity in the dSphs. Furthermore, the isotropic γ-ray background (IGRB) has been studied for the case of p-wave DM as well, the γ-ray flux is added to the astrophysical sources to make a new fit to the FermiLAT IGRB data. Both the prompt and inverse Compton scattering (ICS) emissions have been taken into account with the Sommerfeld enhancement. Only very small regions of between 1 and 50 GeV have been ruled out. However, in the same range of Dark Matter mass, this model provides a better fit than the model without Dark Matter in several annihilation channels.

The DarkSPIDER package is an independent fortran tool, it could be extended to other Dark Matter models and experimental data.

Contents

Chapter 1 Introduction to Dark Matter searches

Human's understanding of nature has been deepened and broadened immensely after the Renaissance. One of the driving forces of the scientific revolution is our comprehension of the Universe, for which we have developed Astronomy, one of the oldest academical disciplines. The spiritual seeds of rationalism scattered by Platon and Aristotle and the other Greek philosophers continue growing and finally give birth to modern science.

The origin, evolution, and components of the Universe are the key questions to astronomers. On the largest scale of space and time, cosmological and astrophysical models have been established; on the smallest scale, particle physics provides tools to study the structure in the subatomic particles. The two branches meet and form the discipline of astroparticle physics. Consequently, the Standard Model (SM) is built and confirmed by the successful prediction of the Higgs boson which gives a precise and fundamental description of the origin of the masses of elementary particles. Unfortunately, the beautiful SM fails to interpret many questions, such as the neutrino mass, the nature and amount of Dark Matter, the accelerating expansion of the Universe, and especially, there is no particle related to gravity in it.

The gravitational effect is the core of physics. By applying mathematics to explain observed phenomena, the study on gravity gives birth to Newtonian dynamics and Einstein's work on general relativity (GR). Now it is still the driving force to push forward our frontier of knowledge with the investigation on Dark Matter and Dark Energy since a lot of evidence shows the necessity to add them into the ΛCDM cosmology. Among the numerous Dark Matter candidates, the weakly interacting massive particle (WIMP) was considered as a promising solver to the problems. Decades-long efforts have been made to look for the signal induced by it, but only null results have been obtained.

To find an explanation of the puzzledom, during this work, efforts have been made to develop the DarkSPIDER package focused on the complementary searches of Dark Matter. With the results obtained in the complementary searches, the phenomenological analysis of p-wave Dark Matter has been performed. Before the description of my contribution, the outline of this thesis is shown.

In the next sections of Chapter 1, the theoretical background and observational evidence of Dark Matter is recalled at first. The ΛCDM cosmology is presented to show the roles of Dark Matter and Dark Energy in the whole Universe. Then the observational evidence of Dark Matter is discussed, including the rotation curves of galaxies, gravitational lensing, merging of galaxy clusters, the large structure

and N-body simulations, and the CMB observations. The other explanations fail to be consistent with all the evidence, only Dark Matter can interpret all of them. At the end of Chapter 1, the other candidates are shown as well.

In Chapter 2, the motivation to develop the DarkSPIDER package is shown firstly. DarkSPIDER consists of three components in general: particle models, astrophysical and cosmological models, analyzing tools. Some tables are given to show some corresponding functions and routines in this package. Then the data involved in DarkSPIDER is listed, including experimental data of indirect, direct, collider-based experiments and the relic density. External data from the existing packages is also included, such as the optical depth, the optical and X-rays data of the dSphs, the cosmological constants. The analyzing tools are composed of the numerical solvers, integrators, and the chi2 technique. The DarkSPIDER package employs several global optimization methods. The most important one is the Particle Swarm Optimization (PSO) which is used for large dimension optimization work. At the end of Chapter 2, some applications of DarkSPIDER are shown in the form of schema.

In Chapter 3, the complementary searches of Dark Matter are presented since the original idea of this thesis is to find complementary constraints on the particle candidates of Dark Matter. The analysis is thus done with generic models of Dark Matter by collecting data from several experiments. The effective field theory (EFT) and simplified models are presented, and then we have discussed the validity of the EFT models. A list of EFT models of annihilation is then shown before applying them to produce constraints by comparing them with the annihilation cross section required by the relic density. This work tried to collect as many models as possible in the package, some of them are described in this thesis, and the detectability is studied for different annihilation channels. Both general coupling and Yukawalike coupling have been considered, and the scanning results are summarized in a table at the end of the section. The case of coannihilation is interesting as well since it may change the constraints, a case of two particles in coannihilation is computed to show how this mechanism works. At the end of Chapter 3, a complementary work is done to collect constraints from the recent achievement in direct detection, indirect detection, collider-based experiments, and the relic density.

Chapter 4 is a study on the p-wave annihilating Dark Matter which is velocity-dependent, so the dynamics of the target systems are extremely important. The Jeans equation is applied to get the projected velocity dispersion in the dSphs. A generic model is developed to contain information on anisotropy and mass density profiles. The PSO method is then applied to get the best fit. The uncertainties are discussed before applying the models to the dSphs data. At the end, the Sommerfeld enhanced annihilation cross section required by the relic density is shown at different velocities. The effective annihilation cross section in the dSphs is computed to extract information about the Dark Matter. The importance of this result and possible improvements are discussed at the end.

Chapter 5 is also focused on the p-wave Dark Matter to extract information

about its nature and properties by adding it to the astrophysical sources of the IGRB flux. A formula of the differential gamma-ray flux of the p-wave annihilation from the extragalactic Dark Matter is described at the beginning. Then simplified p-wave models are presented. In Section 5.4, the prompt and ICS emissions are computed to provide the total flux. The clumpiness factor and the gamma-ray attenuation are added. Since the p-wave annihilation rate is much lower than the case of s-wave, the Sommerfeld enhancement is taken into account. Several numerical solutions have been implemented to obtain the Sommferfed boost factor. Two of them are compared as shown in Section 5.5. The analysis is performed with the Chi2 statistics for all the fermion final states. Then a combined analysis is done to take all the final states into account. There are three background models, so we perform a fit with each of them, and then show an exclusion plot and an improvement plot for each model. The results are summarized and discussed at the end before attaching the plots about all the final states.

To conclude, this work is focused mainly on the generic models of Dark Matter with all the recent data. This work shows a lot of models still could not be ruled out and are interesting to study and remain to be understood.

1.1 The ΛCDM cosmology

Einstein's gravitational field equation of general relativity is the sill of modern cosmology. If we consider a cosmological constant Λ as a term with negative pressure, namely dark energy, then the curvature of space-time is described as [1]

$$R^{\alpha\beta} - \frac{1}{2}g^{\alpha\beta}R = \frac{8\pi G}{c^2}T^{\alpha\beta} - \Lambda g^{\alpha\beta}, \tag{1}$$

where the left side contains the Einstein tensors including the curvature terms: Ricci scalar R and rank-2 Ricci tensor $R^{\alpha\beta}$, the $T^{\alpha\beta}$ on the right side is the symmetric energy-momentum tensor describing the mass-energy distribution in space, G denotes the gravitational constant, $g^{\alpha\beta}$ denotes the metric tensor.

In the Roberston-Walker space, if we introduce the Hubble parameter $H \equiv \dot{a}/a$ to consider the effect of expansion, and let the scale factor vary with time, then Equation (1) could be rewritten into a simple array of two ordinary differential equations:

$$\left(\frac{\dot{a}}{a}\right)^2 = \frac{8\pi G\rho}{3} - \frac{kc^2}{a^2} + \frac{\Lambda}{3}, \tag{2}$$

$$\frac{\ddot{a}}{a} = -\frac{4\pi G}{3}\left(\rho + \frac{3p}{c^2}\right) + \frac{\Lambda}{3}, \tag{3}$$

where $\rho = \rho_m + \rho_r$ denotes the matter and radiation density, p denotes the pressure, the spatial curvature $k = -1, 0, 1$, corresponding respectively to an open, flat, closed Universe.

If we describe the Dark energy term as $\rho_\Lambda \equiv \frac{\Lambda}{8\pi G}$ and consider the Universe to be isotropic and homogeneous, then the Einstein equation is simplified into the Friedmann equation, leading to

$$(\frac{\dot{a}}{a})^2 + \frac{k}{a^2} = \frac{8\pi G}{3}(\rho_m + \rho_r + \rho_\Lambda) = \frac{8\pi G}{3}\rho_{total}. \tag{4}$$

Now, with a relatively small number of parameters (ρ_b, ρ_m, ρ_Λ, $H(t)$, k, Λ) the standard model of cosmology can be built.

The CMB observations demonstrate that the Universe is flat [2, 3, 4, 5, 6], and the critical density could be defined as

$$\rho_{crit} \equiv \rho_{total}(k = 0) = \frac{3H_0^2}{8\pi G}. \tag{5}$$

We remark here the critical density contains all the energy with a given Hubble rate H. For a matter-dominated flat Universe, if we do not consider the Dark Energy, then $\rho_m = \rho_b + \rho_\chi$ is the sum of baryonic matter and Dark Matter.

The numerical value of the Hubble constant evaluated by combined analysis on the CMB is $67.4 \pm 0.5\, km \cdot s^{-1} Mpc^{-1}$ [6], which is lower than the local estimate using pulsating stars $73 \pm 1\, km \cdot s^{-1} Mpc^{-1}$ [7]. Despite the discrepancy, both measurements are precise. In this work, all the calculation is based on the parameters of the first analysis, in which the Dark Matter density $\Omega_{DM} h^2 = 0.120 \pm 0.001$, baryons density $\Omega_b h^2 = 0.0224 \pm 0.0001$.

1.2 Evidence of Dark Matter

1.2.1 Galaxy rotation curves

The word 'Dark Matter' originates from "matière obscure" in French and 'dunkle Materie' in German. The former was hypothesized by Henri Poincaré to discuss Lord Kelvin's estimation on the dark bodies which were supposed to compensate the needed mass to bound the visible stars in the Milky Way [8]. The latter was introduced by Fritz Zwicky in 1933 to name the missing mass in the Coma cluster [9]. Due to his pioneering application of the Virial theorem in his calculation, he surprisingly found the galaxies in this system move too fast to remain bounded by the visible mass. As in Equation (6), for a system with N objects, the averaged velocity squared is proportional to the total mass squared. If the Coma cluster is made only of atoms, then the stars and gases must have escaped from it by overcoming its influence of gravity. So a lot of invisible mass must exist to hold

the system gravitationally together. Although Zwicky's estimation of the mass-to-light ratio was too high, his work paved the way to a new understanding of the composition of the Universe, thus this is regarded as the first major observational indication of Dark Matter.

$$\frac{N}{2}m\langle v^2\rangle = \langle T\rangle = -\frac{1}{2}\langle U\rangle \propto -\frac{GM^2}{r}, \tag{6}$$

where r denotes the radius; T denotes the kinetic energy; U denotes the potential energy; M denotes the total mass.

It took about half a century for people to seriously consider Dark Matter to be the major contributor to the mass in the galaxies and the whole Universe. Between the 1930s and the 1970s, the work on the rotation curve of the Andromeda Nebula [10] and the approaching movement between the Andromeda galaxy and the Milky Way presented new evidence, both indicates most of the total mass is not contributed by the stellar mass in these objects. Strong evidence was rediscovered not until the 1970s and gained broad discussion. According to the Newtonian dynamics, similar to the Solar system, the rotation velocity of an object at large distances to the galaxy center is expected to be $v = \sqrt{\frac{GM}{r}} \propto \frac{1}{\sqrt{r}}$, so it should decrease at large r. However, flat rotation curves have been observed in spiral galaxies with great accuracy, $v \approx$constant at large distances. This intriguing discovery requires an explanation. The simplest hypothesis is also that an additional unseen component exists in the halo, and the mass-to-light ratio is large in the outer parts of the galaxy disks [12, 13]. After that, by combining measurements of 21 cm line of the hydrogen atom (H-I) on the outer parts and optical observations on disks and CO data for the central regions, more and more rotation curves have been observed, one of the recent update results is shown in Fig. 1.

1.2.2 Gravitational lensing

In Newton's *Opticks* in 1704 (page 132) [18], he has asked about the action of bodies upon light at a distance. This question was difficult to answer and lacked observational support in that epoch. According to the calculation in general relativity, Einstein has derived a deflection on light caused by the curvature of space around the Sun, and this prediction was proved to be a great success as it was confirmed in 1919 [19].

The photon trajectory is bent strongly for the light from a distant source if heavy masses exist between the source and the observer. These masses act like a lens, and then multiple images could form for the observer. This deflection is maximum for light transverse closest to the center of the lensing object and gets

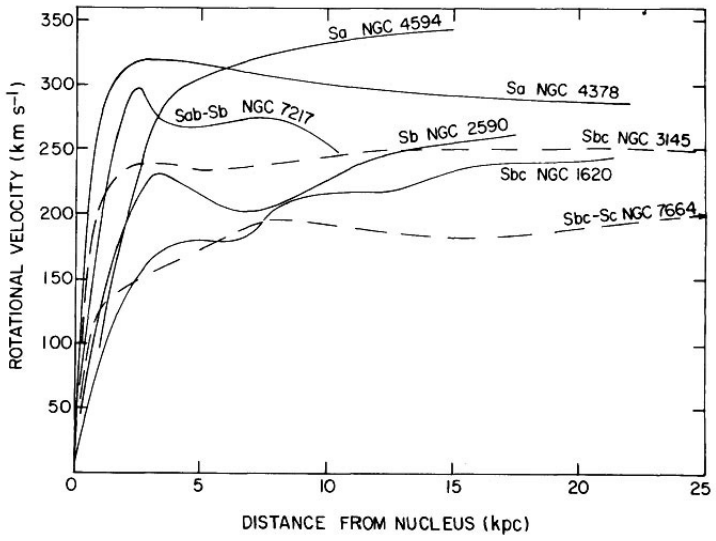

Figure 1: Rotation Curves of 7 galaxies of different Hubble type [14].

weaker if it is farther away from the center. So if the source is located exactly in the direction of the optical axis, then a ring shape of images could be observed. This is called the Einstein ring. For light from a very distant source, if it has passed a large target like a cluster of galaxies, the gravitational distortion of the image could be used to map the mass distribution in the cluster [20].

So the gravitation lensing is a unique probing tool of the observational cosmologist and Dark Matter searchers [21]. The qualification of mass distribution in the galaxies can clearly demonstrate the existence of Dark Matter. There are many observational images to prove it. Two examples are shown in Fig. 2. The lensing effect is evident in this image, according to the calculation in Ref. [22], defining the radius r_{200} of the sphere enclosing an average density $200\rho_{crit}$, the mean mass-to-light ratio of the overall cluster is $35 \pm 5\, M_\odot/L_\odot$ at the r_{200}. This is strong evidence of Dark Matter in this cluster. This result is based on a reasonable NFW density profile over $0.1\, Mpc < r < 5\, Mpc$. The decline of mass density at the large galactocentric radius is a strong constraint on the theory of cluster formation. But in that work, the density profile declines with a power-law index $n > 2.4$, the near-isothermal slopes are rejected. The constant mass-to-light ratio at large radius also shows Dark Matter and baryons coupled tightly in a huge range of environmental densities, so clusters must be growing via accretion of groups, not individual galaxies, which offers information of the characteristics of Dark Matter.

Figure 2: Examples of gravitational lensing.
Left: The Cluster Cl 0024+1654 at z = 0.4 as an example of gravitational lensing. This image was photographed with the Wide Field Planetary Camera 2 on NASA's Hubble Space Telescope. There are several Einstein's rings in this image, including the blue spiral galaxies. They are repeated around to form the shape of a ring. This helps us to study the Dark Matter distribution in this cluster [22].

1.2.3 The Bullet cluster

After the Big Bang, there is no event more energetic than the merges of galaxy clusters. The strong emissions in a broad range of wavelengths and distortion of space make them unique cosmological laboratories to test the hypothesis. With high-resolution optical and X-ray telescopes, the baryonic distribution can be imaged; with weak lensing, the total mass distribution in the clusters could be reconstructed. The combination of X-ray observations and weak lensing gives information about the galactic halo properties in the clusters. One of the most famous events is the merging image of the Bullet clusters. The Bullet cluster consists of two large subclusters. As shown in Fig. 3, the distribution of mass in the merging of the two clusters is shown in two colors. The pink region is the hot gas observed by the Chandra X-rays telescope, the blue region is the total mass imaged by weak lensing. The two parts of the shock do not overlap. This result proves only a small proportion of mass in the Bullet cluster is attributed to luminous baryonic matter; most of the mass in this system is non-baryonic [17]. This is considered as a direct proof of Dark Matter. And since the mass distribution coincides with the galaxies, the self-interaction of the non-baryonic matter must be tiny. Otherwise, it must have been separated from the galaxies. A drag force slows the baryonic matter in this event, and Dark Matter has a weak coupling with baryonic matter and itself, so the Dark Matter in the Bullet cluster moves faster than the baryonic matter. This result in the separated distribution of them shaped a bullet as shown in Fig. 3.

Figure 3: Image of the Bullet cluster. Two merging subclusters passed through each other. The pink region is the X-ray emission from the hot gas observed by the Chandra telescope [11]. The blue part is observed through the gravitational potential from weak lensing [15, 16]. This result shows most of the mass of the cluster is not attributed to the baryonic matter. It is a direct proof of Dark Matter.

1.2.4 Large scale structure and N-body simulation

While the rotation curves gained more interest, the study on the Dark Matter in the galaxy halos was also carried out, the theory of missing mass in the halos was augmented and started to be accepted [24, 25, 26, 27, 28].

Press and Schechter developed the first N-body simulation by implementing a Gaussian initial density to model the expansion and the gravitational evolution of cosmic structure [29]. All the following progress also depends on idealized initial conditions. The debate between the adiabatic and isothermal models of perturbation has lasted for a long time since the first one supposed the small-scale fluctuation of the structure was erased in the later time and the second claimed the small-scale fluctuation has survived [30]. With later achievements in particle physics and cosmology, the neutrino decoupling was believed to be able to provide the energy density as a seed of quantum fluctuation; meanwhile, the non-baryonic massive Dark Matter could also decouple earlier [31]. This hypothesis inspired the classification of Dark Matter candidates from light to heavy particles: hot Dark Matter (HDM), warm Dark Matter (WDM), cold Dark Matter (CDM). These candidates are supposed to produce different histories: for HDM, superclusters were formed earlier and then collapsed to form galaxies; for WDM and CDM, both could form small objects and then hierarchically aggregate and merge to form larger and larger structures. But only CDM could form systems significantly smaller than galaxies, and WDM halos are less concentrated than CDM halos

and allow fewer substructures [32]. For more characteristics of the candidates, cf. section 1.3.

The 3D survey offers a tool to verify the proposals of inflationary fluctuation generation. The effectiveness of the cosmological models is evaluated by confronting the data of surveys with the Dark Matter candidates. For example, the Center for Astrophysics (CfA) galaxy redshift survey shows a discrepancy with the N-body simulation for the HDM, the large and well-defined scale produced by the free-streaming cut-off in the power spectrum is different from the real Universe, this result has eliminated the HDM [33]. The Sloan Digital Sky Survey (SDSS) provides uniquely powerful and versatile data using a 2.50-meter telescope to cover the north Galactic cap up to 35% of the sky, and it images the sky in both photometric and spectroscopic modes, data of around 1 billion objects including stars, galaxies, quasars have been collected [34].

One of the most powerful N-body simulation tools for large-scale structure is the Millennium simulation, which can run a model with more than 10 billion particles in a 2 billion light-years scale to trace the formation history of different scale structures during the evolution of the Universe, such as the Dark Matter substructure in the galaxies, the cluster merges [35]. One of its successes is the realization of a virtual telescope to construct a galaxy map, then the properties of these galaxies and large-scale structure could be compared directly with the real spectroscopic surveys [36]. A representative result of the Millennium simulation is shown in Fig. 4. This result shows a striking structure similarity between the observation and the prediction in the ΛCDM model.

Although the previous simulation results favors the ΛCDM paradigm, only specific and particular problems have been treated in them. The Illustris project aims to make a hydrodynamical simulation to take complex physical processes into account. Accurate and efficient computational methods have been developed for this purpose, so better mock observations will lead to a better understanding of the composition of the Universe [37, 39, 40].

1.2.5 The CMB observation

The Big Bang theory provides a scenario that the Universe could be traced back to 13.8 billion years ago to a primordial origin. It has passed multiple phases in the timeline of expansion [1, 41]. In the early Universe, Cosmic inflation started after about 10^{-35}s. After $3.72 \cdot 10^6$ years, the hot and dense plasma has been cooled down enough ($\sim 3000\,K$ or $\sim 0.26\,eV$), so the charged subatomic particles did not interact with the photons anymore, and the neutral atoms started to be formed by electrons and baryons; this is called the 'Recombination epoch'. These atoms lost their energy to reach a ground energy state by emitting photons. As a result, the photons decoupled from the bath and became freely propagating in the space. And the Universe was no more opaque but transparent. These CMB photons

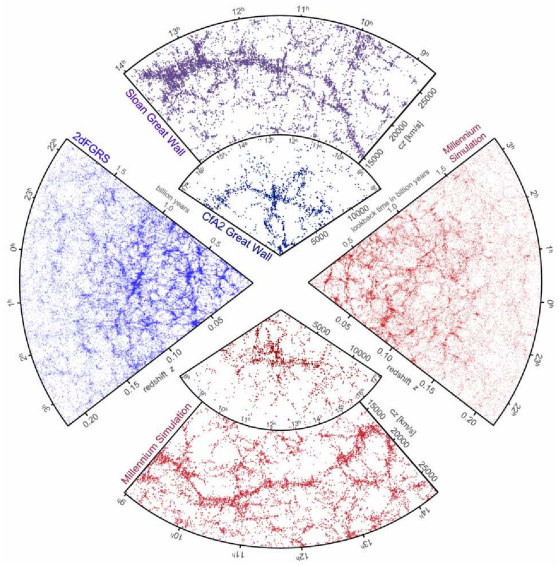

ass.

Figure 4: The galaxy distribution is obtained from spectroscopic redshift surveys and mock catalogs which is constructed from N-body cosmological simulations with the "Millennium" code applying semianalytic techniques [38]. The small slice on the top shows the "Great Wall" centered on the Coma cluster. It is a subregion observed by CfA2. On the same scale, the "Sloan Great Wall" observed by SDSS in the northern sky is shown in the big slice on the top. For the southern sky, one-half of the 2dFGRS is shown on the left cone. These surveys could be compared with the mock catalogs at the bottom and on the right.

have been redshifted since that time, and the wavelength increases as time goes on, the temperature of this black body radiation today reaches $T_0 = 2.727\,K$ or $0.235\,meV$. These relic photons from the early Universe reach us and become a faint noise background in the radio telescope. So by tracing back with these CMB imprints on the last scattering surface, we achieve to extract the information about the initial condition of the Universe.

This Big Bang hypothesis gains support since the Hubble rate is observed, and the thermal black body spectrum predicted has also been observed. A strong proof is the anisotropies in the CMB, which have already been confirmed by several observations. [2, 3, 4, 5, 79, 56].

All the important information of the CMB could be extracted from the power spectra. Right at the moment of recombination, the temperature distribution is isotropic. As time goes on, the anisotropies in the CMB become complex. It is caused by the combination of several factors: the pressure of photons and attraction of baryons in the hot plasma from acoustic oscillations made a spatial variation in the CMB temperature; this causes the primary anisotropy. The location of the peaks in the angular power spectrum shows us details about the perturbation. The secondary anisotropy appeared later after the recombination. The photons lost energy through Thomson scattering on the unbounded electrons, leading to large-scale anisotropy in polarization and a modification on the CMB.

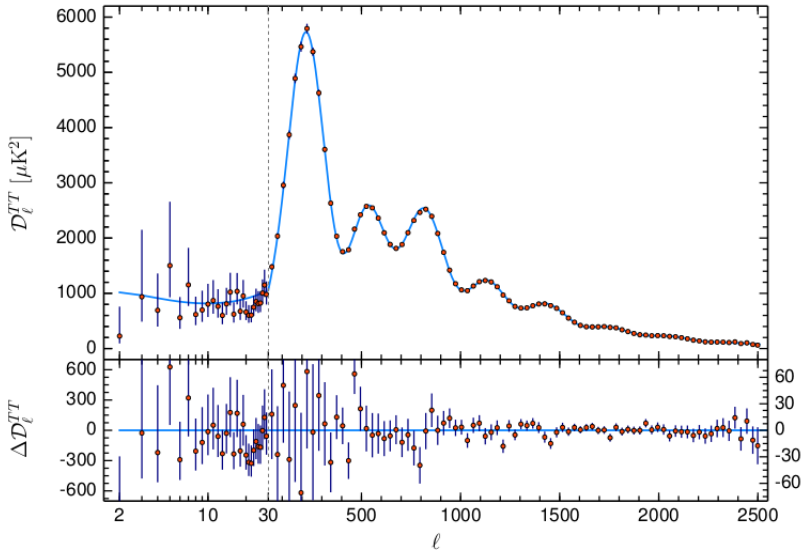

Figure 5: The temperature power spectrum obtained by the PLANCK collaboration in 2018 [6].

This prediction has also been confirmed by the WMAP [77]. The motions of the earth and the Local group also make an anisotropy in the CMB data [78], etc.

The tiny density fluctuation on CMB was firstly found by COBE in 1992 [2]. The harmonic peaks of multipole in Fig. 5 are found by the MAT/TOCO experiment [3], the Wilkinson Microwave Anisotropy Probe (WMAP) [4, 5], the PLANCK satellite, and the other experiments [6, 42, 43, 44].

The peak locations in the temperature power spectrum (as shown in Fig. 5) obtained by PLANCK prove the density perturbation is adiabatic. The energy density ratio of Dark Matter to radiation changes a lot of the peaks. The first peak proves the spatial curvature of the Universe is 0, so it is spatially flat. The second peak indicates substantial amounts of baryonic dark matter. The third peak indicates the dominance of Dark Matter before the recombination. The density of Dark Matter could not be affected by photon pressure. From the height of the third peak, an evaluation of the composition of the mass/energy shows the Universe is made of 26.8% Dark Matter, 4.9% ordinary matter, 68.3% Dark Energy [6].

To conclude, the CMB observation offers strong support for the Big Bang cosmological model, especially the ΛCDM model; no other theory could give a better interpretation of the CMB observations.

1.2.6 The other explanations

Although the hypothesis of Dark Matter is implied by the theory and inspired naturally by all these observations, there are still some other interpretations without Dark Matter, such as the Modified Newtonian Dynamics (MOND), which is well known as a natural modification of gravity at large scale [45]. However, the MOND is Newton's law modified at small acceleration; it could not be tested on a large scale since it is non-relativistic, so it could not explain the other observations except the flat rotation curves. Generalized MOND could also explain CDM with only gravitational force and the missing mass in the clusters, but it is inconsistent with all the data [46]. MOND can neither explain the observation of the Bullet cluster, nor the CMB observations.

The laws of gravity can also be tweaked on a large scale, this leads to the "fifth force". Screening mechanisms are developed to change the fifth force in high-density regions. The Vainshtein screening mechanism is an old idea to suppress the fifth force [55]. The simplest modification is called bimetric gravity, or bigravity. Recent progress shows the gravitational potential in bigravity allows it to form a Vainshtein sphere with a radius r_V. Within r_V, the lensing potential in bigravity is the same as that in GR. Outside r_V, dense and compact objects form the sphere changes the long-range behavior of bigravity, a stronger lensing potential is thus formed. The outer mass does not affect the plasma cloud in the sphere. This theory is consistent with the Bullet cluster. And much less Dark Matter or even no Dark Matter is required by the Vainshtein screening to explain galaxy rotation curves. But the CMB and structure formation remain challenging to explain [56].

In brief, there are some interesting attempts to explain all the observations above in the absence of Dark Matter, but none of them can replace Dark Matter's role.

1.3 Dark Matter candidates and status of searches

Dark Matter has been observed in only gravitational effect with ordinary matter, so it should be electrically chargeless, colorless. The merges of clusters demonstrate Dark Matter must be collisionless or at least no too collisional with normal matter. It was produced in the early Universe, it is thus stable, and its lifetime must be comparable with the age of the Universe. The BBN and CMB observation allow only non-baryonic candidates.

Dark Matter contains a large family of different types of candidates. A classification depending on the velocity is shown in Section 1.2.4. An incomplete list of Dark Matter candidates is shown in this section.

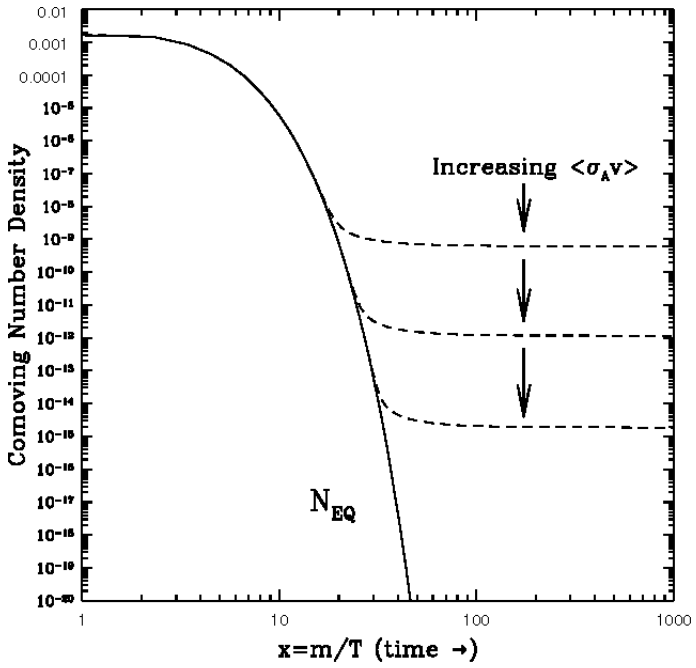

Figure 6: The thermal freeze-out mechanism [57].

1.3.1 The WIMPs

In the ΛCDM cosmology, after the Big Bang, it is natural to introduce a straightforward mechanism to produce Dark Matter, and consider Dark Matter as a thermal relic of the freeze-out [57]. In supersymmetry, the hypothetical weakly interacting massive particle (WIMP) is compatible with the unification of the gauge coupling and the hierarchy problem. WIMPs have been the most popular Dark Matter candidate since the 1980s, and immense experimental efforts have been made to look for it.

In the beginning, all the particles were in thermal equilibrium. They could be created or create the other particles through annihilation and decay; their comoving number densities were almost constant. As time went on, when the temperature decreased during the expansion, the interaction rates decreased as well, and the equilibrium could not be kept anymore. The unstable particles decayed or annihilated into stable particles, the stable particles 'freeze-out' and their comoving density got asymptotically constant, and the relic abundance could be observed today. As shown in Fig. 6, the relic abundance depends on the annihilation cross section, for a conventional calculation, the annihilation cross section of WIMP is supposed to be $\langle \sigma v \rangle \simeq 2.7 \cdot 10^{-26}\, cm^3 s^{-1}$ [58]. This is the so-called 'WIMP miracle'.

The freeze-out temperature of Dark Matter could be obtained by solving the Boltzmann equation of Dark Matter, a standard Boltzmann equation reads

$$\frac{dn_x}{dt} + 3Hn_x = -\langle\sigma v\rangle(n_x^2 - n_{eq}^2)\,, \tag{7}$$

where n_χ denotes the number density of Dark Matter, H denotes the Hubble constant, n_{eq} is the Dark Matter density in thermal equilibrium, $\langle\sigma v\rangle$ denotes the annihilation cross section.

The freeze-out moment is characterized by the variable $x = \frac{m_\chi}{T}$; it is found to be around 25-30. A standard solution to the Boltzmann equation is shown in Chapter 3.

Decades of efforts have been made to look for the experimental signature of the WIMP, including generally three approaches depending on the timeline direction of the Feynman diagram: indirect detection, direct detection, and collider-based detection.

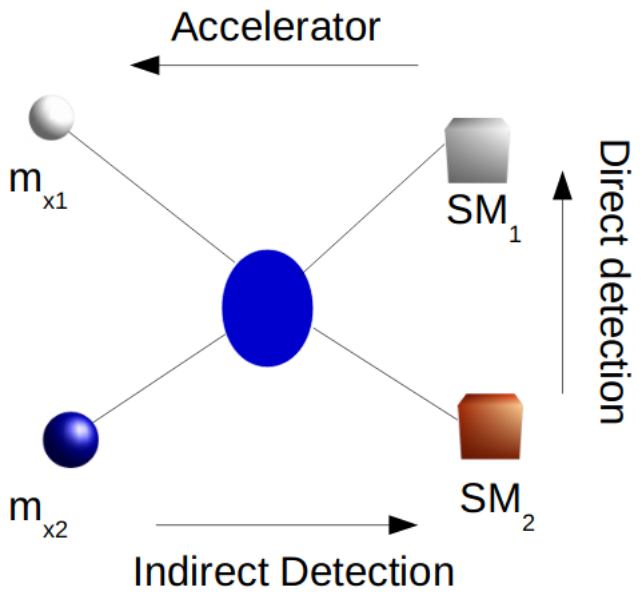

Figure 7: Schema of the three approaches to WIMP detection. Here $m_{\chi 1}$ and $m_{\chi 2}$ denote the two Dark Matter particles, SM_1 and SM_2 denote the two SM particles, the blue ball in the middle represents the intermediate processes. Dark Matter particles (right) annihilate into SM particles (left). The primary and secondary particles are expected to be detected in indirect detection. Accelerators produce relativistic SM particles (right) to annihilate into Dark Matter particles (left). The signal is expected in the collider-based experiments. From the lower to the upper, or inversely, the signal induced by the Dark Matter-nucleon scattering is expected in the cryogenic detectors; this is the case of direct detection.

Indirect detection of Dark Matter studies the primary and secondary particles produced in Dark Matter annihilation and decay. Cosmic ray and gamma-ray detectors have been developed to accumulate flux induced by these processes. Space telescopes and ground-based Cherenkov telescopes are expected to extract a signal from the huge background. The complementary work of the existing experiments and observations has excluded Dark Matter below about 120 GeV,

cf. Chapters 2 and 3. And the planned experiments will improve the sensitivities up to several hundred TeV, cf. Section 6 of Chapter 3.

Direct detection experiments look for the signal induced by the Dark Matter scattering on the nuclei of target material in the sensitive cryogenic detector. They provide the most stringent constraints on Dark Matter-nucleon scattering. The scattering cross section on neutron and protons are very tiny for both spin-dependent and spin-independent interactions. The strongest constraints for spin-independent interactions are obtained by Xenon1T that has performed searches down to sensitivities around $4.1 \cdot 10^{-47}\, cm^2$ in the range under 1 TeV [63]. For spin-dependent interactions, the corresponding limit is below $6 \cdot 10^{-42}\, cm^2$. PandaX-II and LUX have very similar sensitivities in the same energy range as Xenon1T [64, 65]. These instruments start touching the irreducible solar neutrino background, but no signal has been captured.

Collider-based experiments accelerate SM particles to the relativistic speed to simulate the state in the early Universe; the annihilation of SM particles reproduces Dark Matter, then missing transverse energy is expected to be detected. But until now, only null results have been found, ATLAS and CMS failed to find any supersymmetric particle in the range up to several hundred GeV [66, 67]. The planned collider like the ILC [141] may help to understand better in similar energy range, but none of the plans will for sure be put into practice.

Briefly, there is no favorable result supporting the existence of the WIMPs up to several hundred GeV. With the upgrade of the LHC or any other planned collider or more sensitive astrophysical experiment, WIMPs will soon be proved or be moved off the table. We will witness the discovery or the decline of the WIMP paradigm [68]. Otherwise, we should look for the superheavy WIMPzillas candidates [69], but no experimental data has been obtained to test it until now.

However, all these results are based on the standard WIMP hypothesis. Some WIMP models could not be excluded in these experiments. A very interesting example is the p-wave annihilating dark matter, for which the scattering rate and production rate are highly suppressed since the coupling between p-wave Dark Matter and SM particles is extremely tiny. So it is not accessible in direct detection or collider-based experiments [70], but possibly be observed in indirect detection if there are some large boost factors. For more details, cf. Chapters 4 to 5.

1.3.2 The non-WIMP Dark Matter candidates

WISPs The weakly interacting slim particles (WISPs) is a family of prominent candidates, including QCD axions, axion-like particles (ALPs), and hidden photon [71, 72].

Peccei and Quinn found a solution to the strong CP problem by introducing a new global chiral U(1) symmetry in the strongly interacting sector, which is spontaneously broken at the energy scale f_a by the vacuum expectation value (VEV) of a complex scalar field. This suggests a pseudo-Nambu-Goldstone boson

which a mass $m_a \simeq 5.7 \cdot (\frac{10^{12} GeV}{f_a})\, \mu eV$ [73]. In the early Universe, $T \sim f_a$, the axion was massless; it is a non-thermal relic product. When the temperature cooled down to the QCD energy scale, its mass is dynamically generated as the curvature of potential was tilted due to QCD instanton effects. The oscillation around the minimum has a behavior of CDM. The axion mass is predicted to be in the range 30 $\mu eV \lesssim m_a \lesssim$ 130 meV [74]. The couplings of the QCD axion to radiation and matter is proportional to $\frac{1}{f_a}$, the axion-photon coupling $g_{a\gamma\gamma}$ is especially interesting to the axion hunters.

Axion-like particles (ALPs) are pseudo-Nambu Goldstone bosons appearing in various models. ALPs are similar to axions but have wider parameter space as there is no relation between their masses and coupling to photons. ALPs-photon coupling changes the transparency of the Universe and provides an observable.

The detection of Axion and ALPs mainly uses the photon-axion conversion. With cosmological and astrophysical observations and laboratory experiments, limits on the axion mass and the ALPs mass are established. The sensitivities in recent experiments reach $g_{a\gamma\gamma} \simeq 10^{-15}\, GeV^{-1}$ around $3 \cdot 10^{-6}\, eV$ in the haloscopes ADMX [61, 62, 83]. The study on the gamma-ray spectral modulations of Galactic pulsars found the most-likely Alps mass is around $3.6\, neV$ with $g_{a\gamma\gamma} \simeq 2.3 \pm 0.4 \times 10^{-10}\, GeV^{-1}$ at the 5.52σ level, but this signal is in tension with the limits obtained with the CAST helioscope [84].

Ultra-light axions are Dark Matter candidates with a mass $m \gtrsim 10^{-22}\, eV$, they are able to deal with large-scale problems and solve the small scale problem. Study on the effective Particle-Particle interaction is applied to make N-body simulation of the ultra-light axions. The results show a solitonic core forms at the halo center, and this core is able to solve the cusp-core problem [86]. Ultra-light axions have a de Broglie wavelength in the scale of kpc, and it is expected to produce an enhanced signal in periodic oscillations. It could be detected using gravitational wave laser interferometers [87, 88].

Hidden photon is an Abelian boson that kinematically mixes with the SM photon, it can be understood as a particle similar to a normal photon, but it has a finite mass and couples only with charged SM particle. The coupling between the hidden photon and charged particle is suppressed by the small kinetic mixing parameter [89, 90]. The small coupling with charged particles makes the conductors almost transparent to the hidden photons, and also leads it possible to be detected by looking for weak excitation in electromagnetic systems. With a resonant electromagnetic detector in an electromagnetic shield, the hidden photon field can penetrate the shield and move the charges, thus the magnetic field inside is modified. The recent results on WISPDMX have extended the search range down to 0.4 neV, a signal candidate around $0.901 \mu eV$ needs to be checked in the future [91]. The BRASS experiment works in the non-resonating mode, it will broaden notably the sensitive range [74].

SIDM The self-interacting Dark Matter is another popular candidate. It is assumed to have self-interactions to solve small-scale crisis for standard CDM, including the core-cusp problem [47, 48, 49], missing satellite problem [50, 52],

too–big-to-fail problem [51, 52, 53, 54]. The scattering cross section of SIDM is velocity-dependent. A light mediator is usually considered to couple with SM particles. If the SIDM is a fermion, then the annihilation is a p-wave process that can be boosted by the Sommerfeld enhancement [75]. Expensive simulation work provides proof that a cross section per unit mass $\sigma/m \simeq 1cm^2/g$ appears capable of reproducing consistent results with observations on the core sizes and central densities of dwarfs, LSB galaxies, and galaxy clusters when there is no velocity dependence [76]. And $\sigma/m \gtrsim 0.5cm^2/g$ is required by the dwarfs and LSB galaxies for velocities in the range of 30-100 km/s [75]. However, on the cluster scales, different constraints are obtained, such as $\sigma/m < 1cm^2/g$ in Ref. [79]. Despite the progress in the simulation work with SIDM, there is no experimental signature of SIDM. Recent progress show that self-interaction may couple to SM particles through variable interactions such as the Higgs portal, kinetic mixing, and the other renormalizable process. It can also be in the framework of WIMP when Dark Matter mass is large than 10 GeV [80], and light SIDM is expected to produce a detectable signal in electron recoil [81]. By combining constraints of a dedicated study of BBN and direct detection, most of the model's parameter space with significant self-interaction is ruled out, leaving only a small region around $m_\chi \simeq 0.5$ GeV, $m_{med} \simeq 1.1$ MeV to be allowed [82].

Sterile neutrinos It is not clear whether the Higgs mechanism applies to neutrinos as the other fermions or not. By adding new degrees of freedom to the SM, new particles may help to solve the Dark Matter problem, so sterile neutrinos are hypothesized as WDM to overcome the shortcomings of the standard model neutrinos, they were born relativistic and were never in thermal equilibrium. The searches for sterile neutrinos are model-independent. With NuStar, the 3.5 keV excess (11σ) has been observed [59, 92] in the galaxy clusters, Andromeda and the Milky Way galaxies. This sparked wide interest, but it may come from other effects like the atomic transition, and the statistical fluctuation and systematic uncertainties make it difficult to make a convincing interpretation. And this line has not shown presence in the other Dark Matter-dominated objects. Future observation in indirect detection and direct detection, such as the spectroscopic data on the Lyman α forest, β-decay spectra, scattering, or captures on nuclei in laboratory experiments will help to make a better understanding.

ADM The asymmetric Dark Matter (ADM) assumes a matter-antimatter asymmetry. It uses higher dimension operators in the coupling between ADM and baryonic matter. In Ref. [97], ADM is supposed to be around a few GeV, $m_{ADM} \simeq q_{ADM} \cdot (1.6\text{–}5)$ GeV for the late time-fractional asymmetry to be completely asymmetric, where q_{ADM} denotes the dark-baryonic charge. This is interesting since anomalies have been observed to locate in this range in direct detection. ADM could be a prototype of self-interacting Dark Matter (SIDM), so it explains more adequately the small structure than symmetric CDM. One difficulty to capture ADM signal is caused by its low annihilation signal, but if ADM decays into SM particles via flavor-dependent coupling is kinematically allowed. Then energy-dependent asymmetric SM products could be produced, this could

be a powerful signature of flavor-violating decaying DM, and could be used to explain the matter-antimatter excess found by AMS-02 or FermiLAT.

SM Neutrinos The standard model neutrinos used to be considered as a DM candidate if they have nonzero rest mass, but the upper limits of neutrino mass is too low compared with the requirements of the observation, such as the primordial nucleosynthesis, the gravitational roles in dwarfs, the upper bound of the sum of neutrinos [59, 98]. The stringent constraint on the neutrino relic density suggests $\Omega_\nu h^2 < 0.0067$ at a 95% confidence level, which is inconsistent with the Planck observation[6]. Neutrinos decoupled relativistically, so it is an HDM candidate. And N-body simulations combined with the 3D surveys also have made losses of interest in the HDM candidates. All this indicates neutrinos are not suitable to be Dark Matter or could not make up 100% of Dark Matter. However, recently the extended BAHAMAS simulations have revisited the CMB-LSS tension [60], this result form hydrodynamic computation suggests massive neutrinos are still possible a part of Dark Matter.

PBH Primordial black hole (PBH) is another non-particle Dark Matter candidate, PBHs are supposed to be made before big-bang nucleosynthesis. There are various proposed mechanisms of PBH creation corresponding to masses in the range of $[10^{-18}M_\odot, 10^6 M_\odot]$, and a large portion or even all of the Dark Matter in the Universe is expected to be constituted by PBH. PBH became an important candidate with the discovery of gravitation wave (GW) on the Advanced Laser Interferometer Gravitational-Wave Observatory (LIGO). Other GW experiments are also looking for the signal of PBH. The maximal sensitivity of LISA can verify the existence of PBH mass $\sim 10^{-12}M_\odot$ if it was formed via scalar-perturbation enhancement [94]. But recent progress shows stringent constraint on PBH, pure PBH Dark Matter is excluded in the initial range $[10^{-5}\,M_\odot, 10^2\,M_\odot]$ for local density contrast $\delta_{dc} > 10^4$, this is also valid for smaller initial density contrasts with fewer conservative assumptions [95]. Multi-wavelength astronomical data shows PBH could make up to 10^{-3} relic density of Dark Matter, thus disfavors strongly the PBH to constitute a significant of DM in the mass range of interest [96].

MACHOs The massive compact halo object (MACHO) is any kind of dark body such as brown dwarfs, stellar black holes, neutron stars, etc. It plays a role of Dark Matter in the galaxy halos, it is supposed to be composed of normal baryonic matter but not luminous, so no radiation is emitted from it. Direct Studies on CMB, LSS, and observation of baryon abundance do not support MACHOs to be Dark Matter. Recent work on ultra-faint dwarfs, microlensing, wide binaries set limits on MACHOS of masses and rule out MACHOs with mass above $10^{-7}M_\odot$ [93].

Chapter 2 DarkSPIDER methodology

DarkSPIDER is a multi-functional and simply structured tool for Dark Matter searches. It was initially an extension of the AstroFit package [100]. AstroFit is a statistical Fortran tool developed for Dark Matter phenomenology by applying the Chi2 statistics to find the best-fitting parameters. AstroFit employs DarkSUSY to feed particle models and cosmological predictions. AstroFit is specially designed to collect constraining limits from observations and experiments. Data from indirect, direct detection, collider-based experiments, and the relic density are accumulated in AstroFit.

When the work on DarkSPIDER was started, the results on the LHC with p-p collision energy at 13 TeV failed to find any evidence of Supersymmetric Dark Matter particle. The results on the CMS detector excluded neutralino up to 430 GeV [101], and the results on the ATLAS detector excluded neutralino up to 550-850 GeV[102]. At that moment, the generic models were not yet implemented in DarkSUSY. The old models involved in DarkSUSY appeared not as intriguing as before. So we decided to jump out of DarkSUSY and work on the generic and specific models. The former allows having a global view of Dark Matter searches, while the latter provides information about some previously ignored models. As a consequence of this decision, DarkSPIDER becomes an independent tool that consists of particle models, astrophysics and cosmological models, data analyzing tools. So it can analyze input data from experiments independently and keeps open to external model building packages.

2.1 Structure and functionality

Since it is difficult to draw a simple frame of this package, it is necessary to briefly present in this chapter the essential parts to understand how DarkSPIDER is organized and how to work with DarkSPIDER. A manual has been finished for more details. The physics involved in this work is described in the next chapters to focus on specific topics.

2.1.1 Particle models

There are two families of Dark Matter models implemented in DarkSPIDER: the effective field theory (EFT) and simplified models. The EFT and simplified models of dark matter are model-independent approaches [103, 104, 105, 106]. They contain some well-motivated candidates and provide generic descriptions of

unknown interactions between dark matter and standard model particles. The EFT adds only two degrees of freedom: the mass of dark matter and the coupling strength. The EFT is only valid for heavy mediators, which is believed to be a drawback in the Dark Matter searches on the colliders. We keep utilizing the EFT and simplified models since they are the most model-independent tool with the least number of dimensions of parameter space to scan. Simplified models are established to adapt to new search strategies and experimental data. It is between the effective approach and the UV complete models, by adding a mediator into the effective operator. Simplified models are essential in this work since the mediator is introduced to compute the boost factor of the Sommerfeld enhancement. However, the EFT still plays a unique role in the p-wave searches, since a list of p-wave models in the EFT could be found, the information about the p-wave models is complete in the framework of the EFT.

For the EFT, 57 models are collected to calculate Dark Matter annihilation from Ref. [103, 104, 105, 106], including 13 scalar Dark Matter models (s-0), 27 fermion Dark Matter models (s-1/2), 17 vector Dark Matter models (s-1). Especially, both s-channel and t-channel interactions have been considered as shown in Ref. [105]. For direct detection, DarkSPIDER contains 2 scalar Dark Matter models, 5 fermion Dark Matter models, 4 vector Dark Matter models, 5 s-3/2 Dark Matter models. The connections with EFT is computed for simplified models, as shown in Chapter 3. A simplified p-wave Dark Matter model is added as well. Its applications are presented in Chapters 4 and 5.

Some previous work on similar topics is involved in Ref. [106] to discuss the application of EFT and simplified models, which gives an overview of generic models to compare their advantages and drawbacks. Subsequently, it is implemented to compare the CTA sensitivity with direct detection and collider experiments. The limitations of EFTs are shown, and compelling improvements have been done with simplified models in Ref. [107].

To improve the precision of computation, both exact formula and approximative expressions have been developed. For example, in the calculation of the annihilation cross section, the exact formula of the annihilation cross section can be called. Meanwhile, the approximative formulae are also implemented. For most of the models, the Taylor expansion is applied to express the annihilation cross section as a function of the relative velocity. The formulae of 2nd order and 3rd order expansion are added to the package. The corresponding 1st, 2nd, 3rd order terms are called the s, p, d waves. There are in total 214 formulae to calculate the annihilation cross section to be chosen.

Before using a Dark Matter model, it is necessary to define the parameters, such as the mass of Dark Matter, mediator (or the coupling strength). There are two types of couplings between Dark Matter and SM particles: when the coupling strength is independent of the mass of the final state particles, it is the case of universal coupling; when the coupling strength is proportional to the mass, it is the case of Yukawalike coupling. It is defined as coupling = 1 for the former case, and coupling = 2 for the latter case.

2.1.2 Astrophysics and cosmology in DarkSPIDER

As described in Chapter 1, the investigation of Dark Matter originates from astrophysical observations and cosmological simulations. To study the properties of Dark Matter, there are some essential calculations in the two aspects.

All the Dark Matter candidates in DarkSPIDER are thermal relics. The freeze-out moment is characterized by the $x_f = T_f/m_\chi$, with T_f the freeze-out temperature. The value of x_f can be obtained by solving the Boltzmann equation. For annihilation, there are three numerical solvers to deal with this problem. Only when the three methods produce the same result, their outputs could be trusted and used in the next steps of calculation (see next subsection). For coannihilation, the same solvers could be called as well. But the corresponding Boltzmann equation is different. Different derivatives of the Boltzmann equation are implemented as described in [103, 118].

One of the most intriguing Dark Matter candidates to treat is p-wave Dark Matter. The annihilation of p-wave Dark Matter is influenced by the velocity dispersion in the target. To obtain a precise velocity distribution, an N-dimension scan is established to find the best-fitting parameters. There thus exists a detailed study on galactic dynamics in DarkSPIDER. The corresponding details are in Chapter 4.

Another topic that has been treated in DarkSPIDER is the IGRB constraints on p-wave Dark Matter. To study it, the density profile, the halo mass function, the clumpiness boost factor, the inverse Compton scattering on the CMB radiation bath, and the other functions are involved as well (for more details, cf. Chapter 5).

2.1.3 Numerical and statistical tools

The numerical methods in DarkSPIDER are based on some well-known algorithms from Ref. [119].

The integration in DarkSPIDER is performed with four methods: the Simpson's 1/3 rule, the Simpson's 3/8 rule, the Trapezoidal rule, the Gaussian Quadrature rule. Each important integration in DarkSPIDER could be checked by comparing the results from these integrators.

For the differential equations, four algorithms are applied: the bisection method, the iterative method, Newton's method, Runge-Kutta methods. For example, when solving the Boltzmann equation of Dark Matter, the first three algorithms are utilized. When computing the Schrödinger equation to obtain the Sommerfeld factor, Runge-Kutta's method is called, the Rungekutta solver is developed.

There are some specific functions in DarkSPIDER quoted from the existing packages. For example, the Jacobi polynomials are from Ref. [120], the psi function and the hypergeometric function are both from Ref. [121], the Γ function is from Ref. [108, 122].

The χ^2 statistic is applied in this work to evaluate the goodness-of-fit of the

data to an N-parameter model,. With the measured values and uncertainties, the expected values predicted by the theory are compared with binned data, then χ^2 is the sum of all the bins [123]. The corresponding formula to fit a set of data with N bins is given by

$$\chi^2 = \sum_{i=1}^{N} (\frac{x_i - \mu_i}{\sigma_i})^2. \tag{8}$$

In the ith bin, μ_i is the theoretical expectation, x_i is the experimental data, and σ_i is the uncertainty.

By varying the parameters of the model, the best-fitting parameters can be determined by finding the minimal χ^2. The minimal χ^2 corresponds to the point where the difference $x_i - \mu_i$ can be seen as statistic fluctuation.

The confidence levels could be determined by the $\Delta\chi^2$ technique. They are widely applied in Dark Matter searches. In direct detection of Dark Matter, the upper limits on the scattering cross section can be set. For indirect detection, both confidence contours and upper bounds are set. The calculation of $\Delta\chi^2$ is established as follows:

$$\chi^2 = x^2_{min} + \Delta\chi^2. \tag{9}$$

The confidence levels depend on both the value of $\Delta\chi^2$ and the number of parameters. The corresponding value of $\Delta\chi^2$ is listed in Table 1 [124].

Standard deviation	Confidence level	$\Delta\chi^2$ for 1 parameter	$\Delta\chi^2$ for 2 parameters
1σ	68.27%	1.0	2.3
1.645σ	90%	2.71	4.61
1.96σ	95%	3.84	5.99
2σ	95.45%	4.0	6.18
3σ	99.73%	9.0	11.83

Table 1: The confidence levels and the corresponding values of $\Delta\chi^2$ and standard deviation in the case of 1 or 2 parameters.

2.1.4 Data

To gather more information as possible, constraints and sensitivities from all the recent experiments and observations are accumulated in DarkSPIDER, including data as follows:

- Indirect detection (FermiLAT [111, 127], HESS [125], CTA [126], MAGIC [127], IceCube [128], AMS02 [129], HAWC [130], etc).
- Direct detection (PandaX [131, 132, 133], XENON1T [181, 182], LUX [134], PICO [135], COUPP [136], SuperCDMS [137, 138, 139, 140] , etc).

- Collider-based experiments (LHC [143], ILC [105, 141, 142]).
- The relic density, and the other cosmological parameters from the PLANCK collaboration [6, 144].
- Optical data for the dSphs from SDSS, Einstein, ASCA, XMM, etc [117, 292, 293, 295, 296, 297, 300].

There are also some functions to create input and output data, and to treat external data in DarkSPIDER. For more detail, see the manual.

2.1.5 The Particle Swarm Optimization method

The Particle Swarm Optimization (PSO) was invented by James Kennedy and Russell Eberhart in 1995 [145]. It is inspired by animals' social behavior like bird flocking and fish schooling. Very few parameters and relatively short computational time are needed to get the best fit. That's why it is implemented to deal with variable problems [146]. It is a widely applied optimization method in many areas including artificial network training and function optimization.

The workflow of the PSO can be presented simply by an example: how does a bird flock find the tree with the most apples in a N-dimension forest. The procudures are as follows:

1. N_0 birds randomly start their actions at different locations; each tree has N coordinates $(x_1, x_2, x_3...x_n)$ to present its location is the N-dimension space. And the birds are supposed to be intelligent to count the number of apples on the trees. This number is noted as f_n for the nth bird. Each bird knows how to shares its location information with the others, and they fly at the same moments.

2. The birds compare the number of apples to find the global maximum $f_{glo,n}$, and the local maximum $f_{l,n}$ for the nth bird itself. Then at the same time, for the dth bird and in the j-th dimension, it flies to the neighboring tree with a velocity as follows:

$$w = w_2 + (w_1 - w_2) * \frac{g_{tot} - g}{g_{tot}}, \tag{10}$$

$$v_{n+1,j} = w * v_{n,j} + c_1 * r_1 * (f_{glo,n} - f_n) + c_2 * r_2 * (f_{l,n} - f_n), \tag{11}$$

with g denotes the g-th flight, g_{tot} denotes the total number of flights for each bird, w denotes the factor of inertia to describe the heritage of velocity in the previous flight, its value is in the range of $[w1, w2]$. c_1, c_2 denote the tunable coefficients chosen to change the birds' behavior. If large c_1 and small c_2 are set, the birds prefer to scan the neighboring trees (local maximums) longer than flying directly to the global maximum. If large c_2 and small c_1 are set, the birds prefer to fly faster to the global maximum. And r_1, r_2 are two random numbers.

3. Repeat step 2 until $g = g_{tot}$ or when the local maximums are very close to the global maximum. If the birds stop flying in some wrong position, go to step 1 to reinitialize the scan again.

If the largest number of apples is replaced by the least Chi-squared, then it is able to find the minimal Chi2 in a N-dimension parameter space. An example of the application is to fit the velocity dispersion, see more details in Chapter 4.

The simulated annealing method is also implemented but applied less in the DarkSPIDER. The MINUIT tool can also be called in DarkSPIDER. But both take longer time to compute than the PSO, but they can be called to cross-check the result.

2.2 Applications

Several applications of DarkSPIDER have been developed. It can be used independently as external packages. Some examples of its application are shown from Chapter 3 to 5.

A complete list of the applications of DarkSPIDER is shown in the manual.

For more information about the physics in the applications, cf. Chapter 3 to 5 for more details. The workflows in these chapters are shown in Fig. 8 to 10.

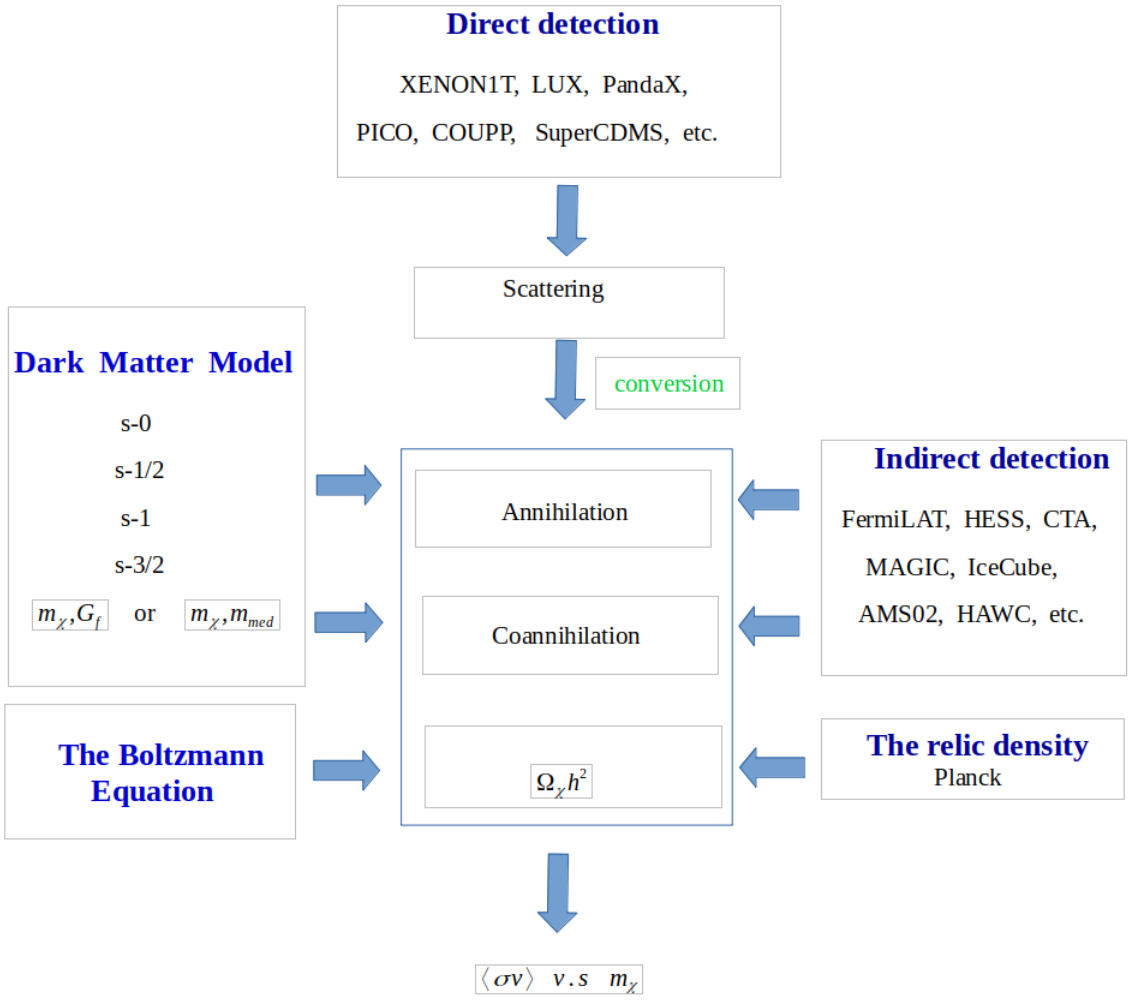

Figure 8: Workflow A of complementary searches of Dark Matter in DarkSPIDER. The theoretical predictions are on the left side. The input data from indirect detection experiments and the relic density [6, 44, 111, 174, 201, 203, 204, 205, 206, 318, 179, 281, 130, 207] are on the right side . The constraints of the scattering cross section from direct detection experiments [130, 207] can be converted to constraints on the annihilation cross section, and then compared with constraints from indirect detection, cf. chapter 3.

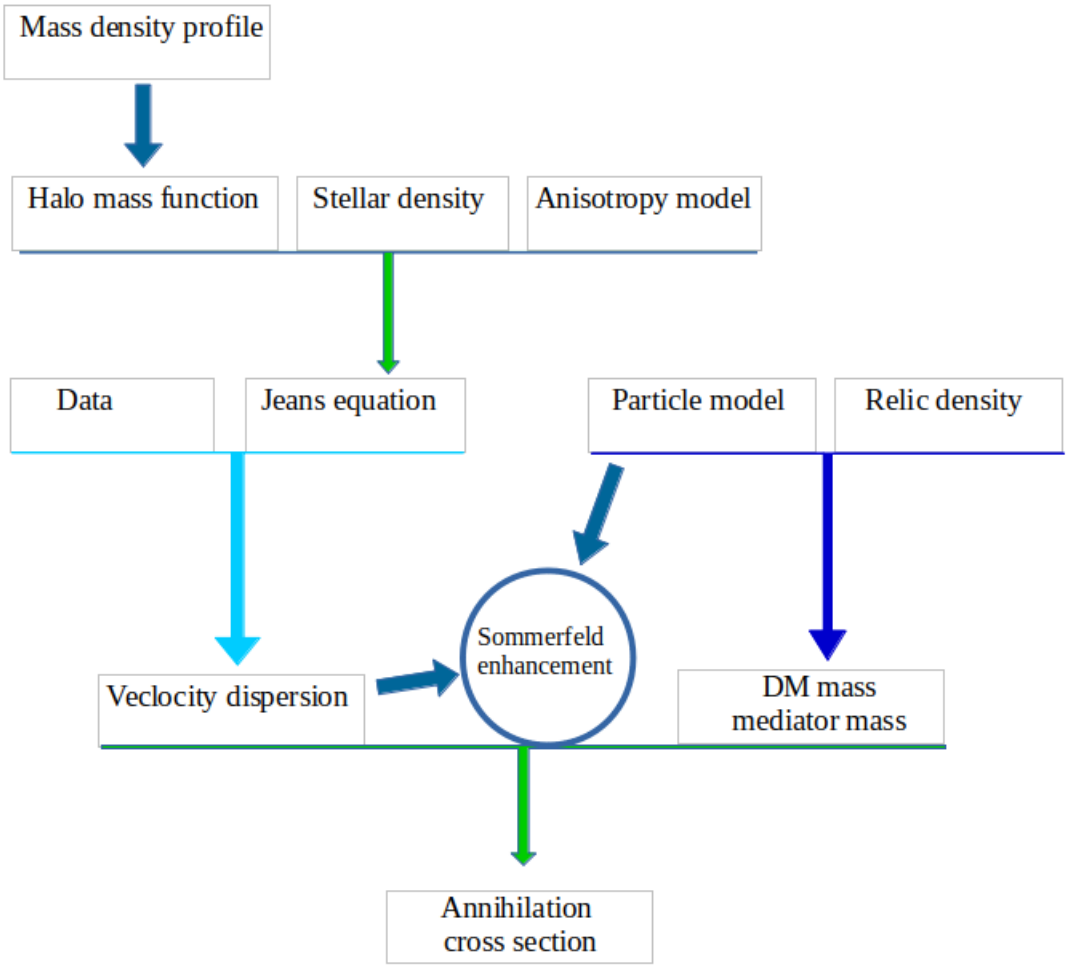

Figure 9: The Workflow of the p-wave Dark Matter annihilation in the dSphs in DarkSPIDER. For the details, cf. Chapter 4.

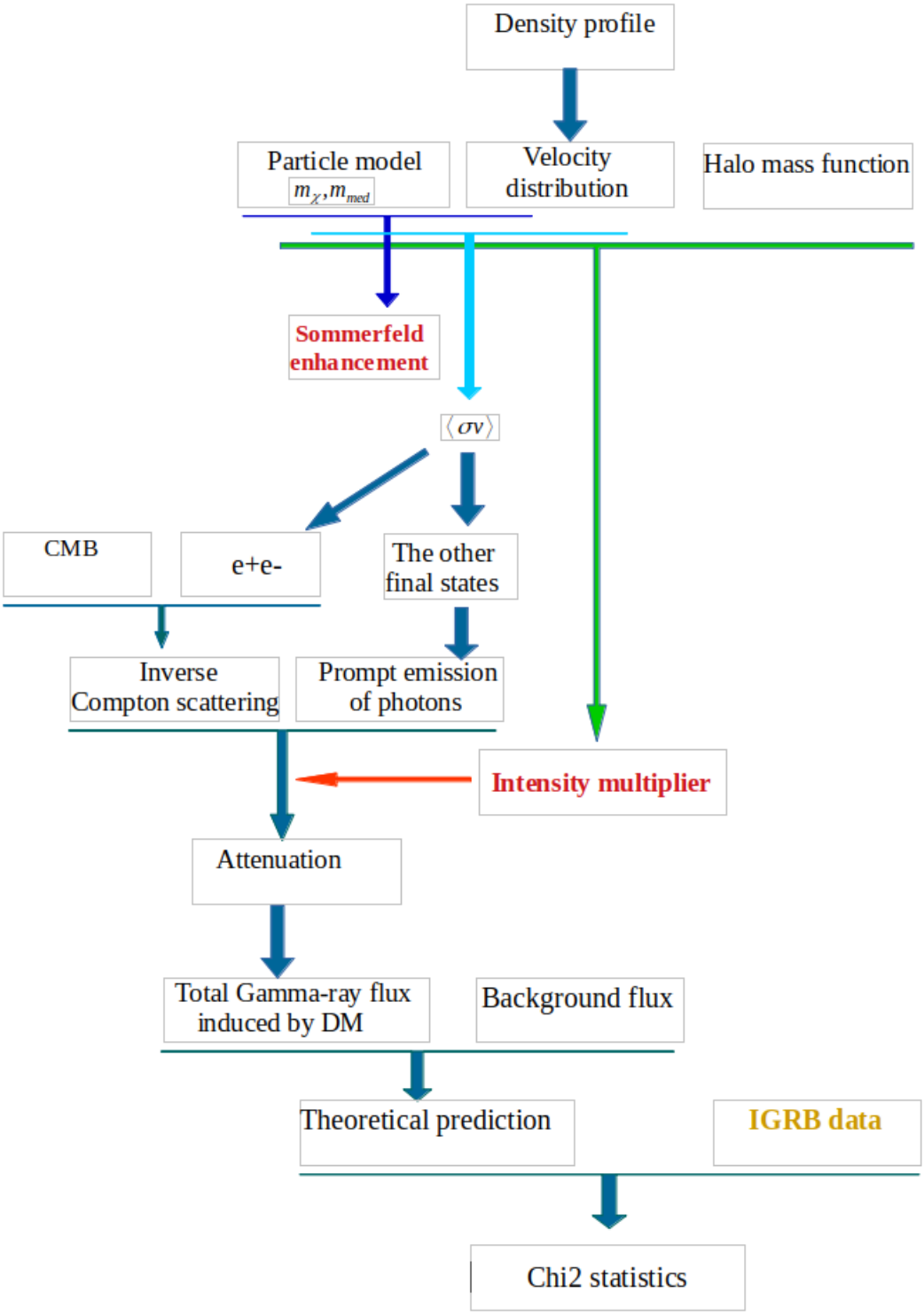

Figure 10: The Workflow of the IGRB constraints on p-wave Dark Matter in DarkSPIDER. Two boost factors (shown in red) are taken into account, the Sommerfeld enhancement boosts the annihilation, then intensity multiplier considers the clumpiness in the halos. For the details, cf. Chapter 5.

Chapter 3 Complementary searches for Dark Matter with generic models

3.1 Introduction

Multi-messengers have been employed to search for Dark Matter, such as the indirect detection observations of electromagnetic radiations in a wide spectral range, high-energy neutrinos, antiparticles, etc. Hence complementary methods have been developed to scan parameter space by combining the information brought by them. Limits from direct detection, indirect detection, collider-based experiments have been combined to find the best-fitting regions in the parameter space.

A pioneering work has been done to apply the minimum χ^2 method in the AstroFit package [100], in which astrophysical components are added to fit BSM physics to collider-based experiments data. The purpose of this kind of work is to rule out some models and show the rest of the parameter space where Dark Matter is allowed to locate. AstroFit confronts theoretical results with observational data by deriving theoretical predictions from the DarkSUSY package [150, 151].

DarkSUSY is an advanced tool widely used for many reasons. It contains many popular SUSY models, such as the MSSM models and self-interacting Dark Matter, it also contains the routines to compute the expected signals from these multi-messengers. There are both routines about cosmological and particle physics in it, such as an extension of the standard thermal decoupling scenario to a detailed description. Hence calling the DarkSUSY routines to feed particle models is a good option for complementary searches. But currently, the non-detection with LHC, indirect and direct detection experiments have put the WIMP hypothesis under scrutiny. In that difficult situation, it is reasonable to jump to generic models to make a scan. And there was no generic model in DarkSUSY when this work started, so the particle models are built independently in DarkSPIDER. MicrOMEGA is another popular option for many Dark Matter hunters [152]. DarkSPIDER is an independent package that allows users to add new particle models, it is much smaller in size compared with DarkSUSY, but similar and supplementary to it.

The GAMBIT package has made great efforts to extend beyond the standard model. Most of the popular BSM models about Dark Matter are implemented in it, it also takes generic models into consideration [153]. GAMBIT has collected popular DM models into consideration by applying profile likelihood to fit experimental data. This chapter of work was done independently at the same time when GAMBIT was developed, it is not comparable with GAMBIT in size, it is a work concentrated on the generic models and some specific relevant questions. It has

used similar data, but DarkSPIDER emphasizes on different theoretical details in both particle physics and astrophysics, the statistical tools in DarkSPIDER are also different from GAMBIT. Efforts have been done to look for the previously ignored problems in GAMBIT and to develop new scanning strategies and to dig as deeply as possible in the relevant direction.

The complete ultraviolet models provide a Dark Matter candidate in complete frameworks of particle physics comprising many parameters to quantify interactions. The effective field theory (EFT) reduces the process between Dark Matter particles and SM particles down to simple operators. Additionally, with fewer parameters the interaction rates could be quantified despite the limitation of its validity. Between the two approaches, another possibility is to use simplified models which also reduce the complexity by using simple operators, but still allow the existence of a mediator to connect Dark Matter and SM particles.

In this work, to cover a wide range of Dark Matter models, it is reasonable to collect the model-independent approaches. So generic models referring to the EFT supplemented by simplified models are utilized. Previously, this type of work has been done for singlet-like Majorana fermion Dark Matter [154]. In this work, both the EFT and simplified model are applied in the calculation. There are various reasons for this choice. For instance, the EFT is a good approximation by integrating out the mediator, but this is also the limitations of the EFT well recognized by the communities of Dark Matter hunters, especially the limits on mediator mass. To overcome these limitations, the UV complete models with Dark Matter candidates can be applied, such as the SUSY models, the codecaying Dark Matter, the superheavy Dark Matter models, the Asymmetric Dark Matter models, the Higgs-portal models, etc. However, since we have no knowledge about the particle species in the dark sector, all these models are based on a lot of new parameters. The EFT contains the least number of parameters, so it is the most economical description of the unknown interaction between Dark Matter particle and Standard Model particles, it is now well developed for a long list of candidates, and only several of them have already corresponding treatments in simplified models. Otherwise, it is convenient to use directly simplified models, which are also generic but allow a mediator to couple with both Dark Matter and SM particles and connect the two sides. With the EFT and simplified models, the advantages of EFT are kept and the drawbacks can be avoided. Together these two approaches allow us to scan the parameter space explicitly for as many models as possible in a comprehensive way.

3.2 Generic models of Dark Matter

The generic models are widely used in indirect detection and direct detection, and collider-based searches for Dark Matter. The EFT work for collider searches has already been done in detail with outstanding performance, such as in [155, 156, 157, 158]. So in this work, we will labor on the other aspects: relic density,

annihilation, and scattering.

There are several generations of generic models for Dark Matter. For the first generation [159], only tree-level interactions have been considered, and the couplings are all regarded to be universal. Then some work has tried to spread it to t-channel, Yukawalike coupling, detailed gauge invariance, etc [160, 161, 162]. There are a lot of common definitions and notations shared by the community, however, even for the same Dark Matter candidate and operator, there are some disagreements among them. For example, the first generation of the EFT is based on the assumption that both universal coupling and Yukawalike coupling are allowed for each type of operator. But the later generation has specified the type of couplings for each operator. It is not realistic to give a complete list of all the possible EFT operators for Dark Matter. The operators which are convenient to study are chosen. Briefly, all of the following work is based on three assumptions:

(1) There is only 1 Dark Matter particle candidate at the electroweak scale.

(2) Any other new particle species in the Dark Sector is heavier than Dark Matter particle.

(3) For each model, there is only one type of operator which is dominant in annihilation, scattering, and production.

The effective Lagrangian for a tree-level 2-to-2 interaction with universal coupling could be written as

$$L_{12\to12} = \sum_{f_1 f_2} \frac{1}{\Lambda^2} (\overline{\chi_1}\Gamma_1\chi_2)(\overline{f_1}\Gamma_2 f_2)\,, \tag{12}$$

here Λ denotes the cut off energy, Γ denotes the operator.

For the final states where $f_1 = f_2$ (fermion-antifermion pair production):

$$L_{12\to11} = \sum_{f_1 f_2} \frac{1}{\Lambda^2} (\overline{\chi_1}\Gamma_1\chi_2)(\overline{f}\Gamma_2 f)\,. \tag{13}$$

To exemplify the calculation in the effective approach, an example is shown for the model with a fermion Dark Matter and a vector operator [103, 104, 154, 168, 187]:

$$L_{12\to11} = \sum_{f} G_{eff} (\overline{\chi_1}\gamma^\mu\chi_2)(\overline{f}\gamma_\mu f)\,. \tag{14}$$

The transition matrix element is:

$$M = G_{eff}\overline{u(p_3)}\gamma^\mu v(p_4)\overline{v(p_2)}\gamma u(p_1)\,. \tag{15}$$

Another example, in the case of Fermion Dark Matter annihilation via a scalar mediator, the first generation of the EFT describes annihilation by the following effective Lagrangian

$$L = \frac{G_f}{\sqrt{2}} \bar{\chi}\chi\bar{f}f\,, \tag{16}$$

where G_f is the coupling constant. Then if the coupling is universal, $\frac{G_f}{\sqrt{2}} = \frac{1}{\Lambda^2}$, it is also written as

$$L = \frac{1}{\Lambda^2} \bar{\chi}\chi\bar{f}f\,. \tag{17}$$

These two expressions are equal to each other.

If the coupling is Yukawalike, then the coupling strength is proportional to the mass of the particle in the final state, $\frac{G_f}{\sqrt{2}} = \frac{m_q}{\Lambda^3}$,

$$L = \frac{m_q}{\Lambda^3} \bar{\chi}\chi\bar{f}f\,. \tag{18}$$

In recent work, some studies prefer to consider only the Yukawalike coupling for a scalar operator. In this work, the definition of coupling is defined as the current generation of the EFT. But since all the calculations in this work are implemented in the DarkSPIDER package, the options are kept for the users to decide which coupling they want to consider.

In the framework of simplified models, for the case of fermion Dark Matter annihilation via a scalar mediator into fermions, the corresponding annihilation cross section [109] is

$$\langle\sigma v\rangle_{Scalar} = c_f \frac{(g_\chi g_q)^2}{16\pi} (\frac{m_q}{m_{HVEV}})^2 \frac{m_\chi^2 (1 - \frac{m_q^2}{m_\chi^2})^{\frac{3}{2}}}{\left(m_{med}^2 - 4m_\chi^2\right)^2 + \Gamma_{s,tot}^2 m_{med}^2} v_{rel}^2\,, \tag{19}$$

with $c_f = 3$ for the quarks to count the colors, $c_f = 1$ for the leptons, m_q as the fermion mass, $m_{HVEV} = 246\,GeV$ as the Higgs vacuum expectation value, $\Gamma_{s,tot}$ as the total decay width into fermions, m_{med} as the mediator mass, g_χ as the coupling factor with Dark Matter (sometimes noted as g_{DM}), g_q as the coupling factor with the final state particles, v_{rel} as the relative velocity of the incoming particles in the C.O.M frame.

To connect the EFT and simplified models in a simple way for this example, there is

$$\frac{G_f}{\sqrt{2}} \simeq \frac{m_q}{m_{HEVE}} \frac{g_\chi g_q}{\left(\left(m_{med}^2 - 4m_\chi^2\right)^2 + \Gamma_{S,tot}^2 m_{med}^2\right)^{1/2}}\,. \tag{20}$$

For a heavy mediator, the effective coupling strength is expressed approximatively

$$\frac{G_f}{\sqrt{2}} \simeq \frac{m_q}{m_{HEVE}} \frac{g_\chi g_q}{m_{med}^2}\,. \tag{21}$$

This example above is for the case of Yukawalike coupling, the coupling strength

depends on the mass of the final state particle. In the case of universal coupling, the $\frac{m_q}{m_{HEVE}}$ term does not exist anymore. Following the notation in Ref.[164], there are two typical connections between the EFT and simplified models.

- for universal coupling:

$$\frac{G_f}{\sqrt{2}} = \frac{\alpha}{\Lambda^2} \simeq \frac{\alpha g_\chi g_q}{M_{med}^2} \,. \tag{22}$$

- for Yukawalike coupling:

$$\frac{G_f}{\sqrt{2}} = \frac{\alpha m_q}{\Lambda^3} \simeq \alpha \frac{m_q}{m_{HEVE}} \frac{g_\chi g_q}{m_{med}^2} \,, \tag{23}$$

where α denotes the factor to quantify the fundamental physics beyond Λ, it is considered to be in the order of 1. To ensure the perturbative unitarity, $\alpha < 4\pi$. For the sake of simplicity, it is often set as 1 in this work. The theory is valid in the perturbative regime only if $0 < g_\chi g_q < 16\pi^2$, in the DMWG benchmark [163], it is often set as $g_\chi = 1$, $g_q = 0.25$ for the O_V (vector) and O_A (axial-vector) operators, $g_\chi = g_q = 1$ for the O_S (scalar) and O_P (pseudoscalar) operators.

3.3 Validity of the EFT and simplified models

Generally, the EFT describes physical interactions at a given energy scale; these interactions are usually non-renormalizable. The momentum transfer Q_{tr} must be less than a cut-off energy: $\Lambda \gtrsim Q_{tr}$. For the operators of the lowest dimension, the expansion of the propagator term can be expressed as a function of m_{med} and Q_{tr} [168, 176]:

$$\frac{g_\chi g_q}{m_{med}^2 - Q_{tr}^2} = \frac{g_\chi g_q}{m_{med}^2} \big(1 + \frac{Q_{tr}^2}{m_{med}^2} + \mathcal{O}(\frac{Q_{tr}^4}{m_{med}^4})\big) \,. \tag{24}$$

The EFT is valid for heavy mediators (or equally $Q_{tr} \ll m_{med}$), so we need only to consider the first term on the right side, leading to

$$\frac{g_\chi g_q}{m_{med}^2 - Q_{tr}^2} \simeq \frac{g_\chi g_q}{m_{med}^2} \,. \tag{25}$$

Introducing the cut-off energy scale Λ, for the universal coupling, there is

$$\Lambda = \frac{m_{med}}{\sqrt{g_\chi g_q}} \,. \tag{26}$$

When $m_{med} \sim Q_{tr}$, there is a resonant enhancement, and the EFT limit is not applicable anymore.

Additionally, the condition for tree-evel s-channel model [103, 179] is

$$m_{med} \gg \sqrt{s} \,, \tag{27}$$

the Mandelstam variable $s = 2m_\chi^2(1 + \frac{1}{\sqrt{1-v_{rel}^2}}) \simeq 4m_\chi^2 + m_\chi^2 v_{rel}^2 \simeq 4m_\chi^2$, and the condition for the EFT at tree level reads

$$\begin{cases} 2m_\chi \ll \Lambda \\ \alpha < 4\pi \end{cases} . \tag{28}$$

In the case of light mediator, $Q_{tr} \gg m_{med}$,

$$\frac{g_\chi g_q}{Q_{tr}^2 - m_{med}^2} \simeq \frac{g_\chi g_q}{Q_{tr}^2}\big(1 + \frac{m_{med}^2}{Q_{tr}^2} + \mathcal{O}(\frac{m_{med}^4}{Q_{tr}^4})\big)\,, \tag{29}$$

since we do not know the value of Q_{tr} in the unknown interaction between Dark Matter and SM particles, it is impossible to quantize the propagator term. For this reason, the calculations is limited in the cases of a heavy mediator. For the cases where the mediator mass is needed, simplified models are recalled.

For the LHC study on the validity of the EFT, $\langle Q_{tr}^2 \rangle^{1/2} > 500\,GeV$, then the high order terms disappear for $m_{med} < 500\,GeV$ [176]. A detailed investigation of the validity of the EFT has been done similarly in Ref. [177].

3.3.1 Fermion Dark Matter

In order to collect constraining limits of different parameters, it is necessary to find the allowed ranges of G_f, Λ, m_{med}, and m_χ. The following subsection is to show how to convert between them.

If $g_q = g_\chi = 1$, then as shown in Ref. [164], the coupling strength follows the following condition

$$G_f \ll \frac{\sqrt{2}\pi}{m_\chi^2}\,, \tag{30}$$

when the mediator and the coupling factors g_q and g_χ are considered, for example, in the case of a vector or an axial - vector operator, from Equations (22), (26) and (27), there is

$$\frac{\big(\alpha g_q g_\chi\big)^{\frac{1}{2}}}{2m_\chi} > \big(\frac{G_f}{\sqrt{2}}\big)^{\frac{1}{2}} = \frac{\sqrt{\alpha}}{\Lambda}\,, \tag{31}$$

leading to

$$G_f \ll \frac{\sqrt{2}\pi}{m_\chi^2} g_q g_\chi\,, \tag{32}$$

or

$$\Lambda \gg \frac{2m_\chi}{\sqrt{g_q g_\chi}}\,. \tag{33}$$

For simplified models, in the case of an axial-vector mediator, the following conditions must be applied to ensure the gauge variance and perturbative unitarity [179]:

$$\begin{cases} m_{\chi,q} < \sqrt{\frac{\pi}{2}}\frac{m_{med}}{g_{\chi,q}} \\ \sqrt{s} < \frac{\pi m_{med}^2}{g_\chi^2 m_\chi} \end{cases}\,. \tag{34}$$

From Equation (23) and (28), if $\frac{G_f}{\sqrt{2}} = \frac{\alpha m_q}{\Lambda^3}$ and $\alpha = g_q = g_\chi = 1$,

$$\Lambda^3 = \sqrt{2}\frac{\alpha m_q}{G_f} \gg (2m_\chi)^3\,, \tag{35}$$

then

$$\frac{G_f}{m_q} \ll \frac{\pi}{\sqrt{2}M_\chi^3}\,. \tag{36}$$

But if $\frac{G_f}{\sqrt{2}} = \alpha\frac{m_q}{m_f}\frac{g_\chi g_q}{M_{med}^2}$,

$$\sqrt{2}\alpha\frac{m_q}{m_f}\frac{g_\chi g_q}{G_f} = m_{med}^2 \gg 4m_\chi^2\,, \tag{37}$$

$$\frac{G_f}{m_q} \ll \frac{\sqrt{2}\alpha}{4M_\chi^2 m_f} g_x g_\chi \ll \frac{\sqrt{2}\cdot 4\pi}{4M_\chi^2 m_f} g_x g_\chi\,, \tag{38}$$

as $g_q = g_\chi = 1$, then

$$\frac{G_f}{m_q} \ll \frac{\sqrt{2}\pi}{M_\chi^2 m_f}\,. \tag{39}$$

Compared with Equation (36), we conclude that

$$\frac{G_f}{m_q} \ll min\{\frac{\pi}{\sqrt{2}m_\chi^3}, \frac{\sqrt{2}\pi}{m_\chi^2 m_f}\}\,. \tag{40}$$

When the mediator and the coupling factors g_q and g_χ are considered, with Equations (23), (27), and (28), thus for example, in the case of scalar and pseudoscalar operators, leading to

$$\Lambda > (\frac{4m_\chi^2 m_f}{g_\chi g_q})^{1/3}\,. \tag{41}$$

This is a correction to the calculations in Ref. [103, 179].

3.3.2 Scalar Dark Matter

The most comprehensive study on the validity of scalar and vector Dark Matter is done in Ref. [165]. The relevant categorization of operators is offered by Ref.[173], where the calculations of complex and real scalar Dark Matter have been derived. Similar methods as the fermion Dark Matter have been used.

For the scalar and scalar - pseudoscalar operators:

$$G_f \ll \frac{2\sqrt{2}\pi}{m_\chi}\,. \tag{42}$$

For the vector and vector - axial-vector operators:

$$G_f \ll \frac{\sqrt{2}\pi}{m_\chi^2}\,. \tag{43}$$

The coupling strength is proportional to the mass of the final state particle: $G_f \sim m_q$.

For the scalar and scalar - pseudoscalar operators:

$$G_f \ll \frac{\sqrt{2}\pi}{m_\chi^2} m_q\,. \tag{44}$$

For the vector and vector - axial-vector operators:

$$G_f \ll \frac{\pi}{\sqrt{2}m_\chi^3} m_q\,. \tag{45}$$

3.3.3 Vector Dark Matter

Similarly, the following conclusion for vector Dark Matter is consistent with Ref. [165].

For the scalar, scalar - pseudoscalar, tensor, and alternative tensor operators:

$$G_f \ll \frac{2\sqrt{2}\pi}{m_\chi}\,. \tag{46}$$

For the vector, vector - axial-vector, alternative vector, and alternative vector - aixial-vector operators:

$$G_f \ll \frac{\sqrt{2}\pi}{m_\chi^2}\,. \tag{47}$$

The coupling strength is proportional to the mass of the final state particle: $G_f \sim m_q$.

For the scalar, scalar - pseudoscalar, tensor, and alternative Tensor operators:

$$G_f \ll \frac{\sqrt{2}\pi}{m_\chi} m_q \,. \tag{48}$$

For the vector, vector - axial-vector, alternative vector, and alternative vector - axial-vector operators:

$$G_f \ll \frac{\pi}{\sqrt{2} m_\chi^3} m_q \,. \tag{49}$$

3.4 Dark Matter annihilation to fermions

3.4.1 The EFT models of annihilation

From Ref. [103, 104, 275, 276], the Dark Matter annihilation to Gauge boson and Higgs boson is assumed to be negligible; then the fermion-antifermion final states become dominant over the other channels.

For Dark Matter annihilation cross section into fermions, two categorizations of operators in this work are collected. One is established in Ref. [159], including fermion and scalar Dark Matter candidates. It has been then quoted popularly as one of the first-generation EFT works of Dark Matter. Then the extension to vector Dark Matter and spin-$\frac{3}{2}$ Dark Matter, and more operators have also been accomplished later [103, 104, 106, 166]. Another categorization is designed for the ILC searches, in which the t-channel interaction has been added. It contains information of the mediator, so the models with scalar, fermion, and vector mediators in the unknown interactions are involved, and chiral interactions are also implemented [105]. Some information about the coupling coefficient and Lagrangian operator on the list is from Ref. [169, 170].

For the sake of clearness and simplicity, only the models with determined information about the coupling type, the transition matrix, is taken in this work as shown in the list of Appendix A. The other models are described in Ref. [105].

3.4.2 Constraints from indirect detection

When Dark Matter annihilation happens at non-relativistic velocity, then the annihilation cross section can be expressed in the term of $\langle \sigma v \rangle = a + bv^2 + cv^4$. Taking again the case of fermion Dark Matter pair which annihilates via a

pseudoscalar operator or a vector operator, two examples are discussed in this section.

Defining $\xi \equiv \frac{m_q}{m_\chi}$ as the ratio of fermion particle mass in the final state to Dark Matter mass, then by calculating the annihilation cross section defined in Table. 11 (Appendix A) and expanding it as a function of v, we get

$$\langle\sigma v\rangle_{pseudoscalar,anni} = \frac{1}{4\pi}\sum_f c_f \cdot G_f^2\sqrt{1-\xi^2}m_\chi^2\big(1+(\frac{\xi^2}{8(1-\xi^2)})v^2+\mathcal{O}(v^4)\big)\,, \quad (50)$$

$$\langle\sigma v\rangle_{vector,anni} = \frac{1}{4\pi}\sum_f c_f\cdot G_f^2\sqrt{1-\xi^2}(2m_\chi^2+m_f^2)\big(1+(\frac{-4+2\xi^2+11\xi^4}{24(1-\xi^2)(2+\xi^2)})v^2+\mathcal{O}(v^4)\big)\,, \quad (51)$$

where $c_f = 3$ for quarks and $c_f = 1$ for leptons. The sum is over all the fermion species.

Define: $z \equiv \frac{m_2}{m_1}$, the mass ratio of the outgoing particle over the incident particle in the annihilation to fermion-antifermion $\bar{\chi}\chi \to \bar{f}f$. The relative velocity of the final-state particles in the C.O.M frame is [171]:

$$v_2 = \big(1-z^2+z^2v^2/4\big)^{\frac{1}{2}} = z(v^2/4+\mu_+^2)^{\frac{1}{2}}\,, \quad (52)$$

with $\mu_+ = (1-z^2)^{\frac{1}{2}}/z$ as the minimal value of v_2. Defining $x \equiv \frac{m}{T}$,

$$\langle\sigma v\rangle = \langle\big(a+bv^2+cv^4\big)v_2\rangle = \frac{x^{3/2}}{2\pi^{1/2}}\int_0^\infty dv v^2 e^{\frac{-v^2x}{4}} v_2\big(a+bv^2+cv^4\big)\,. \quad (53)$$

With the Taylor expansion,

$$\langle\sigma v\rangle = \langle(a+bv^2+cv^4)v_2\rangle, \quad (54)$$

$$\langle\sigma v\rangle \simeq (1-z^2)^{\frac{1}{2}} \times \begin{cases} \big\{a\big(1+\frac{3z^2}{4x(1-z^2)}-\frac{15z^4}{32x^2(1-z^2)^2}+\frac{105z^6}{128x^3(1-z^2)^3}\big)\big) \\ +\frac{6b}{x}\big(1+\frac{5z^2}{4x(1-z^2)}-\frac{35z^4}{32x^2(1-z^2)^2}+\frac{315z^6}{128x^3(1-z^2)^3}\big) \\ +\frac{60c}{x^2}\big(1+\frac{7z^2}{4x(1-z^2)}-\frac{63z^4}{32x^2(1-z^2)^2}+\frac{693z^6}{128x^3(1-z^2)^3}\big)\big\} \end{cases}. \quad (55)$$

z is much smaller than 1, and x is larger than 10, so the thermally averaged annihilation cross section could be expressed as $\langle\sigma v\rangle \simeq a+\frac{6b}{x}+\frac{60c}{x^2}$, if the freeze-out temperature is known, then the averaged annihilation cross section at freeze-out is determined.

The freeze-out temperature of Dark Matter could be obtained by solving the standard Boltzmann equation:

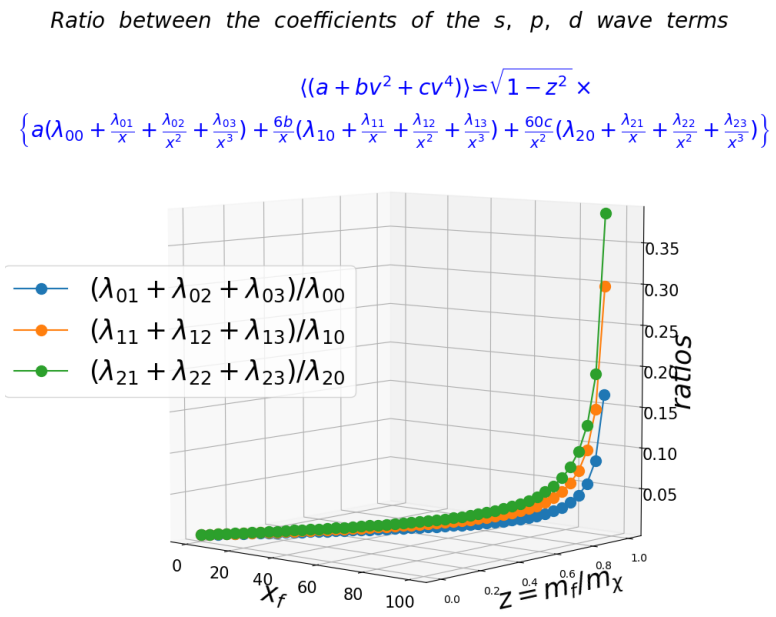

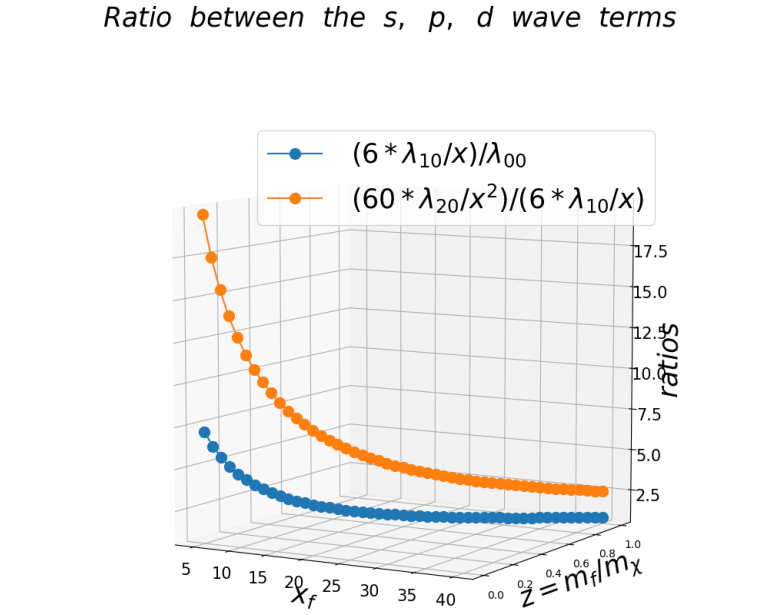

Figure 11: Upper: the ratios between the terms in the s, p, d wave terms in Equation (55). Each term is noted as λ_{ij} and their relative values are shown. The high order terms are small compared with the leading term unless the final state particles are as heavy as Dark Matter particle (this is impossible for the SM fermions), so only the first term is taken in the calculation . Bottom: if a=b=c (which is not true), the ratio between the s, p, d wave terms shows that the p, d waves could be important, indicating that s-wave term is no more dominant if $\frac{a}{b} \to 0$, equally speaking, the p-wave term becomes dominant. This will be further discussed in Chapters 4 and 5.

$$\frac{dn_x}{dt} + 3Hn_x = -\langle\sigma v\rangle(n_x^2 - n_{eq}^2)\,, \tag{56}$$

the second term on the left is the dilution of Dark Matter number density due to the expansion, the right side describes the reduction due to annihilation. Here we use the system units with $c = \bar{h} = k_B = 1$.

The conservation of entropy in equilibrium implies that the entropy density $s = g_{*s}\frac{2\pi^2}{45}T^3 \propto a^{-3}$, where g_{*s} is the effective degree of freedom associated with the entropy all the particle species. A detailed calculation of g_{*s} is discussed in Ref.[172]. Since $T \propto a^{-1}$and $aT = const$, we have $\frac{\dot{a}}{a} = -\frac{\dot{T}}{T}$, then the Boltzmann equation is expressed as

$$\frac{dn_x}{dt} + 3Hn_x = a^{-3}\frac{dna^3}{dt}\,. \tag{57}$$

There are several types of solutions to continue the calculation, depending on the definition of Y, such as $Y = \frac{n}{s}$ or $Y = \frac{n}{T^3}$.

If $Y \equiv \frac{n}{T^3}$, then at thermal equilibrium,

$$Y_{eq} = \frac{n_{eq}}{T^3} = g(\frac{m}{2\pi T})^{\frac{3}{2}}e^{-\frac{m}{T}}\,. \tag{58}$$

From Equation (57),

$$\frac{dY}{dt} = \frac{\dot{n}}{T^3} + n(-3)\frac{1}{T^4}\frac{dT}{dt} = (\dot{n} - 3n\frac{\dot{T}}{T})\frac{1}{T^3} = (\dot{n} - 3n\frac{\dot{a}}{a})\frac{1}{T^3} = (\dot{n} + 3Hn)\frac{1}{T^3}\,, \tag{59}$$

$$\frac{dY}{dt} = \frac{1}{T^3}\langle\sigma v\rangle(Y_{eq}^2T^6 - Y^2T^6) = T^3\langle\sigma v\rangle(Y_{eq}^2 - Y^2)\,. \tag{60}$$

After multiple intermediate steps, the value of x at the freeze-out moment is given by

$$x_f = ln(l(l+2)\sqrt{\frac{45}{8}}\frac{gM_\chi M_{planck}\left(a + \frac{6b}{x_f} + \frac{60c}{x_f^2}\right)}{2\pi^3 g_{tot,f}^{1/2}x^{\frac{1}{2}}}\,. \tag{61}$$

This is the conventional solution in which the d-wave term is involved (these does exist a d-wave model on the list of models, cf. Table 2, where $l = O(1)$, usually it is set to be $\frac{1}{2}$. The Planck mass $M_{planck} = 1.22 \cdot 10^{19}GeV$, $g_{tot,f}$ is the relativistic degrees of freedom in equilibrium at freeze-out, it is usually set to be ~ 100, depending on the transition temperature of the particles and the mass of Dark Matter. If Dark Matter mass is between 500 GeV and 10 TeV and no other particle exists in this range, it is set to 106.75 [172].

Since we have not found Dark Matter at the LHC, Dark Matter is expected to be more massive, so the value of x_f increases again, a typical value of x_f should be in the range [20,30]. If $x_f = 25$, since $\frac{1}{2}m_\chi v^2 = \frac{3}{2}T$, then $v_{freeze-out} \sim 0.34$.

The relic density of Dark Matter is thus written as

$$\Omega_{DM}h^2 = 2 \cdot 1.04 \cdot 10^9 \frac{x_f}{g_{tot}^{1/2} m_{planck}(GeV)\langle a + 3b/x_f + 20c/x_f^2 \rangle}\,, \tag{62}$$

where g is the number of internal degrees of freedom for the Dark Matter particle

$$g = \begin{cases} 1 & real\ scalar \\ 2 & Majorana\ fermion\ or\ complexe\ scalar \\ 4 & Dirac\ fermion,\ spin - \frac{3}{2}\ particle \\ 6 & vector\ with\ different\ antiparticle \end{cases}. \tag{63}$$

For example, for vector Dark Matter which has 3 eigenvalues of spin along any axis, with its antiparticle, the total number of degree of freedom is 6. But if it is the same as its antiparticle, g=3.

The factor 2 in Equation (62) is added for the existence of anti-Dark Matter, this factor exists for all the candidates with an antiparticle. For Majorana fermion and real scalar Dark Matter, this factor does not exist.

With the expressions of the a, b, c terms in the formulae of annihilation cross section, the value of x_f at freeze-out by solving Equation (61) is obtained, the x_f term in Equation (62) should be consistent with the value of relic density $\Omega_c h^2 = 0.120 \pm 0.001$ in Ref. [6].

For each particle model and operator, the benchmarks with different G_f and m_χ are used. G_f varies from 10^{-9} to 10^{-4} and m_χ from 1 GeV to 100 TeV to compare the relic density, then the corresponding G_f and m_χ can be found, and the annihilation cross section can be computed.

The annihilation rate required by the relic density is shown with a gray curve on each panel from Fig. 13 to Fig. 15. Since we concentrate on $\bar{\chi}\chi \to \bar{f}f$, all the 9 fermion species except the neutrinos in the final state are considered, with 3 of them being shown in these figures: $\bar{b}b$, $\tau^+\tau^-$, $\mu^+\mu^-$.

For each species, it is assumed that the only channel through which Dark Matter annihilation happens or equally a 100% branching ratio for each species. So it could be compared with observational limits from gamma-ray or cosmic ray searches. Then if we project the required m_χ on the panels with a plot about the relationship between σv and m_χ (shown by the violet curves), we get the maximal annihilation cross section which could be produced to this species, the value should also not be higher than the observed upper limits.

For each final state, the observations are listed here:

$b\bar{b}$: the constraints from the 15 dSphs by the Planck collaboration and the constraint from the Segue 1 dSphs by the MAGIC gamma-ray telescopes [203].

$\tau^+\tau^-$: the constraints from the 15 dSphs by the Planck collaboration and the constraint from the Segue 1 dSphs by the MAGIC gamma-ray telescopes [203], and the observation of the Galactic halo by H.E.S.S [174].

$\mu^+\mu^-$: the constraints from the 15 dSphs by the Planck collaboration and the

constraint from the Segue 1 dSphs by the MAGIC gamma-ray telescopes [203].

There are in general four types of annihilation, some of the results are shown from Fig. 13 to Fig. 15 in this chapter. And the others are added in Appendix B.

4 types of annihilation:

(1) Universal coupling, s-wave: an example of fermion Dark Matter annihilation via a vector operator is shown in Fig. 41 in Appendix B.

(2) Universal coupling, p-wave: an example of scalar Dark Matter annihilation via a vector - axial-vector operator is shown in Fig. 42 in Appendix B.

(3) Yukawalike coupling, s-wave: an example of scalar Dark Matter annihilation via a scalar operator is shown in Fig. 43 in Appendix B.

(4) Yukawalike coupling, p-wave: an example of fermion Dark Matter annihilation via a scalar operator is shown in Fig. 13.

For (1), in the case of fermion Dark Matter that annihilates via a vector operator, the annihilation is not affected by the velocity, so the annihilation rate it can produce today is the same as that at the freeze-out moment $\langle \sigma v \rangle = 2.7 \cdot 10^{-26}\, cm^3 s^{-1}$. Compared with the observations, it is insensitive in the neutrino final states, for $\bar{b}b$, $G_f > 10^{-6}$ is excluded out up to 110 GeV; for $\tau^+\tau^-$, $G_f > 10^{-7}$ is excluded out up to 1900 GeV; for $\mu^+\mu^-$, $G_f > 10^{-5}$ is excluded out up to 10 GeV.

For (2), in the case of scalar Dark Matter that annihilates via a vector - axial-vector operator, the annihilation is dominated by the velocity, so the annihilation rate in today's Universe is not the same as at the freeze-out moment if we take $v = 220\, km/s$, which is the velocity in the Milky Way halo, then $\langle \sigma v \rangle \ll 2.7 \cdot 10^{-26}\, cm^3 s^{-1}$. Compared with the observations, we conclude that it is insensitive in any of the 3 final states.

For (3), in the case of scalar Dark Matter that annihilates via a scalar operator, the annihilation is not affected by the velocity, but the effective coupling strength is proportional to the particle mass of the final state, $G_f \propto m_f$, so the annihilation rate is much lower in the low mass final states. Compared with the observations, for $\bar{b}b$, $G_f \gtrsim 3 \cdot 10^{-5}$ is excluded out up to 32 GeV; for $\tau^+\tau^-$, $G_f \gtrsim 9 \cdot 10^{-5}$ is excluded out up to 16 GeV.

For (4), in the case of fermion Dark Matter that annihilates via a scalar operator, the annihilation is dominated by the velocity, so the annihilation rate it can produce today is not the same as at the freeze-out moment. If we take $v = 220\, km/s$, which is the velocity in the Milky Way halo, then$\langle \sigma v \rangle \ll 2.7 \cdot 10^{-26}\, cm^3 s^{-1}$. Compared with the observations, we conclude that it is insensitive in any of the 3 final states.

The velocity-dependence in (2) and (4) is so strong that it makes the Dark Matter invisible to indirect detection. This means even if that kind of model is correct, we could not detect it in indirect detection. This may explain the non-detection of Dark Matter. As shown in Fig. 13, we test with $v = 3000\, km/s$, which is in the range of velocity in the galaxy clusters. For this type of model, the sensitivities of the current experiments are still far away from the value required

by the Dark Matter. For $b\bar{b}$, we need to increase the sensitivity by 10^3 to 10^8 times, for the other 5 final states, we need to improve the sensitivity much more.

Beyond the 4 typical annihilations, a very specific case is the d-wave-dominated model with a vector Dark Matter and an alternative tensor operator. This model is more strongly influenced by the velocity of Dark Matter in the dynamical systems. The annihilation cross section decreases as Dark Matter mass increases leading to being more difficult to be detected. The sensitivities of the current experiments are too far away from the annihilation cross section it can produce today. If Dark Matter does belong to this category, and no boosting factor exists, it is almost an impossible mission for astroparticle physicists focusing on indirect detection to find a signal.

It is necessary to point out that the calculation in this section is based on the standard treatment of the Boltzmann equation, and there is no boosting effect considered in the calculation. A brief global view of Dark Matter searches is needed. All the results indicate that if Dark Matter is a WIMP, then it is necessary to go to a much higher energy scale to probe Dark Matter. This is consistent with the previous results in Collider-based and direct detection experiments.

3.4.3 Summary of Section 3.4

A long list of WIMP Dark Matter candidates and operators is made by accumulating information from previous work on the EFT models. The Boltzmann equation is applied to find the x_f at the freeze-out moment which is determined by the observed relic density of Dark Matter. The mass for each coupling strength allowed by this calculation then serves to project on the annihilation cross section in to 3 final states, this annihilation cross section is the maximal annihilation cross section it can produce in today's Universe. The comparison between this value and the observational constraining limits rules out a large chunk of the parameter space. The models are classified into four groups, depending on the types of coupling and dominating wave term. Several models have been computed with fermion, complex scalar, and vector Dark Matter annihilating via various operators. The allowed parameter space is then listed in Table 2. A lot of cases remain insensitive in the current experiments. This is caused either by the velocity-dependence in the p-wave or d-wave, or the mass-dependence in the Yukawalike coupling. In all these results, no signal of Dark Matter has been found, and a lot of models are impossible to be tested by the existing experiments, all these results point to heavier WIMPs.

It is not realistic to make computation for all the existing models in this chapter, but more models are already implemented in the DarkSPIDER packages. For the users who want to do similar work, it is necessary to take information about the

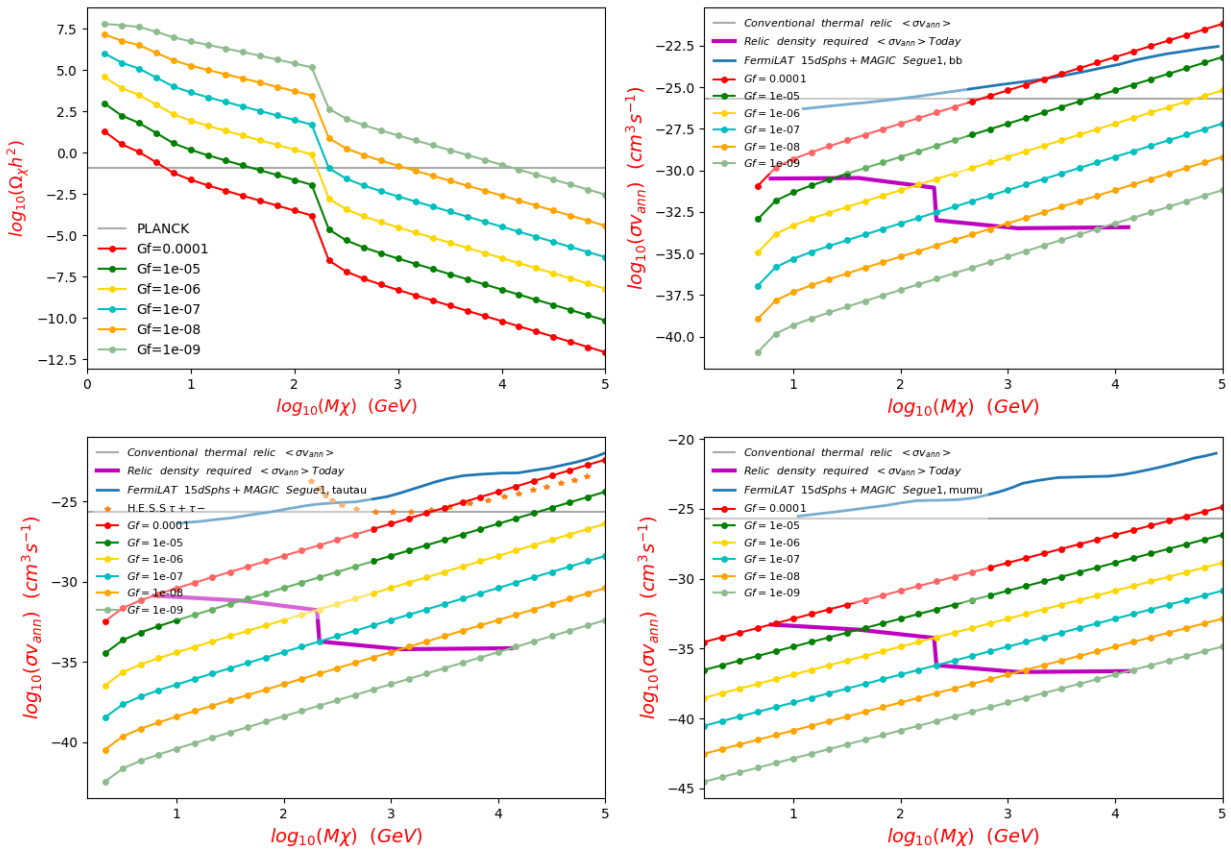

Fermion DM annihilation
via a Scalar operator
with Yukawa like coupling
v = 220km/s

Fig. top left: $log_{10}(\Omega_\chi h^2)$ *VS* $log_{10}(M_\chi)$
Fig. top right: $b\bar{b}$ $log_{10}(\sigma v_{ann})$ *VS* $log_{10}(M_\chi)$
Fig. bottom left: $\tau^+\tau^-$ $log_{10}(\sigma v_{ann})$ *VS* $log_{10}(M_\chi)$
Fig. bottom right: $\mu^+\mu^-$ $log_{10}(\sigma v_{ann})$ *VS* $log_{10}(M_\chi)$

Figure 12: For fermion Dark Matter annihilation via a scalar operator with Yukawalike coupling, the relic density required Dark Matter mass m_χ and coupling constant G_f are shown on the top left panel. If Dark Matter annihilates purely to one final state, the maximal $\langle\sigma v\rangle_{anni}$ to 3 final state particles are shown respectively from top middle to bottom left: $\bar{b}b$, $\tau^+\tau^-$, $\mu^+\mu^-$. The constraints are from the observations of dSphs by FermiLAT and MAGIC [203], and the observation of the galactic halo with H.E.S.S [174]. The gray horizontal line is the conventional $\langle\sigma v\rangle_{anni} = 2.7 \cdot 10^{-26}\, cm^3 s^{-1}$ at the freeze-out moment, the $\langle\sigma v\rangle_{anni}$ it can produce today into each channel is shown as the violet curve (for $v = 220\, km/s$). This is a p-wave annihilation. The constraints are weak in this case. See Table 2 for more explanation.

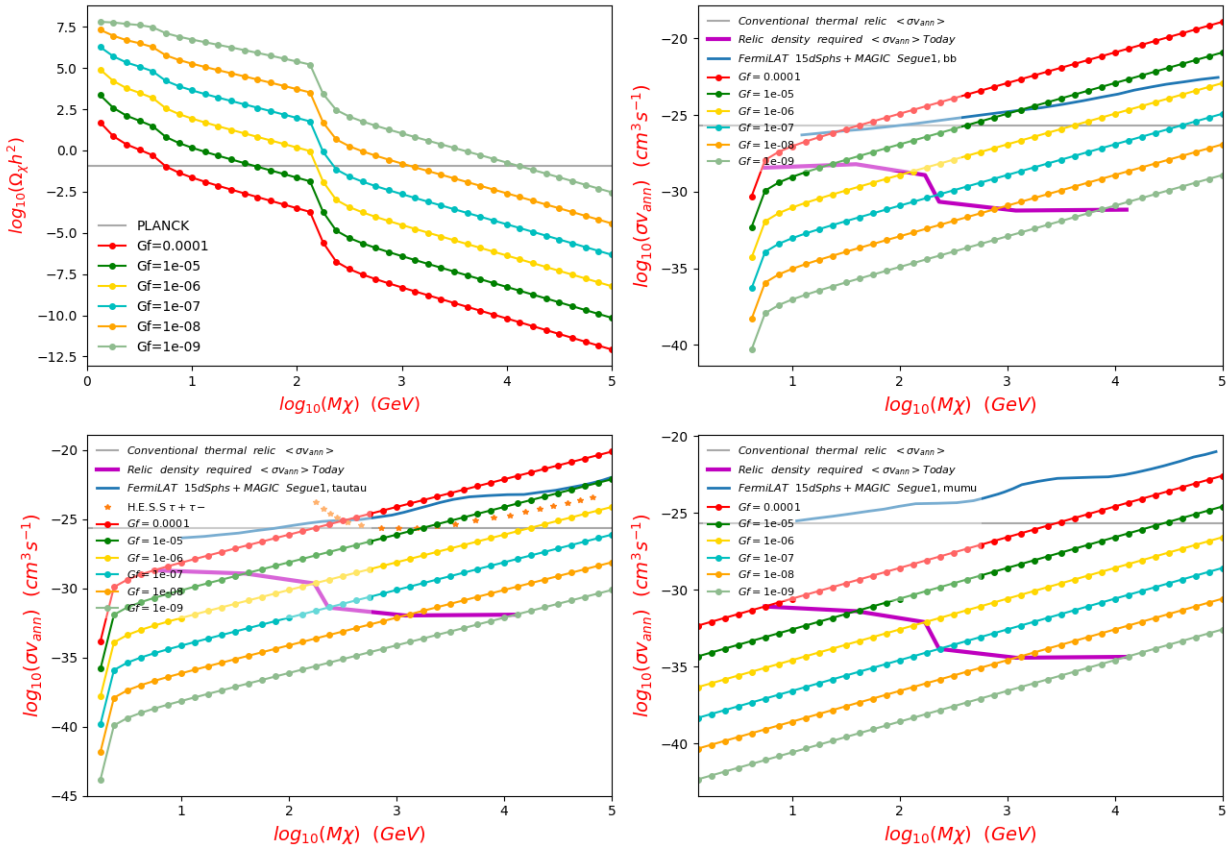

Fermion DM annihilation
via a Scalar tensor operator
with Yukawa like coupling
v = 3000km/s

Fig. top left: $log_{10}(\Omega_\chi h^2)$ *VS* $log_{10}(M_\chi)$
Fig. top right: $b\bar{b}$ $log_{10}(\sigma v_{ann})$ *VS* $log_{10}(M_\chi)$
Fig. bottom left: $\tau^+\tau^-$ $log_{10}(\sigma v_{ann})$ *VS* $log_{10}(M_\chi)$
Fig. bottom right: $\mu^+\mu^-$ $log_{10}(\sigma v_{ann})$ *VS* $log_{10}(M_\chi)$

Figure 13: For fermion Dark Matter annihilation via a scalar operator with Yukawalike coupling. This figure is the same as Fig. 12, but tested with $v = 3000\,km/s$. All the final states are still impossible to detect in the existing experiments. If there is no boost factor, this kind of Dark Matter is invisible to indirect detection.

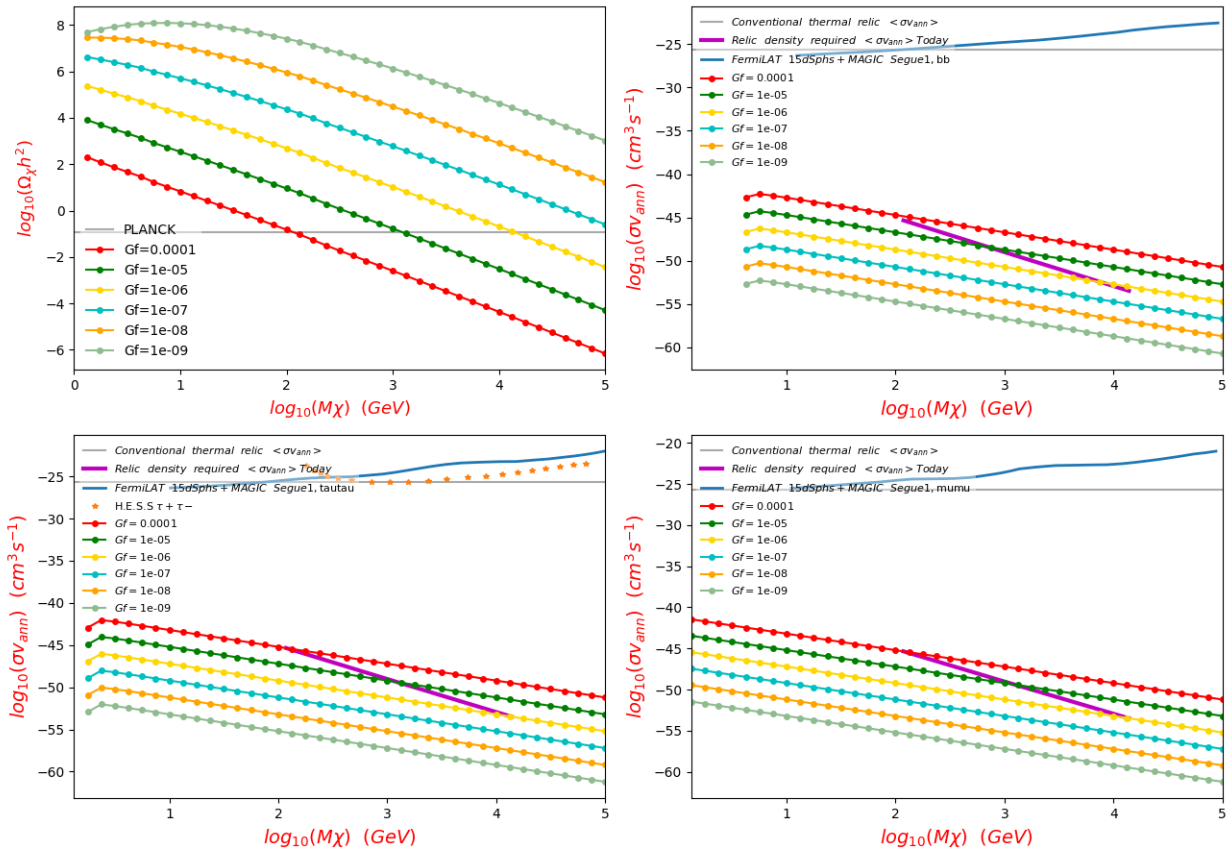

Vector DM annihilation
via Alternative vector operator
with universal coupling

Fig. top left: $log_{10}(\Omega_\chi h^2)$ *VS* $log_{10}(M_\chi)$
Fig. top right: $b\bar{b}$ $log_{10}(\sigma v_{ann})$ *VS* $log_{10}(M_\chi)$
Fig. bottom left: $\tau^+\tau^-$ $log_{10}(\sigma v_{ann})$ *VS* $log_{10}(M_\chi)$
Fig. bottom right: $\mu^+\mu^-$ $log_{10}(\sigma v_{ann})$ *VS* $log_{10}(M_\chi)$

Figure 14: For vector Dark Matter annihilation via an alternative vector operator with universal coupling, the Dark Matter mass m_χ and coupling constant G_f required by the relic density are shown on the top left panel. This is a d-wave annihilating model. None of the 3 final states is sensitive in today's experiment. The slopes of annihilation cross section indicate this kind of model is even more difficult to be probed in indirect detection than the other models. See Table 2 for more explanation.

Operator name	wave	Allowed G_f and m_χ, and Sensitivity		
		$b\bar{b}$	$\tau^+\tau^-$	$\mu^+\mu^-$
		FermiLAT, MAGIC	FermiLAT, MAGIC, H.E.S.S	FermiLAT, MAGIC
Fermion Dark Matter				
Scalar	p-wave	not snsitive	insensitive	insensitive
Pseudoscalar	p-wave	$G_f < 10^{-7}$,$m_\chi > 138\,GeV$	$G_f <\sim 10^{-6}$,$m_\chi > 90.4\,GeV$	insensitive
Vector	s-wave	$G_f < 10^{-6}$,$m_\chi > 110\,GeV$	$G_f < 10^{-7}$,$m_\chi > 1900\,GeV$	$G_f < 10^{-5}$,$m_\chi > 10\,GeV$
axial-vector	s-wave	$G_f < 10^{-6}$,$m_\chi > 23\,GeV$	$G_f < 10^{-4}$,$m_\chi > 13\,GeV$	insensitive
Tensor	s-wave	$G_f < 10^{-6}$,$m_\chi > 107\,GeV$	$G_f < 10^{-7}$,$m_\chi > 1900\,GeV$	$G_f < 10^{-5}$,$m_\chi > 10\,GeV$
Scalar-Pseudoscalar	p-wave	insensitive	insensitive	insensitive
Pseudoscalar-Scalar	p-wave	$G_f < 5 \cdot 10^{-7}$,$m_\chi > 140\,GeV$	$G_f < 10^{-6}$,$m_\chi > 91\,GeV$	insensitive
Vector-axial-vector	s-wave	$G_f < 10^{-6}$,$m_\chi > 107\,GeV$	$G_f < 10^{-7}$,$m_\chi > 1900\,GeV$	$G_f < 10^{-5}$,$m_\chi > 10\,GeV$
AVector-Vector	s-wave	insensitive	insensitive	insensitive
Alternative Tensor	s-wave	$G_f < 10^{-7}$,$m_\chi > 107\,GeV$	$G_f < 6 \cdot 10^{-8}$,$m_\chi > 1900\,GeV$	$G_f < 10^{-5}$,$m_\chi > 10\,GeV$
Chiral	s-wave	$G_f < 6 \cdot 10^{-7}$,$m_\chi > 107\,GeV$	$G_f < 6 \cdot 10^{-8}$,$m_\chi > 1900\,GeV$	$G_f < 10^{-5}$,$m_\chi > 10\,GeV$
Complex Scalar Dark Matter				
Scalar	s-wave	$G_f < 3 \cdot 10^{-5}$,$m_\chi > 32\,GeV$	$G_f < 9 \cdot 10^{-5}$,$m_\chi > 16\,GeV$	insensitive
Scalar-Pseudoscalar	p-wave	insensitive	insensitive	insensitive
Vector	s-wave	insensitive	insensitive	insensitive
Vector-axial-vector	p-wave	insensitive	insensitive	insensitive
Vector Dark Matter				
Scalar	s-wave	$G_f > 10^{-5}$,$m_\chi > 193\,GeV$	$G_f > 10^{-5}$,$m_\chi > 14\,GeV$	insensitive
Vector	p-wave	insensitive	insensitive	insensitive
Scalar-Pseudoscalar	s-wave	$G_f > 10^{-5}$,$m_\chi > 195\,GeV$	$G_f > 10^{-5}$,$m_\chi > 14\,GeV$	insensitive
Vector-axial-vector	p-wave	insensitive	insensitive	insensitive
Tensor	s-wave	$G_f > 10^{-5}$,$m_\chi > 160\,GeV$	$G_f > 10^{-5}$,$m_\chi > 10\,GeV$	insensitive
Alternative vector	d-wave	insensitive	insensitive	insensitive
Alternative Vec- AxialV	p-wave	insensitive	insensitive	insensitive
Alternative Tensor	s-wave	$G_f < 10^{-5}$,$m_\chi > 90\,GeV$	$G_f < 6 \cdot 10^{-5}$,$m_\chi > 22\,GeV$	insensitive

Table 2: Summary of the selected models and the corresponding results. Here we have considered fermion, scalar and vector Dark Matter candidates and the operators. p-wave is dominant in some cases, and d-wave dominates in one case. In the 3 final states ($b\bar{b}$, $\tau^+\tau^-$, $\mu^+\mu^-$), with the constraints/sensitivities from FermiLAT [111, 127], MAGIC [127], H.E.S.S [125], CTA [126], HAWC [130], IceCube [128], and the annihilation cross section each model can produce today, the allowed range of G_f and m_χ are obtained. There are a lot of cases that are beyond the sensitivities of the existing experiments. Remark: here no boost factor has been considered in the calculation, this could be improved if any boost factor exists, for example, coannihilation, the Sommerfeld enhancement, etc.

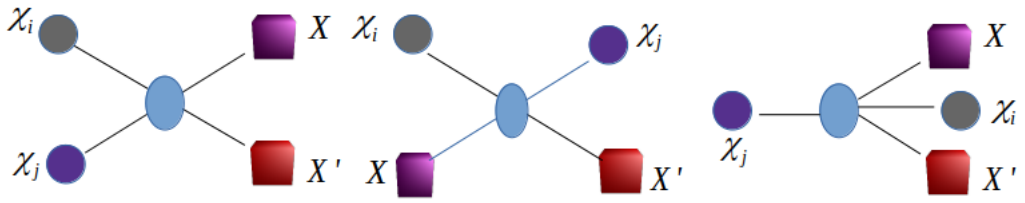

Figure 15: The three types of reactions in the early Universe [171].

type of coupling or the coupling coefficient as shown in Tables 11 to 13 (Appendix A) into consideration.

The calculation in this section does not contain any boosting factor. For some cases, such as the p-wave models, boost factor may play an important role, this needs to be further investigated.

3.5 Coannihilation

In most of the Dark Matter models on the market, when people consider indirect detection, self-annihilation is taken into account. Self-annihilation treats the interaction between a Dark matter particle and its antiparticle, the two incident particles share the same mass. Annihilation could possibly happen between two near-mass particles with small mass splitting. This case is called coannihilation. Assuming the symmetry is not broken, there are two standard methods to treat coannihilation. The first was developed in Ref. [171], it has been widely applied until today, for example in Ref. [195, 196, 197]; the second was developed in Ref. [198], it has also been applied such as in Ref. [199]. Since both methods are practical, here the first method is applied in this work to evaluate all the possible interactions for the incident particles:

$$\begin{cases} \chi_i\chi_j \longleftrightarrow XX' \\ \chi_i X \longleftrightarrow \chi_j X' \\ \chi_j \longleftrightarrow \chi_i XX' \end{cases}, \tag{64}$$

here χ_i, χ_j denote the particles in the dark sector, X, X' denote any particles in the standard model. The three forward and backward interactions need to be taken in to account in the Boltzmann equation

$$\frac{dn_i}{dt} = -3Hn_i - \sum_{j,X}[\langle\sigma_{ij}v\rangle(n_in_j - n_i^{eq}n_j^{eq}) - \left(\langle\sigma'_{ij}v\rangle n_in_X - \langle\sigma'_{ji}v\rangle n_jn_{X'}\right) - \Gamma_{ij}(n_i - n_i^{eq})]\,. \tag{65}$$

This expression could be simplified since all the other heavier particles have finally decayed into Dark Matter particles, so

$$n = \sum_{i=1}^{N} n_i \,, \tag{66}$$

$$\frac{dn}{dt} = -3Hn - \sum_{i,j=1}^{N} \langle \sigma_{ij} v \rangle (n_i n_j - n_i^{eq} n_j^{eq}) \,. \tag{67}$$

At freeze-out, the equilibrium required approximately

$$\frac{n_i}{n} \approx \frac{n_i^{eq}}{n^{eq}} \equiv r \,. \tag{68}$$

So this ratio is defined as

$$r_i = \frac{g_i (1+\triangle)^{3/2} \cdot exp(-x\triangle_i)}{g_{eff}} \,. \tag{69}$$

Suppose $m_1 < m_2 < m_3 ... < m$, and Dark Matter is the lightest particle with mass m_1, the mass splitting is

$$\triangle_i = (m_i - m_1)/m_1 \,, \tag{70}$$

$$g_{eff} = \sum_{i=1}^{N} g_i (1+\triangle)^{3/2} \cdot exp(-x\triangle_i) \,. \tag{71}$$

Then a simple form of the Boltzmann equation of Dark Matter annihilation is obtained

$$\frac{dn}{dt} = -3Hn - \langle \sigma_{eff} v \rangle (n^2 - n_{eq}^2) \,. \tag{72}$$

with

$$\sigma_{eff} = \sum_{ij}^{N} \sigma_{ij} r_i r_j = \sum_{ij}^{N} \sigma_{ij} \frac{g_i g_j}{g_{eff}^2} (1+\triangle_i)^{3/2} (1+\triangle_j)^{3/2} exp[-x(\triangle_i + \triangle_j)] \,. \tag{73}$$

For systems with two Dark matter particles, $\triangle_1 = 0$, we note $\triangle_2$ as $\triangle$.

$$g_{eff} = g_1 + g_2 (1+\triangle)^{3/2} exp(-x\triangle) \,, \tag{74}$$

$$\sigma_{eff} = \sigma_{11} \frac{g_1 g_1}{g_{eff}^2} + \sigma_{12} \frac{g_1 g_2}{g_{eff}^2} (1+\triangle)^{3/2} exp[-x\triangle] + \sigma_{22} \frac{g_2 g_2}{g_{eff}^2} (1+\triangle)^3 exp[-2x\triangle] \,. \tag{75}$$

For two Dirac fermions, $g_1 = g_2 = 4$, then

$$\sigma_{eff} = \sigma_{11}(\frac{4}{g_{eff}})^2 + \sigma_{12}(\frac{4}{g_{eff}})^2(1+\triangle)^{3/2}exp[-x\triangle] + \sigma_{22}(\frac{4}{g_{eff}})^2(1+\triangle)^3 exp[-2x\triangle]\,. \tag{76}$$

The efficiency of the annihilation is defined as

$$J = \int_{x_f}^{\infty} \frac{\langle \sigma_{eff} v \rangle}{x^2} dx = \frac{1}{x_f}\big(a_{eff} + \frac{3b_{eff}}{x_f} + \frac{20c_{eff}}{x_f^2}\big)\,, \tag{77}$$

where the a_{eff}, b_{eff}, c_{eff} are similar to the expression of σ_{eff}, thus can be got by replacing σ_{ij} with a_{ij}, b_{ij}, c_{ij}. For instance

$$a_{eff} = \sum_{ij}^{N} a_{ij} r_i r_j = \sum_{ij}^{N} a_{ij} \frac{g_i g_j}{g_{eff}^2}(1+\triangle_i)^{3/2}(1+\triangle_j)^{3/2} exp[-x(\triangle_i + \triangle_j)]\,. \tag{78}$$

Then the freeze-out temperature is

$$x_f = ln(l(l+2)\sqrt{\frac{45}{8}}\frac{g M_\chi M_{planck}\big(a_{eff} + \frac{6b_{eff}}{x_f} + \frac{60c_{eff}}{x_f^2}\big)}{2\pi^3 g_{tot,f}^{1/2} x^{\frac{1}{2}}}\,. \tag{79}$$

And the relic density is

$$\Omega_c h^2 = \frac{1.07\cdot 10^9}{J g_{tot,f}^{1/2} m_{planck}} = 1.07{\cdot}10^9 \frac{x_f}{g_*^{1/2} m_{planck}(GeV) < a_{11} I_a + 3b_{11} I_b/x_f + 20 c_{11} I_c/x_f^2 >}\,, \tag{80}$$

$$\text{with } \begin{cases} I_a = \frac{x_f}{a_{11}} \int_{x_f}^{\infty} x^{-2} a_{eff} dx \\ I_b = \frac{2\cdot x_f^2}{b_{11}} \int_{x_f}^{\infty} x^{-3} a_{eff} dx \\ I_c = \frac{3\cdot x_f^3}{c_{11}} \int_{x_f}^{\infty} x^{-4} c_{eff} dx \end{cases}\,.$$

For the case of 2 near-mass particles in coannihilation. As shown in Fig. 16 and Fig. 17, for fermion Dark Matter, we scan the parameter space $\{m_{\chi 1}, \Lambda\}$ to find the parameters which satisfy $\Omega_c h^2 = 0.120 \pm 0.001$ [6]. For δm = 0.05, 0.1, 0.15, 0.2, 0.25, Dark Matter mass $m_{\chi 1}$ is varied to scan in the range $1\,GeV < m_{\chi 1} < 1\,GeV$ and $1 < \Lambda/m_{\chi 1} < 9$.

It is found that for all these models, if $m_{\chi 1}$ is fixed, higher Λ is needed to produce the right relic density, and Λ is larger for smaller δm. For several models, it is impossible to produce the required relic density if δm is not small, such as the case of a pseudoscalar operator. For $\delta m > 0.20$, there is no Dark Matter and Λ that could satisfy the requirement of relic density. For the vector interaction, this is more evident since only $\delta m < 0.15$ is allowed. And lower mass is preferred if coannihilation exists; for high Dark Matter mass, Λ must not be too large. An-

other indication is: for several types of operators, even with a very tiny δm, lower Dark Matte mass is allowed if coannihilation exists, if $\delta m \leqslant 0.05$ for the pseudoscalar, vector, pseudoscalar-scalar operators, $m_{\chi 1} > 400\,GeV$ is not allowed. This is important since the EFT is only valid when $\Lambda \gg 2m_{\chi 1}$, the corresponding line is added (black horizontal) on each plot. It is found that $m_{\chi 1} > 400\,GeV$ is only valid for the tensor, alternative tensor, and chiral interactions.

All these figures are for the case of universal coupling. It is more complicated for Yukawa coupling. For example, in the case of fermion Dark Matter and scalar mediator, when being considered to annihilate via Yukawalike coupling, it is not allowed to satisfy the correct relic abundance in the same range of the parameter space of universal coupling. That is why only the case of universal coupling is shown in this work.

3.6 Complementary constraints

The upper limits of the annihilation cross section in the indirect detection experiments are collected, as shown in Fig. 18.

For the $b\bar{b}$ channel, the envelope of the strongest constraining limits from the experiments is applied.

In the range $10\,GeV < m_\chi$, the CMB observations by PLANCK put the strongest constraint [44].

In the range $[10\,GeV, 162\,GeV]$, the strongest constraints are obtained by the observations of dSphs by VERITAS, FermiLAT and MAGIC [203, 204].

In the range $[162\,GeV, 2.23\,TeV]$, the IGRB observation obtained by FermiLAT is stronger than the other experiments [202].

In the range $[2.23\,TeV, 66.7\,TeV]$, the H.E.S.S observations of the Galactic halo give the strongest limits [174].

In the range $[66.7\,TeV, 92.9\,TeV]$, the TAIGA Cherenkov air shower array has the best sensitivity [207], while the best constraint is obtained by HAWC [130].

In the range of $m_\chi > 92.9\,TeV$, the HAWC γ-ray observatory has put the strongest limits with its observations of the Galactic halo [130].

With the precise annihilation cross section required by the relic density obtained in [200], the standard thermal decoupling has been computed with a variation of the relativistic degrees of freedom associated with the total entropy density. The corresponding limit is shown with a gray dotted horizontal line. The range below 100 GeV has been ruled out for this kind of calculation.

The CTA sensitivity in this plot is conservative [179], this may be caused by the uncertainty of the project, better sensitivities have been shown in previous work [126] but now is reduced to this level, this might be improved in the future.

This fine partition of the energy range into segmentation is important in the next step, not just because they are from different observations, but also because it is required by the calculation of the annihilation cross section. For example, properties such as the velocity of Dark Matter in these targets need to be con-

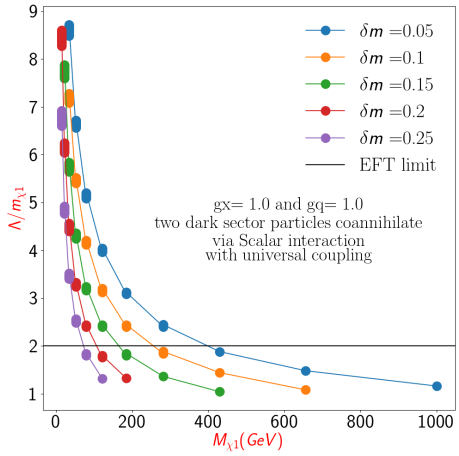

(a) Scalar

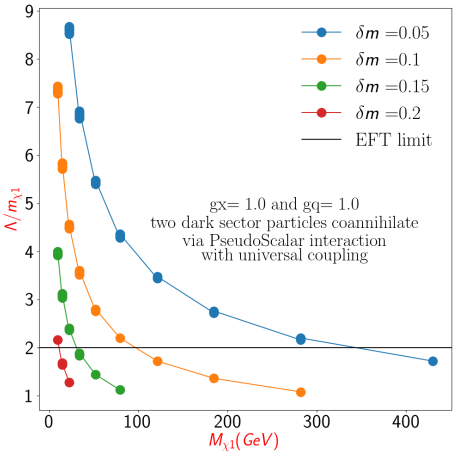

(b) Pseudoscalar

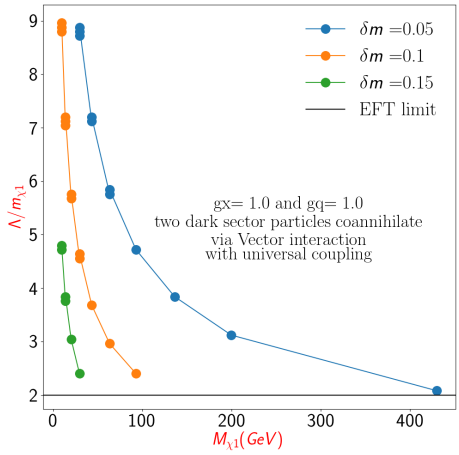

(c) Vector

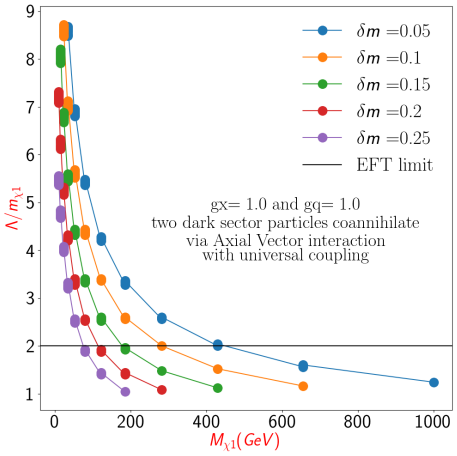

(d) Axial Vector

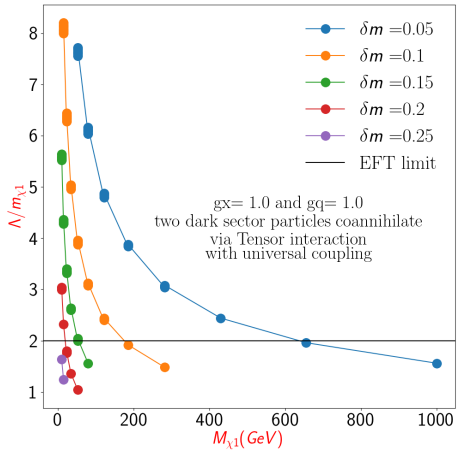

(e) Tensor

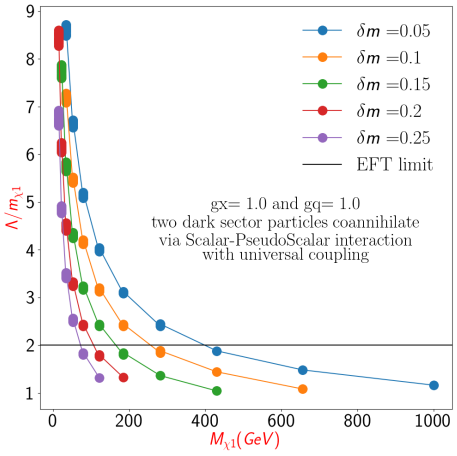

(f) Scalar - Pseudoscalar

Figure 16: Contours of the mass splitting in coannihilation required by the relic density for fermion Dark Matter (Part I). The gray horizontal line is set as the EFT is valid only when $\Lambda > 2m_\chi$. In the subplots, there are curves corresponding to different interactions. The dotted lines with different colors are the relic density required value of $\{\Lambda/m_{\chi 1}, m_{\chi 1}\}$ for different mass splitting δm from 0.05 to 0.25.

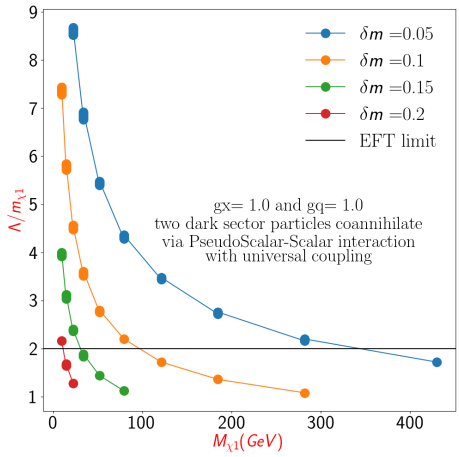

(a) Pseudoscalar - Scalar

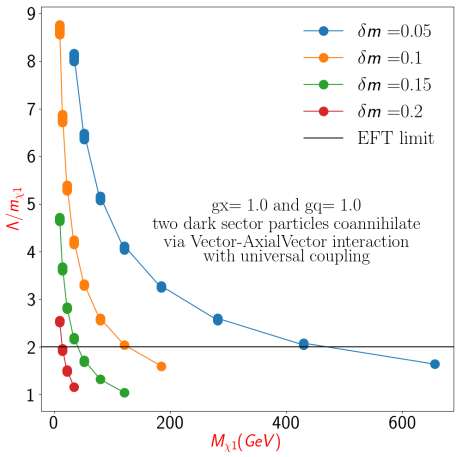

(b) Vector - axial-vector

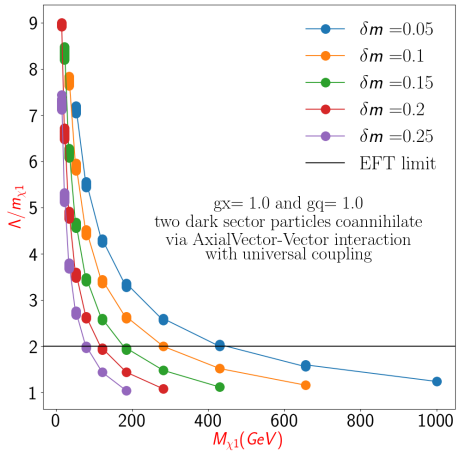

(c) axial-vector - Vector

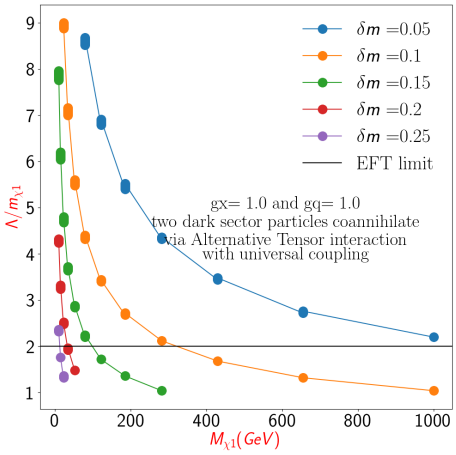

(d) Alternative Tensor

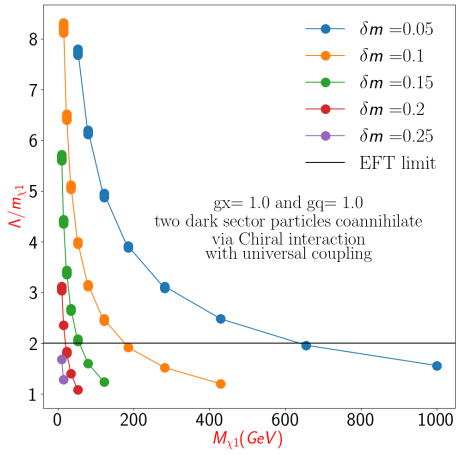

(e) Chiral Vector

Figure 17: Contours of the mass splitting in coannihilation required by the relic density for fermion Dark Matter (Part II). The gray horizontal line is set as the EFT is valid only when $\Lambda > 2m_\chi$. In the subplots, there are curves corresponding to different interactions. The dotted lines with different colors are the relic density required value of $\{\Lambda/m_{\chi 1}, m_{\chi 1}\}$ for different mass splitting δm from 0.05 to 0.25.

sidered (as shown in Section 3), especially for the velocity-dependent annihilation models. In this section, the averaged velocity in the targets are considered in the calculation, for dSphs, $v = 10\,km/s$ [209], for the Galactic halo, $v = 220\,km/s$ [210]. For more details about the velocity-dependent annihilation, cf. Chapters 4 and 5.

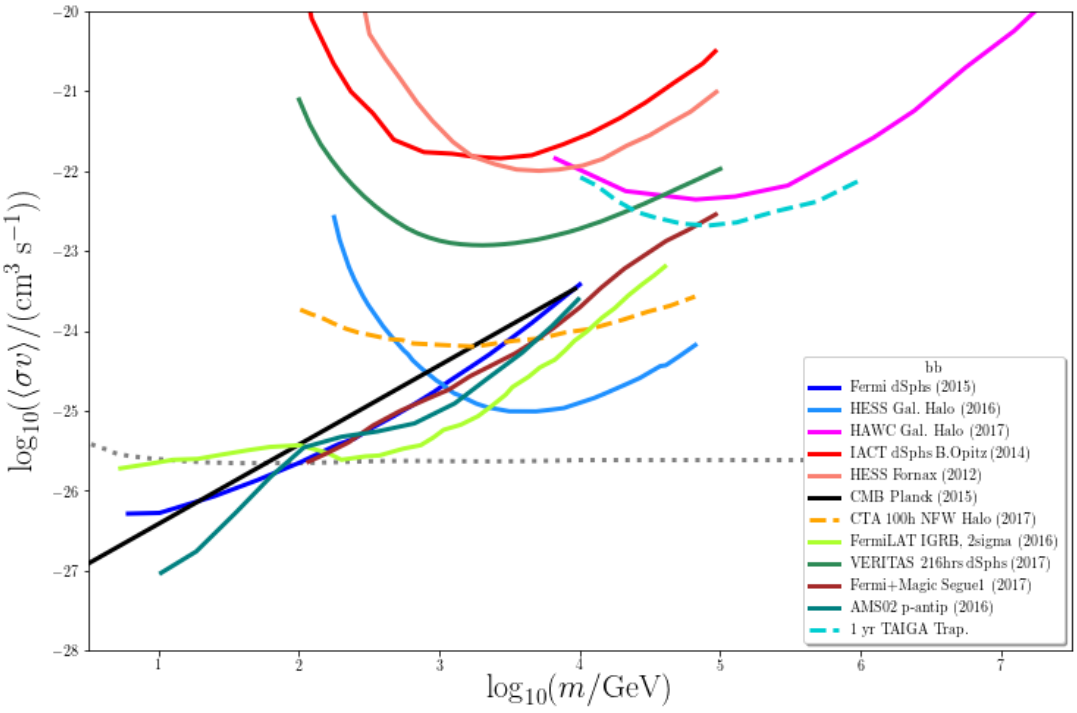

Figure 18: A collection of bounds (final state $b\bar{b}$) from existing instruments and observations (solid lines) as well as bounds from future installations (dashed lines) compared with the cross section to match the relic density in standard thermal decoupling scenarios (dotted line) [200]. The most constraining limits are obtained with Fermi-LAT observations of dwarf galaxies [201] and (more model-dependent) from the intergalactic gamma-ray background [202]. At the TeV-mass range, H.E.S.S. observations of the Galactic halo are most constraining [174], while observations of dwarf galaxies fall behind [203, 204, 205]. The CTA sensitivity for observations from the inner Galactic halo from [179], using a similar method as in [174], is obviously rather conservative. At even higher energies, the air shower arrays HAWC [130] and TAIGA [207] provide the best sensitivities. Complementary to the gamma-ray observations, measurements of the anti-proton component of cosmic rays (AMS-02 [129]) and constraints from the CMB with Planck data [44] provide excellent constraints at the low mass end [206].

With the envelope of limits in indirect detection experiments, we can scan the parameter space in $\{m_\chi, m_{med}\}$, here $g_q = g_{DM} = 1$ is set as well with universal coupling for fermion Dark Matter and 4 types of mediators. The results are shown with orange curves in Fig. 19 and Fig. 20. It is found that the sensitivity

of indirect detection is relatively weaker than direct detection, but it covers the highest energy range.

The constraints and sensitivities of the collider-based experiments are accumulated as follows.

ILC: the reach of the ILC Dark Matter searches on the ILC project has been studied for three different proposed energies (250 GeV, 500 GeV. 1000 GeV) and five types of operators (scalar s-channel, scalar t-channel, vector axial-vector, chiral vector) in Ref. [211], then the comparison of sensitivity for two operators (vector, axial-vector) between ILC and LHC has been shown in Ref. [141]. The latest results are shown in [142]. To compare with the other experiments, the best sensitivities of ILC are extracted in this work, so the 3σ CL sensitivities for a 1 TeV ILC are computed and convert to the relationship between m_χ and m_{med} in this work. Here the scalar operator is also considered to have universal coupling in this work, so this assumption is applied in the calculation.

LHC: for vector operator and axial-vector operator, the CMS mono-jet searches for different CoM energies (8 TeV, 13 TeV and 14 TeV) and integrated luminosities ($30fb^{-1}$, $300fb^{-1}$,$3000fb^{-1}$) have been studied [143]. 3 scenarios of them are taken to make a comparison in this work.

The limits of scattering cross section in the direct detection have been accumulated from the following experiments.

The strongest constraints in direct detection are obtained in Pandax-II [131], Xenon1T [181], Pico-60 [135].

The other experiments which predict excellent sensitivities include DARWIN, PANDAX30T, PandaX-4T [133], XENONnT, SuperCDMS-1700 kg, LZ 15.6t-y [213]. The neutrino background is also shown in these plots to make a boundary of detectability.

The pink region on the upper left is the part where the EFT is not valid. For each value of m_χ, a corresponding m_{med} to produce the correct relic density is found. This leads to the gray curves in Fig. 19 and Fig. 20.

For all the four operators, only the small regions at high (> 10 TeV) and very low mass (< 10 GeV) are still allowed. An interesting problem in these plots is that the sensitivities of indirect detection vary a lot for different operators. For the case of a scalar operator, the sensitivities of the indirect detection experiments are extremely incompetent compared with the other experiment which is caused by the velocity-dependent annihilation. But it offers a unique probe for Dark Matter searches, cf. Chapters 4 and 5.

Beyond the limitation set by the direct detection experiments, a heavy mediator is always allowed but impossible to be detected.

3.7 Conclusion and discussion

This chapter applies the EFT supplemented by simplified models to put con-

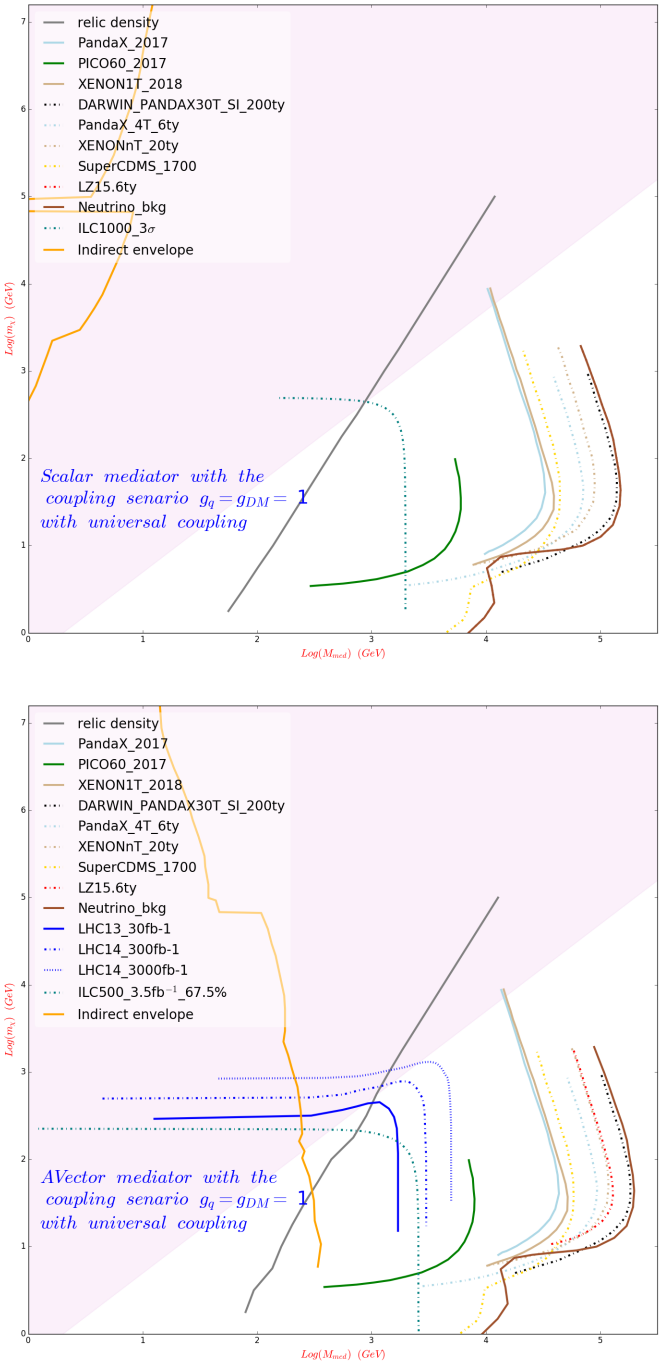

Figure 19: Complementary limits for a fermion Dark Matter and a scalar operator (top) or axial-vector (bottom) with universal coupling: The constraints from direct searches, indirect searches, relic density, and collider searches are included. Only a small region at high (> 10 TeV) and very low mass (< 10 GeV) is still allowed. For axial-vector, the mediator mass could be larger than that of the scalar mass. Here we have used the ILC sensitivity (dashed) from [141] and LHC constraints (solid) and sensitivities (dashed) from [143]. For indirect detection, we have combined the constraints in Fig. 18. For the relic density, we have used the data from the Planck collaboration [212]. For direct detection, we have collected all the constraints (solid, spin-independent cross sections) and sensitivities (dashed) with data from [131, 194, 213]. The results of direct detections are similar to [143].

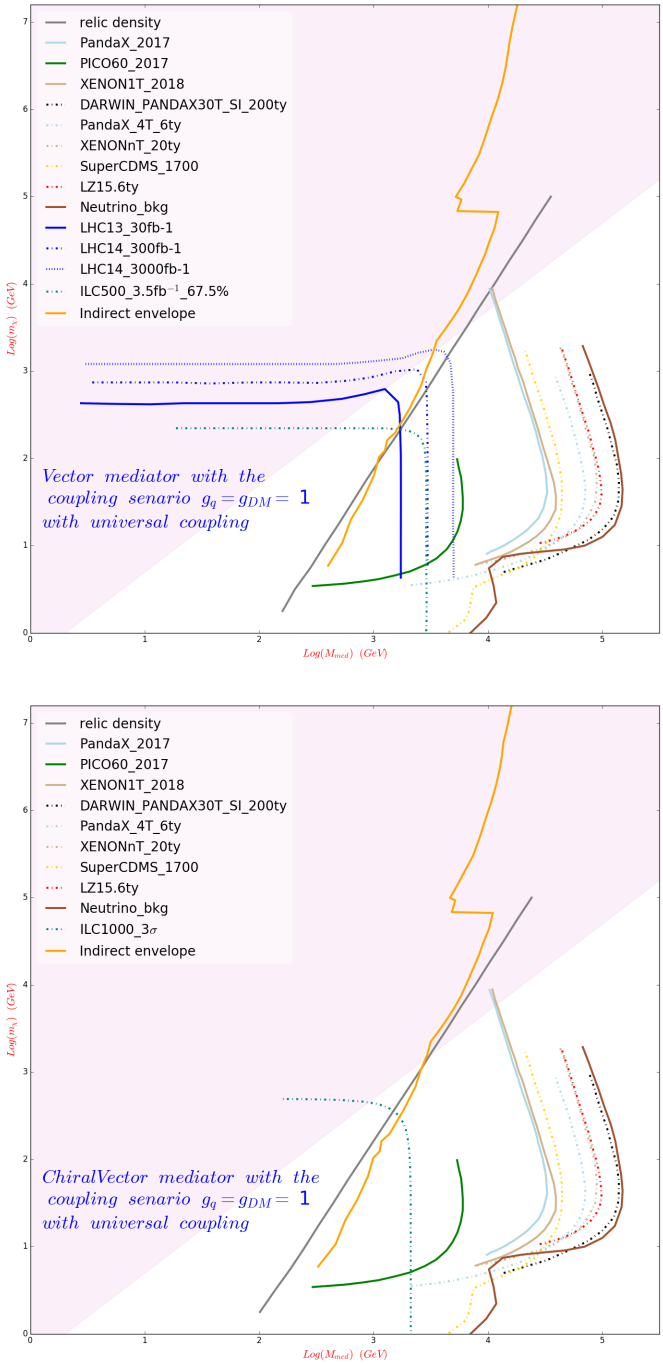

Figure 20: Complementary limits for a fermion Dark Matter and a vector operator (top) or chiral-vector operator (bottom) with universal coupling: the constraints from direct searches, indirect searches, relic density, and collider searches are included. Only a small region at high ($>$ 10 TeV) and very low mass ($<$ 10 GeV) is still allowed. Here we have used the ILC sensitivity (dashed) from [141] and LHC constraints (solid) and sensitivities (dashed) from [143]. For indirect detection, we have combined the constraints in Fig. 18. For the relic density, we have used the data from the Planck collaboration [212]. For direct detection, we have collected all the constraints (solid, spin-independent cross sections) and sensitivities (dashed) with data from [131, 194, 213]. The results of direct detections are similar to [143].

straints on Dark Matter. Multifunctional codes have been developed to compare theoretical expectation with observational limits.

The validity of EFT and the connection between the EFT and simplified models have been discussed for the fermion, scalar, and vector Dark Matter models. The EFT validity has been investigated to find the valid range of the parameters (G_f, Λ, m_{med}, m_χ).

The constraints from indirect detection have been derived at first, the standard treatment of the Boltzmann equation is revisited to find the x_f at freeze-out, which is then used to get the theoretical value of the relic density today. Dark Matter models are collected with various operators from several previous publications and added to the codes. Then 4 general modes of annihilation are found depending on the types of coupling and the dominating wave term in the annihilation cross section. With the limits from FermiLAT, H.E.S.S., CTA, MAGIC, and PLANCK, we have made a comparison with the theoretical values. We find only one of the 4 modes gives the same annihilation cross section required by the conventional treatment: the case of universal coupling and s-wave. For the other 3 modes, a lot of the models (as summarized in Table 2) contain non-sensitive Dark Matter candidates in the current experiments. This means this type of WIMP hypothesis could not be ruled out. All the scanning work shows heavy Dark Matter remains to be probed in the future.

The calculation of coannihilation is a natural extension of the hypothesis of a single particle in the dark sector. A model with two near-mass fermion particles has been scanned. When they coannihilate, their mass and mass splitting is limited by the relic density. In all these cases, small mass splitting produces significant annihilation, and larger cut off energy is needed for low mass Dark Matter. These results means, in the range where the EFT is valid, Dark Matter is preferred to be not too high if another unknown near-mass particle exists. This calculation could be extended easily to the cases with more unknown particles in DarkSPIDER.

The bounds are collected from existing indirect detection experiments, all the most constraining limits are shown in Fig. 18. The envelope of indirect detection is then applied to put limits on the 2D map of $\{m_\chi, m_{med}\}$. The strongest constraints are from the direct detection experiments, for which we could also put limits on the 2D map of $\{m_\chi, m_{med}\}$. So are the collider-based experiments (LHC and ILC) and the relic density. Four operators in total are considered for fermion Dark Matter. Most of the regions in the low Dark Matter mass in the parameter space $\{m_\chi, m_{med}\}$ have been ruled out. Only some small regions below 10 GeV and above 10 TeV are allowed. This is consistent with the results in the other methods in this chapter. An interesting case is a fermion Dark Matter and a scalar mediator; this p-wave annihilating model shows weak constraints if there is no other boost factor, this is important since a very high energy range could only be probed with indirect detection observations. And complicated physics exists in this problem. For this reason, efforts for p-wave annihilating Dark Matter are done and shown in Chapters 4 and 5.

Chapter 4 Velocity dependence of Dark Matter annihilation in the dSphs

4.1 Introduction

Indirect detection looks for primary and secondary particles from the final states of Dark Matter annihilation and decay. In the non-relativistic limits, the annihilation cross section can be written as a function of the relative velocity of the incident particles, it is given by $\langle\sigma v\rangle \approx a + bv^2 + cv^4$. Most of the indirect detection studies have concentrated on the s-wave annihilation for which the b, c terms are negligible; the corresponding combined results have ruled out Dark Matter particle below about 120 GeV as shown in Fig. 18. The latest analysis from the FermiLAT collaboration found the constraints improved via new associations could potentially rule out thermal WIMPs up to 400 GeV ($b\bar{b}$) and 250 GeV ($\tau^+\tau^-$) [222]. Futural gamma-ray observations from the ground-based imaging air/water Cherenkov technique like TAIGA, LHAASO, CTA will have better sensitivities in the TeV energy scale [223], but all of them are still under construction. The direct scattering experiments such as PandaX-II and LUX [64, 65] will also play a sensitive role, they start touching the irreducible neutrino background, but no signal has been reported until now. Neutrino detectors like ANTARES, IceCube, KM3NeT are playing irreplaceable roles and will open a window to the Wimpzillas (10^{15} to $10^{18}eV$) world [224, 225].

Unlike s-wave annihilation, when the b term dominates, the differential gamma-ray flux induced by the so-called p-wave annihilation is characterized by Equation (81), in which we need to consider the influence of velocity on both the annihilation and the dynamics of the target system. For the sake of simplicity, to compare with the s-wave case, we convert it to Equation (81). This $\langle\sigma v\rangle_{eff}$ term could thus be added to the s-wave $\langle\sigma v\rangle$ plots to show us the difference in an intuitive way.

$$\langle\sigma v\rangle_{eff} = \frac{\int_{\triangle\Omega}\int_{l.o.s}\rho^2(l,\Omega)\langle\sigma v(l,\Omega)\rangle dl d\Omega}{\int_{\triangle\Omega}\int_{l.o.s}\rho^2(l,\Omega) dl d\Omega} = \frac{\int_0^R r^2\rho^2(r)\langle\sigma\nu(r)\rangle dr}{\int_0^R r^2\rho^2(r) dr} \quad . \quad (81)$$

The total gamma-ray flux from the Dark Matter from a dSph is defined as

$$\Phi = \frac{1}{8\pi m_\chi^2}\int\frac{dN_\gamma}{dE_\gamma}dE_\gamma \cdot \int_{\triangle\Omega}\int_{l.o.s}\rho^2(l,\Omega)\langle\sigma v(l,\Omega)\rangle dl d\Omega \quad (82)$$

$$= \frac{\langle\sigma v\rangle_{eff}}{8\pi m_\chi^2}\int\frac{dN_\gamma}{dE_\gamma}dE_\gamma \cdot \int_{\triangle\Omega}\int_{l.o.s}\rho^2(l,\Omega) dl d\Omega \quad , \quad (83)$$

where m_χ denotes the Dark Matter mass, $\frac{dN_\gamma}{dE_\gamma}$ denotes the initial differential gamma-ray spectrum per Dark Matter pair annihilation, $\rho(l, \Omega)$ the inner mass density profile in the target.

We have observed the GeV excess from the Galactic center (GC), but this is now less and less likely to be caused by Dark Matter, the most promising explanation is the unsolved millisecond pulsars in the Galactic center [226]. If there is still any possibility to show the existence of Dark Matter in the GC, we must have a better understanding of the physics in it. The biggest difficulty to study the GC is the gamma-ray background, this forces us to pay attention to the targets with low background.

The Local Group dwarf spheroidal galaxies (dSphs) are key targets to study particle physics, astrophysics, and cosmology. Each of them has a high mass to light ratio and a relatively short distance to us. They are Dark Matter dominated and baryonic emission-free. On the other hand, by studying the Dark Matter annihilation and decay, stringent constraints on Dark Matter particle from gamma-ray indirect detection have been given in the last decades by FermiLAT, HESS, and the other gamma-ray experiments [178, 205, 245, 291, 301, 379, 381]. And it has been sold for years that we are on the threshold of discovery of Dark Matter particle [227] or the moment of ruling out it. The astrophysical difficulties in gamma-ray indirect detection of Dark Matter concentrate on several widely known problems which could be tested by investigating the dSphs, like the 'core-cusps' problem [47, 48, 49], the 'missing satellite problem' [50, 52], the 'too-big-to-fail' problem [51, 52, 53, 54], all these rises up during a long time in the Optical and X-ray observations like the SDSS and Chandra which help in the understanding of the mass distribution and velocity dispersion profiles in the galaxies [117, 292, 293, 295, 296, 297, 300].

Until now, unfortunately, there is no observational evidence from dSphs to support any dynamical Dark Matter hypothesis [228]. There are three possible reasons for the non-observation: first, we have not yet found the proper model of the Dark Matter candidate nor the astrophysical targets; second, our detectors need to be improved for a better sensitivity to get more data; third, we have a wrong explanation of the existing data.

To find a candidate solution to this problem, we try to develop a method to revisit the dSphs data with a model-independent analysis. For the dSphs, a generalized model is developed to describe the dynamics, the anisotropy, and the mass density; for the Dark Matter particle model, simplified models are called to calculate the annihilation cross section. Another aspect needed to be considered consists of the astrophysical uncertainties and boost factors in the calculation, hence the Sommerfeld enhancement is taken into account since this is the largest boost factor we know. The other uncertainties and boost factors are discussed in Section 4.2.4.

Comparison of the properties among different targets shows one of the most important differences is the velocity dispersion profile which describes statistically how the stars' velocity differs from the average value. It is able to reach the order

of $10\,km/s$ in the dSphs and several $10^3\,km/s$ in the galaxy clusters [285].

This work starts with confronting the theoretical calculation of the p-wave annihilation with observations in the dSphs in the absence of the Sommerfeld enhancement. The Sommerfeld enhancement is then taken into consideration to make a comparison. The Sommerfeld enhancement can boost the annihilation when the relative velocity is small ($\ll c$), and the resonances may play a dramatic role to improve the detectability of p-wave annihilating Dark Matter. A predictable signal is expected to be found by applying this effect in the calculation.

4.2 Relative Velocity in annihilation

To calculate the l.o.s projected velocity dispersion, the mass density profile (NFW [286], Einasto [287, 27], Burkert [288]), anisotropy profile, and stellar density profiles need to be understood first. A method to free all the parameters within generic models is developed to establish an N-dimension fast scanning algorithm.

The dSphs are clean targets today since the baryonic matter has been stripped out during the long history. The formation of dSphs is still unknown to us, otherwise, we should consider the annihilation and decay during the full history as in the N-body simulation. The dSphs we have observed today are usually assumed as a steady system in dynamical equilibrium since they have no hot gases anymore [298]. They contain tiny photon backgrounds since they are old, star formation in them has stopped a long time ago. There are two ways to treat it: applying the standard spherical Jeans equation [229, 230, 232, 234] or the Schwarzschild method [299]. In this work, the former method is chosen.

4.2.1 Jeans Equation

For a spherical and Dark-Matter-dominated system, if it is in a steady state without streaming motions, its dynamical properties have been studied explicitly [229, 230, 232, 234] and could be expressed by the standard Jeans equation, reads

$$\frac{d(l\sigma_r^2)}{dr} + 2\frac{\beta(r)}{r}l(r)\sigma_r^2 = -l(r)\frac{GM(r)}{r^2}, \tag{84}$$

where the following definitions have been recalled:
r: the heliocentric distance to the system center.
M(r): the total enclosed mass within r.
ł(r): the 3D stellar volume mass density.
$\beta(r)$: the velocity anisotropy factor, $\beta = 0$ is the isotropic case, cf. Section 4.2.2.
σ_r: the radial velocity dispersion in the system.

To solve this spherical Jeans equation, all these definitions must be computed first. The corresponding computation is based on the following calculations.

4.2.1.1 Mass density profile

The Zhao-Hernquist profile and the Einasto profile have been applied in many papers [149], most of the popular models are included in these two families. The conventional expression of the Zhao-Hernquist profile is chosen, it is given as

$$\rho(r) = \rho_s \left(\frac{r}{r_s}\right)^{-\gamma} \left[1 + \left(\frac{r}{r_s}\right)^{\alpha}\right]^{\frac{\gamma - w}{\alpha}}, \tag{85}$$

where α denotes the transition slope, w denotes the outer slope, γ denotes the inner slope, r_s denotes the scale radius. The profile is cored when $\gamma = 0$, and 'cuspy' when $\gamma > 0$. When $\{\alpha, w, \gamma\} = \{1, 3, 1\}$, it becomes the NFW profile [286]; When $\{\alpha, w, \gamma\} = \{arbitrary, 4, 1\}$, it becomes the generalized NFW profiles [377]; when $\{\alpha, w, \gamma\} = \{7/9, 31/9, 4/9\}$, it becomes the Dehnen & McLaughlin profile [378]; etc.

A more general model has been established to unify more models by one formula [231], but its compact mathematical expression makes it hard to be implemented in this work.

4.2.1.2 Halo mass function

The enclosed mass depends on the density profile as $M(r) = 4\pi \int_0^r s^2 \rho(s) ds$. With the Zhao-Hernquist profile, the mass profile can be written as

$$M(r) = 4\pi \int_0^r s^2 \rho(s) ds = \frac{4\pi \rho_s r_s^3}{3 - \gamma} \left(\frac{r}{r_s}\right)^{3-\gamma} F_1\{\frac{3-\gamma}{\alpha}, \frac{w-\gamma}{\alpha}, \frac{3-\gamma}{\alpha} + 1, -(\frac{r}{r_s})^{\alpha}\}, \tag{86}$$

where $F_1(a, b, c, d)$ denotes Gaussian's hypergeometric function [117, 148].

4.2.1.3 The stellar density

The luminosity density is the deprojection of the surface brightness profile. There are several popular models of the stellar density, such as the Plummer, Sersic, and King profiles [235, 236, 237]. In this work, the Plummer profile is applied. The Plummer profile of luminosity density reads

$$l(R) = \frac{L}{\pi r_e^2} \frac{1}{(1 + \frac{R^2}{r_e^2})^2}, \tag{87}$$

with L denotes the total luminosity, r_e denotes the half-light radius.

For a given $I(R)$, the 3-D dimension density of the Plummer profile reads

$$l(r) = \frac{3L}{4\pi r_e^3 (1 + \frac{r^2}{r_e^2})^{5/2}}. \tag{88}$$

4.2.2 Velocity anisotropy profile

The anisotropy profile of a non-rotating spherical system has been studied explicitly [230, 232, 238], it is defined as

$$\beta(r) = 1 - \frac{\sigma_T^2(r)}{2\sigma_r^2} = 1 - \frac{\sigma_\theta^2(r) + \sigma_\phi^2(r)}{2\sigma_r^2(r)} = 1 - \frac{\overline{v_\theta^2(r)}}{v_r^2(r)}, \tag{89}$$

where σ_T, σ_r are respectively the tangential and radial velocity dispersions with the relationship $\sigma_T = \sigma_\theta^2(r) + \sigma_\phi^2(r)$, with $\sigma_\theta, \sigma_\phi$ respectively the longitudinal and azimuthal velocity dispersions, and $\overline{v_\theta}, \overline{v_r}$ are the mean components of the velocity in the spherical coordinate system (r, θ, ϕ), and $v_t^2 = v_\theta^2 + v_\phi^2$ in this kind of system.

A general anisotropy profile is proposed for any smooth monotonic anisotropy model on the market [239], as in Equation (90). We vary the parameters to get the isotropic profile ($\beta(r) = 0$), constant anisotropy, the Osipkov Merritt (OM) anisotropy profile and the generalized OM profiles as shown in Table 3, where $'-'$ means an arbitrary value. And the normalization factor $g(r)$ corresponds to the g term in Equation (91).

$$\beta(r) = \frac{\beta_0 + \beta_\infty (r/r_a)^{2\delta}}{1 + (r/r_a)^{2\delta}}, \tag{90}$$

$$\beta(r) = -\frac{1}{2}\frac{dlng}{dlnr}. \tag{91}$$

where r_a is a free parameter.

Name	δ	β_0	β_∞	β_r	$g(r)$
Isotropic	-	-	0	0	1
Constant	0	const	0	β_0	$r^{-2\beta}$
Osipkov Merritt	1	0	1	$\frac{\beta(r/r_a)^{2\delta}}{1+(r/r_a)^{2\delta}}$	$(1 + \frac{r^2}{r_a^2})^{-1}$
General O.M.1	1	-	1	$\beta(r) = \frac{\beta_0+(r/r_a)^{2\delta}}{1+(r/r_a)^{2\delta}}$	$(\frac{r}{r_a})^{-2\beta_0}(1 + \frac{r^2}{r_a^2})^{\beta_0-1}$
General O.M.2	1	-	-	$\frac{\beta_0+\beta_\infty(r/r_a)^2}{1+(r/r_a)^2}$	$(\frac{r}{r_a})^{-2\beta_0}(1 + \frac{r^2}{r_a^2})^{\beta_0-\beta_\infty}$
General O.M.3	-	-	-	$\frac{\beta_0+\beta_\infty(r/r_a)^{2\delta}}{1+(r/r_a)^{2\delta}}$	$(\frac{r}{r_a})^{-2\beta_0}(1 + \frac{r^2}{r_a^2})^{\frac{\beta_0-\beta_\infty}{\delta}}$

Table 3: Anisotropy profiles. With more parameters, as shown in $g(r)$, the models are more generalized.

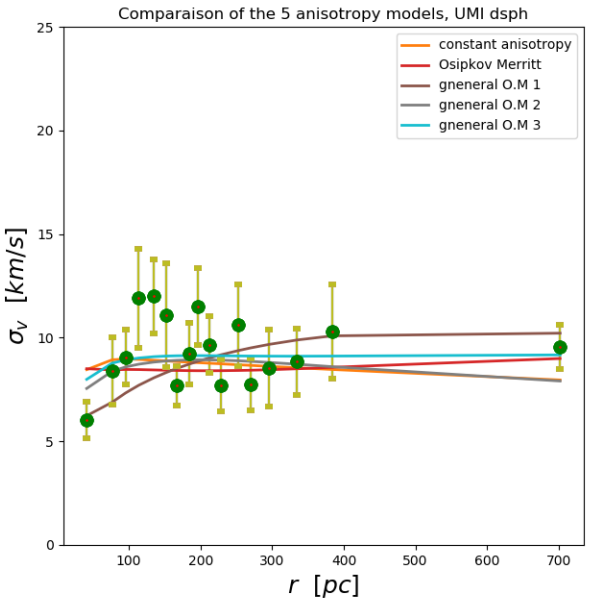

Figure 21: Comparison of the five anisotropy models. The data of the projected velocity dispersion profile of the UMi dSph is from [117]. Five anisotropy models are shown on this plot. Here the PSO fitting method is applied with 120 swarms and 10 iterations. The five curves are the best-fitting results for the five models. The corresponding values of χ^2 are shown in Table 4.

4.2.3 The velocity dispersion

The continuity and closure conditions are taken into account in the Jeans equation, and it can be solved and compared with experimental data. But equilibrium does not guarantee stability, slight anisotropy can make the system unstable, so this method should be used carefully[234]. For simple anisotropy profiles, a detailed solution to the Jeans equation has been provided [232, 241]. It is consistent with a more widely applied method proposed by Binney & Mamon [242]. It has been extended to all the recent papers for the case of the non-constant anisotropy, as in Ref. [148, 243, 244, 245, 246]. To simplify the analysis, we follow this idea and extend it to the generalized Osipkov Merritt anisotropy profile (gOM) including

Anisotropy model	$min(\chi^2)$	d.o.f	p-value
constant	22.08	12	0.036633
Osipkov Merritt	22.38	11	0.023761
Generalized Osipkov Merritt 1	19.87	10	0.014702
Generalized Osipkov Merritt 2	18.14	9	0.008629
Generalized Osipkov Merritt 3	17.31	8	0.00477

Table 4: The χ^2 for the PSO fitting to the projected velocity dispersion data of the UMi dSph [117].

several simple anisotropy profiles as in Table 4.

In order to calculate $\overline{\sigma_r^2}$, the general solution as Equation (92) is taken from Ref. [232, 241].

$$\overline{\sigma_r^2(r)} = \frac{g(r)}{l(s)} \int_r^\infty \frac{l(s)}{g(s)} \frac{GM(s)}{s^2} ds, \tag{92}$$

where g(r) is defined by the anisotropy factor defined in Equation (91), G is the gravitational constant.

Projecting along the line of sight (l.o.s), together with the anisotropy profile, the l.o.s velocity dispersion [232] can be obtained.

$$\sigma_V^2(R) = \frac{2}{I(R)} \int_R^\infty \left(1 - \beta(r)\frac{R^2}{r^2}\right) \frac{l(r)\overline{\sigma_r^2}}{\sqrt{r^2 - R^2}} dr. \tag{93}$$

The velocity dispersion could be observed with red/blue shift. The data is fitted with Equation (93) to get the best-fitting parameters. With the parameters in Equation (92), the value of v_p is obtained. In [246], an approximate relationship shows $v_p^2 \approx 2\sigma_r^2$.

Generalized or modified Schwarzschild's method [251, 252, 253] searches for equilibrium solutions, it tries to find appropriate statistical expression to combine various types of orbit-based models in equilibrium and count the relative contribution of these orbits. It successfully describes axisymmetrical models or triaxial galaxies. There is no restriction on the potential, the distribution function, and all the kinetic parameters are included. But the continuity is not considered in this method; and it causes the so-called fold/cusp catastrophe when unrealistic line/points are formed as a result of the superposition of the orbits. Another shortage is its high precision is based on time-consuming [254], it is a great tool, but to simplify the work, we choose the Jeans equation which is precise enough for this work.

The binaries can increase the velocity dispersion with the movement of stars in the system. The study on the ultrafaint dSphs suggested a possible explanation of the velocity dispersion even without Dark Matter. But Former work found binary motion may contribute only significantly to low-velocity dispersion $\lesssim 3-4\,km\cdot s^{-1}$ such as the ultrafaint dSphs, but highly unlikely can contribute significantly to the classical dSphs with higher velocity dispersion studied in this work [240].

Different from the CLUMPY code, the substructure as shown in Ref.[255] is not considered since this boost factor is small compared with the Sommerfeld boost factor. Another motivation to develop this part is we need to make it compatible with the DarkSPIDER package. The other uncertainties in the astrophysical calculations are discussed in the following subsection 4.2.4.

4.2.4 The astrophysical boost uncertainties

Systematic and astrophysical uncertainties need to be evaluated to calculate the photon flux. A brief and quantitative description is given to show the astrophysical effects which play non-negligible roles.

a) The foreground effect

The foreground effect investigates the fore-ground contamination for classical dSphs and makes us overestimate or underestimate the signal flux and J-factor. The signal flux could be boosted by a factor ≈ 3 if the foreground contamination for classical dSphs is less than 5% [256]. For the case of Ursa Major II, the constant velocity-dispersion bias non-negligibly derives an underestimation of the J-factor by a factor up to 5.

b) The clumpiness

Astrophysical uncertainties of the clumpiness are not negligible. Previous analysis claims the clumpiness boost factor in the Dark Matter annihilation is up to 100-1000 in the halo [257]. In Ref.[258], it shows a boost factor around 4-15. It is claimed in Ref. [259] that the clumpiness boost factors are negligible and strongly disfavored. The CLUMPY group confirmed this boost factor is negligible for the dSphs, and up to 100 for the galaxy clusters [247, 248]. In Ref. [260], a factor is obtained up to $\sim$10 for the largest halos (clusters) at small redshift. Furthermore, some studies at low masses indicate that the concentration-mass relation likely flattens, making this enhancement negligible [261, 262, 263].

c) The non-spherecity

The non-sphericity of the baryons and Dark Matter of the Galactic dSphs is among the major systematic uncertainties in the astrophysical calculation related with Dark Matter annihilations and decays [265]. It is of particular interest to us since it is a natural outcome of the merges of galaxies or clusters. The strong asphericity of individual clusters on surface density profiles may vary by up to a factor of 3 in the projected density at a given radius depending on the line of sight [264].

d) The baryonic infall

Baryon infall into forming Dark Matter halos begins at recombination. The modified gravitation could either steepen the inner Dark Matter profile and then the velocity dispersion profile by adiabatic contraction, and results in a gamma-ray flux boost factor between 2-7 in a conservative analysis [266] or even up to 1000 in some radical analysis [227, 267, 268, 269]. It could flatten the Dark Matter profile since star bursts will be triggered if the local density passes the limit. So the boost could be balanced out by the stellar feedbacks. This effect is thus a natural explanation of the core-cusp problem. An extreme case is a CBH dominated core, which has been studied for a galaxy with spiky profile. This could be used to exclude a very large chunk of the Dark Matter parameter space, but that work is also focused on s-wave [270].

To conclude, it is clear that all these effects can boost the annihilation rate or enlarge the photon flux to enable the possibility of detection. But all of them can not produce a boost factor as high as the Sommerfeld enhancement. So this

Name	2D r_e $[pc]$	L_{tot} $[L_\odot]$	Distance $[kpc]$	$\sqrt{\langle\sigma_V^2\rangle}$ $[kms^{-1}]$	References
Carina	254 ± 28	$4.3^{+1.1}_{-0.9} \times 10^5$	105 ± 3	6.4 ± 0.2	[117, 292]
Draco	220 ± 11	$2.2^{+0.7}_{-0.6} \times 10^5$	76 ± 5	10.1 ± 0.5	[117, 293, 295, 296]
Fornax	714 ± 40	$1.7^{+0.5}_{-0.4} \times 10^7$	147 ± 3	10.7 ± 0.2	[117, 292, 293]
LEO I	295 ± 49	$5.0^{+1.8}_{-1.3} \times 10^6$	254 ± 18	9.0 ± 0.4	[117, 293, 294]
LEO II	177 ± 13	$7.8^{+2.5}_{-1.9} \times 10^5$	233 ± 15	6.6 ± 0.5	[117, 293, 297]
Sculptor	282 ± 41	$2.5^{+0.9}_{-0.7} \times 10^6$	86 ± 5	9.0 ± 0.2	[117, 292, 293]
Sextans	768 ± 47	$5.9^{+2.0}_{-1.4} \times 10^5$	96 ± 3	7.1 ± 0.3	[117, 292, 293, 300]
Ursa Minor	445 ± 44	$3.9^{+1.7}_{-1.3} \times 10^5$	77 ± 4	11.5 ± 0.6	[295]

Table 5: Parameters of the luminous dSphs. Here the J-factor is not listed since there is a new definition in Equation (81).

work concentrates on the Sommerfeld factor and ignores the others to get a simple estimation.

4.2.5 Data

For the observed projected velocity dispersion, it is averaged over the entire galaxy, and given by $3\langle\sigma_V^2\rangle_{obs} = \frac{\int\langle\sigma_V^2(r)\rangle\rho dV}{\int\rho dV}$.

The dSphs are difficult to be found due to their high mass-to-light ratio. The Sculptor and Fornax dSph were first discovered with the 24-inch Bruce refractor at Boyden Observatory. With the improvement of sensitivities in multi-wavelength (optical, X-ray, gamma-ray) observations, more dSphs have been found [285]. For example, we have already confirmed more and more dSphs and their light of sight velocity up to thousands of stars in them with the SDSS. And the GAIA space telescope can now characterize the 3D proper motion in the Sculptor, it is found that $\sigma_r = 11.5 \pm 4.3\, km \cdot s^{-1}$ and $\sigma_t = 8.5 \pm 3.2\, km \cdot s^{-1}$[289]. On the other hand, the annihilation cross section of Dark Matter in the dSphs has also been studied with different experiments, including HESS [290], HAWC [291], FermiLAT [379], etc. The latest data of the 8 classical luminous dSphs is collected in this work. The corresponding parameters and references are listed in Table 5.

4.2.6 The PSO Fitting method

The Particle Swarm Optimization (PSO) has been presented in Chapter 2. This algorithm can be used for N-dimension scanning. In this work, for the best-fit curve to the data, the χ^2 technique is applied, cf. Chapter 2. The corresponding parameters are listed as shown in Table 6, with the coordinates given by

$$(\rho_s, r_s, \alpha, \beta, \gamma, r_a, \delta, \beta_0, \beta_\infty) = (x_1, x_2, x_3 ... x_9). \tag{94}$$

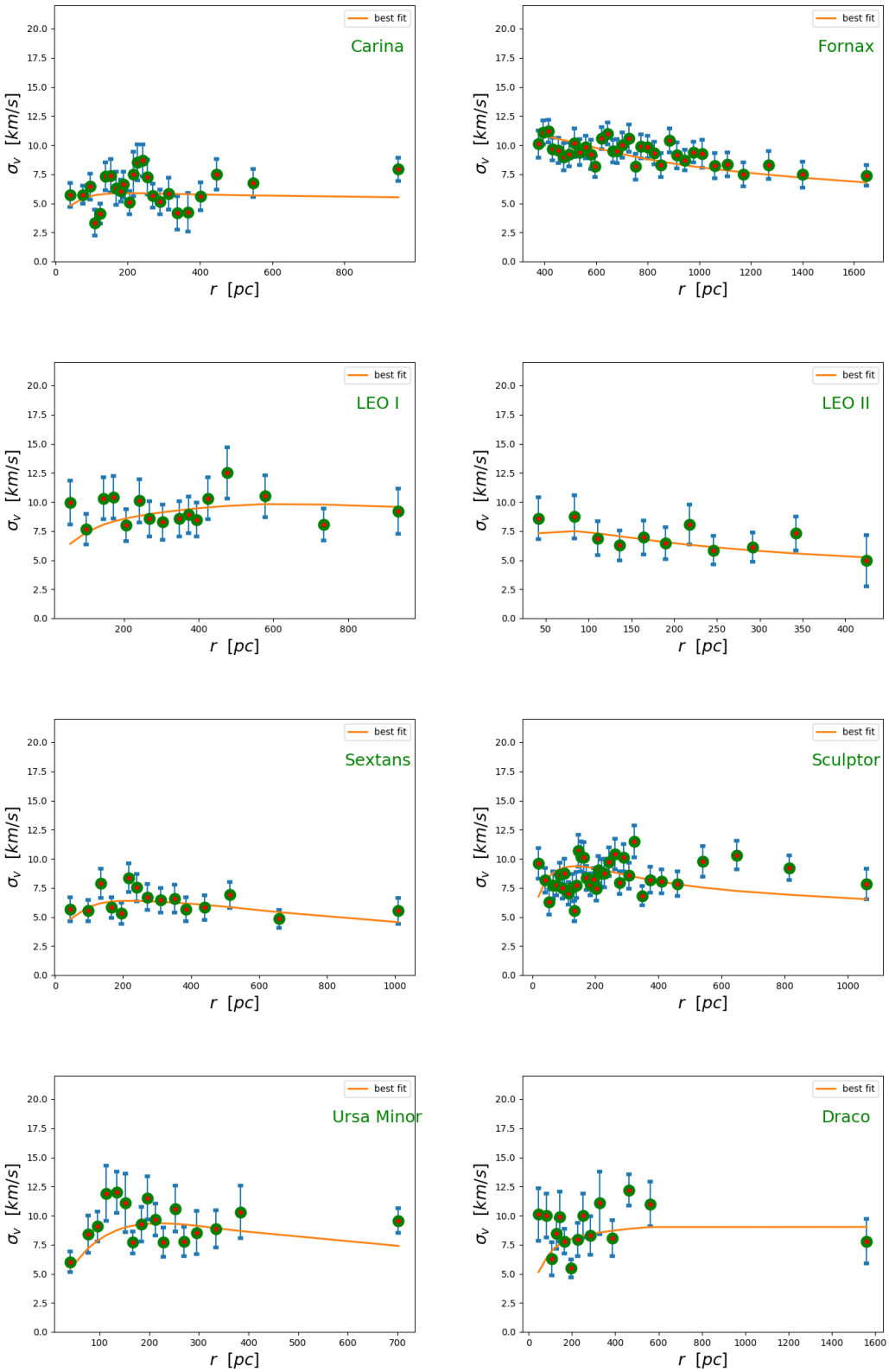

Figure 22: The velocity dispersion of the 8 dSphs being considered in this work. The fit is performed with the PSO method. The best-fit results are shown with the red curves. The data of the Draco, Fornax, Leo I, Leo II, Sculptor, Sextans dSphs are from Ref. [293]; the data of the UMi, Carina dSphs are from Ref. [117].

Name	Range
ρ_s	$[10^{-10}, 10^4]$
$r_s(pc)$	[100,3000]
α	[0.5,3]
w	[3,7]
γ	[0,2]
$r_a(pc)$	[100,1000]
δ	[0,5]
β_0	[-9,0.9]
β_∞	[-9,0.9]

Table 6: Range of the PSO fitting parameters.

$log_{10}(\rho_s)$	r_s[pc]	α	w	γ	r_a [pc]	δ	β_0	β_∞	χ^2	Ref
-0.665	474.354	1.873	4.153	0	282.093	2.111	0.271	-0.756	7.085	[293]
-1.229	611.645	1.851	3.045	1.0	635.588	1.359	-1.666	-1.676	5.763	[293]
-0.712	394.310	2.591	5.163	0	498.249	3.718	-0.209	-6.673	22.722	[117]
-1.399	863.525	1.913	6.299	1.0	454.842	4.404	-0.786	-4.906	20.482	[117]

Table 7: The best-fit parameters and χ^2 for the fit to the velocity dispersion data of the Draco dSph from Ref. [293]. Here the anisotropy profile is the Generalized Osipkov Merritt 3; and the inner slope γ is set to be 0 or 1. The degree of freedom is 9.

4.2.7 Results and interpretations of the fit

The optical observations on the Fornax, Sculptor, and UMi dSphs show a core profile ($\propto r^0$, with $\gamma = 0$) in their inner part [117, 256, 282, 283, 306], and the N-body cosmological simulations indicate a steeper (cusp) profile, which is $\propto r^{-1}$ with $\gamma = 1$. This discrepancy is named as the 'core-cusp' problem. The inner slope γ determines the shape of the profile. Profiles with $\gamma = 0$ are centrally cored. Profiles with $\gamma = 1$ are centrally cuspy, it is the same as the NFW profile.

Two types of fit are performed in this part. In the first fit, all the 9 parameters are free, and we let them vary in the range defined in Table 6. In the second, the

$log_{10}(\rho_s)$	r_s[pc]	α	w	γ	r_a [pc]	δ	β_0	β_∞	χ^2	Ref
0.123	557.680	0.845	4.953	0	440.334	1.133	-0.499	-4.043	49.794	[293]
-1.358	1146.117	1.213	6.699	1.0	999.609	1.704	-1.432	-6.729	51.111	[293]
-0.022	1577.549	0.619	4.844	0	747.265	4.780	-0.140	0.303	36.943	[117]
-1.864	2345.055	1.517	4.797	1.0	206.478	2.048	-0.715	-0.101	40.706	[117]

Table 8: The parameters and χ^2 for the fit to the velocity dispersion data of the Sculptor dSph from Ref. [117, 293]. Here the anisotropy profile is the Generalized Osipkov Merritt 3; the inner slope γ is set to be 0 or 1. The degree of freedom is 28.

inner slope γ is fixed to be 0 or 1 and the other 8 parameters are free. In the PSO, 120 swarms are sent to scan the parameters space in 100 iterations.

The Draco dSph is scanned with the two methods. Two groups of data are extracted from Ref. [117, 293]. As the best-fitting results of the first method shown in Table 7, both groups of data are better fitted when the inner slope $\gamma \simeq 1$. With the second fitting method, the results show a similar conclusion. As shown in Tables 16 to 19, for both data set, it is easy to get to a better fit wit when γ is set to 1, and $\chi^2_{min} = 5.763$. When γ is set to 0, the $\chi^2_{min} = 7.085$. But the difference between them is small.

The previous study shows the Sculptor dSph suggests a cuspy profile [289], this is not consistent with this work, as shown from Table. 20 to 23 (Appendix C). $\gamma \simeq 0$ is preferred by the fit to the data from Ref. [117, 293].

As shown in the other tables in Appendix C, similarly, the second fit method is applied to the data of the other 6 dSphs. The fitting results for $\chi^2_{min}(\gamma = 0)$ and $\chi^2_{min}(\gamma = 1)$ are listed in Tables 14 to 49. The χ^2_{min} of the fits to the LEO2, LEO1, Carina dSphs data from Ref. [117, 293] are smaller when $\gamma \simeq 1$. This is similar to the results of the Draco dSph. The χ^2_{min} of the fit to the Sculptor dSph is smaller when $\gamma \simeq 0$. For the Sextans and UMi dSphs, the χ^2_{min} of the fit to the data from Ref. [293, 295] is larger with $\gamma \simeq 1$ than with $\gamma \simeq 0$, but smaller when the fit is done to the data from Ref. [117].

However, the differences between the $\chi^2_{min}(\gamma = 0)$ and $\chi^2_{min}(\gamma = 1)$ are very small for all the dSphs. It is not reasonable to claim they are cored or cuspy from this analysis.

If we strictly classify the dSphs by the inner slope γ, it must be more cored, and the Draco, LEO2, LEO1, Carina dSphs are more likely to be cuspy. In Ref. [273], the APOSTLE simulations show a solution that does not require cores in the Dark Matter profiles in the dSphs. This work shows a similar conclusion for the 8 dSphs.

To conclude, with different parameters of the anisotropy, halo mass function, and density profiles, both $\gamma = 0$ and 1 allow a good fit to the data.

4.3 Velocity-dependent annihilation cross section

In the non-relativistic limit, the annihilation cross section can be parameterized as

$$\sigma\nu = a + bv^2 + cv^4, \tag{95}$$

where a, b, c terms denote the s, p, d waves, cf. Chapter 3. The s-wave annihilation cross section has been studied for decades, few efforts have been made on p-wave until recently. A list of p-wave models has been collected as shown in Ref. [274].

Simplified models are characterized by four independent parameters

$$\{m_\chi,\, m_{med},\, g_{SM},\, g_\chi\}, \tag{96}$$

which denote respectively the mass of Dark Matter; the mass of mediator; the coupling factor between the mediator and particles in the SM; the coupling factor between the mediator and Dark Matter particle.

One of the most studied p-wave models is the case of a fermion Dark Matter and a scalar mediator [168]. In simplified models, the corresponding thermally averaged annihilation cross section reads

$$\langle \sigma v \rangle = N_c(f) \frac{g_{SM}^2 g_\chi^2}{16\pi} y_f^2 \frac{m_\chi^2 (1 - \frac{m_f^2}{m_\chi^2})^{3/2}}{(m_{med}^2 - 4m_\chi^2)^2 + \Gamma_{s,tot}^2 m_{med}^2} v^2, \tag{97}$$

$$\Gamma_{s,tot} = \sum_f \Gamma_s^{f\bar{f}} + \Gamma_s^{\chi\bar{\chi}} + \Gamma_s^{\chi\bar{\chi}}, \tag{98}$$

where Γ denotes the decay width of mediator, it is the sum of the decay widths into all the possible SM particle pairs and reproduction of Dark Matter pair. For the fermion, Dark Matter, and gluon channels, their contributions read respectively as

$$\Gamma_s^{f\bar{f}} = \sum_f N_c(f) \frac{y_f^2 g_{SM}^2 m_{med}}{16\pi} (1 - \frac{4m_f^2}{m_{med}^2})^{\frac{n}{2}}, \tag{99}$$

$$\Gamma_s^{\chi\bar{\chi}} = \frac{y_\chi^2 m_{med}}{8\pi} (1 - \frac{4m_f^2}{m_{med}^2})^{\frac{n}{2}}, \tag{100}$$

$$\Gamma_s^{gg} = \frac{\alpha^2 g_{SM}^2}{32\pi^3} \frac{m_{med}^3}{v^2} |f_{scalar}(\frac{4m_t^2}{m_{med}^2})|^2, \tag{101}$$

where

$$f_{scalar}(\tau) = \tau \cdot (1 + (1 - \tau) \cdot (tan^{-1}(\frac{1}{\sqrt{\tau} - 1}))^2), \tag{102}$$

and the color number of fermion $N_c(f) = 3$ for quarks and 1 for leptons, the power index n = 3 for the scalar mediator.

The Yukawa potential in the fermion Dark Matter annihilation via a scalar mediator is characterized by the coupling term y_f. It is proportional to the mass of the final state particle with $m_q = y_f m_f/\sqrt{2}$, where $m_f \simeq 246$ GeV is the Higgs vacuum expectation value [107, 370, 109, 374].

Assuming the particles in an isothermal sphere have a velocity distribution described by the Maxwellian or Maxwell-Boltzmann distribution, the relative velocity distribution is characterized by $f(v_{rel}) = v_{rel}^2 \frac{1}{2\sqrt{\pi}\sigma_v^2} exp(-\frac{v_{rel}^2}{4\sigma_v^2})$. For the particles at a point in the isothermal sphere, the mean square speed $\overline{v^2} = 3\sigma^2$ [234].

For the annihilation of two particles with the same mass $m_1 = m_2 = m$, the reduced mass is $\mu = \frac{m_1 \cdot m_2}{m_1 + m_2} = \frac{m}{2}$. We note v_{rel} as the relativistic relative velocity,

and v_r the non-relativistic relative velocity. In the comoving frame, the non-relativistic case means $v_{rel} \simeq v_r \leq 1$, the thermally averaged annihilation cross section $\langle \sigma\nu(r) \rangle$ in Equation (81) is

$$\langle \sigma v_r \rangle_{nr} = \int_0^\infty \sigma_{nr} v_r f(v_{rev}) d\nu_r = \sqrt{\frac{2}{\pi}} \int_0^\infty d\nu_r x^{\frac{3}{2}} \nu_r^2 e^{-x\frac{\nu_r^2}{4}} \sigma_{nr} v_r, \tag{103}$$

with $x = \mu/T$ depending on the reduced mass μ and temperature T [250].

For systems with low-velocity dispersion, like the old dSphs, the non-relativistic formula is applicable. If there are violent dynamic behaviors in the system, like the cluster merges or collision between huge targets, we can cut off at $v \geqslant 0.1c$ and start to consider the relativistic case. In this case we have [198]

$$\langle \sigma v_{rel} \rangle_{rel} = \frac{\int_{(m_1+m_2)^2}^\infty ds \frac{\lambda(s, m_1^2, m_2^2)}{\sqrt{s}} K_1(\frac{\sqrt{s}}{T}) \sigma}{8T\Pi_i m_i^2 K_2(x_i)}, \tag{104}$$

with $x = m/T$, $K_n(x)$ is the n-th kind modified Bessel function, s is the Mandelstam variable defined as $s = (p_1 + p_2)^2$, and λ is the triangular function defined as Eqaution (96) [249, 250].

$$\lambda(s, m_1^2, m_2^2) = [s - (m_1 + m_2)^2][s - (m_1 - m_2)^2]. \tag{105}$$

4.4 Thermal relic density

The solution to the Boltzmann equation allows us to find the masses which could produce the required relic density in today's Universe. We continue to find the annihilation cross section of the Dark Matter in the dSphs. The value varies since the velocity dispersion varies between the targets, but it is always considerably lower than $\langle \sigma v \rangle = 2.7 \cdot 10^{-26} cm^3 s^{-1}$ [58]. The value also depends on the final state in the annihilation.

The standard freeze-out scenario happens when the WIMP particles in the early Universe is cooled down to an average velocity at about $\overline{v_{dcp}} \approx 0.25c - 0.3c$ [306, 307, 308]. After this moment, the annihilation rate is balanced by the expansion, when it is below the Hubble rate H, chemical equilibrium is thus established and kept until now, this related to $x = m/T \approx 20 - 30$, and the frozen Dark Matter relic density is the so-called 'WIMP miracle'. If we consider the simple case, the corresponding Boltzmann equation and chemical decoupling equation read as follows:

$$\frac{dn_\chi}{dt} = -3Hn_\chi - \langle \sigma v_{rel} \rangle_{eq} (n_\chi^2 - n_{\chi,eq}^2), \tag{106}$$

$$\frac{dY}{dx} = \frac{s\langle\sigma v\rangle}{Hx}[1 + \frac{1}{3}\frac{d(lng_s)}{d(lnT)}](Y_{eq}^2 - Y^2). \tag{107}$$

Here we have considered the variation of g_s when the temperature T decreases. For more details of the Boltzmann equation, cf. Section 3.4 in Chapter 3.

Choosing the masses of Dark Matter and mediator, applying them to solve the Boltzmann equation, we get the relic density of Dark Matter today. Compare with the relic density found by the Planck collaboration, $\Omega h^2 = 0.1211$ [6], the required parameter set m_χ, m_{med} can be found. In the simple case, we assume naively the annihilation cross section at the freeze-out is $\langle\sigma v\rangle = 2.7 \cdot 10^{-26}\, cm^3 s^{-1}$, as the temperature drops down, the velocity is slowed down to several km/s in the dSphs. As shown in Chapter 3, if we project the required mass for each coupling strength on the top left panel, we can get the annihilation cross section in the targets. For the example of the Cluster MS-1054.4-0321 with an average velocity dispersion ≈ 1113 km/s, if Dark Matter is a fermion, and the mediator is a scalar, then the total annihilation cross section is around $10^{-28}\, cm^3 s^{-1}$. If we assume the Dark Matter pair annihilates to each type of SM particle pair with a 100% branching ratio, then the annihilation cross section reaches as low as $10^{-31}\, cm^3 s^{-1}$. But in the dSphs, as shown in the last section, the typical velocity is around 10 km/s, if there is no other boost factor, it is impossible to be detected.

4.5 The Sommerfeld Enhancement

This work focus on the enhanced p-wave annihilation mediated via a Yukawalike potential. For the details of calculation of the Sommerfeld boost factor, cf. Section 5.5 in Chapter 5.

4.6 Analysis

With the Dark Matter model, the annihilation cross section required by the relic density can be obtained by solving the Boltzmann equation. With the velocity dispersion in the dSphs, the parameters allowed by the correct relic density is applied to calculate the annihilation cross section. The annihilation cross section without the Sommerfeld enhancement is calculated first, and then the Sommerfeld enhancement is taken into consideration.

4.6.1 Without the Sommerfeld enhancement

For the simplest case, in a p-wave annihilating Dark Matter model, since $\sigma v \approx bv^2$, the annihilation cross section increases as the velocity increases, so it is much lower in the low-velocity dispersion systems (like the dSphs) than in the high-velocity dispersion systems like the galaxy clusters. An example is shown in

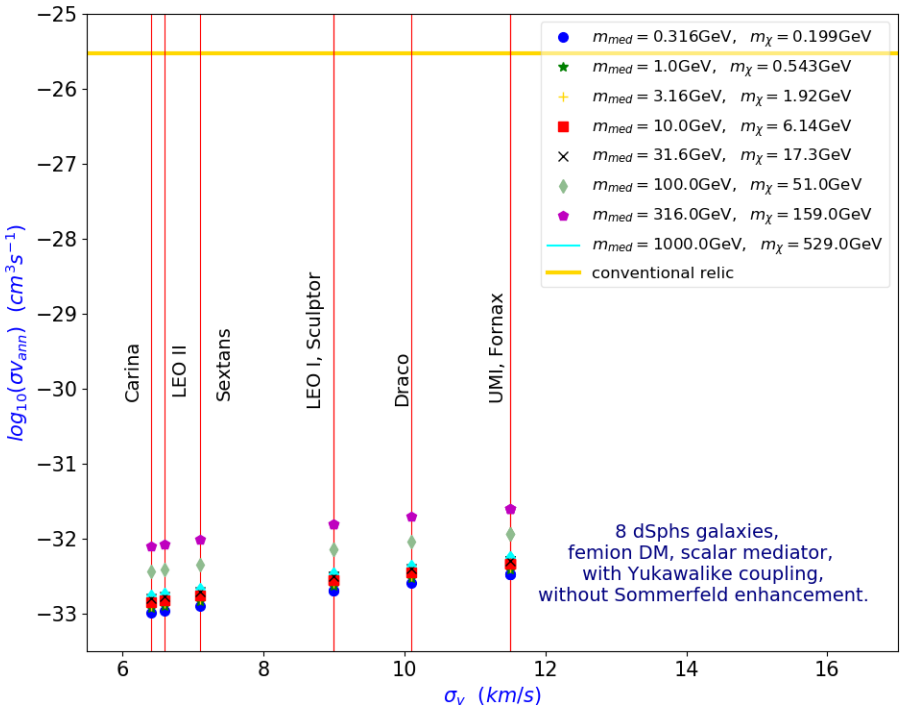

Figure 23: The total effective annihilation cross section of fermion Dark Matter via a scalar mediator. Here the effective annihilation cross section to the 12 fermion final states are summed up. The mediators is set to 8 constant values, the Dark Matter masses required by the relic density are shown on the upper right. As required by the model, we found m_{med} must be$\simeq 2m_\chi$.

Fig. 12 of Chapter 3. The annihilation cross section in the dSphs is much lower than the s-wave annihilation cross section. In that example, it reaches as low as $< 10^{-31} cm^3 s^{-1}$ in the $\bar{b}b$ channel, it is much less than the conventional value required by the relic density ($2.7 \times 10^{-26} cm^3 s^{-1}$), which means we need much better sensitivity to find it. The systems with high-velocity dispersion are interesting to study. A simple estimation shows detectable signal can only be produced in the targets with a relative velocity $\gtrsim \sqrt{\frac{2.7\times10^{-26}}{10^{-31}}} = 519.6$ times larger than that in the dSphs. This kind of targets contains the galaxy clusters, the merge of clusters. But they have complicated photon background, and are unlikely to be good laboratories to study p-wave annihilating Dark Matter since photons from annihilation is a small fraction of the mement of freeze-out.

With the p-wave model treated here, as shown in Fig. 23, the masses of Dark Matter and the mediator allowed by the relic density can only produce a very tiny annihilation cross section in the dSphs. It is impossible to be detected in the existing indirect detection experiments.

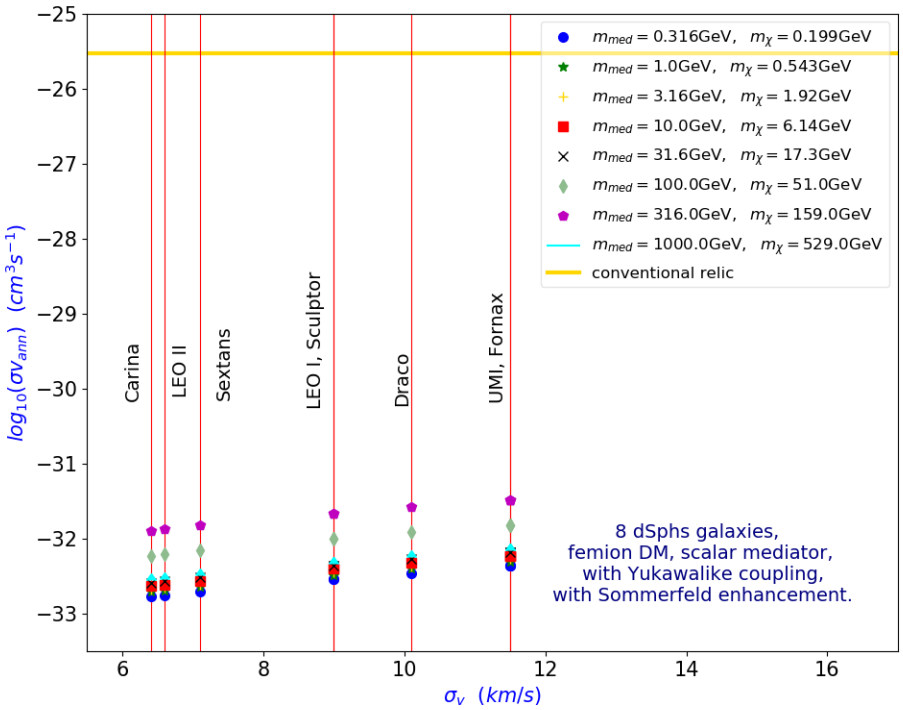

Figure 24: The Sommerfeld enhanced effective annihilation cross section in the dSphs. It is still tiny compared with $2.7 \times 10^{-26} cm^3 s^{-1}$. This means there is no possibility to detect this type of p-wave Dark Matter in the dSphs.

4.6.2 With the Sommerfeld Enhancement

We expect p-wave annihilation in the low velocity systems to be boosted a lot by the Sommerfeld enhancement, such as in Ref. [216, 330]. So the calculation is repeated with the Sommerfeld enhancement, as shown in Fig. 24. Unfortunately, the boost factor for the parameters allowed by the relic density do not possess a large Sommerfeld factor. The effective boosted annihilation cross section is still much lower than that required by the relic density.

4.7 Conclusions and outlook

Inspired by M.G.Walker's idea of a universal mass profile for the dSphs, a N-dimension global optimization tool is developed to describe the velocity dispersion profile. This model is defined without pre-assumption on the density, anisotropy, and luminosity profiles. The generic Zhao-Hernquist density profile is applied, along with the generalized Osipkov Merritt profiles.

There are two kinds of fit to the dSphs data in this work. In the first method, all the parameters are set to be free in the efficient N-Dimension PSO scanning

algorithm. The best-fit parameters of the velocity dispersion in the dSph galaxies appear to fall into two categories. The differences between the core and cusp profiles arise thus from different values of these parameters. In the second method, the inner Dark Matter slope γ is fixed to be 0 and 1 to compare the corresponding χ^2_{min}. It is found that their differences are very small in the fits to all the data treated here. Both the cored and cuspy profiles can describe the dSphs with different parameters of the density, anisotropy, and luminosity. It shows that neither core nor cuspy is really needed, this conclusion is the same as Ref. [273]. But this is just a phenomenological description, a better understanding of the physics in the dSphs is needed to make a clear explanation of this result. For example, in Ref. [311], the "cusp vs core" issue is better characterized as an "inner mass deficit" problem than as a density slope mismatch.

There are several ways to improve the calculation of the velocity dispersion in the dSphs, two of them are interesting to this work. First, the generic Zhao-Hernquist density profile has been upgraded to unify more density profiles [231] into a compact mathematical expression, that work is still underappreciated, and could be compatible mathematically with G.Mamon's work in [241, 232] which has also taken the baryonic matter into account. Second, in these generic profiles the black hole in the galaxies is not considered, with which the velocity dispersion curves in this work should be different, and useful to rule out some particle models as shown in [270].

This chapter tries to develop a new Dark Matter particle/mediator identification method with only dSph data, but does not succeed with the models in this work to find any signal. This type of Dark Matter is still not detectable with only the dSph data. The Dark Matter parameter allowed by the relic density does not allow a large Sommerfeld boost factor. There are several possibilities to improve this work. For example, as shown in Fig. 24, only Dark Matter masses close to $\sim 2\, m_{med}$ are allowed by the relic density. The Boltzmann equation in this work is standard, there are other derivatives of the Boltzmann equation. If the detailed time scales are taken into account, the kinetic decoupling happens much later than the chemical decoupling, this case is more complicated. Subsequent analysis has been done in Ref. [302, 303, 304, 305].

Originally, the particle model is specially designed for the Dark Matter searches on the collider, any other particle model with annihilation boosted by the Sommerfeld enhancement can replace the particle model in this work. The difficulty is there is not enough investigation on the Sommerfeld enhancement. Until now, only in a few particle models the Sommerfeld enhancement have been computed [417]. Once the Sommerfeld enhancement in any other p-wave Dark Matter model has been treated, this work could be extended to it.

In this calculation, there is no other boost factor, as discussed in Section 4.2.4. But the substructures, the non-sphericity may also contribute to improving this work, but they need to be studied quantitatively.

This chapter is prepared for publication at JCAP

Chapter 5 IGRB constraints on p-wave annihilating Dark Matter

The leading term in the p-wave annihilation cross section is proportional to the velocity squared. As many p-wave models have parametrically suppressed couplings to SM particles, they are not accessible in direct detection or collider-based experiments [70, 310]. Then astrophysical searches become the unique probes of p-wave Dark Matter. We attempt to interpret the FermiLAT IGRB data by adding p-wave Dark Matter annihilation via a single or two mediators to the extragalactic γ-ray sources. With a fermion p-wave Dark Matter and a scalar mediator, We attempt to model the γ-ray signal from the prompt emission along with the inverse Compton scattering on the cosmic microwave background (CMB) photon bath. The Sommerfeld enhancement acts as a boost factor to raise the possibility to detect Dark Matter. Our analysis is derived by varying Dark Matter mass and mediator mass to perform a fit to the data, the $\Delta\chi^2$ analysis points out the excluded parameter regions of the existence of Dark Matter at different C.L.s and the improved ereas with reduced χ^2. With three background models implemented in the χ^2 statistic, no significant signal has been found in this analysis. And only some regions below 50 GeV are excluded. No solid conclusion could be made for the range of higher mass up to 100 TeV.

5.1 Introduction

Despite decades-long efforts, the properties of Dark Matter remain elusive. In the view of a quantitative description, only the relic abundance of Dark Matter $\Omega_c h^2 = 0.120 \pm 0.001$ was obtained by the Planck collaboration [6], which constitutes about 85% of the total mass content of today's Universe. One of the most studied Dark Matter candidates is the weakly interacting massive particle (WIMP), which is a thermal relic produced by decoupling from the thermal bath and then cooling during the expansion. It becomes constant since the freeze-out. Classified by the interactions with the Standard Model particles, there are in general three approaches to look for its signal according to the timeline of the Feynman diagram in possible relevant interactions: the indirect detection to look for the final products from the annihilation and decay; the direct detection to look for the nucleon-Dark Matter scattering product in the target materials; and the collider-based experiments to probe the production of Dark Matter particles. Unfortunately, none of them has provided any convincing proof of Dark Matter

in the energy range up to several hundred GeV [313, 314, 315].

Experimental progress has been made to improve the sensitivity in indirect detection from GeV scale to TeV scale [207, 223, 316, 317, 318, 319, 320, 321, 322]. In the theoretical aspect, under the assumption that there could be some hidden signal in the existing data but previously ignored, it is reasonable to pay more attention to the specific particle models. Efforts have been made in pioneering papers on boost factors in indirect detection of Dark Matter, such as the coannihilation, the Breit-Wigner effect [323, 324] , the overdensity [325], the substructure [326], etc.

Most of the previous work is focused on s-wave annihilation, which is velocity-independent thus irrelevant to the dynamics in the investigated targets. Recently velocity-dependent annihilating Dark Matter has spurred interest, and efforts has been made to probe its signature, such as [327, 328, 329]. Some of the plausible targets for the p-wave Dark Matter have already been investigated with data from different experiments. In Ref. [330], the indirect detection constraint on p-wave Dark Matter from the anisotropy of the CMB is presented by considering annihilation to bound states before decaying to SM particles. For the galactic center (GC), Dark Matter particles receive higher velocities since a massive central black hole is assumed and causes spike-like overdensity of Dark Matter. That analysis shows no significant excess of γ-rays in the energy range 6 GeV - 600 GeV [310]. The combination of the Sommerfeld effect and the other boost factors has exceptional attention, for example, the combination with coannihilation [335], the combination with substructure [336].

The origin of the isotropic diffuse γ-ray background (IGRB) remains unclear and is one of the most intriguing questions in astrophysics. The IGRB anisotropy has been studied as a tool for the indirect Dark Matter searches with gamma rays [312]. Work on the p-wave annihilating Dark Matter in the GC excess predicted an enhanced annihilation in galaxy clusters and then a signal in the IGRB [337]. Some analysis on the energy spectrum observed by FermiLAT suggests that the main contribution is from the unresolved misaligned Active Galactic Nuclei (AGN), Blazars (BL), and Star-Forming Galaxies (SF) [111]. Another work shows it may be dominated by Radio Galaxies and Radio Quasars [338]. The debate on this question is still undergoing. A possible contribution may arise from Dark Matter annihilation or decay in the halos of the galaxies. Previous inspiring work on IGRB has been done for velocity-dependent Dark Matter annihilation boosted by the s-wave Sommerfeld enhancement in Ref. [339] where an extension to MSSM has been considered in a robust calculation to predict the γ-ray intensity. This could be renewed now with generic models to confront the latest observations. Hence in this work, pure p-wave annihilating Dark Matter is considered to probe Dark Matter signature in the FermiLAT data.

5.2 The total γ-ray flux from the extragalactic sources

The total extragalactic γ-ray background (EGB) is the sum of the flux from resolved and unresolved sources. The isotropic γ-ray background (IGRB) is attributed to all the faint or diffuse extragalactic emissions difficult to be resolved, namely thus the unresolved sources and any isotropic residual Galactic foregrounds [111, 340].

Dark Matter can produce additional emissions to the known signal sources; thus it is popular to look for its contribution by analyzing the high energy cosmic ray or γ-ray excesses, such as the positron excess by PAMELA [341, 342] and AMS-02 [343, 344], γ-ray excess by FermiLAT and DAMPE [345, 346]. The difficulty in the interpretation of astrophysical observations is that they could also be explained by other astrophysical effects.

γ-ray emission induced by Dark Matter and its contribution to IGRB has been studied a lot, but only for s-wave annihilating Dark Matter. The corresponding upper limits have been derived [111, 347]. SIDM has been discussed recently in Ref. [368], but it focuses on the prediction strategy and modeling uncertainty, so no limit has been derived.

Boosted factors are needed to provide detectable signals since p-wave annihilation rate is tiny compared with s-wave annihilation rate. The substructure needs to be considered for astrophysics at the scale of galaxy clusters. Hence in this work, we focus on the clumpiness factor. For particle physics, since we are interested in p-wave models, the Sommerfeld effect is taken into account.

The astrophysical background sources

We recall the former work on IGRB in [111], in which the astrophysical interpretation of the FermiLAT IGRB data in the energy range 100 MeV - 820 GeV has been fitted with different extragalactic populations.

These background sources consist of the components as follows:

(1) Active Galactic Nuclei with misaligned jet (MAGN);

(2) Milky Way-like star-forming galaxies (SF MW);

(3) Starburst galaxies (SF PL);

(4) Blazars with strong broad lines in the optical and UV spectrum which is named flat-spectrum radio quasars (FSRQs);

(5) Blazars with the absence of a strong broad line in their optical and UV spectrum named BL Lacertae (BL lacs).

The components of the Galactic foreground have been studied. Three models referring to the FermiLAT data are obtained, namely models A, B, C. The differences between these models are characterized by the normalization factors of these components in the best fit. In order to apply the $\Delta\chi^2$ analysis, we extract data from their results. Then the flux from the p-wave Dark Matter annihilation is added to the interpretation and calculate the new χ^2, see details in Sec. VI.

The expected Dark Matter signal

The flux induced by Dark Matter in a single target such as a dSph is too small to be observed, as shown in Chapter 4. The IGRB might help to overcome this problem since all the photons induced by the extragalactic Dark Matter at different redshifts are accumulated. Therefore, although the uncertainties in the analysis of the IGRB components are large, the investigation on the contribution of the Dark Matter- induced γ-ray flux in the halo of the galaxies remains a possible way to reveal the nature and properties of Dark Matter.

The conventional calculation of s-wave Dark Matter is no longer valid in the case of p-wave annihilation.

In Ref. [303], the Sommerfeld enhanced velocity-dependent annihilation of Dark Matter has been especially mentioned. A similar calculation has also been proposed in Ref. [348], but no further work on p-wave has ever been done. In this work, the expression of the differential γ-ray flux for the p-wave annihilation from the extragalactic Dark Matter [366, 368] is recalled, reads

$$\Phi_{EG}^{p-total}(E, z_{min}) = \frac{(1+z_{min})^2 \Omega_\chi^2 \rho_{c,0}^2}{4\pi \cdot 2m_\chi^2} \int_{z_{min}}^{z_{max}} dz' c \frac{(1+z')^3 \triangle^2(z')}{H(z')} \frac{dN_{tot}(E')}{dE'} \cdot e^{-\tau(z_{min};,z',E')}, \tag{108}$$

with a boost factor

$$\triangle^2(z) = \frac{\triangle_{vir}(z)}{3\rho_{\chi,0}} \int dM_{vir} M_{vir} \frac{dn(z)}{dM_{vir}} \frac{\int \tilde{\rho}^2(x) \langle \sigma v \rangle x^2 dx}{(\int \tilde{\rho}(x) x^2 dx)^2} x_{max}^3, \tag{109}$$

where z_{min} is the minimal redshift, usually set to 0, or a tiny value, it is fixed as 10^{-6}; and $z_{max} = m_\chi/E - 1$ is the maximum redshift that a photon with energy E can reach us [147]. The attenuation of γ-ray in the intergalactic medium is expressed as $exp(-\tau(z;, z', E'))$.

This expression differs from the equation of s-wave annihilation with a J-factor involving the $\langle \sigma v \rangle$ term in the substructure factor $\triangle^2(z)$. For s-wave, the annihilation cross section is a constant supposed to be $\langle \sigma v \rangle \simeq 3.0 \times 10^{-26} cm^3 s^{-1}$, so the particle physics factor is independent of the astrophysics factor (the J-factor) in the calculation of the differential flux, or the intensity. But p-wave annihilation depends on the relative velocity of the incident particles, thus also depends on the velocity dispersion in the studied system. If there is no other boost factor, for a flattened rotation curve, the corresponding annihilation rate is tiny in the core, then it increases until the plateau is reached, and gets its maximum on the plateau of the rotation curve. For p-wave, this $\langle \sigma v \rangle$ term can not be kept in the particle physics factor, as shown in Equation (109). The 3D squared total velocity dispersion is defined as $\langle v^2(r) \rangle = 3 v_V^2(r)$ where $v_V(r)$ is the projected line-of-sight velocity dispersion [217]. In the same paper, a similar calculation has been proposed to consider the energy injection into the intergalactic medium induced by Dark Matter annihilation.

In Ref. [368], the isotropic extragalactic γ-ray intensity from Dark Matter annihilation has been computed and updated by reducing the modeling uncertainties. The total intensity is boosted by a factor of 1.5 by considering the substructure. For the SIDM candidates, the signal of the low bound of the intensity is reduced by a factor of 3.

5.3 Generic models of p-wave Dark Matter

In general, the velocity averaged annihilation cross section of Dark Matter could be expressed as $\langle\sigma v\rangle = a + b \cdot v^2 + c \cdot v^4$ for any type of Dark Matter particle and mediator. These annihilations are classified according to the values of the a, b, c terms, named respectively the s, p, d waves. Since the Dark Matter particles in the dynamic systems in equilibrium are believed to be nonrelativistic in today's Universe, the b, c terms are thus negligible compared with the s-wave term. But there are some Dark Matter particle models with an s-wave term close or equal to 0, and the p-wave dominates. In the p-wave cases, the annihilation cross section is $\propto v^2$, not anymore a constant, thus it depends on the dynamics in the target systems.

Simplified models are primarily designed to analyze data from the collider-based experiments, such as in Ref. [371], and then extended to the other approaches, such as the γ-ray probe of Dark Matter with data from the solar observation [372].

Simplified models of Dark Matter are model-independent approaches that contain some well-motivated candidates. They provide a generic description of interactions between Dark Matter and particles in the SM. Simplified models add only a few degrees of freedom, and they overcome the drawbacks of the EFT. Simplified models are used since they are among the most model-independent tools with the least number of dimensions of parameter space. Simplified models are established to adapt to new search strategies and experimental data, it is between the effective approach and the UV complete models. For this work, simplified models are essential since we need to introduce the mediator to compute the boost factor of the Sommerfeld enhancement.

However, there are several p-wave models as shown in Chapter 3,. Instead of investigating all of them, it is better to focus on only one of them to present what kind of changes p-wave Dark Matter will bring to us in the IGRB. One of the most popular generic models is composed by light Majorana fermionic Dark Matter χ which is coupled to the SM final states particles via a light scalar mediator ϕ. In the allowed annihilation case $m_\chi > m_\phi$, and the annihilation is dominated by the p-wave process $\chi\chi \to \phi\phi$ with two mediators. The corresponding annihilation cross section [373] is:

$$\langle\sigma v_{rel}\rangle \simeq \frac{k^4 m_\chi}{24\pi}\sqrt{m_\chi^2 - m_\phi^2}\frac{9m_\chi^4 - 8m_\chi^2 m_\phi^2 + 2m_\phi^4}{(2m_\chi^2 - m_\phi^2)^4}v_{rel}^2 \tag{110}$$

where k is a factor found to be insensitive to $m_\chi$and m_ϕ, and $k \approx 0.1$.

This value is proportional to v_{rel}^2, so it is much larger at target systems with higher velocities. The Sommerfeld enhancement boosts a lot the annihilation in the annihilation process, which could be dominant in the contribution to the gamma-ray flux at low velocity (see section 5.5).

Although the annihilation via two mediator dominates, the annihilation process via a single mediator $\chi\chi \to \phi \to f\bar{f}$ is still kept in this work with a relatively much smaller branching ratio $< 10\%$, the corresponding Simplified models are characterized by four independent parameters

$$\{m_\chi,\, m_{med}(or\ denoted\ as\ m_\phi),\, g_{SM},\, g_\chi\} \tag{111}$$

which denote respectively the mass of Dark Matter, the mass of mediator, the coupling factor between the mediator and particles in the SM, the coupling factor between the mediator and Dark Matter particle. The corresponding annihilation cross section reads as

$$\langle \sigma v_{rel} \rangle = N_c(f) \frac{g_{SM}^2 g_\chi^2}{16\pi} y_f^2 \frac{m_\chi^2 (1 - \frac{m_f^2}{m_\chi^2})^{3/2}}{(m_{med}^2 - 4m_\chi^2)^2 + \Gamma_{s,tot}^2 m_{med}^2} v_{rel}^2. \tag{112}$$

5.4 Prompt emission and inverse Compton scattering

The processes involved in this work can be presented as

$$\chi\bar{\chi} \longrightarrow \begin{cases} \phi\phi & +Sommerfeld \\ \phi & +Sommerfeld \end{cases} \to \begin{cases} SM\overline{SM} & \longrightarrow \ \gamma\gamma & Prompt \\ e^+e^- & \xrightarrow{ICS} \ \gamma\gamma & ICS \end{cases}. \tag{113}$$

The Sommerfeld enhancement plays a role when there are one or two mediators. After the annihilation, photons are produced via different mechanisms including intermediate and final state radiation, decay and hadronization of the final state particles from the prompt emission. The other important processes contain inverse Compton scattering on the low energy photon bath, synchrotron emission from the Dark Matter-induced electrons and positrons, and bremsstrahlung emission. With relativistic electrons induced by Dark Matter annihilation, the ICS dominates in the galactic halo with a typical magnetic field $\sim 1\mu G$ [394]. Similarly, for the extragalactic study, there are several reasons to neglect synchrotron and bremsstrahlung in this work. There is insufficient knowledge of the magnetic field in the halos, so it is natural to do the similar treatment as that for the galactic halo. These processes are subdominant with respect to the ICS. And Dark Matter-induced synchrotron signal lies at radio frequencies, which is beyond the range of $\gamma-$ray [375]. Finally, the total γ-ray flux is given by the sum of the prompt emission and the ICS emission, reads

$$\frac{dN_{tot}(E')}{dE'} = \frac{dN_{prompt,tot}}{dE'} + \frac{dN_{ICS,tot}}{dE'}, \tag{114}$$

where the photon energy range at redshift z reads

$$E' = E \cdot (1+z)/(1+z_{min}). \tag{115}$$

Here $\frac{dN_{prompt,tot}}{dE'}$ denotes the spectrum of photons from prompt emission per Dark Matter annihilation, and $\frac{dN_{ICS,tot}}{dE'}$ denotes the spectrum from Inverse Compton scattering per annihilation.

The total spectrum contains all the final states. It is characterized by the branching ratios and the spectrum of each final state. A general expression can be applied to sum up the final states as follows

$$\begin{cases} \frac{dN_{prompt,tot}}{dE'} = \sum_i B_i \frac{dN_i}{dE}(E) & Prompt \\ \frac{dN_{ICS,tot}}{dE'} = \int_{m_e}^{m_i} \sum_i B_i \frac{dN_i}{dE_e}(E_e) \cdot I_{IC}(E_e, E, r(\lambda,\phi)) dE_e & ICS \end{cases}. \tag{116}$$

Here B_i denotes the branching ratio into the ith final state, I_{IC} denotes the halo function for the ICS. For more details about this part, cf. Section 5.4.1 and 5.4.4.

5.4.1 Prompt emission

8 SM final states are considered for the annihilation via two mediators:
$\chi\bar{\chi} \to \phi\phi \to \{\gamma\gamma, W^+W^-, b\bar{b}, h\bar{h}, g\bar{g}, \tau^+\tau^-, \mu^+\mu^-, e^+e^-\}$.
9 final fermionic states are considered for the annihilation via a single mediator:
$\chi\bar{\chi} \to \phi \to \{t\bar{t}, b\bar{b}, s\bar{s}, c\bar{c}, d\bar{d}, u\bar{u}, \tau^+\tau^-, \mu^+\mu^-, e^+e^-\}$.
The spectrum of photon $\frac{dN_i}{dE}(E)$ and electron $\frac{dN_i}{dE_e}(E_e)$ can be read from the CascadeSpectra table [349] and the PPPC4DMID table [112, 350]. For the case of $\gamma-$ray emission, the value of $\frac{dN}{dlog10x}$ is presented in this table; we have

$$\frac{dN}{dE'_{ph}} = \frac{dN}{dE_{ph}} \frac{dE_{ph}}{dE'_{ph}} = \frac{1+z}{1+z'} \frac{dN}{dE_{ph}}, \tag{117}$$

with $E'_{ph} \equiv E_{ph}(1+z')/(1+z)$ the redshifted photon energy at z'.
Defining $x \equiv E_{ph}/m_\chi$,

$$\frac{dN}{dE_{ph}} = \frac{dN}{dx}\frac{dx}{dE_{ph}} = \frac{1}{ln(10)x}\frac{dN}{dlog_{10}(x)}\frac{dx}{dE_{ph}} = \frac{1}{E_{ph}\cdot ln(10)}\frac{dN}{dlog_{10}(x)}, \tag{118}$$

$$\frac{dN}{dE'_{ph}} = \frac{1+z}{1+z'}\frac{1}{E_{ph}\cdot ln(10)}\frac{dN}{dlog_{10}(x)} = \frac{1}{E'_{ph}\cdot ln(10)}\frac{dN}{dlog_{10}(x)}, \tag{119}$$

	γ-ray spectra				e^+e^- spectra		
	dependence	1st column	type		dependence	1st column	type
$\gamma\gamma$	no	ϵ_f	0		yes	m_ϕ	1
W^+W^-	yes	ϵ_f	2		yes	ϵ_f	2
$b\bar{b}$	yes	ϵ_f	2		yes	ϵ_f	2
$h\bar{h}$	yes	ϵ_f	2		yes	ϵ_f	2
$g\bar{g}$	yes	m_ϕ	1		yes	m_ϕ	1
$\tau^+\tau^-$	yes	ϵ_f	2		no	ϵ_f	0
$\mu^+\mu^-$	yes	ϵ_f	2		no	ϵ_f	0
e^+e^-	yes	ϵ_f	2		no	ϵ_f	0

Table 9: Summary of the method to read the γ-ray spectra and e^+e^- spectra in the CascadeSpectra table. These final states are classified into 3 types. Here $\epsilon_f = \frac{\sum m_{SM}}{m_\phi}$ represents the level of final state radiation and hadronization. The first columns in the tables are different, depending on the mass of the final state particles and the mediators.

$$\frac{dN}{dx} = \frac{1}{x \cdot ln(10)} \frac{dN}{dlog_{10}(x)}. \tag{120}$$

There are 3 types of data in the CascadeSpectra table as summarized in Table 9. The CascadeSpectra is obtained by considering a dark-sector state that decays to the SM via multi-step cascade $\chi\chi \to \phi_n\phi_n \to 2 \times \phi_{n-1}\phi_{n-1} \to ...2^{n-1} \times \phi_1\phi_1 \to 2^n \times SM$ final states. Some examples are shown in Fig. 25.

5.4.2 Clumpiness boost factor

The intensity multiplier δ characterizes the annihilation booster caused by the inhomogeneous Dark Matter distribution, $\rho(\Omega, z) = \delta(\Omega, z) \times \tilde{\rho}(\Omega, z)$. The boosted annihilation rate is proportional to the squared density, so the intensity multiplier could be expressed as $\langle\delta^2\rangle = 1 + Var(\delta)$. It is equal to $Var(\delta)$ for high overdensity [368]. The smoothly distributed Dark Matter gives a unity multiplier $\delta = 1$, and it is also named as the clumpiness factor [366], and noted as $\triangle^2$ in Equation (121):

$$\triangle^2(z) = \frac{\triangle_{vir}(z)}{3\rho_\chi} \int dM_{vir} M_{vir} f_1(M_{vir}) \,, \tag{121}$$

with $\frac{dn(z)}{dM_{vir}}$ the halo mass function, $\triangle_{vir}(z)$ the virial overdensity, M_{vir} the virial mass, and ρ_χ the Dark Matter density, the function form reads

$$f_1(M_{vir}) = \frac{dn(z)}{dM_{vir}} \frac{\int \tilde{\rho}^2(x) x^2 dx}{(\int \tilde{\rho}(x) x^2 dx)^2} x^3_{max}. \tag{122}$$

All the plots about the functions utilized in this part are shown in Fig. 26 and 27.

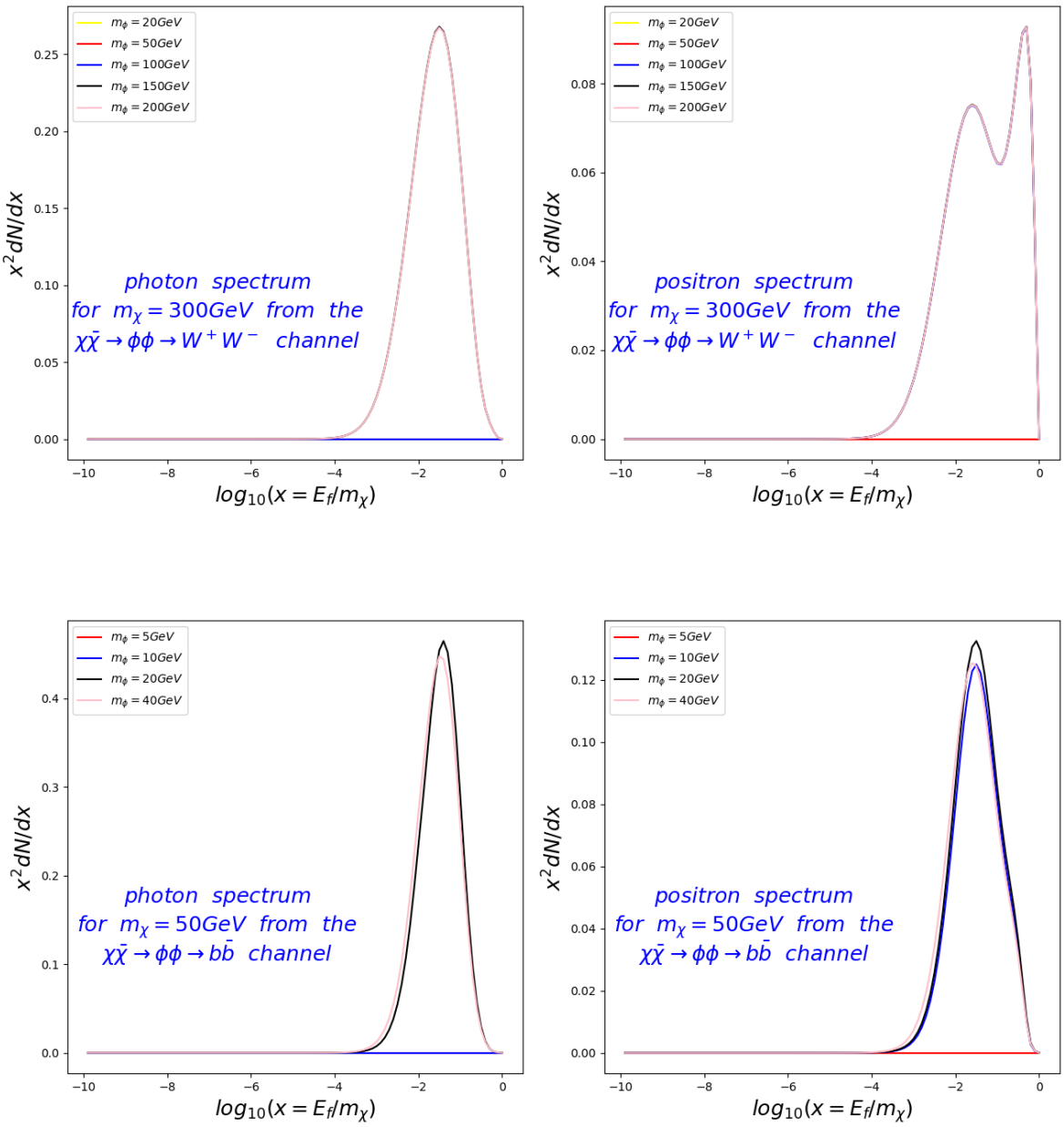

Figure 25: The photon spectra (left) and positron spectra (right) emitted from the Dark Matter annihilation to $b\bar{b}$ via two mediators $\chi\bar{\chi} \to \phi\phi \to b\bar{b}$, with two different examples of Dark Matter mass $m_\chi = 300\ GeV$ (top) in the W^+W^- channel, $m_\chi = 50\ GeV$ (bottom) in the $b\bar{b}$ channel. The colors represent different mediator mass m_ϕ. Here the 1st step ($n = 1$) is chosen in the multi-step cascade.

5.4.2.1 Halo mass function

For a structure formation that originates from a Gaussian perturbation, the halo abundance could be expressed analytically by the Dark Matter halo mass function [351, 352, 353]. At redshift z, the halo mass function is the comoving number density distribution defined as the number of halos of M per unit volume per unit mass. A general form of this function is given by

$$\frac{dn}{dM_{vir}}(M,z) = f(\sigma)\frac{\rho_{m,0}}{M_{vir}}\frac{dln[\sigma^{-1}(M,z)]}{dM}\,, \tag{123}$$

with $\sigma(M,z)$ the shape-governing function (see Equation (139)), $f(\sigma)$ the function form, M_{vir} the virial mass, $\rho_{m,0}$ the average matter density today.

There are several accurate models of the Gaussian initial condition, such as the Press & Schechter model [355], the Tinker model [353], the Sheth & Tormen model [354], etc. A summary of these models has been done in Ref. [356].

The Sheth & Tormen model provides a description of small halo mass with high accuracy, so it is applied in this work, the corresponding function form reads

$$f_{ST}(\sigma) = A\sqrt{\frac{2a}{\pi}}\frac{\delta_c(z)}{\sigma(M_{vir})}exp(-\frac{a\delta_c^2(z)}{2\sigma^2(M_{vir})})\big[1+(\frac{\sigma^2(M_{vir})}{a\delta_c^2(z)})^p\big]\,, \tag{124}$$

with $A = 0.322$, $a = 0.707$, $p = 0.3$.

Then if we note $v = \frac{\delta_c}{\sigma}$, the following expression is obtained

$$\sigma_c = 1.686 \cdot D(z), \tag{125}$$

where the growth factor reads

$$D(z) \simeq \frac{5\Omega_m}{2(1+z)[\Omega_m^{4/7}(z) - \Omega_\Lambda + (1+\Omega_{m(}(z)/2)(1+\Omega_\Lambda(z)/70)]}, \tag{126}$$

it is normalized as $D(t) = 1$ at $z = 0$, leading to the following expressions (See Fig. 27 for the plot):

$$v = \frac{\delta_c(z)}{\sigma(M_{vir})} \tag{127}$$

$$\frac{dn}{dM_{vir}}(M,z) = A\frac{\rho_{x,0}}{M_{vir}}\sqrt{\frac{2a}{\pi}}(1+(av^2)^{-p})e^{-av^2/2}\frac{dv}{dM_{vir}}. \tag{128}$$

The matter density is the sum of the baryons and Dark Matter, so

$$\rho_m = \rho_\chi + \rho_b = \rho_c(\Omega_c + \Omega_b). \tag{129}$$

At redshift z,

$$\rho_\chi(z) = \rho_{\chi,0}(1+z)^3 = \rho_c\Omega_c(1+z)^3. \tag{130}$$

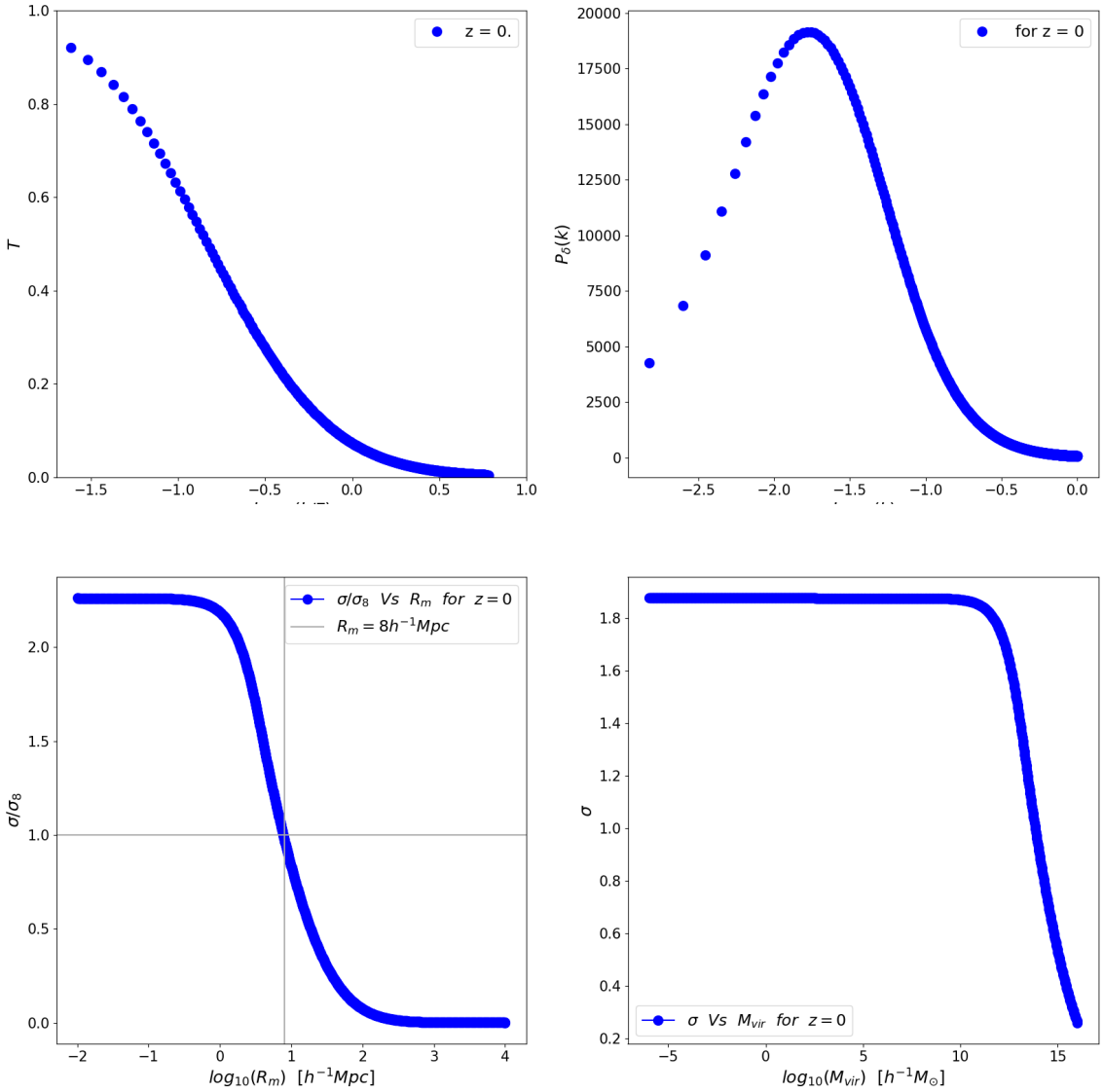

Figure 26: The functions applied in the calculation of the intensity multiplier. The linear transfer function for CDM decreases as the wave number k decrease (top left panel). The matter power spectrum for CDM model with cosmological parameters from Ref. [361], this result is consistent with previous results [357] (top right panel). The normalization method is applied to find the As, with $\sigma_8 = 0.830 \pm 0.015$ at $R_m = 8h^{-1}Mpc$ (bottom left panel), this plot is consistent with page.268 in Ref. [358]. The root of the mean variance of the density field is shown in bottom-rgiht panel. It is constant for small virial mass and decreases a lot at large virial mass.

For an infinite volume, the rms overdensity field σ is characterized by the average variance

$$\sigma^2(M_{vir}) = \frac{1}{2\pi^2}\int W^2(kR_m)P_\delta(k)k^2dk, \tag{131}$$

where the density field is smoothed with a filter to enclose the viral mass M_{vir} at the average matter density. The window function here is the top-hat filter, it is described as

$$W(x) = 3(sin(x) - x\cdot cos(x))/x^3. \tag{132}$$

The formula of the virial mass is given by

$$M_{vir} = \frac{4\pi}{3}\rho_m(z)r_{vir}^3\triangle_{vir}(z), \tag{133}$$

and for the expression with the mean radius R_m in the region enclosing the viral mass, leading to

$$M_{vir} = \frac{4\pi}{3}\rho_m R_m^3 = \frac{4\pi}{3}\rho_c\Omega_m R_m^3. \tag{134}$$

Then

$$R_m = (\frac{3M_{vir}}{4\pi\rho_c\Omega_m})^{\frac{1}{3}} = (\frac{\rho_c\Omega_m(1+z)^3r_{vir}^3\triangle_{vir}(z)}{\rho_c\Omega_m})^{\frac{1}{3}} = r_{vir}(1+z)\triangle_{vir}^{1/3}(z). \tag{135}$$

$P_\delta(k)$ is the matter power spectrum reads as

$$P_\delta(k) = A_s(k\cdot Mpc)^{n_s}T^2(k) \tag{136}$$

with the linear transfer function T(k) expressed as the following form [360]:

$$T(k) = \frac{ln(1+2.34q)}{2.34q}[1+3.89q+(16.1q)^2+(5.46q)^3+(6.71q)^4]^{-1/4}. \tag{137}$$

where $q = k/\Gamma$, and $\Gamma = \Omega_{m,,0}h_0\cdot exp(-\Omega_{b,0}(1+\frac{\sqrt{2h}}{\Omega_{m,0}}))hMpc^{-1}$.

For the normalization factor A_s, it is determined by $\sigma_8 \equiv \sigma(M_8, 0)$, leading to

$$M_8 \equiv (8h^{-1}Mpc)H_0^2\Omega_m/2G. \tag{138}$$

The recent result of the Planck collaboration and the other related observations (PLANCK+ JLA + BAO + R18) show $\sigma_8 = 0.830\pm0.015$ [361], and $\rho_{\chi,0} = \rho_{c,0}(1+z)^3 = \frac{3H^2}{8\pi G}(1+z)^3 = 2.77537h^{-1}(1+z)^3M_\odot/(h^{-1}Mpc)^3$, then $A_s = 2.992\cdot10^7$.

The power spectrum depends also on the redshift, so does σ^2. For different redshifts, the linear growth factor is taken into account [362, 363, 364].

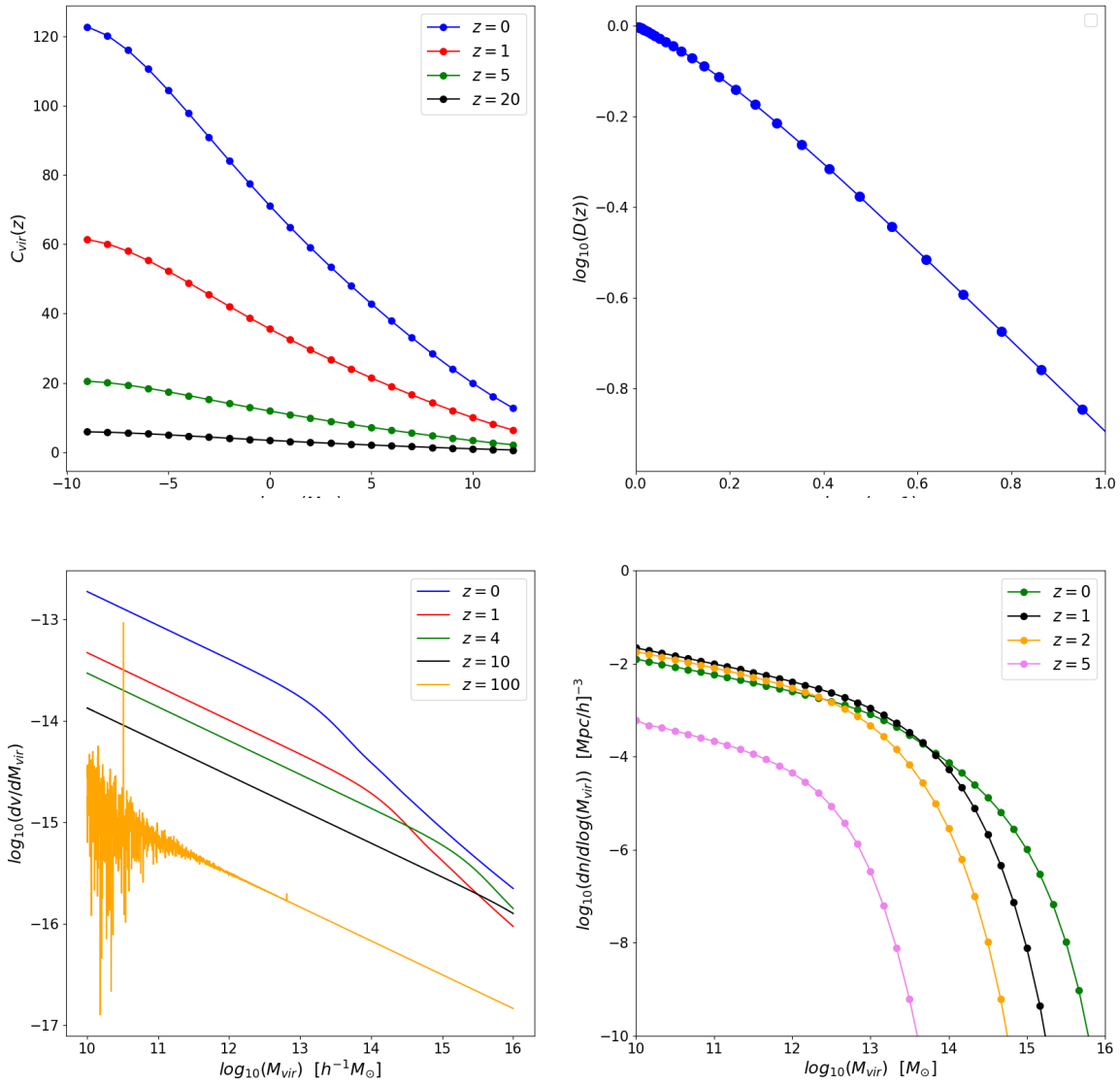

Figure 27: The functions applied in the calculation of the intensity multiplier. The C_{vir} depends on the redshift, it is close at high M_{vir} and much larger at low M_{vir}. The linear growth factor is large at small redshift and decreases to almost 0 at large redshift (top right) with cosmological parameters from Ref. [361]. The critical overdensity is larger for small viral mass, and it decreases as the redshift increases (top right). For small z, the halo mass functions are very close, but it decreases a lot at high redshift (bottom left).

$$\sigma^2(z, M_{vir}) = \frac{D^2(z)}{2\pi^2 D^2(0)} \int W^2(kR_m) P_\delta(k) k^2 dk, \tag{139}$$

$$\frac{dv}{dM_{vir}} = -\frac{1.686}{D(z)\sigma^2(M_{vir})} \frac{d\sigma}{dM_{vir}}. \tag{140}$$

The Hubble constant depends also on the redshift, it is given by

$$H^2(z) = H_0^2 E^2(z), \tag{141}$$

with $E(z) = [\Omega_{m,0}(1+z)^3 + \Omega_{r,0}(1+z)^4 + \Omega_{k,0}(1+z)^2 + \Omega_{\Lambda,0}]^{1/2}$.
So for the cosmological parameters, it is given by

$$\Omega_m(z) = \frac{\rho_m(z)}{\rho_{crit}(z)} = \frac{\rho_m(z)}{3H^2(z)} 8\pi G = \frac{\rho_m(0)(1+z)^3}{3H_0^2(z)E^2(z)} 8\pi G = \Omega_{m,0} \frac{(1+z)^3}{E^2(z)}, \tag{142}$$

$$\Omega_\Lambda(z) = \Omega_{\Lambda,0} \frac{1}{E^2(z)}. \tag{143}$$

The recent result of the Planck collaboration and the other related observations show $\Omega_{m,0} = 0.3000 \pm 0.0067$, $\Omega_{r,0} = \Omega_{k,0} = 0$, $\Omega_{\Lambda,0} = 0.7000 \pm 0.0067$ [361].
Now there are three terms depending on the redshift z: ρ_x,M_{vir} and $\frac{dv}{dM_{vir}}$.

5.4.2.2 Density profile

The density profiles have been discussed in Chapter 4. A general description has been developed to characterize the structure of CDM halos. One of the most popular profiles for the cluster-scale systems is the Navarro-Frenk-White form (NFW), it fits well with the observations and simulations of clusters. A generalized NFW profile (gNFW) [377] reads

$$\tilde{\rho}(x) = \frac{\rho}{\rho_s} \frac{1}{(\frac{r}{r_s})^\gamma (1 + \frac{r}{r_s})^{3-\gamma}}, \tag{144}$$

where a central power-law cusp is estimated with $\frac{dlog\rho_\chi}{dlogr}|_{r\to 0} = -\gamma$. When the slope $\gamma = 1$, the universal NFW density profile can be expressed as

$$\tilde{\rho}(x) = \frac{\rho}{\rho_s} = \begin{cases} \frac{1}{x^\gamma (1+x)^2} & for\ r < r_{vir} \\ 0 & otherwise \end{cases}, \tag{145}$$

and the characteristic overdensity for an NFW profile ρ_s reads

$$\rho_s(c) = \frac{200\rho_c}{3} \frac{c^3}{log(1+c) - \frac{c}{1+c}}. \tag{146}$$

The power-law fit can be applied to get the concentration-to-mass parameter c. Otherwise, defining $x \equiv \frac{r}{r_s}$, with r_s as the scale radius describing the transition between the different slopes β, the maximal value of this x term is $x_{max} \equiv \frac{r_{max}}{r_s} = \frac{r_{vir}}{r_s}$. The value of r_s can be got from the virial mass M_{vir} with Equation (134) since

$$r_s = \frac{r_{vir}}{c_{vir}}. \tag{147}$$

For the concentration-to-mass parameter $c \equiv \frac{r_{200}}{r_s}$, with r_{200} the radius which encloses M_{200} with a overdensity of 200 times of the critical density [377]. The polynomial formula of the concentration-to-mass parameter [379] is given by

$$ln(c_{vir}^{FHM}) = \sum_{i=0}^{4} c_i^{FHM} \times [ln(\frac{M}{M_\odot})]^i, \tag{148}$$

$$c_{vir}(z) = \frac{1}{1+z} c_{vir}(0), \tag{149}$$

with $c_i^{FHM} = \{4.265, -0.0384, -3.91 \times 10^{-4}, -2.2 \times 10^{-6}, -5.5 \times 10^{-7}\}$.

The minimal halo mass M_{min} has been investigated for a long time [383, 384]. A parametrization for the concentration-to-mass relation c works precisely down to Earth-mass halos ($\sim M_{min} = 10^{-6} M_\odot$) [385]. This limit has been cited by several work such as [366], in which the low M_{min} can produce about 10 times the gamma ray flux as that from high M_{min}, but the resolution of the N-body simulation to get this conclusion is not good. Additionally, it is known that parametrization fits are treated with a lot of cautions of the halo mass, redshift or cosmological parameters, thus the results are less reliable [388]. On the other hand, most of the well resolved simulations consistently limit the halo mass in the range from 10^{10} to $10^{15} M_\odot$ [386, 387, 388] despite their larger uncertainties at high redshifts, the report data also confirm the abudance of halos in this range [385]. The mean halo mass at $z = 0$ is of $8.6 \cdot 10^{13} M_\odot$ [389] and the available data is scarce below $5 \cdot 10^8 M_\odot$. At larger redshift, the simulated number density of low mass halos decrease evidently when the mass is smaller than $10^7 M_\odot$ in most of the dwarf galaxies. With the models in this section, we found the clumpiness factor depends slightly on the minimal halo mass at high redshift compared with the Sommerfeld enhancement. A robust lower bound on the sensitivity in Ref. [368] shows a factor of 5 to relax the limit on extragalactic Dark Matter annihilation compared with the FermiLAT collaboration by revising the gamma-ray data from it.

5.4.3 γ-ray attenuation

The mechanism of γ-ray attenuation is complicated at a cosmological distance, it is composed of several processes such as pair production on the baryonic matter

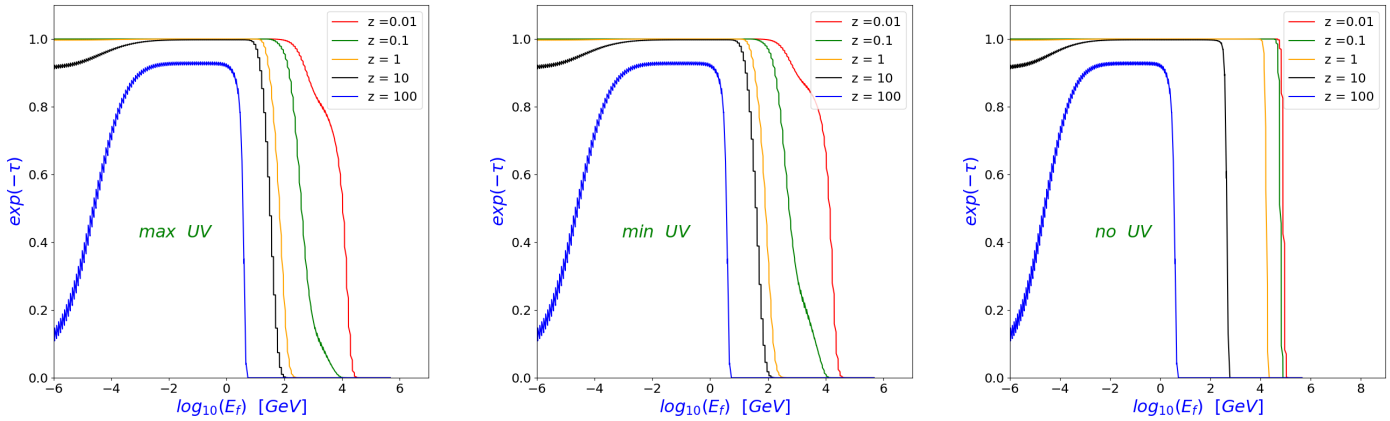

Figure 28: Optical depth due to γ-ray attenuation. The data is read from the PPPC4DMID table [113]. Three modes are shown for different UV background models. The minimal UV background model involves the blazars, the maximal UV background model corresponds to 1.5 times minimal UV background. The no UV background model assumes UV background does not exist. The attenuation is strong for more energetic photons, but tiny for low-energy photon.

and ambient Photon Background Radiation (PBR), photon-photon scattering on PBR, and Compton scattering, etc [367].

Detailed work on the opacity of the Universe has been done for high and very high energy γ-ray [365]. All the popular extragalactic background light (EBL) models have been collected in it. However, in all the accumulated tables, the maximal redshift is 200 in the Kneiske EBL model.

Meanwhile, the attenuation value could also be read from the PPPC4DMID table as well [113], including optical depth in the redshift from 10^{-5} to 1000. Three distinct models are taken into account depending on their UV background models: non UV, maximal UV, minimal UV. The corresponding optical depth is shown in Fig. 28.

5.4.4 Inverse Compton scattering

After Dark Matter annihilation, the primary or secondary electrons and positrons from the final states do not keep their high energy; they are cooled down due to several mechanisms, including inverse Compton scattering on background photon radiation, synchrotron radiation, ionization, Bremsstrahlung, and Coulomb losses [394]. The scattering between an electron and a photon changes the energy state of the two incident particles. When the electron gains energy from the incident photon, it is the Compton scattering; when the incident photon gains energy from the electron, it is the case of inverse Compton scattering. For relativistic electrons, the inverse Compton scattering becomes important in magnetized and compact systems, such as in pulsars, microquasars, and SNs; it is also the dominant energy loss channel in some extended systems such as the CMB radiation [396, 397, 398, 399].

The densest photon background in the extragalactic scale is the CMB photon, $n_\gamma \simeq 407$ photons/cm^3. The second important sources are the infrared and optical

radiation produced in the combinations of galaxies, which is less than 1/1000 of the CMB density [400]. Additionally, as discussed at the beginning of this section, the ICS is dominant over the other mechanisms in the halos [394]. The energetic electrons enter into the thermal bath and lose energy in elastic scattering with low energy photons and the photons gain energy and thus give birth to a γ-ray emission. Finally, the energy of the initial Dark Matter particles transfers finally into the CMB. The cooling rate of electrons is higher than at low redshift, since the number density of photon depends on T^3 and the energy depends on T, then the photons energy density obeys a power law dependence on T^4, or R^{-4}, or on z as $(1+z)^4$. The CMB black body spectrum [403] is given by

$$n_{ph1}(E_{ph1}, z) = \frac{1}{\pi^2(\hbar c)^3} \frac{E_{ph1}^2}{exp(\frac{E_{ph1}}{K_B T_{CMB}(z)}) - 1}, \tag{150}$$

with $T(z) = T_{CMB}(0) \cdot (1+z)$, E_{ph1} the energy of the incident photon, K_B the Boltzmann constant.

To study this effect, we refer to two excellent papers highly cited in the last 5 decades [404, 405]. There are two derivatives developed based on the 2 papers in the application of Dark Matter searches.

For the first derivative, if we note the Lorentz factor of the electron as γ , the first derivative gives the approximative computation in the Thomson regime where $\frac{4E_{ph1}\gamma}{m_e c^2} \ll 1$, and extreme Klein Nishina regime $\frac{4E_{ph1}\gamma}{m_e c^2} \gg 1$, corresponding to the outgoing soft γ-ray photon with energy peaked at X-ray range band [110, 391, 392, 393]. For $E < 10^6$GeV, ICS on the CMB is presented in the Thomson regime. To reduce computational time, the Delta-function approximation has been introduced [395]; it is believed to be precise in any energy range. A more detailed theoretical approximative expression has been done in Ref. [359, 401].

The second derivative offers a generic formula that is also available in any energy range, it is applied in the IGRB Dark Matter searches such as in Ref. [147].

Both methods are applied in this calculation. To ensure their validity, their results are compared and shown in Fig. 29. A study on the general appearance and temporal behavior of spectral features has been done to provide a simple and efficient computation as in Ref. [402]. The results in this work are consistent with the conclusions in that paper.

The differential spectrum of the Inverse Compton scattering is written as:

$$\frac{dN_{ICS}}{dE_{ph2}} = \frac{1}{E_{ph2}} \int_{m_e}^{m_\chi} \frac{P(E_{ph2}, E_e, z)}{b(E_e, z)} \{ \int_{E_e}^{m_\chi} \frac{dN}{dE'_e} dE'_e \} dE_{ph2}, \tag{151}$$

where E_{ph2} denotes the energy of the outgoing photon.

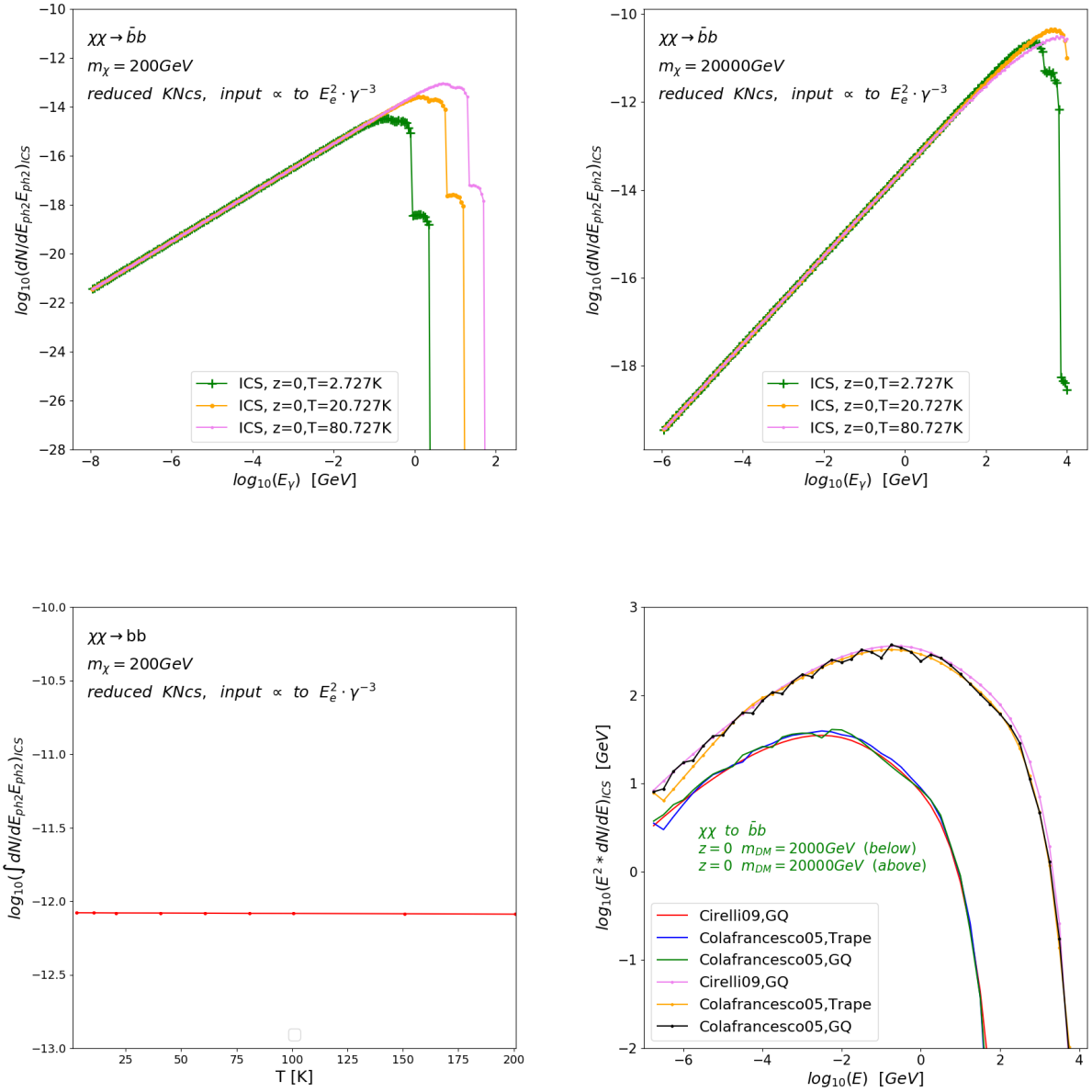

Figure 29: The functions applied in the calculation of the ICS. As proved in this section, with the condition in Equation (171), if Equation (169) is multiplied with E_{ph2}, its value is independent of T^4. The test is done with $z = 0$, and $T = 2.727$K, 20.727K, 80.727K, and $m_\chi = 200$GeV, 20000GeV. It is evidently true in the Thomson limit, as shown on the top left panel and the top right panel. Some curves are not smooth at high energy beacuase there is some missing information between the bins in the PPPC4DMID table. The independence of Equation (175) on T is shown on the bottom left panel. Different methods are applied to ensure the precision. The formulae in [391, 408] are taken to compare with $m_\chi = 2000$ GeV, 20000GeV at $z = 0$. GQ and Trape denote the Gaussian Quadrature and Trapezoidal integration methods. The three methods produce the same result, as shown on the bottom right panel. .

In the PPPC4DMID table [112], the value of $\frac{dN}{dlog10x}$ for e^+ is presented, the value for e^- is assumed to be the same. The e^- channel differs from the photon channel, the effect of redshift is neglected, then the spectrum per annihilation reads

$$\frac{dN_e}{dE'_e} = \frac{dN_e}{dE_e}\frac{dE_e}{dE'_e} = \frac{dN_e}{dE_e}. \tag{152}$$

Defining $x \equiv E_e/m_\chi$, finally the electron spectrum per annihilation is given by

$$\frac{dN_e}{dE_e} = \frac{dN}{dx}\frac{dx}{dE_e} = \frac{1}{ln(10)x}\frac{dN}{dlog_{10}(x)}\frac{dx}{dE_e} = \frac{1}{m_\chi x \cdot ln(10)}\frac{dN}{dlog_{10}(x)} = \frac{1}{E_e \cdot ln(10)}\frac{dN}{dlog_{10}(x)}. \tag{153}$$

From Blumenthal's calculation in 1970 [405], for a blackbody radiation, the total energy density reads

$$\int_0^\infty E_{ph1}^{(a-1)/2} n(E_{ph1}) dE_{ph1} = \frac{8\pi}{h^3c^3}(KT)^{(a+5)/2}\int_0^\infty q^{(a+3)/2}(e^q-1)^{-1}dq, \tag{154}$$

with $q = \frac{E_{ph2}}{4\gamma^2 E_{ph1}}$, a is the power law index of the electron energy distribution follows the power law: $N(\gamma) = K_e\gamma^{-a}$, and

$$\int_0^\infty q^{(a+3)/2}(e^q-1)^{-1}dq = \Gamma(\frac{a+5}{2})\zeta(\frac{a+5}{2}). \tag{155}$$

The emissivity reads

$$j_{E_{ph2}} = \int\limits_{E_{ph1}}\int\limits_{\gamma}\frac{1}{4\pi}E_{ph2}\frac{dN}{dtdE_{ph1}dE_{ph2}}N(\gamma)d\gamma dE_{ph1}, \tag{156}$$

$$j_{E_{ph2}} = \frac{3c\sigma_T E_{ph2}}{16\pi}\int\limits_{E_{ph1}}[\frac{n(E_{ph1})}{E_{ph1}}\int\limits_{\gamma}F_c(q)\frac{N(\gamma)}{\gamma^2}d\gamma]dE_{ph1}, \tag{157}$$

$$j_{E_{ph2}} = f(a)\frac{8\pi\sigma_T}{h^3c^2}\Gamma(\frac{a+5}{2})\zeta(\frac{a+5}{2})(KT)^{(a+5)/2}K_e E_{ph2}^{-(\frac{a-1}{2})}, \tag{158}$$

with $f(a) = \frac{3}{\pi}2^{a-2}\frac{a^2+4a+11}{(a+1)(a+3)^2(a+5)}$ and $\sigma_T = 6.65246\cdot10^{-25}\,cm^2$ the Thomson cross section, $F_c(x) = 2xln(x) + x + 1 - 2x^2$.

In the Thomson limit, $E_{ph2} = E_{ph1}\gamma^2$. For electrons at z with energy E_e, the differential power emitted to the outgoing photon with energy E_{ph2} is given by

$$P(E_{ph2}, E_e, z) = \frac{3\sigma_T}{4\gamma^2}E_{ph2}\int_0^1\frac{n(E_{CMB}, z)}{y}[2ylny + y + 1 - 2y^2]dy. \tag{159}$$

The energy loss rate is:

$$b(E_e, z) = \dot{\varepsilon}(E_e, z) = \frac{4\sigma_T \gamma^2}{3} \int_0^\infty dE_{ph1} n(E_{ph1}, z) \cdot E_{ph1}. \quad (160)$$

In the inverse Compton scattering, $m_e < E_{e,min}$ and $E_{ph1} < E_{ph2} < E_e < E_{e,max} < m_\chi$. The Thomson limit is valid when

$$\Gamma_e = \frac{4E_{ph1}\gamma}{m_e} = \frac{4E_{ph1}E_e}{m_e^2} \ll 1, \quad (161)$$

and $\tilde{E_1} = \frac{E_{ph2}}{\gamma m_e} \ll 1$, so $E_{ph2} \ll E_e$ (from Equation (2.68) in Ref. [405]), it is not valid when E_{ph2} gets close to m_χ.

In the Thomson limit, with the Klein-Nishina method, there is

$$KN_{cs}(E_{ph1}, E_e, E_{ph2}) = \frac{3\sigma_T}{4\gamma^2 E_{ph1}}[2qlnq + (1+2q)(1-q) + \frac{(\Gamma_e q)^2(1-q)}{2(1+\Gamma q)}]. \quad (162)$$

This is valid for $\frac{1}{4\gamma^2} \leq q \leq 1$ and $\Gamma_e \to 0$. Otherwiese: $KN_{cs}(E_{ph1}, E_e, E_{ph2}) = 0$, with

$\sigma_T = 6.65246 \cdot 10^{-25} cm^2$ as the Thomson cross section,

$\gamma = E_e/(m_e c^2)$ as the Lorentz factor of the electron,

$\Gamma_e = \frac{4E_{ph1}\gamma}{m_e c^2} = \frac{4E_{ph1}E_e}{(m_e c^2)^2}$,

$q = \frac{E_{ph2}}{\Gamma_e(E_e - E_{ph2})}$.

Following the calculation for the CMB radiation and ICS in Ref. [406, 407], the density of photons of a blackbody radiation field is expressed as

$$n_{CMB}(\Theta) = \int_0^\infty dE_{ph1} n_{CMB}(E_{ph1,}\Theta), \quad (163)$$

where $\Theta = k_B T/m_e c^2$ is the dimensionless temperature of the radiation field. Here $n_{CMB}(E_{ph1,}\Theta)$ is the spectral photon density $(dN/dVdE_{ph1})$ of blackbody radiation.

$$n_{CMB}(\Theta) \simeq 407(1+z)^3(\frac{T}{2.727K})^3 cm^{-3}. \quad (164)$$

The mean photon energy of a blackbody radiation field is

$$\langle E_{CMB}(\Theta)\rangle = \frac{\int_0^\infty dE_{ph1} E_{ph1}^3/[exp(E_{ph1}/\Theta) - 1]}{\int_0^\infty dE_{ph1} E_{ph1}^2/[exp(E_{ph1}/\Theta) - 1]} = 1.24 \times 10^{-9}(1+z)(\frac{T}{2.727K})\, eV, \quad (165)$$

The CMB energy density is

T $[K]$	$\int \frac{dN}{dE_{ph2}} E_{ph2} dE_{ph2}$
2.727	$8.3379 \cdot 10^{-13}$
10.727	$8.3302 \cdot 10^{-13}$
20.727	$8.3139 \cdot 10^{-13}$
40.727	$8.3034 \cdot 10^{-13}$
60.727	$8.2835 \cdot 10^{-13}$
80.727	$8.2575 \cdot 10^{-13}$
100.727	$8.2485 \cdot 10^{-13}$
150.727	$8.2093 \cdot 10^{-13}$
200.727	$8.1596 \cdot 10^{-13}$

Table 10: The numerical results of Equation (175). The integral is proved to be independent of T (see Fig. 29).

$$U_{CMB}(\Theta) = m_e c^2 \langle E_{CMB}(\Theta) \rangle n_{CMB}(\Theta) = 0.25789(1+z)^4 (\frac{T}{2.727})^4 eV \cdot cm^{-3}. \tag{166}$$

Then

$$b(E_e, z) = |\frac{dE_e}{dt}| = \frac{4}{3} \sigma_T U_{CMB}(z=0)(1+z)^4 c (\frac{E_e}{m_e})^2 \tag{167}$$

$$= 2.655 \cdot 10^{-17} (1+z)^4 (\frac{E_e}{GeV})^2 GeV s^{-1} (\frac{T}{2.727K})^4. \tag{168}$$

To conclude, the energy loss rate is $\propto T^4$.
From Equation (157),

$$\frac{dN}{dE_{ph2}} = \frac{1}{BT^4} \frac{3c\sigma_T}{4} \int\limits_{E_{ph1}} [\frac{n(E_{ph1})}{E_{ph1}} \int\limits_{\gamma} F_{c,1}(q) \frac{f_e(m_\chi, \gamma)}{\gamma^4 m_e} d\gamma] dE_{ph1}, \tag{169}$$

$$j_{E_{ph2}} = \frac{3c\sigma_T E_{ph2}}{16\pi} \int\limits_{E_{ph1}} [\frac{n(E_{ph1})}{E_{ph1}} \int\limits_{\gamma} F_c(q) \frac{N(\gamma)}{\gamma^2} d\gamma] dE_{ph1}. \tag{170}$$

From Equation (157), if we take $a = 3$, so $N(\gamma) = K_e \gamma^{-3}$, then $j_{E_{ph2}} \propto T^4$.
Compare Equations (169) and (170), if $\frac{f_e(m_\chi, \gamma)}{\gamma^2 m_e} \propto N(\gamma) = \gamma^{-3}$, for example, if

$$f_e(m_\chi, \gamma) = E_e^2 \gamma^{-3}, \tag{171}$$

and we multiply Equation (169) with E_{ph2}, then $\frac{dN}{dE_{ph2}} E_{ph2}$ must be independent of T, as shown in Fig. 29.

The total energy of the outgoing photons is expressed as

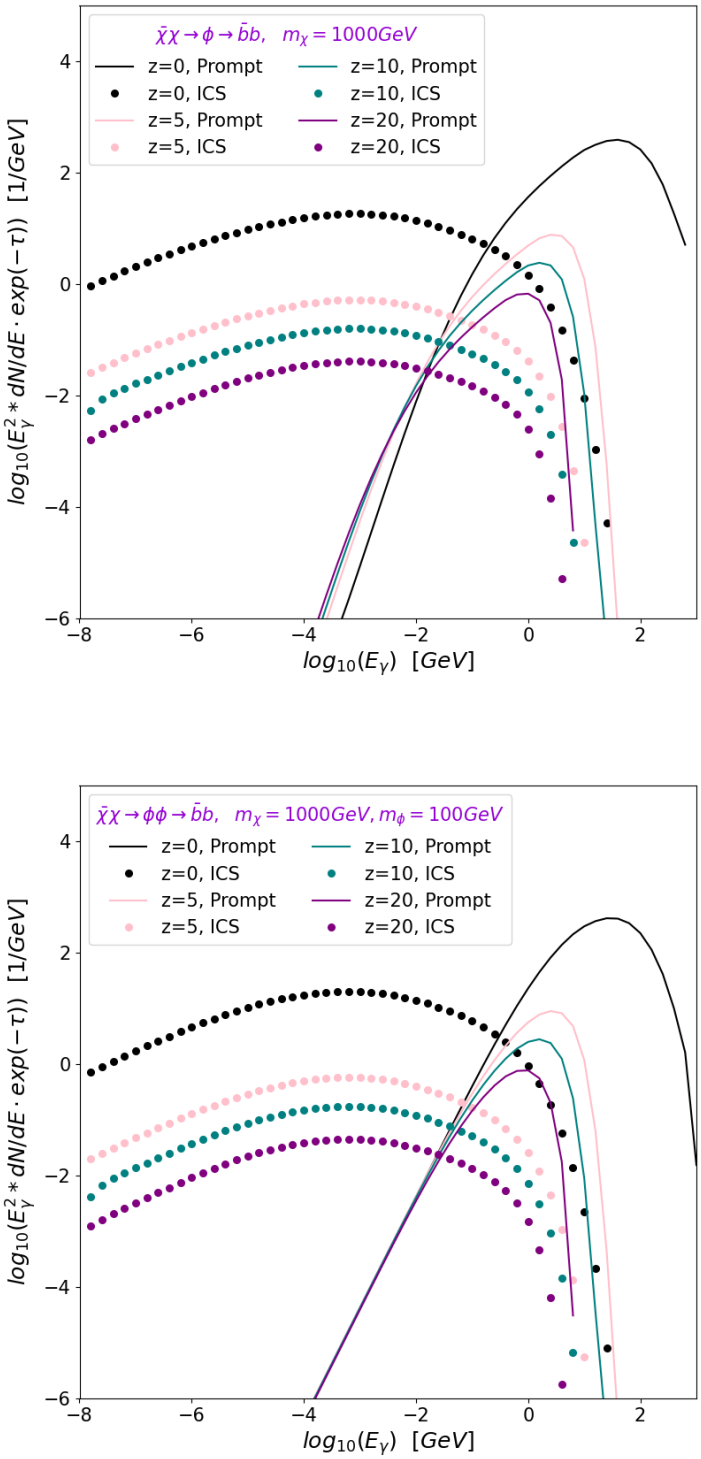

Figure 30: The comparison between the prompt and the ICS emission of gamma-ray induced by Dark Matter annihilation to $b\bar{b}$ via a single mediator (top) and two mediators (bottom). Four groups of results with different redshifts (z=0, 5, 10, 20) are shown for a Dark Matter of 1TeV. In these examples, the ICS on the CMB contributes much less than the prompt emission at high energy, but it is dominant at lower energy. And the flux at the higher redshift is higher than that at the lower redshift. The case of two mediators also depends on the mediator mass m_ϕ.

$$E_{tot} = f(a)\frac{8\pi\sigma_T}{h^3c^2}\Gamma(\frac{a+5}{2})\zeta(\frac{a+5}{2})(KT)^{(a+5)/2}K_e\int\limits_{E_{ph2}} E_{ph2}^{-(\frac{a-1}{2})}dE_{ph2}. \tag{172}$$

In the Thomson limit, $E_{ph2} \sim \gamma^2 KT$, so there is

$$\int\limits_{E_{ph2}} E_{ph2}^{-(\frac{a-1}{2})}dE_{ph2} = \frac{1}{-\frac{a-1}{2}+1}E_{ph2}^{-\frac{a-1}{2}+1}|_{E_{ph2,min}}^{E_{ph2,max}} = \frac{1}{-\frac{a-3}{2}}((KT)\gamma^2)^{-\frac{a-3}{2}}|_{\gamma_{min}}^{\gamma_{max}}, \tag{173}$$

$$E_{tot} = f(a)\frac{8\pi\sigma_T}{h^3c^2}\Gamma(\frac{a+5}{2})\zeta(\frac{a+5}{2})(KT)^4K_e\frac{2}{3-a}(\gamma_{max}^{3-a}-\gamma_{min}^{3-a}). \tag{174}$$

Then we get

$$\int\frac{dN}{dE_{ph2}}E_{ph2}dE_{ph2} = \int\limits_{E_{ph2}}\{\frac{E_{ph2}}{BT^4}\frac{3c\sigma_T}{4}\int\limits_{E_{ph1}}[\frac{n(E_{ph1})}{E_{ph1}}\int\limits_{\gamma}F_c(q)\frac{N(\gamma)}{\gamma^2}d\gamma]dE_{ph1}\}dE_{ph2}, \tag{175}$$

which must give a T-independent value. The results are shown in Table 10, and the plot is in Fig. 29.

To ensure the accuracy of computation, three integrators (the Simpson's 3/8 rule, the Trapezoidal rule, the Gaussian Quadrature) are developed by applying expressions from Ref. [391, 408]. Very close results are found by implementing the Trapezoidal integration and Gaussian Quadrature methods as shown on the bottom right panel of Fig. 29.

5.5 Sommerfeld Enhancement for p-wave Dark Matter

The exchange of mediators in a non-relativistic two-particle system creates a Yukawalike potential in a short interaction range. This potential distorts the wave function of the incoming particles, thus a bound state is formed. The annihilation cross section can be boosted a lot when they drop to enough low kinetic energy. Since Dark Matter is cooled to low velocity in today's Universe, it falls into the non-relativistic regime. So it is natural to take the Sommerfeld effect into account.

Until now, the Sommerfeld enhancement for s-wave annihilation of Dark Matter via a single mediator has been widely studied [410, 411, 412], and much less work has been done for the case of p-wave annihilation. The Sommerfeld effect can be considered as the limit of perturbative Feynman diagrams with specific mediators,

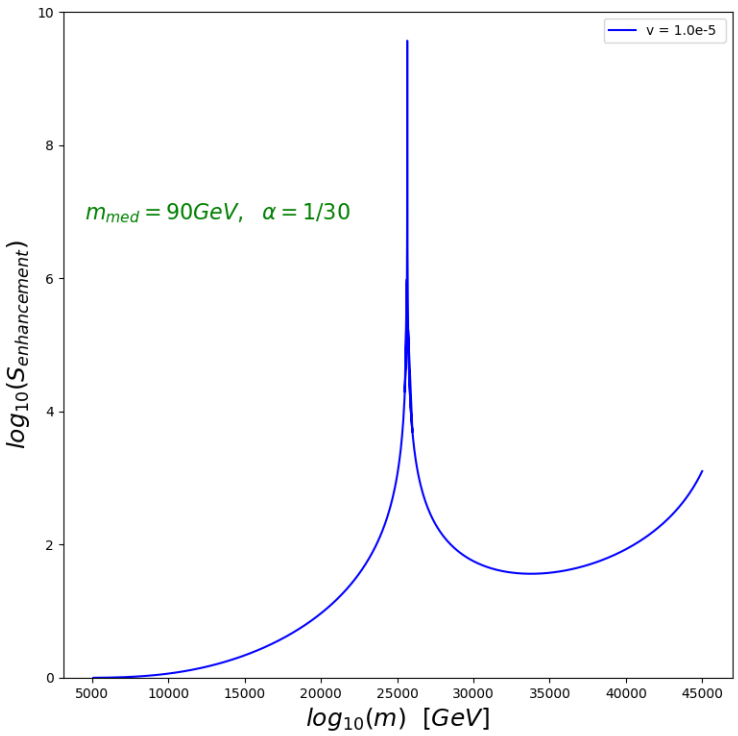

Figure 31: An example of the Sommerfeld enhancement as a function of m_r for the case of a single mediator, this result is the same as that in Ref.[115, 116]. There is a peak around $2.5 \cdot 10^4$ GeV.

and the value of this effect depends on the non-perturbative 4-point vertex Γ, as in [327, 328, 329]. For the sake of simplicity, an approximative analytical Sommerfeld factor of Yukawa interactions is given for arbitrary partial wave processes. And a corresponding numerical solution was developed independently in Ref. [115, 116] by applying the field theory diagrams and finally be expressed in the form of a wave function.

In [413], the Sommerfeld enhancement for Dark Matter annihilation via a vector, scalar, and pseudoscalar mediator have been reviewed to gain constrains from the AMS-02 positron excess. The force-carrier plays an important role in the understanding of the Sommerfeld enhancement in Dark Matter annihilation and in the production of the relic density. All these three types of force-carriers are able to accommodate the AMS-02 and FermiLAT results.

The interaction between two Dark Matter particles is considered to proceed under a Yukawa-like potential V_Y when the force carrier is a scalar or vector. The partial wave function can be obtained by solving the Schroedinger equation

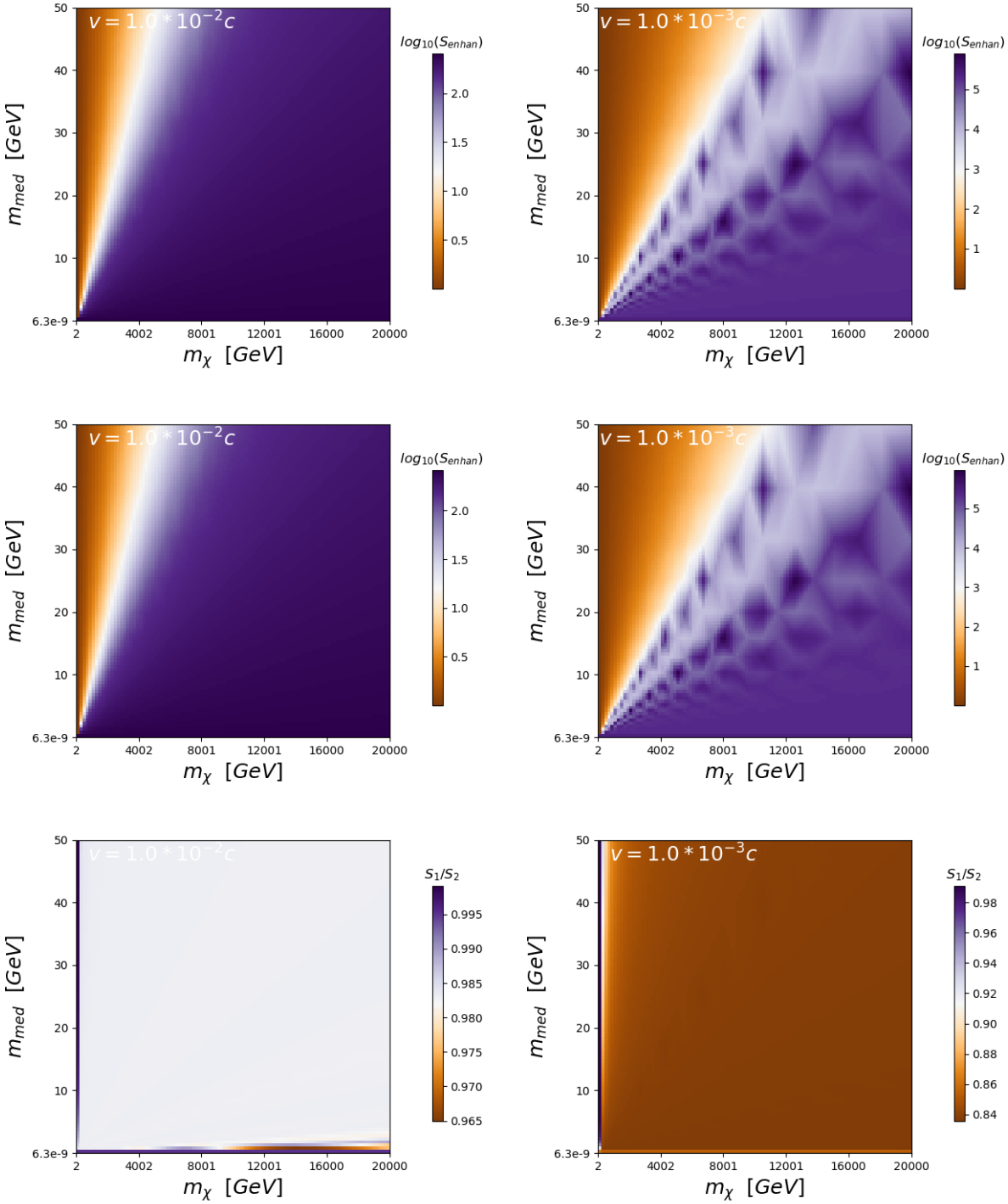

Figure 32: Distribution of the Sommerfeld boost factor on the 2D map of $\{m_\chi, m_{med}\}$ for $V_0 = 1/30$. Two methods have been implemented here to compute the boost factor, (the top panels: method 1, the middle panels: method 2). The distribution of the boost factor for two relative velocities $v = 1.0 \cdot 10^{-2}c$ (the left panels) and $v = 1.0 \cdot 10^{-3}c$ (the right panels) are shown respectively on the left and right sides. The relative value S_1/S_2 is shown on the two bottom panels. The two methods produce very close results, and they are close at higher velocity. The maximums are located in the regions with a higher ratio of mass $\frac{m_\chi}{m_{med}}$.

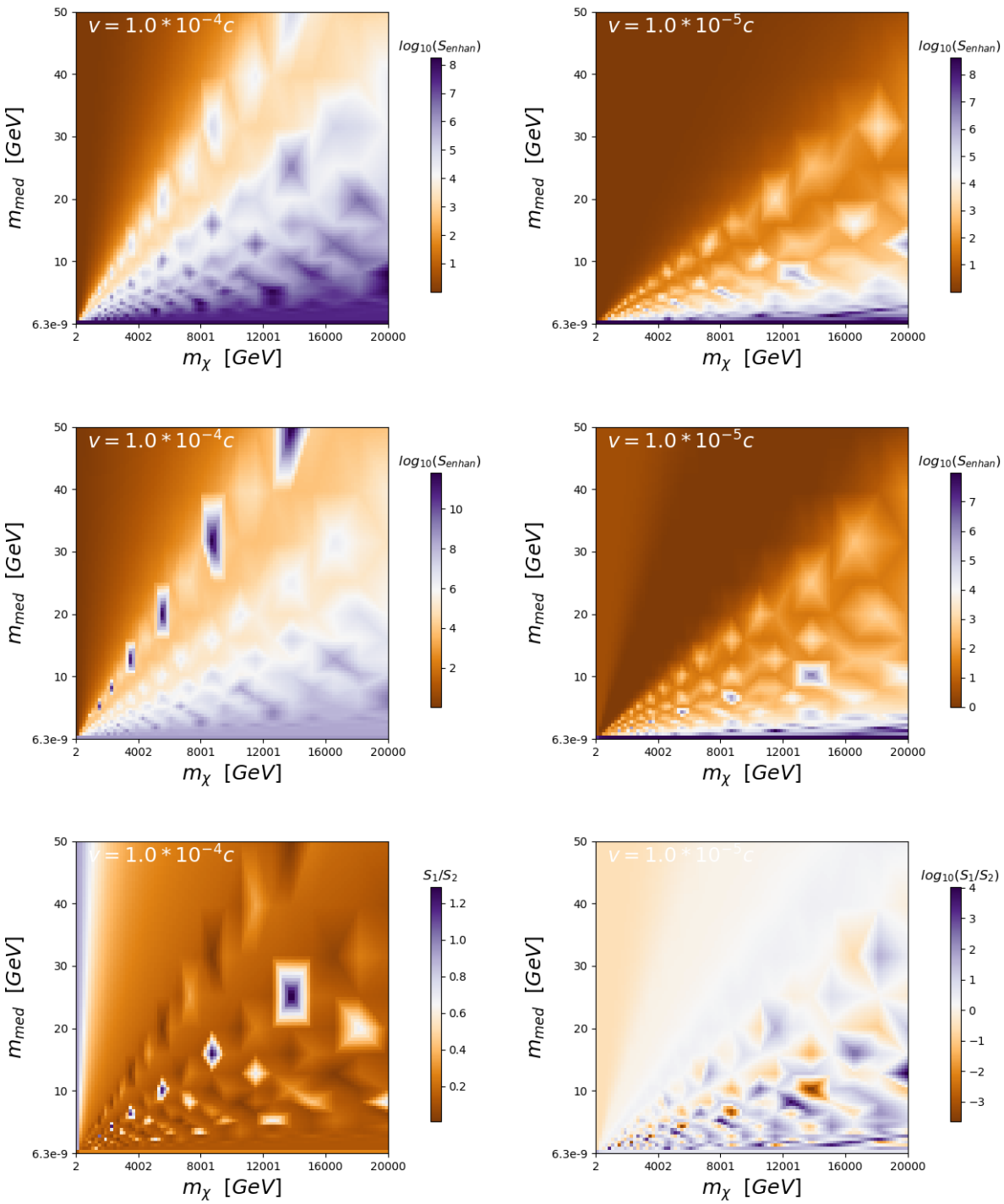

Figure 33: Distribution of the Sommerfeld boost factor on the 2D map of $\{m_\chi, m_{med}\}$ for $V_0 = 1/30$. Method 1 (top) and Method 2 (middle) are compared here to compute the boost factor. The distribution of the boost factor for two relative velocities $v = 1.0 \cdot 10^{-4} c$ (left) and $v = 1.0 \cdot 10^{-5} c$ (right) are shown here. The two methods produce very close results for $v = 1.0 \cdot 10^{-4} c$ (bottom left). But evidently, the difference between the two methods at $v = 1.0 \cdot 10^{-5} c$ is large in certain regions on the 2D map (bottom right). The maximums are located in the regions with higher ratio of mass $\frac{m_\chi}{m_{med}}$.

$$-\frac{1}{2m_r}(\frac{d^2R_{p,l}}{dr^2}+\frac{2}{r}\frac{dR_{p,l}}{dr}-\frac{l(l+1)R_{p,l}}{r^2})-(\frac{p^2}{2m_r}+\frac{V_0e^{-\mu r}}{r})R_{p,l}=0, \tag{176}$$

where the Yukawa potential is given by

$$V_Y=-\frac{V_0e^{-m_{med}r}}{r}, \tag{177}$$

with m_{med} denotes the mediator mass, r denotes the distance between the two particles, $m_r=m_\chi/2$ denotes the reduced mass, $R_{p,l}$ denotes the radial part of the wave function. Unfortunately, there is no exact analytical solution to Equation (176). We take 3 values of $V_0=\frac{1}{30},\frac{1}{100},\frac{1}{1000}$ in the calculation. Two numerical strategies have been proposed in Ref. [115, 116] to solve this problem. They are similar, so only one of them is recalled here.

$R_{p,l}$ could be written as

$$R_{p,l}(x)=Np\varphi_l(x)/x, \tag{178}$$

where $p=m_rv=\frac{m}{2}v$ and $x=pr$. And $\varphi_l(x)$ is a second order differential equation given by

$$\varphi_l^{''}+\left(1+\frac{2a}{x}e^{-bx}-\frac{l(l+1)}{x^2}\right)\varphi_l=0, \tag{179}$$

where $a=(g^24\pi)/v$ and $b=\mu/(m_rv)$ with the initial condition

$$\varphi_l(x)_{x\to0}=x^{l+1}. \tag{180}$$

For the p-wave case, l =1. And the asymptotic behavior of φ_l is estimated as

$$\varphi_l(x)_{x\to\infty}=C\cdot\left(sin(x-\frac{l\pi}{2}+\delta_l)+\frac{cos(x-\frac{l\pi}{2}+\delta_l)}{x}\right). \tag{181}$$

Then the Sommerfeld factor is given by

$$S=\left(\frac{1\cdot3\cdot5\cdots(2l+1)}{C}\right)^2, \tag{182}$$

where C denotes the amplitude of the asymptotic expression of φ_l.

For a massless mediator, the analytical solution also exists since the Yukawa potential can be approximated as a Coulomb potential or a Hulthén potential [327, 348, 416]. But this is not the best solution in this work since massive mediator is taken into account. In the DarkSPIDER package, routines about the approximative methods are kept for the users.

Then we can either follow the method in Ref.[115, 116] to get the value of C^2 at large x, or numerically solve Equation (179). Here C is the maximal value of

$\varphi_l(x)$.

The results of the two methods are shown and compared in Fig. 32 and Fig. 33 for $V_0 = 1/30$. At certain Dark Matter and mediator masses, the Sommerfeld factor is large, which leads to an enhanced annihilation cross section. The Sommerfeld factor is scanned over a 2D map for m_χ in the range of [2 GeV, 20000 GeV], m_{med} in the range of [$6.3 \cdot 10^{-9}$GeV, 50 GeV]. Four velocities have been tested. Large Sommerfeld factors are achieved on the lower right of the map. The two methods show almost the same results at higher velocities, but differ a lot at $v = 10^{-5}$c. The largest boost factors are obtained at $10^{-4}c$.

For the case of multiple mediators exchanges, the calculation follows the method in Ref. [331, 332] where the Yukawa potential approximates to a Hulthén potential, then the Sommerfeld boost factor (method 3) for s-wave and p-wave annihilation are respectively

$$S_s = \frac{\pi}{j} \frac{sinh(2\pi jk)}{cosh(2\pi jk) - cos(2\pi\sqrt{k - (jk)^2})}, \tag{183}$$

$$S_p = \frac{(k-1)^2 + 4(jk)^2}{1 + 4(jck)} S_s, \tag{184}$$

where $j = v/2V_0$ and $k = 6V_0 m_\chi/(\pi^2 m_{med})$.

The comparison in Fig. 34 shows the Hulthén approximation is close to method 2 (so also method 1) at relatively high velocity, but it produces a much smaller boost factor at relatively low velocity and a slightly larger boost factor at high velocity. For the parameters $\{m_\chi, m_{med}\}$ giving tiny annihilation cross section, the gamma-ray flux induced by them contributes slightly to the total flux compared with the background in the IGRB. When the Sommerfeld factor is large enough, the flux induced by Dark Matter annihilation is comparable with the other sources. So methods 1 and 2 are preferred in this analysis to find an optimistic result.

In Ref. [334], for the s-wave Sommerfeld enhancement, the partial-wave unitarity limit is compared with the naive Sommerfeld factor obtained with the Hulthén approximation near a resonance peak. It is found the naive factor is above the limit at low velocity and below the limit at high velocity. Since the p-wave Sommerfeld enhancement factor is proportional to that of the s-wave at a certain velocity as in Equation (184), although there is no previous study yet on the generalization of this unitarity work to p-wave, it is clear in Fig. 34 that method 2 (so also method 1) in this work behaves similarly as the unitarity limit at both low and high velocities. But a quantitative study will show how well they match each other once the generalization to p-wave is ready.

At the freeze-out, Dark Matter particles have velocity $\sim \frac{c}{3}$ (See section 3.2 of Chapter 3). Then during the expansion Dark Matter cools down to low velocity, so the p-wave annihilation rate is tiny if there is no large boost factor. This explains why we have not yet found its signal in indirect detection. In today's Universe, the typical mean velocity of Dark Matter is around 10km/s in the dSphs , around 200-300km/s in the galactic halo, and up to several thousand km/s in the

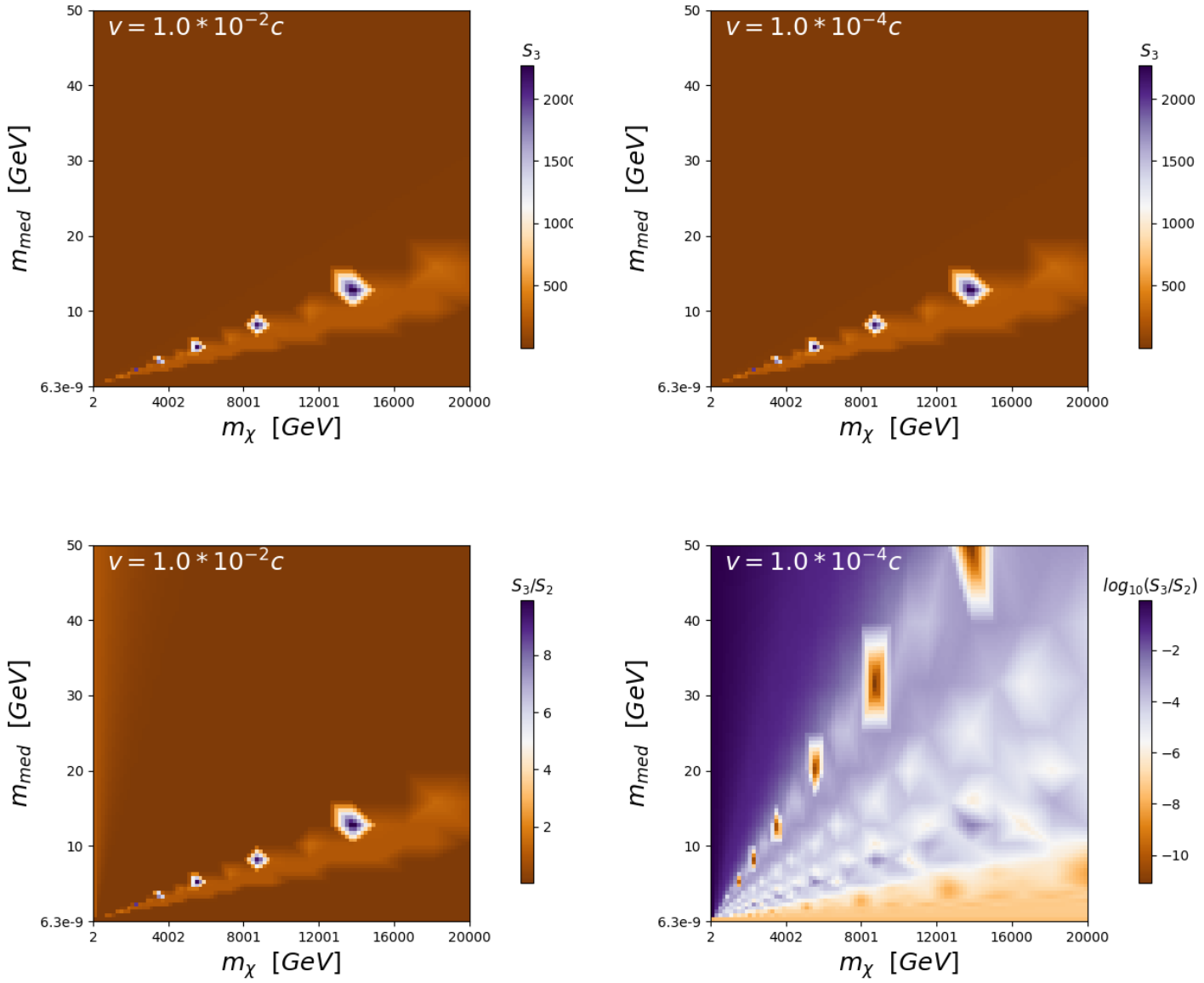

Figure 34: Comparison of method 3 and method 2 to compute the Sommerfeld enhancement. The distribution of the boost factor for two relative velocities $v = 1.0 \cdot 10^{-2}c$ (left) and $v = 1.0 \cdot 10^{-4}c$ (right) are shown here. The two methods produce very close results for $v = 1.0 \cdot 10^{-2}c$ (bottom left). But at $v = 1.0 \cdot 10^{-4}c$, method 3 with the Hulthén approximation produces much smaller Sommerfeld boost factor.

galaxy clusters. If there is an overdensity in the substructures, relative velocity gets higher. The Sommerfeld effect is more significant at a certain low velocity, it is negligible at the freeze-out, and becomes important again at certain moments during the long cooling time. when $v \ll c$, the p-wave enhancement behaves roughly like $\propto 1/v^3$ and saturates at around $v \sim m_{med}/2m_\chi$ [216, 333].

5.6 Analyses

5.6.1 Method

The parameter space $\{m_\chi, m_{med}\}$ is scanned in different energy ranges. Two scanning results are shown in this chapter: in the first, the Dark Matter msss m_χ is chosen in the range $[1, 101]\,GeV$, the mediator mass m_{med} is in $[10^{-8}, 1]\,GeV$; in the second, the Dark Matter msss m_χ is in $[101, 1001]\,GeV$, the mediator mass m_{med} is in $[10^{-4}, 400]\,GeV$. The gamma-ray flux contains photons from the annihilation via two mediators $\bar{\chi}\chi \to \phi\phi \to \overline{SM}SM$ and one mediator $\bar{\chi}\chi \to \phi \to \overline{SM}SM$. The total contribution from them is expressed by

$$\Phi_{tot,DM} = \alpha \cdot \Phi_2(\chi\bar{\chi} \to \phi\phi \to \overline{SM}SM) + (1-\alpha) \cdot \Phi_1(\chi\bar{\chi} \to \phi \to \overline{SM}SM), \quad (185)$$

where $\Phi_{tot,DM}$ denotes the total flux from Dark Matter annihilation, Φ_2 and Φ_1 denotes respectively the flux from annihilation via two mediators and one mediator. Different ratios α are set to test the contribution of χ^2 from the two types of annihilation. The annihilation via two mediators is considered to be dominant, so $\alpha = 1$ and $\alpha = 0.9$ are assumed firstly.

The new fit is done by adding the Dark Matter-induced flux to the background flux to make a theoretical prediction of the total flux [123, 202]. The Chi-2 statistics in this work reads

$$\chi^2 = \sum_{i=1}^{N} \left(\frac{\Phi_{i,obs} - \Phi_{0,i} - \Phi_{i,DM}}{\sigma_i}\right)^2. \quad (186)$$

In the ith bin, the photon flux from the other extragalactic sources $\Phi_{0,i}$ is the background, and the flux induced by Dark Matter $\Phi_{i,DM}$ is the sum of the contributions from prompt emission and ICS emission, $\Phi_{i,obs}$ is the FermiLAT IGRB data.

The IGRB data is firstly fitted with the Models without Dark Matter, and the corresponding χ^2 is calculated. The main γ-ray sources of IGRB contain BL Lacertae (BL Lac), active galactic nuclei with misaligned jet (MAGN), star-forming galaxies (SF), flat-spectrum radio quasars (FSRQ). Three models have been established in Ref.[376] by varying the weighting factors of these extragalactic sources. Fixing the contributions from them, a fit is performed with m_χ and m_{med}.

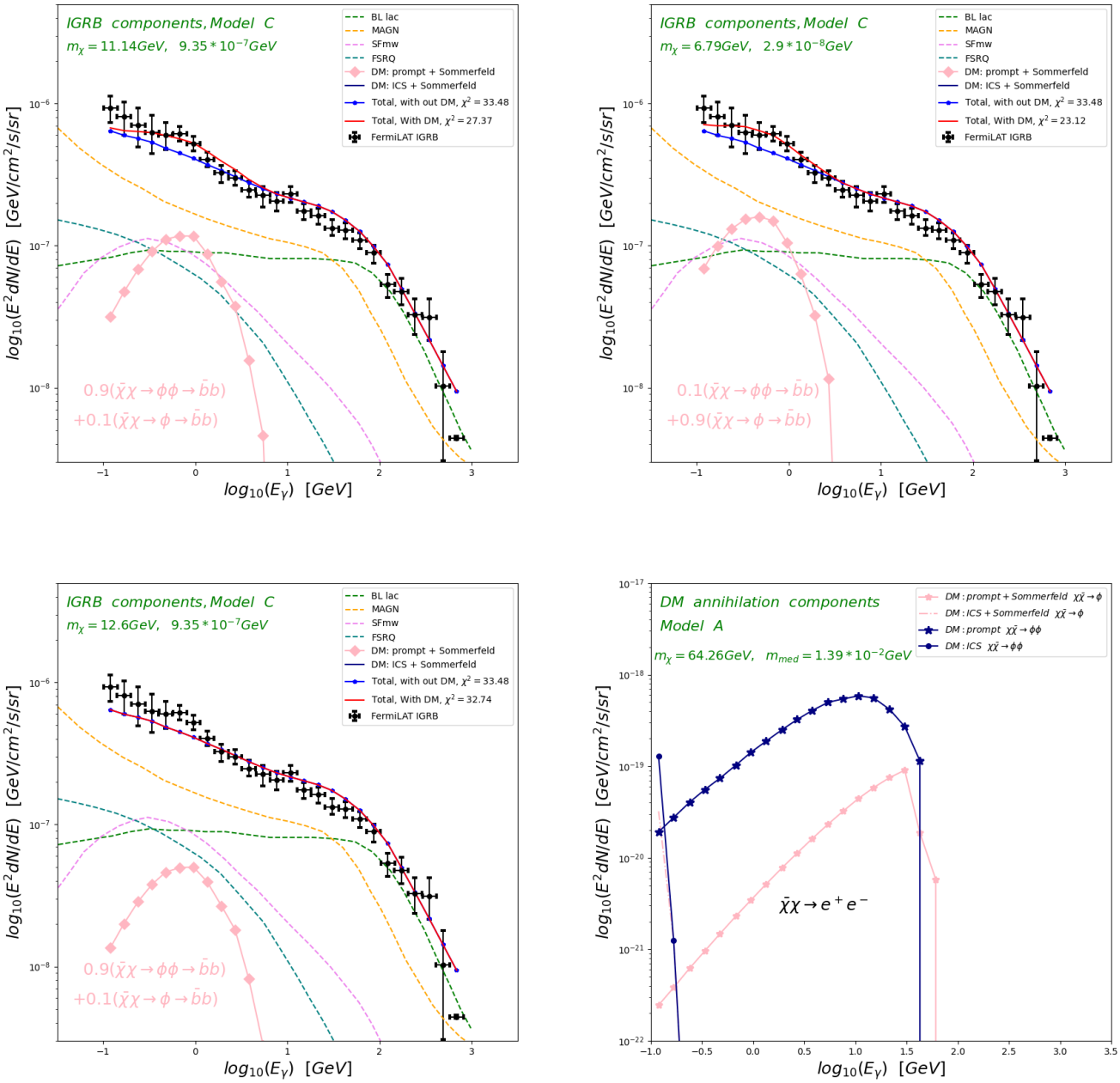

Figure 35: Four examples of fitting the FermiLAT IGRB data with Dark Matter and the other extragalactic sources are shown on the two top panels. The dashed lines correspond to the best fitting results with baryonic components to a model without Dark Matter (model C in Ref. [111]). In this work, a Dark Matter and a mediator are added to do a new fit. Three examples are considered by assuming $\bar{\chi}\chi \to b\bar{b}$ with a 100% branching ratio (two left panels and bottom left panel). Two different contributions of Dark Matter-induced γ-ray flux are shown. The best-fitting result is shown. The χ^2 has been reduced by 6.11 with $\alpha = 0.9$ (top left) and 10.36 with $\alpha = 0.1$ (top right). Another example with slightly different m_χ (bottom left) produces a much smaller flux since it does not allow strong Sommerfeld enhancement. This shows the Sommerfeld enhancement can play an important role in the detection. In most of the parameter regions of this p-wave annihilating Dark Matter, the flux from Dark Matter annihilation via two mediators or a single mediator is very tiny compared with the background radiation, even when boosted by the Sommerfeld enhancement. An example with both $\bar{\chi}\chi \to \phi\phi \to e^+e^-$ and $\bar{\chi}\chi \to \phi \to e^+e^-$ is shown on the bottom right panel. In this example, the flux from annihilation via two mediators is larger than that via one mediator, but both are too tiny to be detected in the IGRB.

Then among all the configurations with a $\chi^2 \leq \chi^2_{min} + \Delta\chi^2$, the parameters which give $\Delta\chi^2$ =2.3, 6.18, 11.83, 19.33, 28.74 determine respectively the 1 to 5 σ limits.

It is found that χ^2 can be reduced only in the range $m_\chi < 100\,GeV$, in which the branching ratios of of the $b\bar{b}$, $\tau^+\tau^-$, $g\bar{g}$, $c\bar{c}$ channels are set as they dominate subsequently the annihilation of the Higgs boson [421].

So it is reasonable to assume a naive branching ratio $B(\chi\bar{\chi} \to b\bar{b}) = 100\%$ as the first step in the calculation.

The results for the annihilation via both the $\chi\bar{\chi} \to \phi \to b\bar{b}$ and $\chi\bar{\chi} \to \phi\phi \to b\bar{b}$ channels are presented in Fig. 35. The previous work without Dark Matter fits well in the range of several hundreds GeV. The annihilation cross section of p-wave Dark Matter is tiny compared with the s-wave models if there is no boost factor. If the Sommerfeld enhancement factor is large, a bump of flux could be produced. The total differential flux could also be overproduced if the boost factor is too large. Two examples in the two top panels of Fig. 35 show improved fits by adding a p-wave Dark Matter and a mediator, the Δ^2 has been reduced by 6.11 and 10.36 in them. An example of the $\chi\bar{\chi} \to \phi \to e^+e^-$ and $\chi\bar{\chi} \to \phi\phi \to e^+e^-$ channels is shown on the bottom right panel. For p-wave Dark Matter with higher mass, not only the annihilation via two mediators but also the flux from the Sommerfeld boosted annihilation is tiny compared with the background, so this kind of candidate could not be detected in the IGRB.

If we assume the annihilation channel $\chi\bar{\chi} \to b\bar{b}$ dominates, an example of the distribution of χ^2 of this new fit is shown in Fig. 36. This example assumes Dark Matter annihilates with $\alpha = 0.9$. For model C, the χ^2_{min} of the fit without Dark Matter is 33.48. The new $\chi^2_{min} = 27.37$ is obtained at $m_\chi = 27.37$ GeV and $m_{med} = 9.35 \cdot 10^{-7}$ GeV. The flux induced by this annihilation helps to improve the fit to the IGRB data. However, in most of the parameter space, the annihilation cross section of p-wave Dark Matter is tiny compared with the contribution from the other sources. Thus even if this Dark Matter candidate does exist, the γ-ray flux induced by its annihilation is still not detectable with FermiLAT. Additionally, there is not yet IGRB data above 1TeV, thus no further conclusion could be made for masses in this range.

It is found in the regions with reduced χ^2, there are also some regions with extremely large χ^2, where the corresponding Dark Matter should be excluded. This makes the plots difficult to read. We split this kind of plots into two parts: one plot to show the excluded parameter regions, another plot to show the parameter regions where the fit is improved as shown in Fig. 36.

On the left side, the contours correspond to the 1σ to 5σ parameters regions accounting for a larger theoretically predicted γ-ray flux than the observations of IGRB. On the right side, the colored regions show the parameters of $\{m_\chi, m_{med}\}$ which give an improved fit to the IGRB data.

5.6.2 Results

The scanning work is done from $m_\chi = 1$ GeV to 1001 GeV, but only in the range of $m_\chi < 100$ GeV a reduced χ^2 could be found. In this range, there is still some

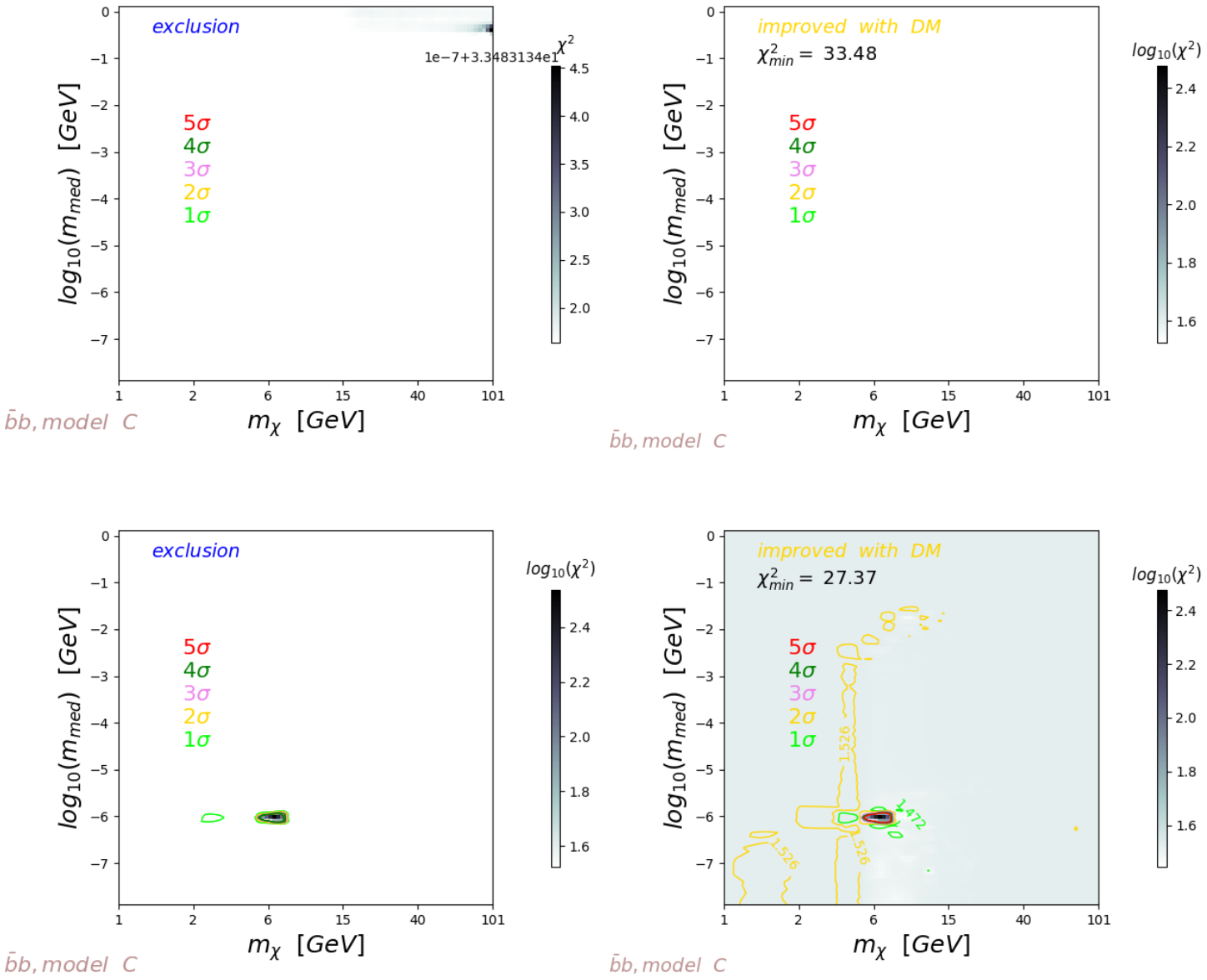

Figure 36: Two examples of the original distribution of χ^2 of the new fit with Dark Matter with $\alpha = 1.0$ (top) and $\alpha = 0.9$ (bottom). The fit is performed by adding two parameters $\{m_\chi, m_{med}\}$ to the model C of the background extragalactic sources, by utilizing the FermiLAT IGRB data [376]. The χ^2_{min} of the old fit without Dark Matter is 33.48. Here we assume only $b\bar{b}$ quark pairs are produced in the annihilation. The contours (right) show the χ^2 could be reduced in the new fit with Dark Matter annihilation. It is found that $\alpha = 0.9$ fits better. There are small regions needed to be excluded (left) where the flux induced by this Dark Matter annihilation is too large compared with the IGRB data.

space that allows Dark Matter to exist. So the results between 1 GeV and 101 GeV is firstly shown.

There are three models of the background named as models A, B, C in Ref. [111]. The fit without Dark Matter is repeated, the corresponding χ^2_{min} for them are respectively 29.87, 25.71, 33.48. The best-fitting results from each of them are extracted to do the new fit by adding the flux induced by Dark Matter annihilation.

Two kinds of scanning work are performed: firstly, the final states with only one type of particle, secondly, the final states with multiple types of particles.

For $\chi\bar{\chi}\rightarrow$ the SM final states including

$\chi\bar{\chi} \rightarrow \phi\phi \rightarrow \{\gamma\gamma,\ W^+W^-,\ b\bar{b},\ h\bar{h},\ g\bar{g},\ \tau^+\tau^-,\ \mu^+\mu^-,\ e^+e^-\}$,

$\chi\bar{\chi} \rightarrow \phi \rightarrow \{t\bar{t},\ b\bar{b},\ s\bar{s},\ c\bar{c},\ d\bar{d},\ u\bar{u},\ \tau^+\tau^-,\ \mu^+\mu^-,\ e^+e^-\}$,

the differential flux of each final state is calculated independently for the first kind of scanning work.

In Fig. 37, the distribution of χ^2 on the 2D map $\{m_\chi,\ m_{med}\}$ is shown for the $\chi\bar{\chi} \rightarrow \tau^+\tau^-$ channel. Both the exclusion plot and improvement plot show weaker statistics when α is larger. The reason is that in most of the parameter space, the flux from annihilation via two mediators is small even the Sommerfeld enhancement exists.

The calculations in the other channels to a single type of final state particles show similar results.

In the $b\bar{b}$, $\tau^+\tau^-$, $c\bar{c}$ channels, the flux induced by p-wave Dark Matter annihilation to a single type of final state particle excludes some regions in the parameter space. For the other channels to a single type of final state particle, they are insensitive to the IGRB data. Some examples are shown in Appendix D.

In the generic models, it is popular to assume that all the fermion final states share equally the branching ratio with a color factor 3 for the quarks and 1 for the leptons [103, 104, 275, 109]. The Higgs decay suggests that $B(\chi\bar{\chi} \rightarrow b\bar{b}) \simeq 60\%$ in the energy range below 100 GeV [421, 422], followed by the other sub-dominant channels which share the rest of the BR.

So for the annihilation to multiple types of final state particles, three naive assumptions are made as:

(1) $B(\chi\bar{\chi} \rightarrow e^+e^-, \mu^+\mu^-, \tau^+\tau^-) = 33.3\%$ for each of them [349] (see an example in Fig. 38),

(2) $B(\chi\bar{\chi} \rightarrow b\bar{b}) = 60\%$, and $B(\chi\bar{\chi} \rightarrow e^+e^-, \mu^+\mu^-, \tau^+\tau^-) = 13.3\%$ for each of them (see an example in Fig. 39),

(3) $B(\chi\bar{\chi} \rightarrow e^+e^-, h^+h^-, gg, \mu^+\mu^-, \tau^+\tau^-, \gamma\gamma) = 3.33\%$ for each of them, $B(\chi\bar{\chi} \rightarrow b\bar{b}) = 60\%$, and $B(\chi\bar{\chi} \rightarrow W^+W^-) = 20\%$ (see an example in Fig. 40).

The same scanning work is also performed from 101 GeV to 1001 GeV, but neither improved nor excluded region is found. This suggests this kind of p-wave annihilating Dark Matter is not detectable in the IGRB data. Some examples are in Appendix D.

The improved regions locate mostly between 1 GeV to 50 GeV. When Dark

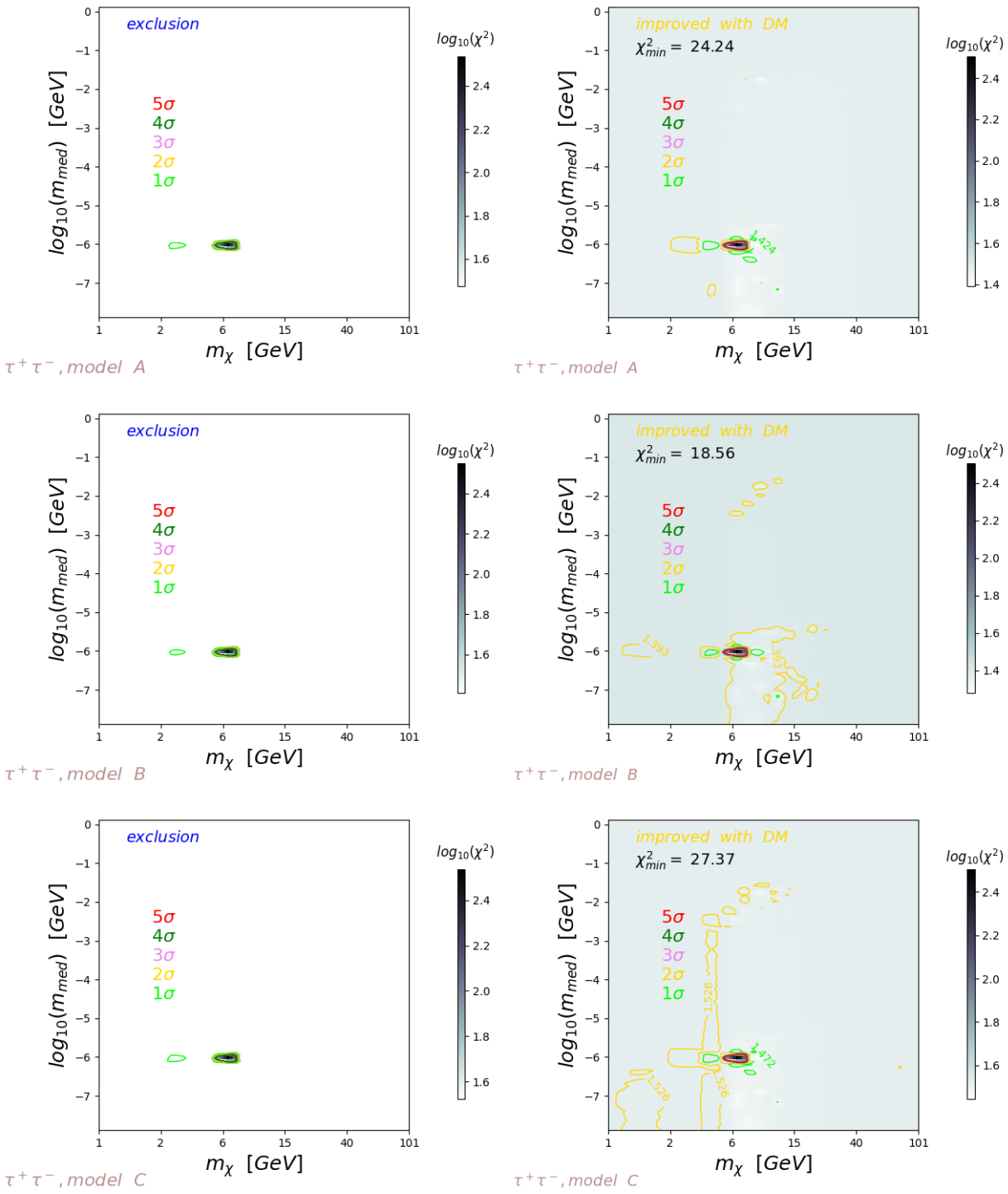

Figure 37: The Distribution of χ^2 on the 2D map of m_χ and m_{med}.

$$\Phi_{tot,DM} = \alpha \cdot \Phi_2(\bar{\chi}\chi \to \phi\phi) + (1-\alpha) \cdot \Phi_1(\bar{\chi}\chi \to \phi) \tag{188}$$

with $\alpha = 0.9$ and $B(\chi\bar{\chi} \to \tau^+\tau^-) = 100\%$. And the annihilation of Dark Matter is Sommerfeld boosted. The extragalactic sources of IGRB are considered together with Dark Matter to fit the FermiLAT IGRB data [376]. The confidence contours are shown in different colors to enclose the best-fitting regions. The exclusion fit and improved fit are respectively on the left and right side with colored contours. The models A, B, C of the extragalactic sources producing similar results are from the top to the bottom panels.

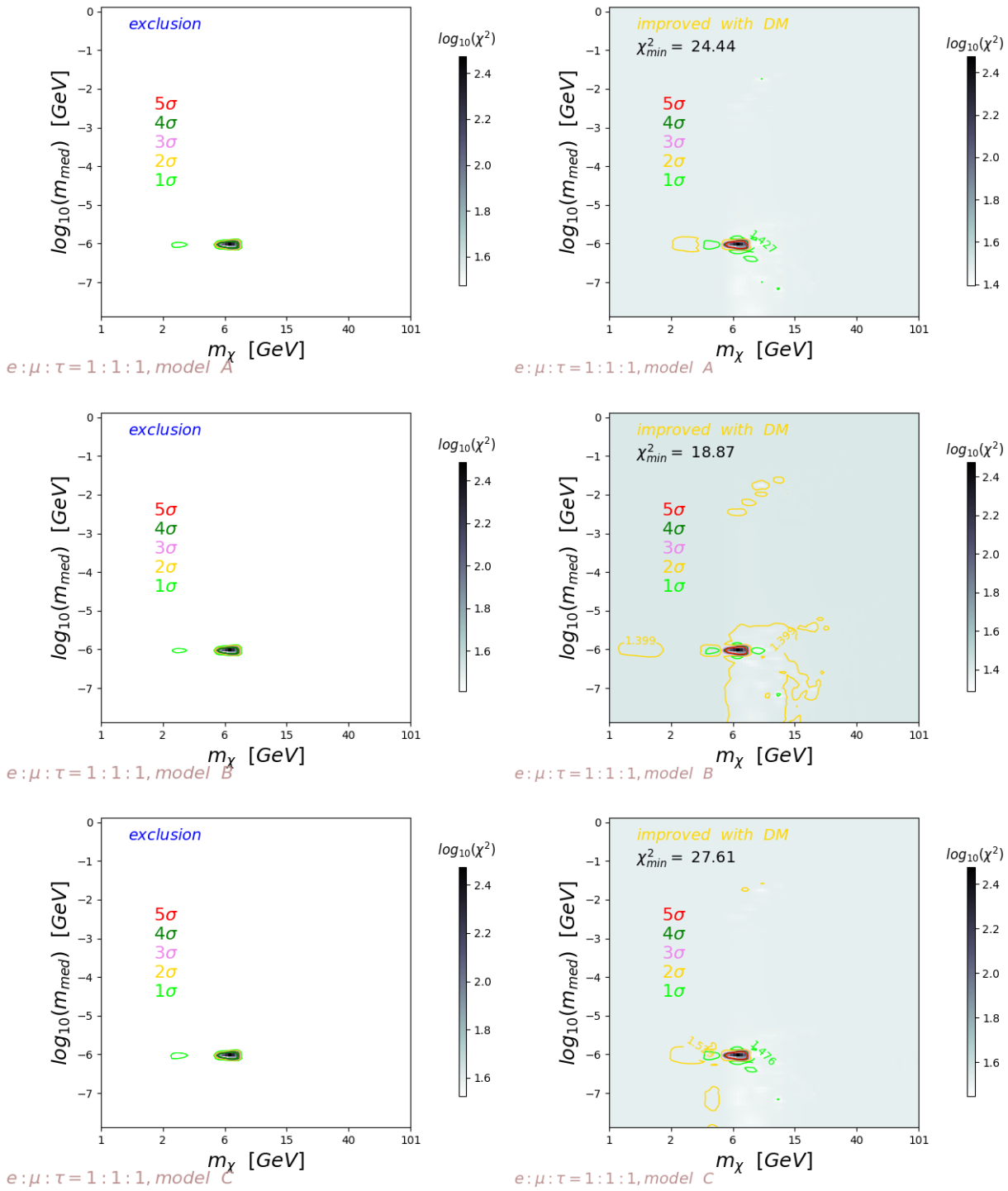

Figure 38: The Distribution of χ^2 on the 2D map of m_χ and m_{med}.

$$\Phi_{tot,DM} = \alpha \cdot \Phi_2(\bar{\chi}\chi \to \phi\phi) + (1-\alpha) \cdot \Phi_1(\bar{\chi}\chi \to \phi) \tag{190}$$

with $\alpha = 0.9$. The branching ratios of the 3 final states are assumed to be the same, $B(\chi\bar{\chi} \to e^+e^-, \mu^+\mu^-, \tau^+\tau^-) = 33.3\%$. And the annihilation of Dark Matter is Sommerfeld boosted. The extragalactic sources of IGRB are considered together with Dark Matter to fit the FermiLAT IGRB data [376]. The confidence contours are shown in different colors to enclose the best-fitting regions. The exclusion fit and improved fit are respectively on the left and right side with colored contours. The A, B, C models of the extragalactic sources producing similar results are shown from the top to the bottom panels.

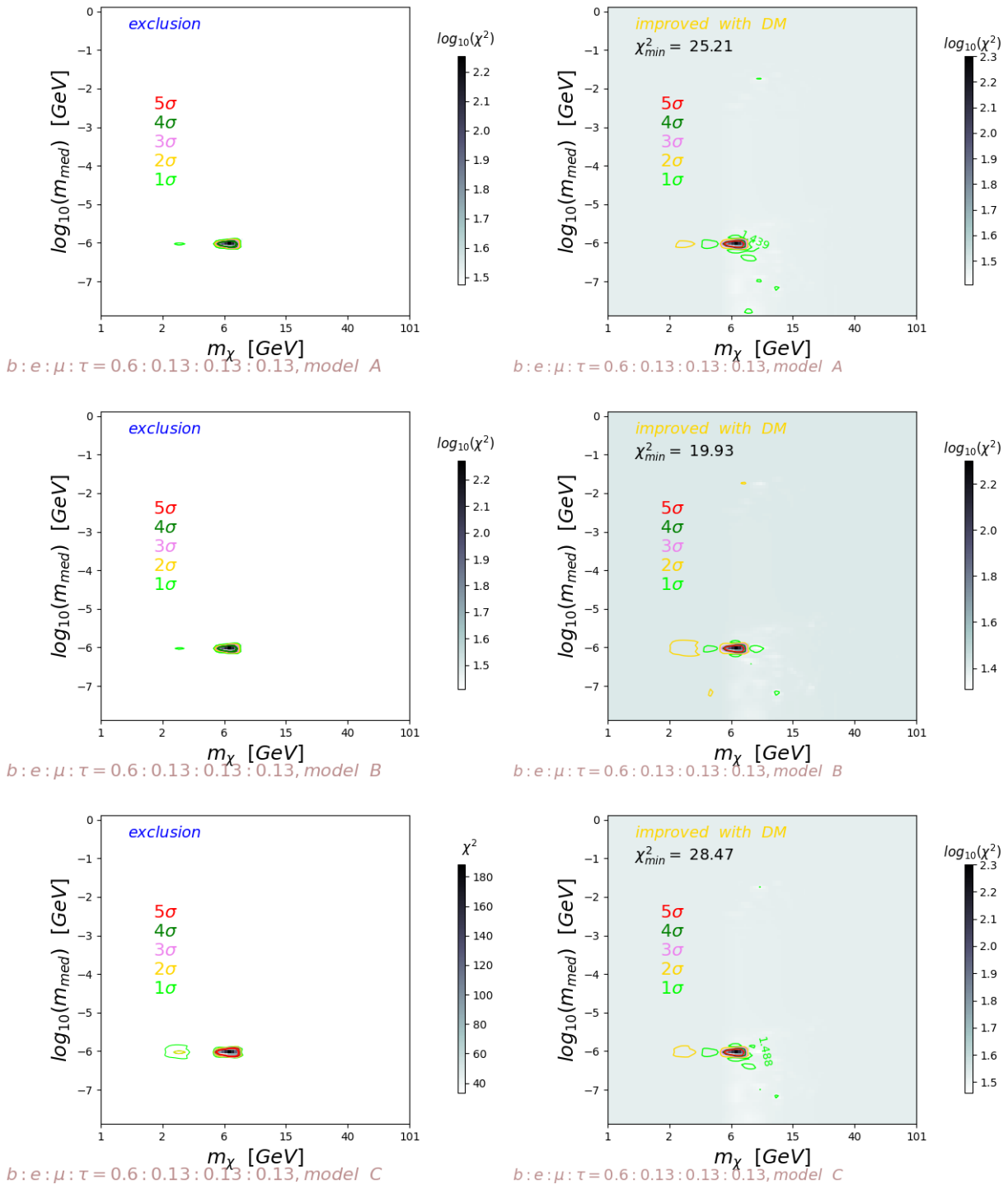

Figure 39: The Distribution of χ^2 on the 2D map of m_χ and m_{med}.

$$\Phi_{tot,DM} = \alpha \cdot \Phi_2(\bar{\chi}\chi \to \phi\phi) + (1-\alpha) \cdot \Phi_1(\bar{\chi}\chi \to \phi) \tag{192}$$

with $\alpha = 0.9$. The branching ratio of the *each* channel is naively assumed to be $B(\chi\bar{\chi} \to b\bar{b}) = 60\%$, $B(\chi\bar{\chi} \to e^+e^-, \mu^+\mu^-, \tau^+\tau^-) = 13.3\%$. And the annihilation of Dark Matter is Sommerfeld boosted. The extragalactic sources of IGRB are considered together with Dark Matter to fit the FermiLAT IGRB data [376]. The confidence contours are shown in different colors to enclose the best-fitting regions. The exclusion fit and improved fit are respectively on the left and right side with colored contours. The A, B, C models of the extragalactic sources producing similar results are shown from the top to the bottom panels.

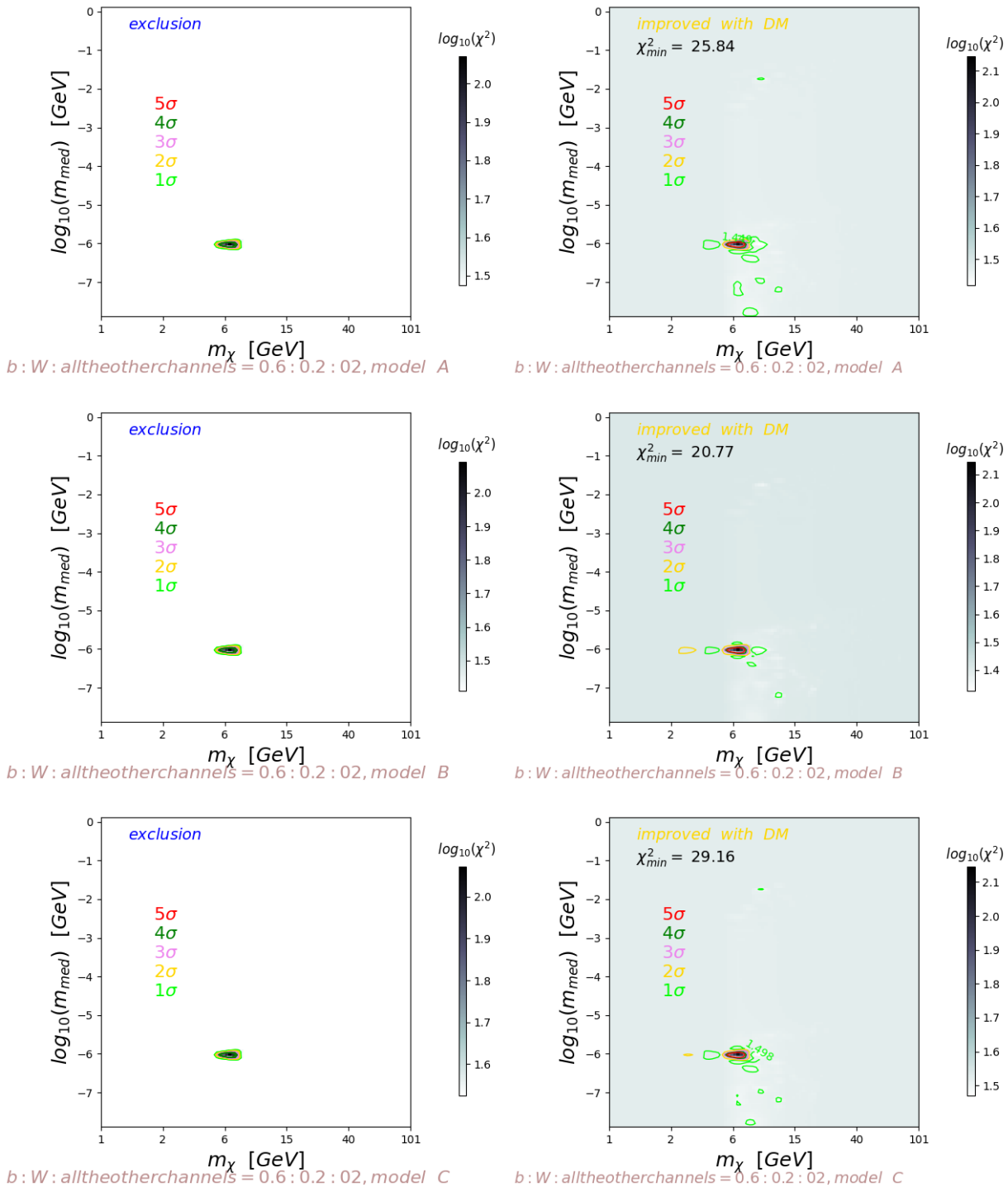

Figure 40: The Distribution of χ^2 on the 2D map of m_χ and m_{med}.

$$\Phi_{tot,DM} = \alpha \cdot \Phi_2(\bar{\chi}\chi \to \phi\phi) + (1-\alpha) \cdot \Phi_1(\bar{\chi}\chi \to \phi), \tag{194}$$

with $\alpha = 0.9$. The branching ratio of the *each* channel is assumed naively to be $B(\chi\bar{\chi} \to b\bar{b}) = 60\%$,$B(\chi\bar{\chi} \to W^+W^-) = 20\%$, $B(\chi\bar{\chi} \to e^+e^-, h^+h^-, g\bar{g}, \mu^+\mu^-, \tau^+\tau^-, \gamma) = 3.33\%$. And the annihilation of Dark Matter is Sommerfeld boosted. The extragalactic sources of IGRB are considered together with Dark Matter to fit the FermiLAT IGRB data [376]. The confidence contours are shown in different colors to enclose the best-fitting regions. The exclusion fit and improved fit are respectively on the left and right side with colored contours. The A, B, C models of the extragalactic sources producing similar results are shown from the top to the bottom panels.

Matter is in this range, its contribution to the total flux is comparable with the other sources. For the other masses, the annihilation cross section is too small, so it is invisible in the IGRB observation. The combined analysis shows only some small regions in the same range are excluded. And masses in the range from 1 GeV to 50 GeV also allow improving the fit a lot.

5.7 Summary and Discussions

P-wave Dark Matter has suppressed coupling to SM particles, so the signal from current collider-based experiments and direct detection is not accessible [415]. In this work, the analysis of p-wave annihilating Dark Matter is accomplished to seek the signal in the IGRB data. Both prompt and ICS emissions have been taken into account. The Fermi-LAT data is studied for the γ-ray signature of p-wave annihilating particle Dark Matter in IGRB in the photon energy range from 0.1 GeV to 686 GeV. By applying the Chi2 technique, a fit is performed to exclude the parameter regions which overproduce γ-ray flux.

A scanning work is performed from $m_\chi = 1$ GeV to 1001 GeV. Different from the prediction in [337], no signal has been found. This analysis excludes only some regions; most of the parameter region remains elusive to us. This work shows a Dark Matter model helps to improve the fit only when the annihilation via two or a single mediator is considered. By assuming simple branching ratios of different annihilation channels, an optimistic analysis shows weak statistics, but in some channels, the region around $m_\chi \approx 6$ GeV allows an improvement of fit with DM with a significance of 5σ, which is neighboring to small excluded ereas at a comparable significance level. In the parameter space being considered in this work, p-wave Dark Matter can not be excluded except in small regions in the range of 1 GeV to 50 GeV.

Around 6 GeV, there are some regions where the fit is improved but with weak statistics. The IGRB data is well fitted by the background flux around several hundred GeV. Adding a new component into the model may lead to an overpredicted flux if the Sommerfeld factor is too large. If Dark Matter does possess a high mass above several TeV, there is no data yet in the nearby energy range to verify it. Future observations in the ultrahigh-energy range may help to answer this question.

Most of the annihilation channels with a 100% branching ratio to a SM particle pair are insensitive to p-wave Dark Matter. Some parameter regions can be excluded only when the $b\bar{b}$, $\tau^+\tau^-$, $c\bar{c}$ channels via a single mediator is important. Additionally, when we consider all the final states, 9 final states for the case of a single mediator and 8 final states for the case of two mediators have been taken into account. This summation aslo reduces the sensitivity, so fewer regions are excluded in this combined analysis than in the channels of an SM particle pair.

There are 70 bins for each of m_χ and m_{med}, there might be missing information

between the neighboring bins. Increasing the number of bins may help to provide more details, but longer computational time is needed for such a task. The most time-consuming calculation in this work is the ICS emission with the Sommerfeld enhancement although several approximation methods have been developed to shorten the computational time in DarkSPIDER.

Several p-wave Dark Matter models are being studied recently. For the other p-wave Dark Matter candidates, a similar analysis could be done for the IGRB. There are in total seven methods to compute the Sommerfeld enhancement in DarkSPIDER. Three of them are employed in this work. The results are obtained with methods 1 and 2 that produce similar boost factors. They are larger than the boost factor obtained with method 3 in some regions of the parameter space. This work utilizes methods 1 and 2, so the conclusion is optimistic. If method 3 is employed, the flux induced by Dark Matter annihilation is even smaller in most of the parameter space considered in this work, which will make the statistics weaker. This comparison show consistent results with the unitarity of the Sommerfeld enhancement.

The Sommerfeld enhancement depends on the velocity dispersion in the targets. Any factor changing the velocity dispersion may improve the analysis. The Sheth & Tormen model of halo mass is applied in this work, it provides accurate descriptions especially of the small halos and an overestimation of the massive halo objects [356]. Although there are a lot of discussions on the minimal halo mass, in this work, the influence of the minimal value is not evident in the calculation of the p-wave Dark Matter. For the high mass halos, there are some other models. The Warren model [352] characterizes better the high mass halos. The uncertainty in this part might be important. For example, the mass-concentration relation with different masses and redshifts needs a complete investigation. The different models of the mass-concentration show a scatter of 15% in the differential flux [368] for the s-wave models. For p-wave models, this has not yet been studied.

The NFW density model is applied in the IGRB analysis, and this cuspy profile is widely applied to study galaxy clusters. However, most of the related astrophysical boost factors have not been considered, such as the substructure, the overdensity. The discrepancies exist in the simulational and observational results of halo density profiles. The cusp and core problem has been discussed in Chapter 4. It agrees with the NFW profile in the dSphs. But there might be different profiles in the clusters. A supermassive black hole window into the p-wave annihilation has been studied, and it demonstrates FermiLAT is sensitive to the two models in that work [415]. This could be done for the model for this work in the future.

In this work, neutrino channels are insensitive in IGRB with the FermiLAT data. But it may be an interesting topic to look for neutrino constraints with observations on IceCube and the other neutrino telescopes.

This work does not provide any solid conclusion on Dark Matter mass in the range between 101 GeV and 1001 GeV. Strong CMB and BBN constraints on p-

wave annihilating Dark Matter have been shown in Ref. [416]. All mediators with a mass lower than several GeV are excluded for Dark Matter under 50 TeV. That analysis is based on the s-wave dominated process in the bound state formation, and it considers the ejection of energy to CMB mediated by the Higgs portal. However, another work shows CMB is far away from the required sensitivity of p-wave Dark Matter by orders of magnitude [217]. Additionally, some work suggests p-wave Dark Matter evade constraints from CMB [420]. There is no conflict between this IGRB analysis and the previous work. IGRB data in the TeV scale will help to deal with the problem.

Dark Matter decay into standard model particles is not calculated in the IGRB analysis. This leads to a higher flux, but there is no boost factor as large as the Sommerfeld enhancement in Dark Matter decay. So the flux induced by decay is not considered in this work.

Dark Matter could contain multi-components including a p-wave Dark Matter, pioneering efforts in this direction have been discussed in [419]. This could change the differential flux and could be another interesting topic to work on in the future.

Chapter 6 Summary and outlook

The DarkSPIDER package with 32k Fortran lines of code is slim and specific. Despite its small size, its routines cover the calculation of particle physics, astrophysics, and the statistical tools to confront theoretical predictions with data.

DarkSPIDER collects as much data as possible, as shown in this thesis, many recent experiments in indirect, direct, collider-based experiments have been taken into account. The other multi-wavelength observations on the dSphs, the CMB have been used as well. The generic models including the EFT and simplified models are chosen to make a global view of Dark Matter searches.

As shown in Chapter 3, Dark Matter models are collected with various operators from several previous publications. And complementary constraints have been derived to exclude a large chunk of parameter space. Dark Matter models are collected with multiple operators from several previous publications and added to the codes. With the limits from FermiLAT and the other experiments, a comparison is made with the theoretical values. Only one of the 4 annihilation modes, the case of universal coupling and s-wave gives the same annihilation cross section required by the conventional treatment. The other models contain Dark Matter candidates non-sensitive in the current experiments, hence could not be ruled out. All these scanning shows heavy Dark Matter remains to be probed in the future.

In all these cases of coannihilation in this work, small mass splitting produces large annihilation, and a larger cut-off energy is needed for low mass Dark Matter. These results means that Dark Matter is preferred to be not too massive in the range where the EFT is valid if another unknown near-mass particle exists. This calculation could be extended to the cases with more unknown particles, which could be generalized later with DarkSPIDER.

The strongest constraints are from the direct detection experiments, for which we could also put limits on the 2D map of $\{m_\chi, m_{med}\}$. So are the collider-based experiments (LHC and ILC) and the relic density. Four operators for fermion Dark Matter are considered. Most of the regions in the low Dark Matter mass in the parameter space have been ruled out. Only some small ereas below 10 GeV and above 10 TeV are allowed. This is consistent with the results in the other methods. An interesting case is the p-wave annihilating model a fermion Dark Matter and a scalar mediator. It shows weak constraints if there is no other boost factor. This is important since a very high energy range could only be probed with indirect detection observations. And complicated physics exists in this problem. For this reason, efforts for p-wave annihilating Dark Matter are made later in Chapters 4 and 5.

A PSO optimization tool is developed to describe the velocity dispersion profile. The corresponding model is defined without pre-assumption on the density, anisotropy, and luminosity profiles. With the generic Zhao-Hernquist density profile and the generalized Osipkov Merritt profiles, we found both cored and cuspy profiles can describe the dSphs. Neither core nor cuspy is really needed. This conclusion is the same as that in Ref. [273]. But this is just a phenomenological description, a better understanding of the physics in the dSphs is needed to make a clear explanation.

The generic Zhao-Hernquist density profile has unified several density profiles [231] in a compact mathematical expression. That paper has not arrtacted enough attetion, and could be compatible mathematically with G.Mamon's work in [241, 232] which has also taken the baryonic matter into account. Additionally, in these generic profiles the black hole in the galaxies is not considered, with which the velocity dispersion curves in this work should be different. It should be useful to rule out some particle models as shown in [270].

A Dark Matter particle/mediator identification method is tried with only dSph data, but the Dark Matter models used in this work do not produce a promising result. The Dark Matter parameter allowed by the relic density does not allow a large Sommerfeld boost factor. There are several possibilities to improve this method. Different derivatives of the Boltzmann equation could be employed in this work. If the detailed time scales are taken into account, the kinetic decoupling happens much later than the chemical decoupling, this case becomes more complicated. An analysis has been done in Ref. [302, 303, 304, 305]. The difficulty is that there is not enough investigation on the Sommerfeld enhancement. Until now, the Sommerfeld enhancement have only been computed for a few particle models [417]. Once the Sommerfeld enhancement in any other p-wave Dark Matter models has been treated, this work could be extended. We can also try to improve with other boost factors such as the substructures, the non-sphericity to improve this work.

In this work, the analysis of p-wave annihilating Dark Matter via a single mediator or two mediators is accomplished to seek the signal in the IGRB data. Both prompt and ICS emissions have been taken into account. This analysis excludes some regions of the parameter space, but most of the parameter space remains elusive to us. This work shows a Dark Matter model in the range from 1 GeV to 50 GeV helps to improve a lot the fit with some regions around 6 GeV significantly improved or excluded. However, this improvement or exclusion is weakened at higher mass from 100 GeV to 1001 GeV since the flux from this case is too tiny. The IGRB data is well fitted by the background flux around several hundred GeV. Adding a new component into the model leads to an over-predicted flux. If Dark Matter does possess a high mass in several TeV, there is not yet data in this energy range to verify it. To solve this problem, we should wait for the observations in the ultrahigh-energy range.

Appendix

Appendix A
List the EFT models in DarkSPIDER

Fermion Dark Matter		
Operator name	EFT Coupling coefficient	Transition matrix
Scalar	$\frac{m_q}{\Lambda^3}$	$\bar{\chi}\chi\bar{f}f$
Pseudoscalar	$\frac{m_q}{\Lambda^3}$	$\bar{\chi}\gamma_5\chi\bar{f}\gamma_5 f$
Vector	$\frac{1}{\Lambda^2}$	$\bar{\chi}\gamma^\mu\chi\bar{f}\gamma_\mu f$
axial-vector	$\frac{1}{\Lambda^2}$	$\bar{\chi}\gamma^\mu\gamma_5\chi\bar{f}\gamma_\mu\gamma_5 f$
Tensor	$\frac{1}{\Lambda^2}$	$\bar{\chi}\sigma^{\mu\nu}\chi\bar{f}\sigma_{\mu\nu}f$
Scalar-Pseudoscalar	$\frac{m_q}{\Lambda^3}$	$\bar{\chi}\chi\bar{f}i\gamma_5 f$
Pseudoscalar-Scalar	$\frac{m_q}{\Lambda^3}$	$\bar{\chi}i\gamma_5\chi\bar{f}f$
Vector-axial-vector	$\frac{1}{\Lambda^2}$	$\bar{\chi}\gamma^\mu\chi\bar{f}\gamma_\mu\gamma_5 f$
AVector-Vector	$\frac{1}{\Lambda^2}$	$\bar{\chi}\gamma^\mu\gamma_5\chi\bar{f}\gamma_\mu f$
Alternative Tensor	$\frac{1}{\Lambda^2}$	$\varepsilon^{\mu\nu\rho\sigma}\bar{\chi}\sigma_{\mu\nu}\chi\bar{f}\sigma_{\rho\sigma}f$
Chiral (LL/RR/LR/RL)	$\frac{1}{\Lambda^2}$	$\bar{\chi}\gamma^\mu(1\pm\gamma_5)\chi\bar{f}\gamma_\mu(1\pm\gamma_5)f$
FtS Scalar (t-channel)	$\frac{m_q}{\Lambda^3}$	$\bar{f}\chi\bar{\chi}f$
FtS Pseudoscalar (t-channel)	$\frac{m_q}{\Lambda^3}$	$\bar{f}\gamma_5\chi\bar{\chi}\gamma_5 f$
FtV Vector (t-channel)	$\frac{1}{\Lambda^2}$	$\bar{f}\gamma^\mu\chi\bar{\chi}\gamma_\mu f$
FtV axial-vector (t-channel)	$\frac{1}{\Lambda^2}$	$\bar{f}\gamma^\mu\gamma_5\chi\bar{\chi}\gamma_\mu\gamma_5 f$
FtV Chiral (t-channel)	$\frac{1}{\Lambda^2}$	$\bar{f}\gamma^\mu(1\pm\gamma_5)\chi\bar{\chi}\gamma_\mu(1\pm\gamma_5)f$

Table 11: List of EFT operators (Dimension 6) involving Dirac fermion Dark Matter. The second column is the coupling coefficient, $\frac{1}{\Lambda^2}$ and $\frac{m_q}{\Lambda^3}$ correspond respectively to universal coupling and Yukawalike coupling. The effective Lagrangians are not invariant under the SM $SU(2)_W \times U(1)_Y$ gauge symmetry, but valid below the energy scale of electroweak symmetry breaking. Some t-channel cases are shown at the bottom. For the other EFT operators for Dirac fermion Dark Matter, cf. the User's guide or Ref. [105].

complex Scalar Dark Matter		
Operator name	EFT coupling coefficient	Transition matrix
Scalar	$\frac{m_q}{\Lambda^2}$	$\phi^\dagger\phi\bar{f}f$
Scalar - Pseudoscalar	$\frac{m_q}{\Lambda^2}$	$\phi^\dagger\phi\bar{f}i\gamma_5 f$
Vector	$\frac{1}{\Lambda^2}$	$\phi^\dagger\overleftrightarrow{\partial_\mu}\phi\bar{f}\gamma_\mu f$
Vector - Axial-vector	$\frac{1}{\Lambda^2}$	$\phi^\dagger\overleftrightarrow{\partial_\mu}\phi\bar{f}\gamma_\mu\gamma_5 f$
Real Scalar Dark Matter		
Scalar	$\frac{m_q}{2\Lambda^2}$	$\phi\phi f f$
Scalar - Pseudoscalar	$\frac{m_q}{2\Lambda^2}$	$\phi\phi f i\gamma_5 f$

Table 12: List of EFT operators involving Dirac fermion Dark Matter. The second column is the coupling coefficient, $\frac{1}{\Lambda^2}$ and $\frac{m_q}{\Lambda^2}$ correspond respectively to universal coupling (Dimension 6) and Yukawalike coupling (Dimension 5). Here $\overleftrightarrow{\partial_\mu} = \overrightarrow{\partial_\mu} - \overleftarrow{\partial_\mu}$. The effective Lagrangians are not invariant under the standard model $SU(2)_W \times U(1)_Y$ gauge symmetry, but valid below the energy scale of electroweak symmetry breaking. For the other EFT operators for scalar Dark Matter, cf. the User's guide or Ref. [105].

Vector Dark Matter		
Operator name	EFT coupling coefficient	Transition matrix
Scalar	$\frac{m_q}{\Lambda^2}$	$B^\mu B_\mu f f$
Vector	$\frac{1}{2\Lambda^2}$	$B^{\dagger\mu}\overleftrightarrow{\partial_v} B_\mu \bar{f}\gamma^v f$
Scalar-Pseudoscalar	$\frac{m_q}{\Lambda^2}$	$B^\mu B_\mu f i\gamma_5 f$
Vector-axial-vector	$\frac{1}{2\Lambda^2}$	$B^{\dagger\mu}\overleftrightarrow{\partial_v} B_\mu \bar{f}\gamma^v\gamma_5 f$
Tensor	$\frac{m_q}{\Lambda^2}$	$(B^\dagger_\mu B_v - B^\dagger_v B_\mu) f\sigma^{\mu v} f$
Alternative vector	$\frac{1}{2\Lambda^2}$	$\varepsilon_{\mu\nu\rho\sigma} B^v \overleftrightarrow{\partial^\rho} B^\sigma \bar{f}\gamma^\mu f$
Alternative vector - axial-vector	$\frac{1}{2\Lambda^2}$	$\varepsilon_{\mu\nu\rho\sigma} B^v \overleftrightarrow{\partial^\rho} B^\sigma \bar{f}\gamma^\mu\gamma_5 f$
Alternative Tensor	$\frac{m_q}{\Lambda^2}$	$\varepsilon^{\mu\nu\rho\sigma}(B^\dagger_\mu B_v - B^\dagger_v B_\mu) f\sigma_{\rho\sigma} f$

Table 13: List of EFT operators involving vector Dark Matter. The second column is the coupling coefficient, $\frac{1}{\Lambda^2}$ and $\frac{m_q}{\Lambda^2}$ correspond respectively to universal coupling (Dimension 6) and Yukawalike coupling (Dimension 5). Here $\overleftrightarrow{\partial_\mu} = \overrightarrow{\partial_\mu} - \overleftarrow{\partial_\mu}$. The effective Lagrangians are not invariant under the standard model $SU(2)_W \times U(1)_Y$ gauge symmetry, but valid below the energy scale of electroweak symmetry breaking. For the other EFT operators for vector Dark Matter, cf. the User's guide or Ref. [105].

Appendix B
Constraints from indirect detection, for the EFT models

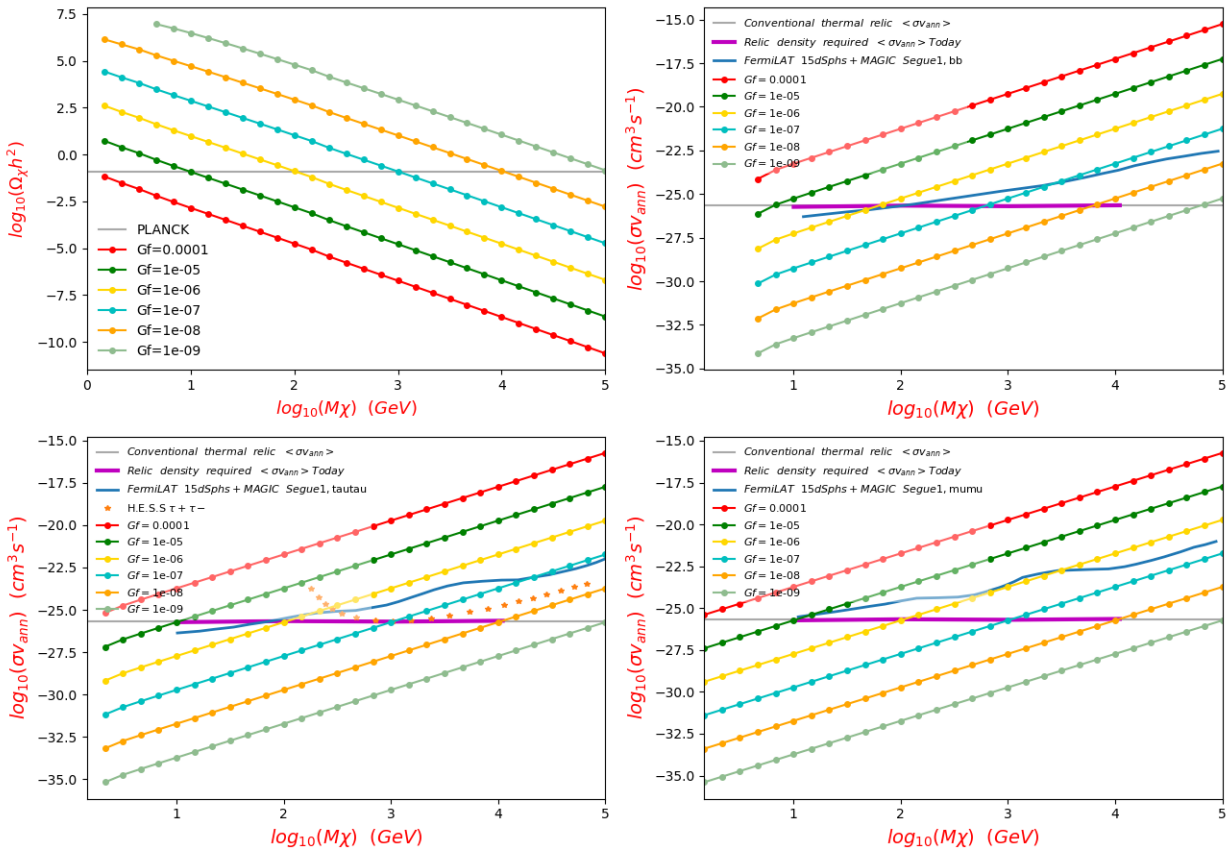

Fermion DM annihilation
via Vector operator
with universal coupling

Fig. top left: $log_{10}(\Omega_\chi h^2)$ *VS* $log_{10}(M_\chi)$
Fig. top right: $b\bar{b}$ $log_{10}(\sigma v_{ann})$ *VS* $log_{10}(M_\chi)$
Fig. bottom left: $\tau^+\tau^-$ $log_{10}(\sigma v_{ann})$ *VS* $log_{10}(M_\chi)$
Fig. bottom right: $\mu^+\mu^-$ $log_{10}(\sigma v_{ann})$ *VS* $log_{10}(M_\chi)$

Figure 41: For fermion Dark Matter annihilation via a vector operator with universal coupling, the relic density required Dark Matter mass m_χ and coupling constant G_f are shown on the top left panel. If Dark Matter annihilates purely to one final state, the maximal $\langle\sigma v\rangle_{anni}$ to 3 final state particles are respectively shown from top middle to bottom left: $\bar{b}b$, $\tau^+\tau^-$, $\mu^+\mu^-$. The constraints are from the observations of dSphs by FermiLAT and MAGIC [203], and the observation of the galactic halo with H.E.S.S [174]. The gray horizontal line is the conventional $\langle\sigma v\rangle_{anni} = 2.7 \cdot 10^{-26}\, cm^3 s^{-1}$ at the freeze-out moment, the $\langle\sigma v\rangle_{anni}$ it can produce today into each channel is shown as the violet curve (for $v = 220\, km/s$). See Table 12 for more explanation.

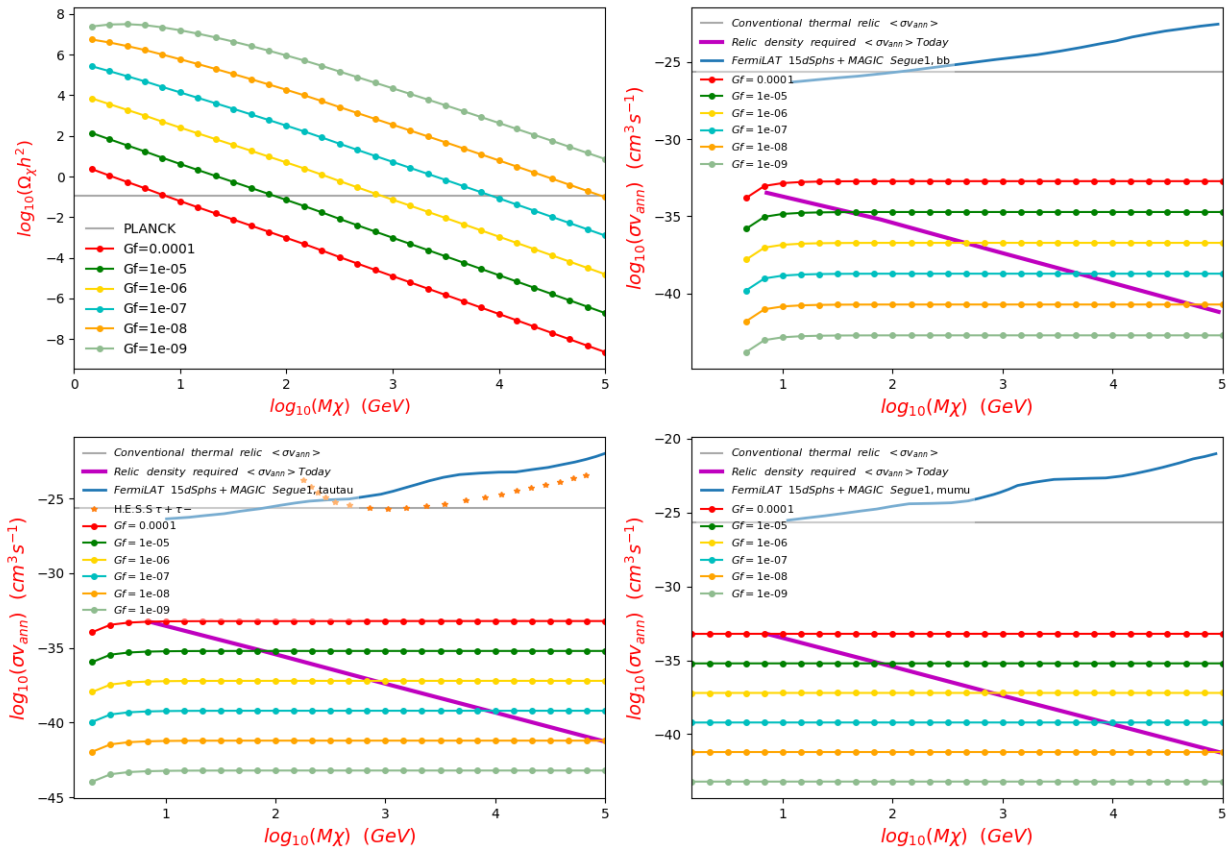

Scalar DM annihilation
via Vector-Axialvector operator
with universal coupling

Fig. top left: $log_{10}(\Omega_\chi h^2)$ *VS* $log_{10}(M_\chi)$
Fig. top right: $b\bar{b}$ $log_{10}(\sigma v_{ann})$ *VS* $log_{10}(M_\chi)$
Fig. bottom left: $\tau^+\tau^-$ $log_{10}(\sigma v_{ann})$ *VS* $log_{10}(M_\chi)$
Fig. bottom right: $\mu^+\mu^-$ $log_{10}(\sigma v_{ann})$ *VS* $log_{10}(M_\chi)$

Figure 42: For scalar Dark Matter annihilation via a vector - axial-vector operator with universal coupling, the relic density required Dark Matter mass m_χ and coupling constant G_f are shown on the top left panel. If Dark Matter annihilates purely to one final state, the maximal $\langle\sigma v\rangle_{anni}$ to 3 final state particles are respectively shown from top middle to bottom left: $\bar{b}b$, $\tau^+\tau^-$, $\mu^+\mu^-$. The constraints are from the observations of dSphs by FermiLAT and MAGIC [203], and the observation of the galactic halo with H.E.S.S [174]. The gray horizontal line is the conventional $\langle\sigma v\rangle_{anni} = 2.7 \cdot 10^{-26}\, cm^3 s^{-1}$ at the freeze-out moment, the $\langle\sigma v\rangle_{anni}$ it can produce today is shown as the violet curve (for $v = 220\, km/s$). This is a p-wave annihilation, it is beyond the sensitivities in all the existing experiments. See Table 12 for more explanation.

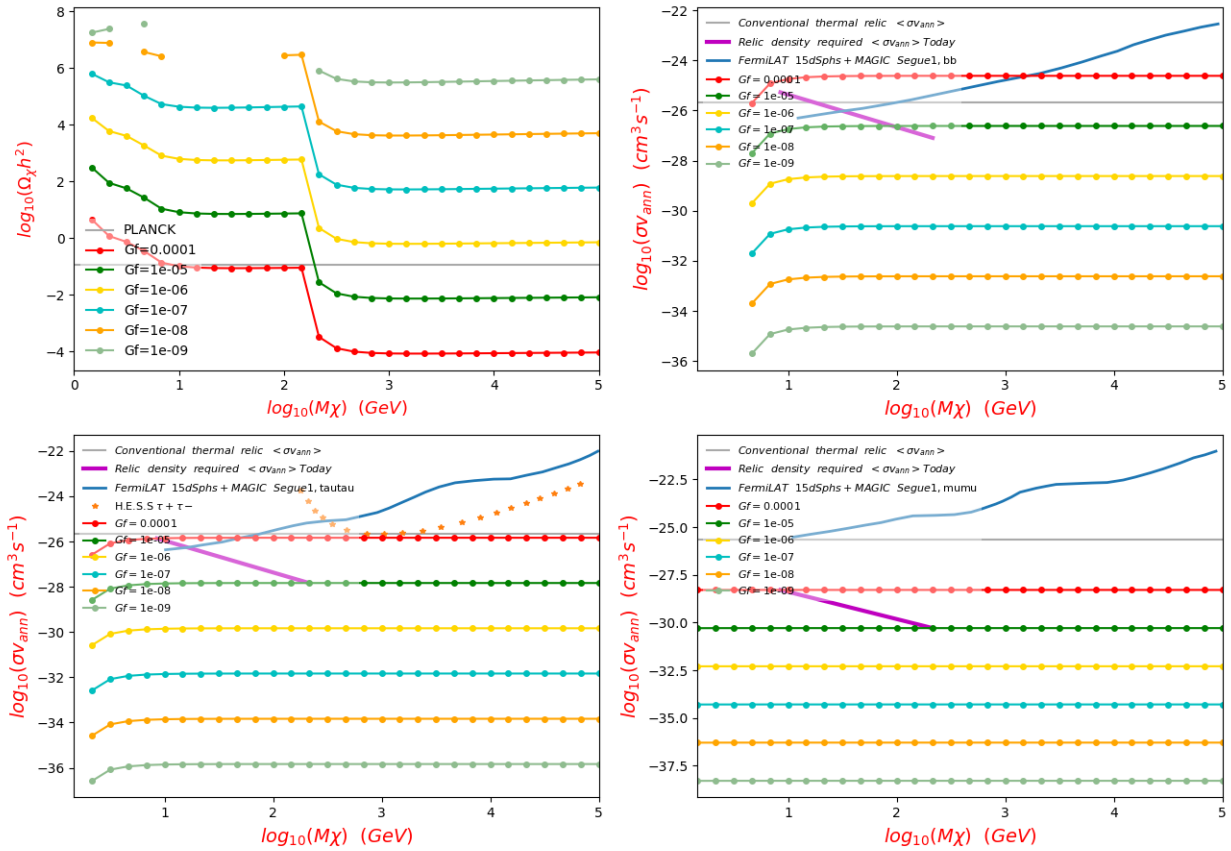

Scalar DM annihilation
via Scalar operator
with Yukawa like coupling

Fig. top left: $log_{10}(\Omega_\chi h^2)$ *VS* $log_{10}(M_\chi)$
Fig. top right: $b\bar{b}$ $log_{10}(\sigma v_{ann})$ *VS* $log_{10}(M_\chi)$
Fig. bottom left: $\tau^+\tau^-$ $log_{10}(\sigma v_{ann})$ *VS* $log_{10}(M_\chi)$
Fig. bottom right: $\mu^+\mu^-$ $log_{10}(\sigma v_{ann})$ *VS* $log_{10}(M_\chi)$

Figure 43: For scalar Dark Matter annihilation via a scalar operator with Yukawalike coupling, the relic density required Dark Matter mass m_χ and coupling constant G_f are shown on the top left panel. If Dark Matter annihilates purely to one final state, the maximal $\langle\sigma v\rangle_{anni}$ to 3 final state particles are shown respectively from top middle to bottom left: $\bar{b}b$, $\tau^+\tau^-$, $\mu^+\mu^-$. The constraints are from the observations of dSphs by FermiLAT and MAGIC [203], and the observation of the galactic halo with H.E.S.S [174]. The gray horizontal line is the conventional $\langle\sigma v\rangle_{anni} = 2.7 \cdot 10^{-26}\, cm^3 s^{-1}$ at the freeze-out moment, the $\langle\sigma v\rangle_{anni}$ it can produce today into each channel is shown as the violet curve (for $v = 220\, km/s$). It is sensitive only in the final state with heavy particles. See Table 12 for more explanation.

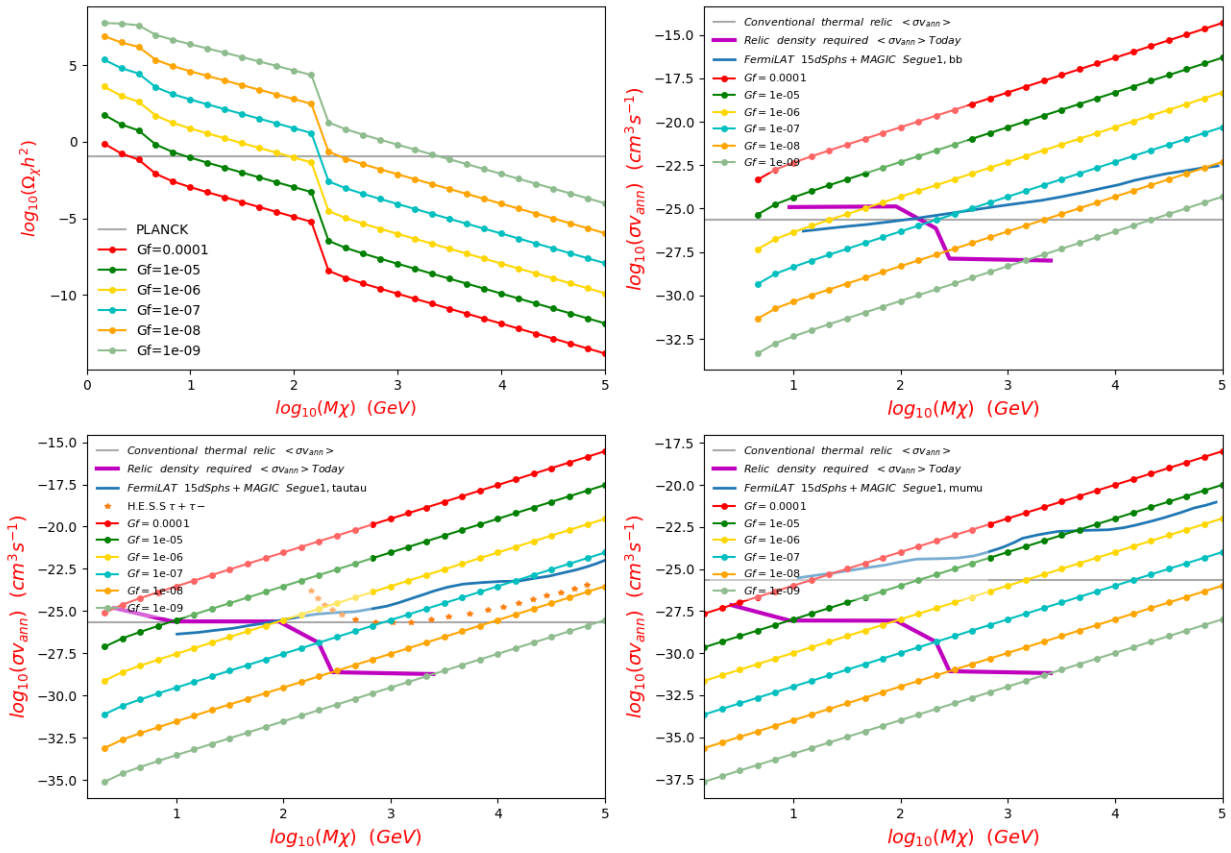

Fermion DM annihilation
via a pseudoscalar operator
with Yukawa like coupling

Fig. top left: $log_{10}(\Omega_\chi h^2)$ *VS* $log_{10}(M_\chi)$

Fig. top right: $b\bar{b}$ $log_{10}(\sigma v_{ann})$ *VS* $log_{10}(M_\chi)$

Fig. bottom left: $\tau^+\tau^-$ $log_{10}(\sigma v_{ann})$ *VS* $log_{10}(M_\chi)$

Fig. bottom right: $\mu^+\mu^-$ $log_{10}(\sigma v_{ann})$ *VS* $log_{10}(M_\chi)$

Figure 44: For fermion Dark Matter annihilation via a pseudoscalar operator with universal coupling, the relic density required Dark Matter mass m_χ and coupling constant G_f are shown on the top left panel. If Dark Matter annihilates purely to one final state, the maximal $\langle\sigma v\rangle_{anni}$ to 3 final state particles are respectively shown from top middle to bottom left: $\bar{b}b$, $\tau^+\tau^-$, $\mu^+\mu^-$. The constraints are from the observations of dSphs by FermiLAT and MAGIC [203], and the observation of the galactic halo with H.E.S.S [174]. The gray horizontal line is the conventional $\langle\sigma v\rangle_{anni} = 2.7 \cdot 10^{-26} cm^3 s^{-1}$ at the freeze-out moment, the $\langle\sigma v\rangle_{anni}$ it can produce today into each channel is shown as the violet curve (for $v = 220\, km/s$). See Table 12 for more explanation.

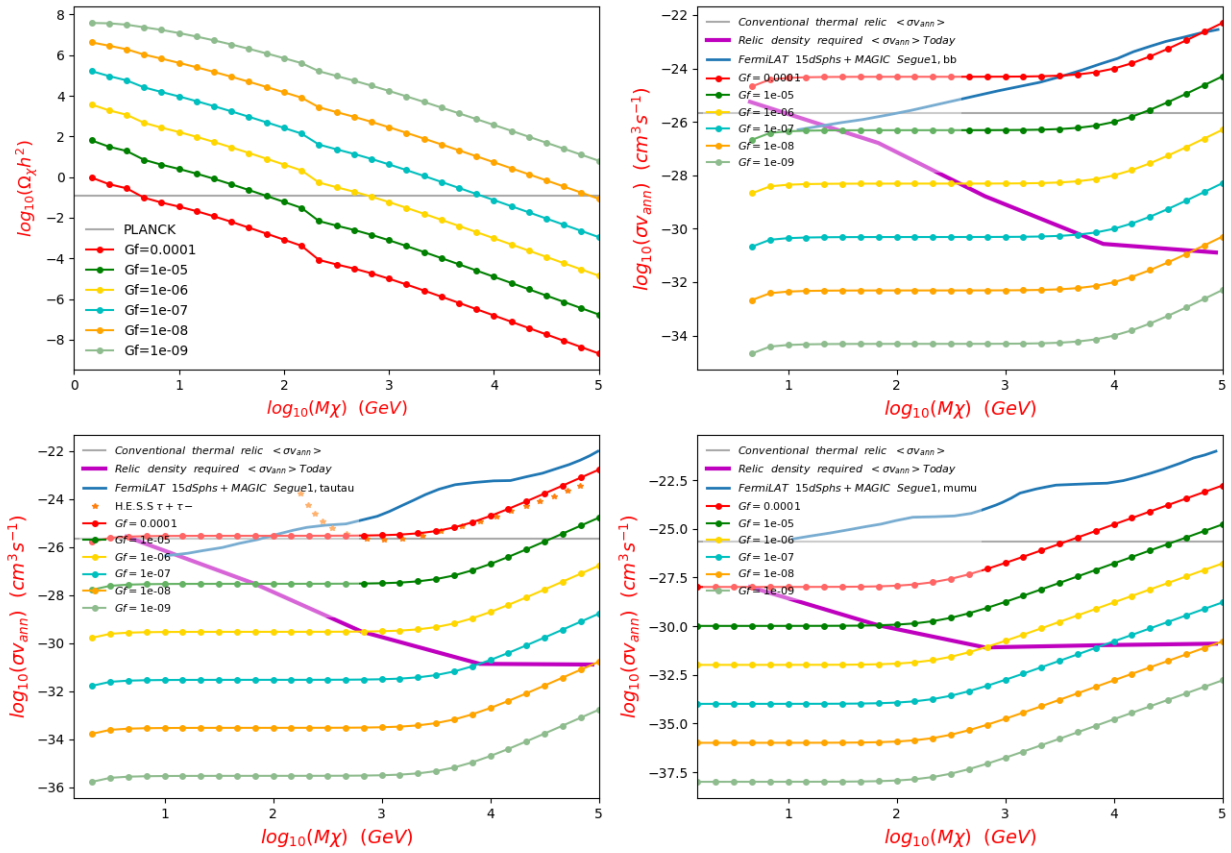

Fermion DM annihilation
via an Axialvector operator
with universal coupling

Fig. top left: $log_{10}(\Omega_\chi h^2)$ *VS* $log_{10}(M_\chi)$
Fig. top right: $b\bar{b}$ $log_{10}(\sigma v_{ann})$ *VS* $log_{10}(M_\chi)$
Fig. bottom left: $\tau^+\tau^-$ $log_{10}(\sigma v_{ann})$ *VS* $log_{10}(M_\chi)$
Fig. bottom right: $\mu^+\mu^-$ $log_{10}(\sigma v_{ann})$ *VS* $log_{10}(M_\chi)$

Figure 45: For fermion Dark Matter annihilation via an axial-vector operator with universal coupling, the relic density required Dark Matter mass m_χ and coupling constant G_f are shown on the top left panel. If Dark Matter annihilates purely to one final state, the maximal $\langle\sigma v\rangle_{anni}$ to 3 final state particles are respectively shown from top middle to bottom left: $\bar{b}b$, $\tau^+\tau^-$, $\mu^+\mu^-$. The constraints are from the observations of dSphs by FermiLAT and MAGIC [203], and the observation of the galactic halo with H.E.S.S [174]. The gray horizontal line is the conventional $\langle\sigma v\rangle_{anni} = 2.7 \cdot 10^{-26} cm^3 s^{-1}$ at the freeze-out moment, the $\langle\sigma v\rangle_{anni}$ it can produce today into each channel is shown as the violet curve (for $v = 220\, km/s$). See Table 12 for more explanation.

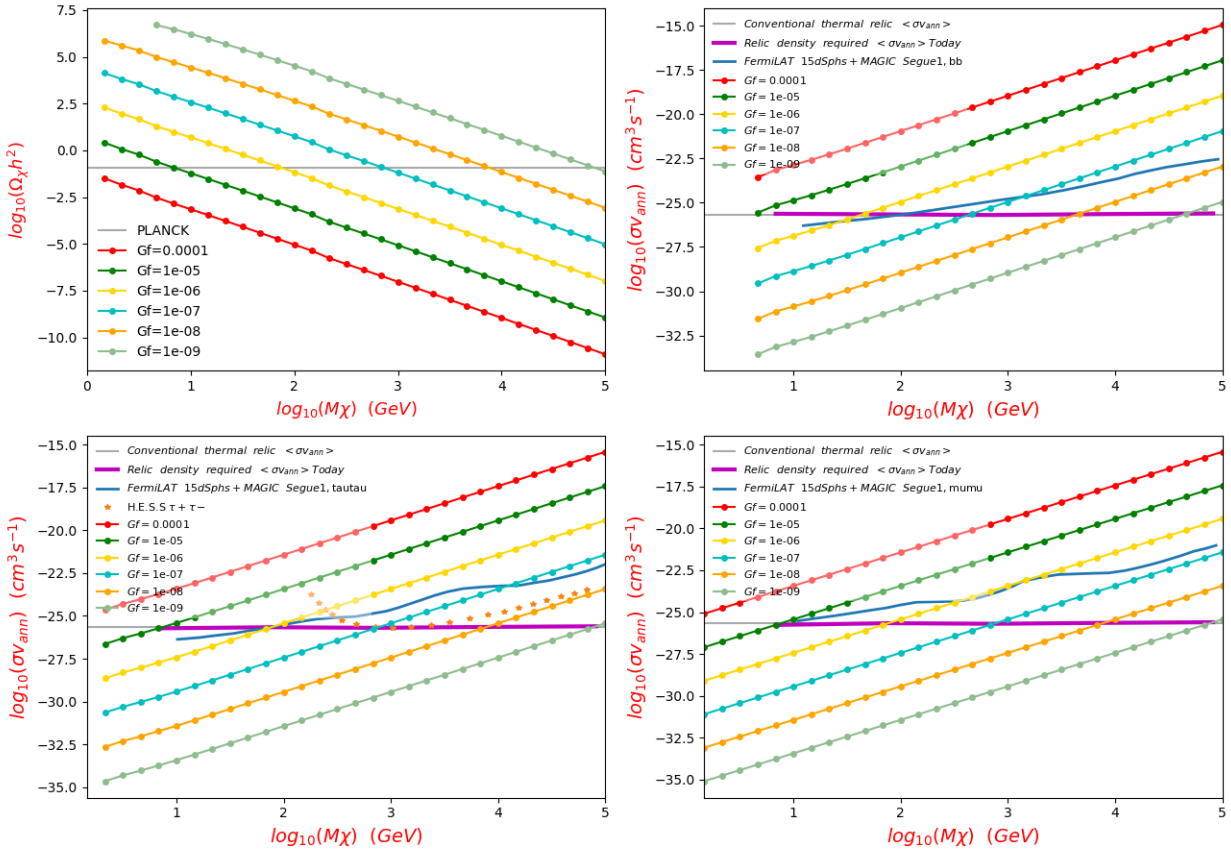

Fermion DM annihilation
via a Tensor operator
with universal coupling

Fig. top left: $log_{10}(\Omega_\chi h^2)$ *VS* $log_{10}(M_\chi)$
Fig. top right: $b\bar{b}$ $log_{10}(\sigma v_{ann})$ *VS* $log_{10}(M_\chi)$
Fig. bottom left: $\tau^+\tau^-$ $log_{10}(\sigma v_{ann})$ *VS* $log_{10}(M_\chi)$
Fig. bottom right: $\mu^+\mu^-$ $log_{10}(\sigma v_{ann})$ *VS* $log_{10}(M_\chi)$

Figure 46: For fermion Dark Matter annihilation via a tensor operator with universal coupling, the relic density required Dark Matter mass m_χ and coupling constant G_f are shown on the top left panel. If Dark Matter annihilates purely to one final state, the maximal $\langle\sigma v\rangle_{anni}$ to 3 final state particles are respectively shown from top middle to bottom left: $\bar{b}b$, $\tau^+\tau^-$, $\mu^+\mu^-$. The constraints are from the observations of dSphs by FermiLAT and MAGIC [203], and the observation of the galactic halo with H.E.S.S [174]. The gray horizontal line is the conventional $\langle\sigma v\rangle_{anni} = 2.7 \cdot 10^{-26}\, cm^3 s^{-1}$ at the freeze-out moment, the $\langle\sigma v\rangle_{anni}$ it can produce today into each channel is shown as the violet curve (for $v = 220\, km/s$). See Table 12 for more explanation.

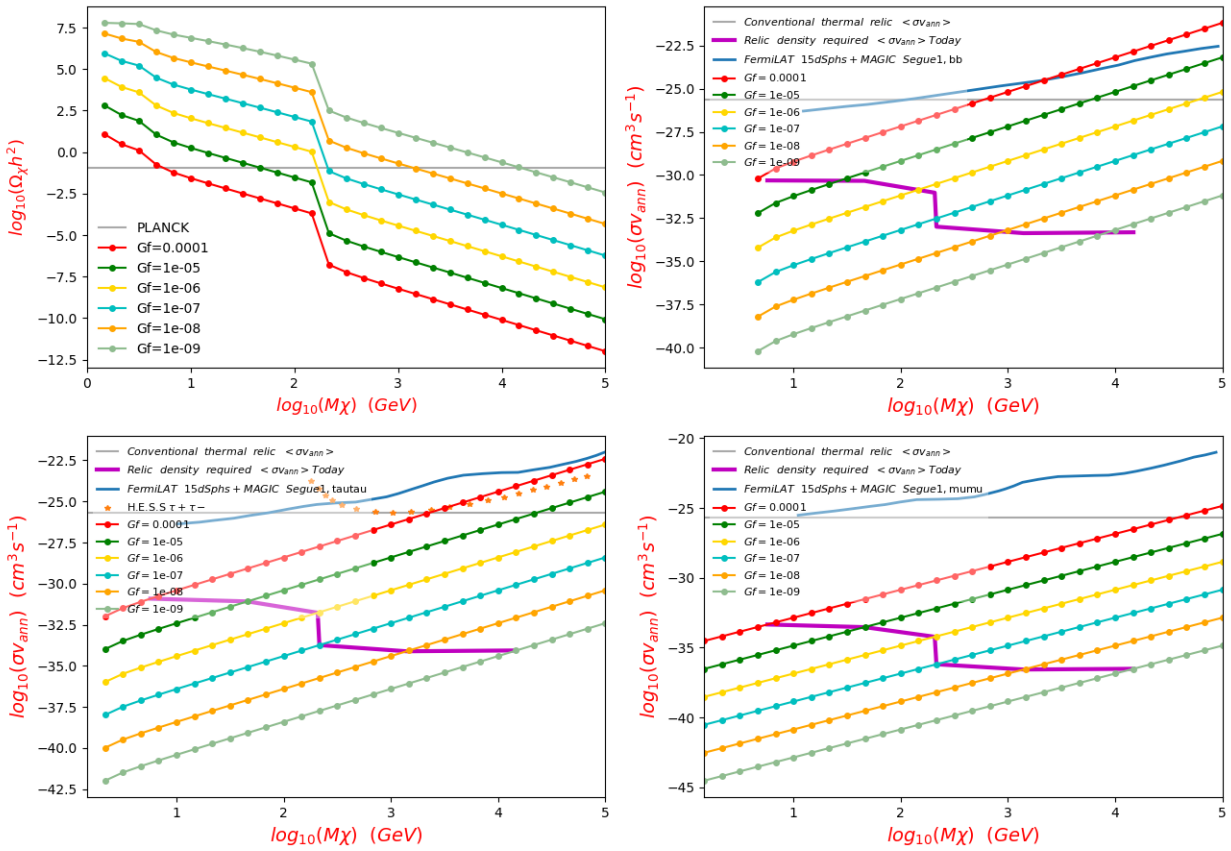

Fermion DM annihilation
via a Scalar-Pseudoscalar operator
with Yukawa like coupling

Fig. top left: $log_{10}(\Omega_\chi h^2)$ *VS* $log_{10}(M_\chi)$
Fig. top right: $b\bar{b}$ $log_{10}(\sigma v_{ann})$ *VS* $log_{10}(M_\chi)$
Fig. bottom left: $\tau^+\tau^-$ $log_{10}(\sigma v_{ann})$ *VS* $log_{10}(M_\chi)$
Fig. bottom right: $\mu^+\mu^-$ $log_{10}(\sigma v_{ann})$ *VS* $log_{10}(M_\chi)$

Figure 47: For fermion Dark Matter annihilation via a tensor operator with universal coupling, the relic density required Dark Matter mass m_χ and coupling constant G_f are shown on the top left panel. If Dark Matter annihilates purely to one final state, the maximal $\langle\sigma v\rangle_{anni}$ to 3 final state particles are respectively shown from top middle to bottom left: $\bar{b}b$, $\tau^+\tau^-$, $\mu^+\mu^-$. The constraints are from the observations of dSphs by FermiLAT and MAGIC [203], and the observation of the galactic halo with H.E.S.S [174]. The gray horizontal line is the conventional $\langle\sigma v\rangle_{anni} = 2.7 \cdot 10^{-26}\, cm^3 s^{-1}$ at the freeze-out moment, the $\langle\sigma v\rangle_{anni}$ it can produce today into each channel is shown as the violet curve (for $v = 220\, km/s$). See Table 12 for more explanation.

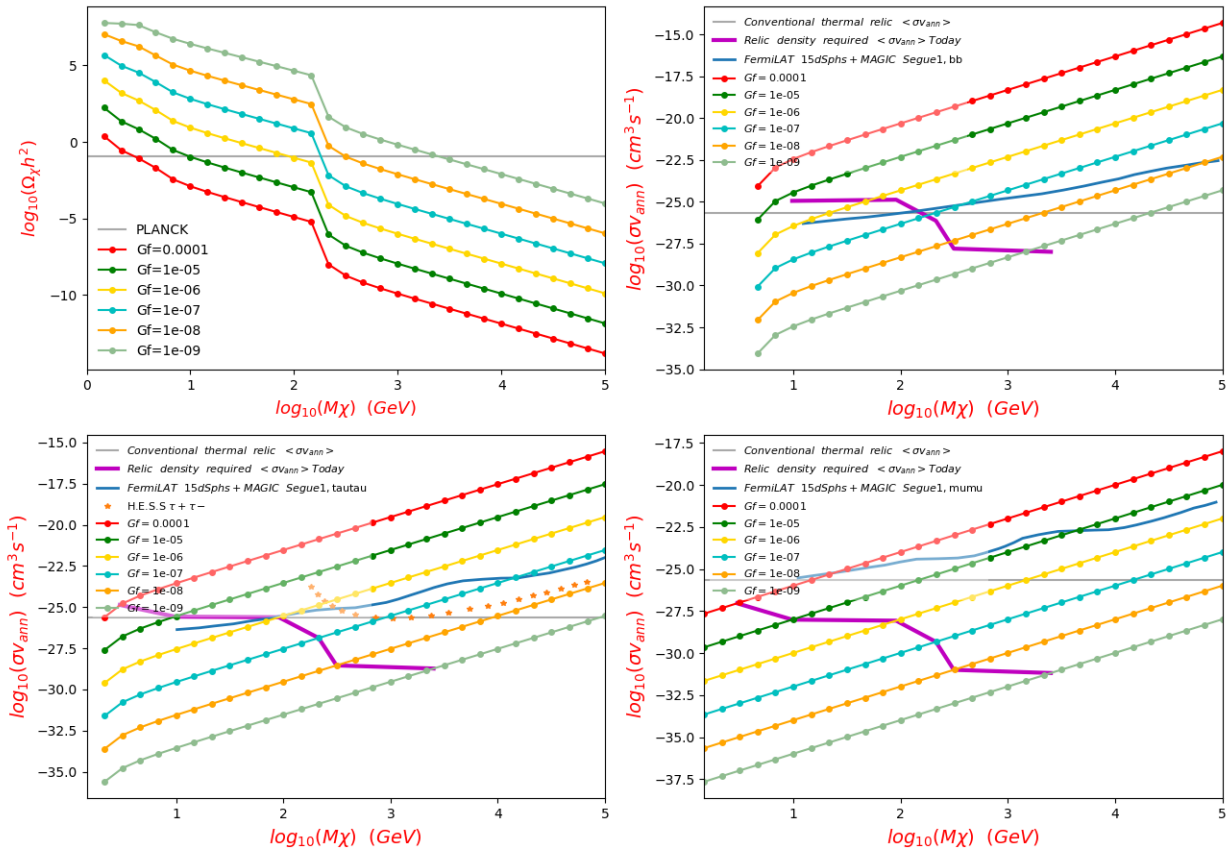

Fermion DM annihilation
via a Pseudoscalar-Scalar operator
with Yukawa like coupling

Fig. top left: $log_{10}(\Omega_\chi h^2)$ *VS* $log_{10}(M_\chi)$
Fig. top right: $b\bar{b}$ $log_{10}(\sigma v_{ann})$ *VS* $log_{10}(M_\chi)$
Fig. bottom left: $\tau^+\tau^-$ $log_{10}(\sigma v_{ann})$ *VS* $log_{10}(M_\chi)$
Fig. bottom right: $\mu^+\mu^-$ $log_{10}(\sigma v_{ann})$ *VS* $log_{10}(M_\chi)$

Figure 48: For fermion Dark Matter annihilation via a pseudoscalar-scalar operator with universal coupling, the relic density required Dark Matter mass m_χ and coupling constant G_f are shown on the top left panel. If Dark Matter annihilates purely to one final state, the maximal $\langle\sigma v\rangle_{anni}$ to 3 final state particles are respectively shown from top middle to bottom left: $\bar{b}b$, $\tau^+\tau^-$, $\mu^+\mu^-$. The constraints are from the observations of dSphs by FermiLAT and MAGIC [203], and the observation of the galactic halo with H.E.S.S [174]. The gray horizontal line is the conventional $\langle\sigma v\rangle_{anni} = 2.7 \cdot 10^{-26}\, cm^3 s^{-1}$ at the freeze-out moment, the $\langle\sigma v\rangle_{anni}$ it can produce today into each channel is shown as the violet curve (for $v = 220\, km/s$). See Table 12 for more explanation.

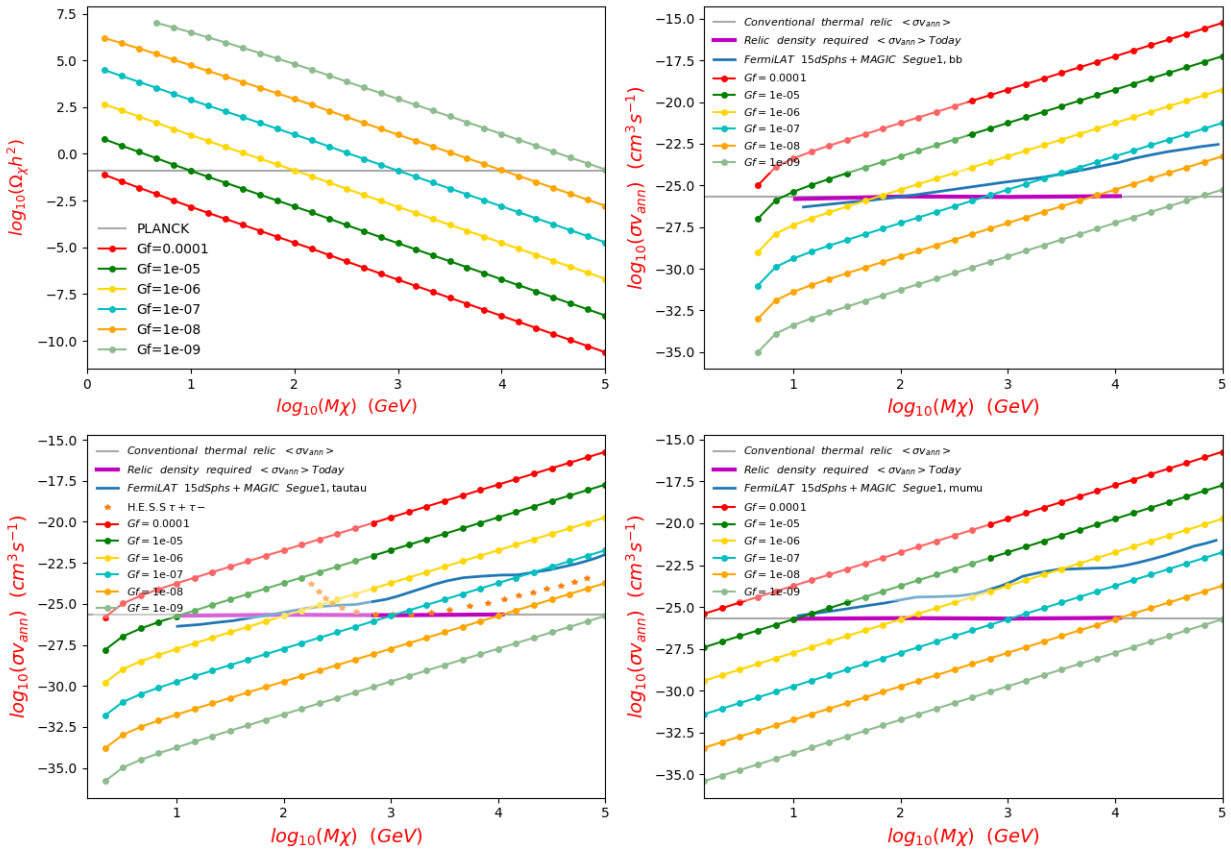

Fermion DM annihilation
via a Vector-Axialvector operator
with universal coupling

Fig. top left: $log_{10}(\Omega_\chi h^2)$ *VS* $log_{10}(M_\chi)$
Fig. top right: $b\bar{b}$ $log_{10}(\sigma v_{ann})$ *VS* $log_{10}(M_\chi)$
Fig. bottom left: $\tau^+\tau^-$ $log_{10}(\sigma v_{ann})$ *VS* $log_{10}(M_\chi)$
Fig. bottom right: $\mu^+\mu^-$ $log_{10}(\sigma v_{ann})$ *VS* $log_{10}(M_\chi)$

Figure 49: For fermion Dark Matter annihilation via a vector-axialvector operator with universal coupling, the relic density required Dark Matter mass m_χ and coupling constant G_f are shown on the top left panel. If Dark Matter annihilates purely to one final state, the maximal $\langle\sigma v\rangle_{anni}$ to 3 final state particles are respectively shown from top middle to bottom left: $\bar{b}b$, $\tau^+\tau^-$, $\mu^+\mu^-$. The constraints are from the observations of dSphs by FermiLAT and MAGIC [203], and the observation of the galactic halo with H.E.S.S [174]. The gray horizontal line is the conventional $\langle\sigma v\rangle_{anni} = 2.7 \cdot 10^{-26}\, cm^3 s^{-1}$ at the freeze-out moment, the $\langle\sigma v\rangle_{anni}$ it can produce today into each channel is shown as the violet curve (for $v = 220\, km/s$). See Table 12 for more explanation.

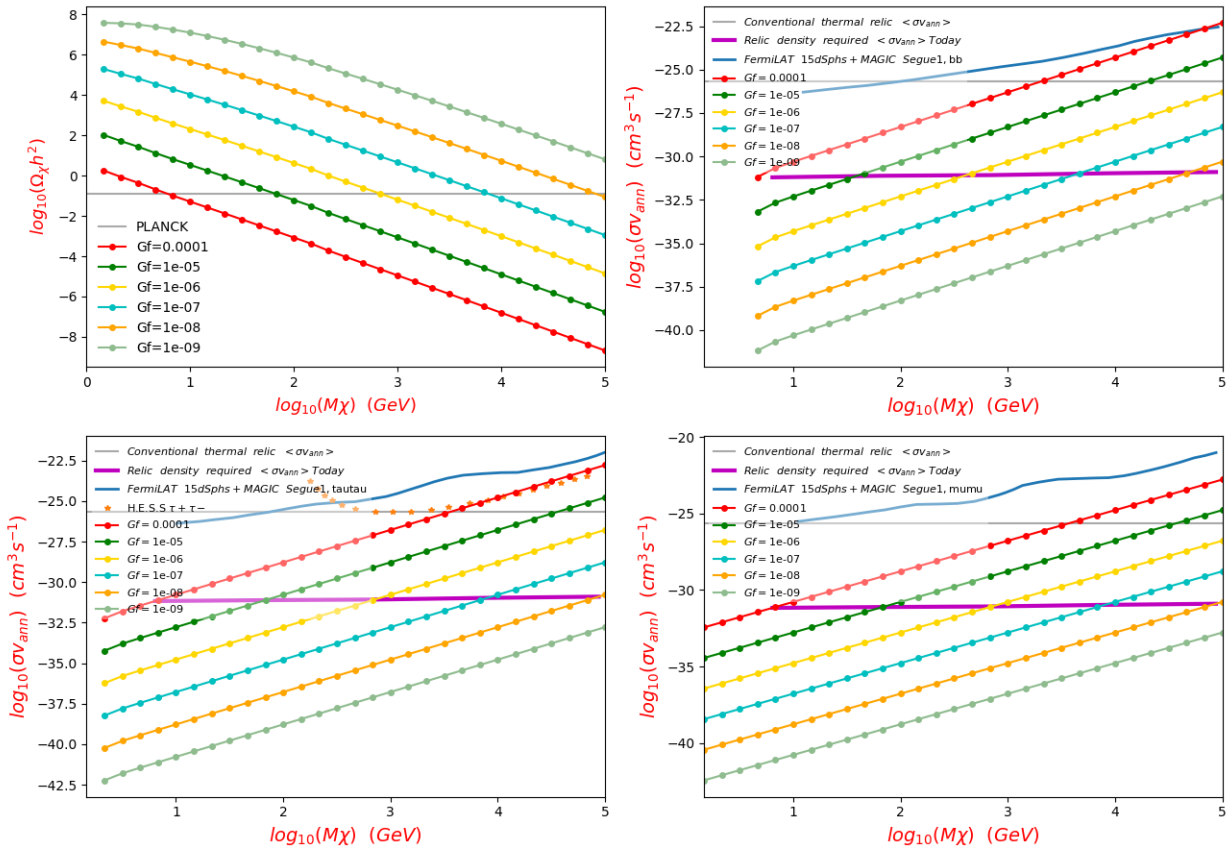

Fermion DM annihilation
via a Axialvector-Vector operator
with universal coupling

Fig. top left: $log_{10}(\Omega_\chi h^2)$ *VS* $log_{10}(M_\chi)$
Fig. top right: $b\bar{b}$ $log_{10}(\sigma v_{ann})$ *VS* $log_{10}(M_\chi)$
Fig. bottom left: $\tau^+\tau^-$ $log_{10}(\sigma v_{ann})$ *VS* $log_{10}(M_\chi)$
Fig. bottom right: $\mu^+\mu^-$ $log_{10}(\sigma v_{ann})$ *VS* $log_{10}(M_\chi)$

Figure 50: For fermion Dark Matter annihilation via an axialvector-vector operator with universal coupling, the relic density required Dark Matter mass m_χ and coupling constant G_f are shown on the top left panel. If Dark Matter annihilates purely to one final state, the maximal $\langle\sigma v\rangle_{anni}$ to 3 final state particles are respectively shown from top middle to bottom left: $\bar{b}b$, $\tau^+\tau^-$, $\mu^+\mu^-$. The constraints are from the observations of dSphs by FermiLAT and MAGIC [203], and the observation of the galactic halo with H.E.S.S [174]. The gray horizontal line is the conventional $\langle\sigma v\rangle_{anni} = 2.7 \cdot 10^{-26} cm^3 s^{-1}$ at the freeze-out moment, the $\langle\sigma v\rangle_{anni}$ it can produce today into each channel is shown as the violet curve (for $v = 220\, km/s$). See Table 12 for more explanation.

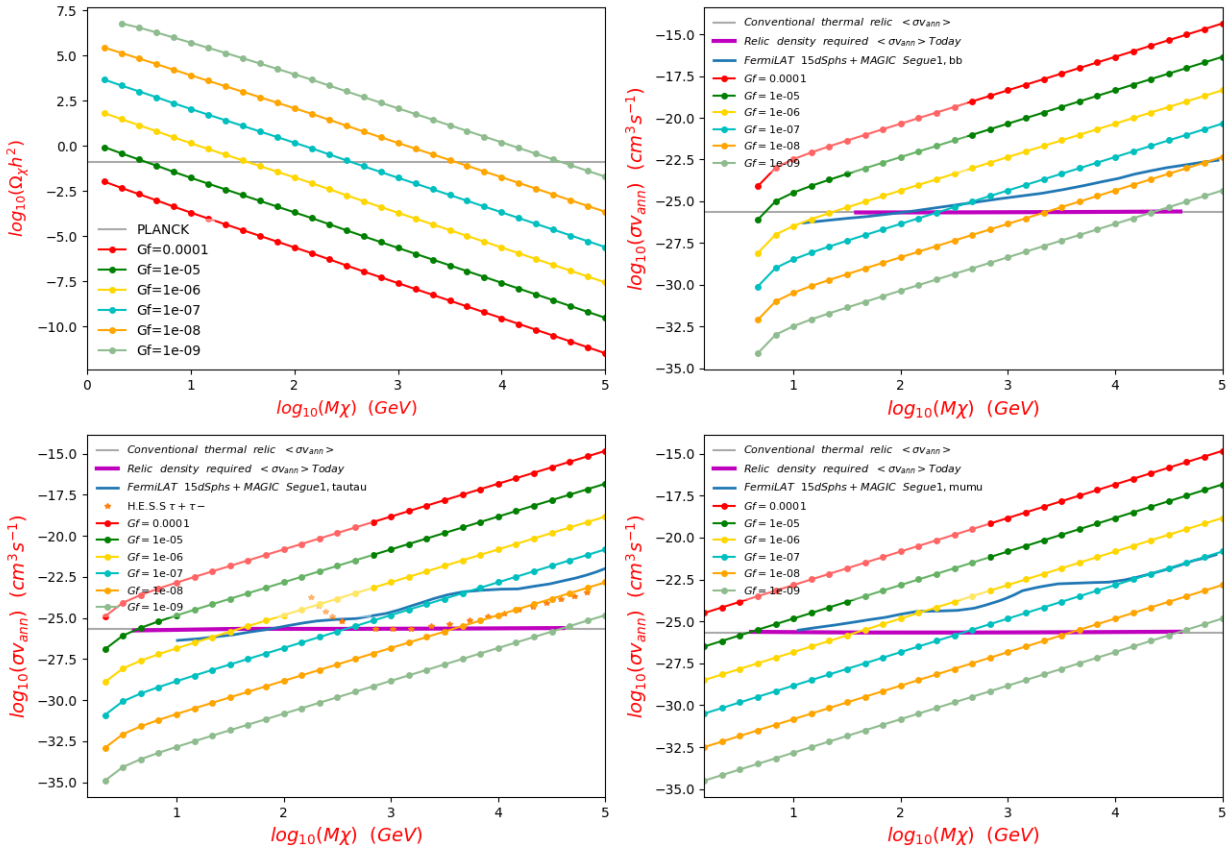

Fermion DM annihilation
via an Alternative tensor operator
with universal coupling

Fig. top left: $log_{10}(\Omega_\chi h^2)$ *VS* $log_{10}(M_\chi)$
Fig. top right: $b\bar{b}$ $log_{10}(\sigma v_{ann})$ *VS* $log_{10}(M_\chi)$
Fig. bottom left: $\tau^+\tau^-$ $log_{10}(\sigma v_{ann})$ *VS* $log_{10}(M_\chi)$
Fig. bottom right: $\mu^+\mu^-$ $log_{10}(\sigma v_{ann})$ *VS* $log_{10}(M_\chi)$

Figure 51: For fermion Dark Matter annihilation via an alternative tensor operator with universal coupling, the relic density required Dark Matter mass m_χ and coupling constant G_f are shown on the top left panel. If Dark Matter annihilates purely to one final state, the maximal $\langle\sigma v\rangle_{anni}$ to 3 final state particles are respectively shown from top middle to bottom left: $\bar{b}b$, $\tau^+\tau^-$, $\mu^+\mu^-$. The constraints are from the observations of dSphs by FermiLAT and MAGIC [203], and the observation of the galactic halo with H.E.S.S [174]. The gray horizontal line is the conventional $\langle\sigma v\rangle_{anni} = 2.7 \cdot 10^{-26} cm^3 s^{-1}$ at the freeze-out moment, the $\langle\sigma v\rangle_{anni}$ it can produce today into each channel is shown as the violet curve (for $v = 220\, km/s$). See Table 12 for more explanation.

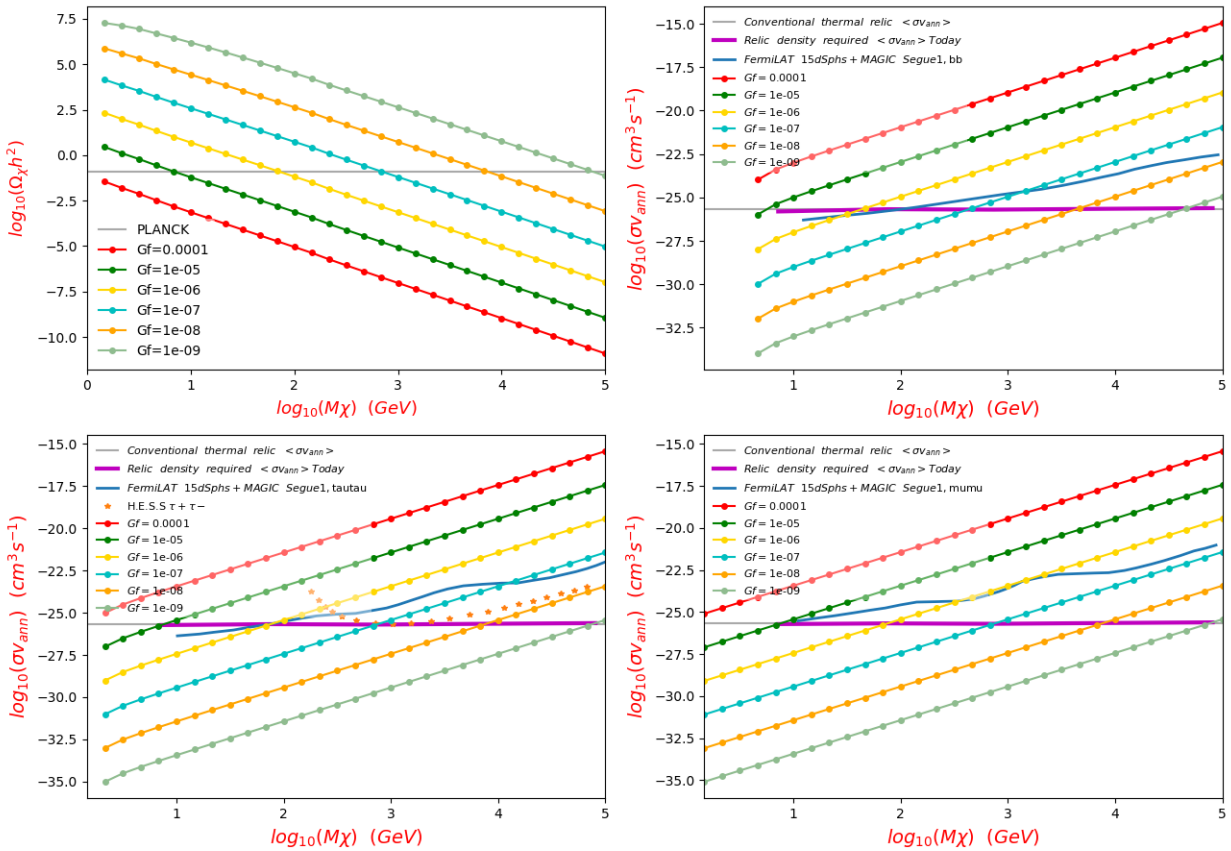

Fermion DM annihilation
via a Chiral operator
with universal coupling

Fig. top left: $log_{10}(\Omega_\chi h^2)$ *VS* $log_{10}(M_\chi)$
Fig. top right: $b\bar{b}$ $log_{10}(\sigma v_{ann})$ *VS* $log_{10}(M_\chi)$
Fig. bottom left: $\tau^+\tau^-$ $log_{10}(\sigma v_{ann})$ *VS* $log_{10}(M_\chi)$
Fig. bottom right: $\mu^+\mu^-$ $log_{10}(\sigma v_{ann})$ *VS* $log_{10}(M_\chi)$

Figure 52: For fermion Dark Matter annihilation via a chiral operator with universal coupling, the relic density required Dark Matter mass m_χ and coupling constant G_f are shown on the top left panel. If Dark Matter annihilates purely to one final state, the maximal $\langle\sigma v\rangle_{anni}$ to 3 final state particles are respectively shown from top middle to bottom left: $\bar{b}b$, $\tau^+\tau^-$, $\mu^+\mu^-$. The constraints are from the observations of dSphs by FermiLAT and MAGIC [203], and the observation of the galactic halo with H.E.S.S [174]. The gray horizontal line is the conventional $\langle\sigma v\rangle_{anni} = 2.7 \cdot 10^{-26}\, cm^3 s^{-1}$ at the freeze-out moment, the $\langle\sigma v\rangle_{anni}$ it can produce today into each channel is shown as the violet curve (for $v = 220\, km/s$). See Table 12 for more explanation.

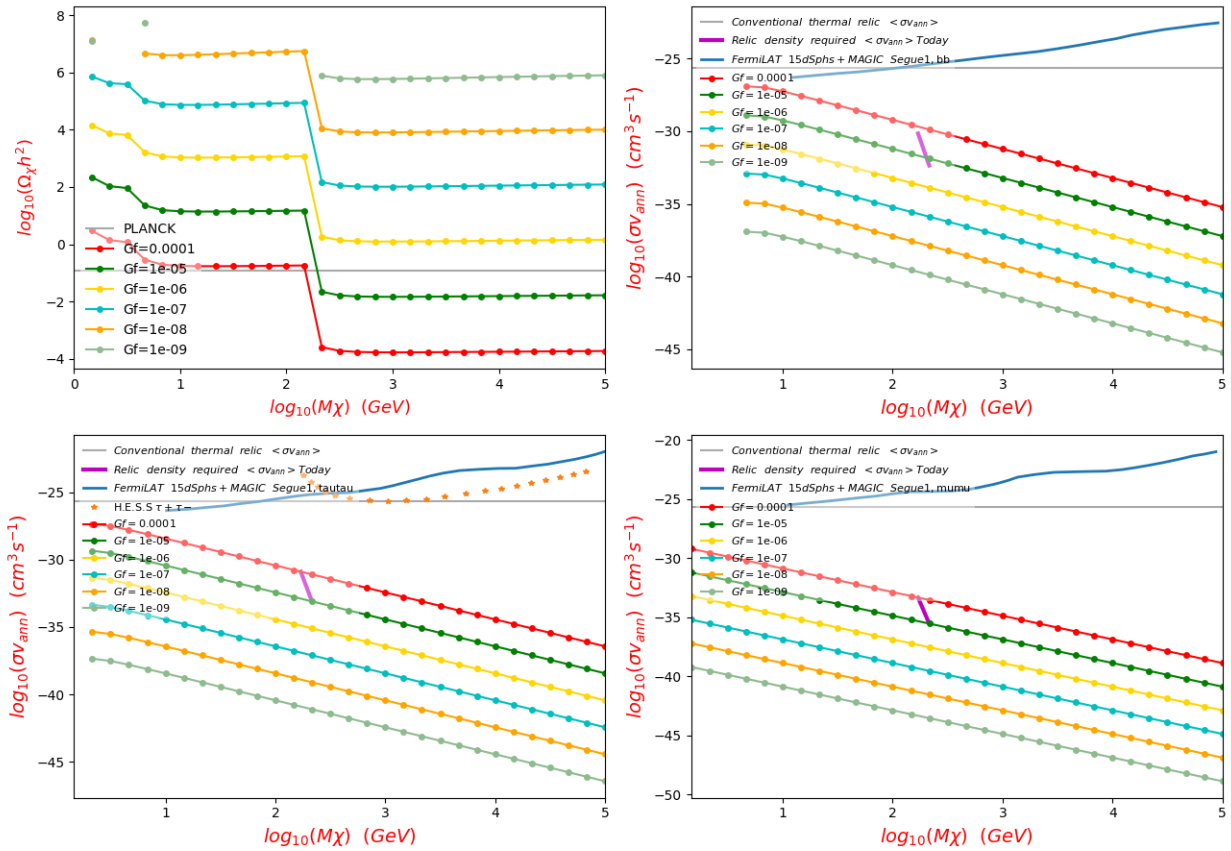

Scalar DM annihilation
via a Scalar-Pseudoscalar operator
with Yukawa like coupling

Fig. top left: $log_{10}(\Omega_\chi h^2)$ *VS* $log_{10}(M_\chi)$
Fig. top right: $b\bar{b}$ $log_{10}(\sigma v_{ann})$ *VS* $log_{10}(M_\chi)$
Fig. bottom left: $\tau^+\tau^-$ $log_{10}(\sigma v_{ann})$ *VS* $log_{10}(M_\chi)$
Fig. bottom right: $\mu^+\mu^-$ $log_{10}(\sigma v_{ann})$ *VS* $log_{10}(M_\chi)$

Figure 53: For scalar Dark Matter annihilation via a scalar-pseudoscalar tensor operator with universal coupling, the relic density required Dark Matter mass m_χ and coupling constant G_f are shown on the top left panel. If Dark Matter annihilates purely to one final state, the maximal $\langle\sigma v\rangle_{anni}$ to 3 final state particles are respectively shown from top middle to bottom left: $\bar{b}b$, $\tau^+\tau^-$, $\mu^+\mu^-$. The constraints are from the observations of dSphs by FermiLAT and MAGIC [203], and the observation of the galactic halo with H.E.S.S [174]. The gray horizontal line is the conventional $\langle\sigma v\rangle_{anni} = 2.7 \cdot 10^{-26}\, cm^3 s^{-1}$ at the freeze-out moment, the $\langle\sigma v\rangle_{anni}$ it can produce today into each channel is shown as the violet curve (for $v = 220\, km/s$). See Table 12 for more explanation.

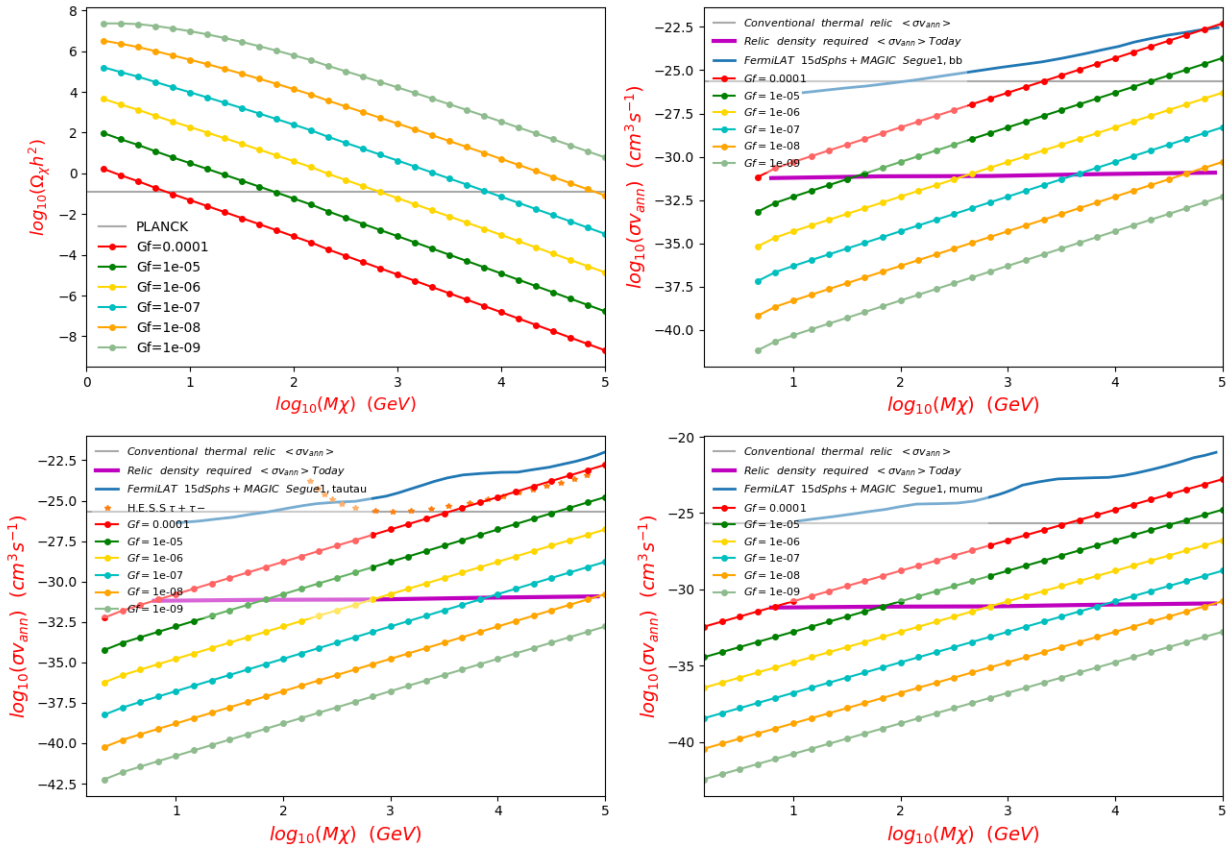

Scalar DM annihilation
via a Vector operator
with universal coupling

Fig. top left: $log_{10}(\Omega_\chi h^2)$ *VS* $log_{10}(M_\chi)$
Fig. top right: $b\bar{b}$ $log_{10}(\sigma v_{ann})$ *VS* $log_{10}(M_\chi)$
Fig. bottom left: $\tau^+\tau^-$ $log_{10}(\sigma v_{ann})$ *VS* $log_{10}(M_\chi)$
Fig. bottom right: $\mu^+\mu^-$ $log_{10}(\sigma v_{ann})$ *VS* $log_{10}(M_\chi)$

Figure 54: For scalar Dark Matter annihilation via a vector tensor operator with universal coupling, the relic density required Dark Matter mass m_χ and coupling constant G_f are shown on the top left panel. If Dark Matter annihilates purely to one final state, the maximal $\langle\sigma v\rangle_{anni}$ to 3 final state particles are respectively shown from top middle to bottom left: $\bar{b}b$, $\tau^+\tau^-$, $\mu^+\mu^-$. The constraints are from the observations of dSphs by FermiLAT and MAGIC [203], and the observation of the galactic halo with H.E.S.S [174]. The gray horizontal line is the conventional $\langle\sigma v\rangle_{anni} = 2.7 \cdot 10^{-26} cm^3 s^{-1}$ at the freeze-out moment, the $\langle\sigma v\rangle_{anni}$ it can produce today into each channel is shown as the violet curve (for $v = 220\, km/s$). See Table 12 for more explanation.

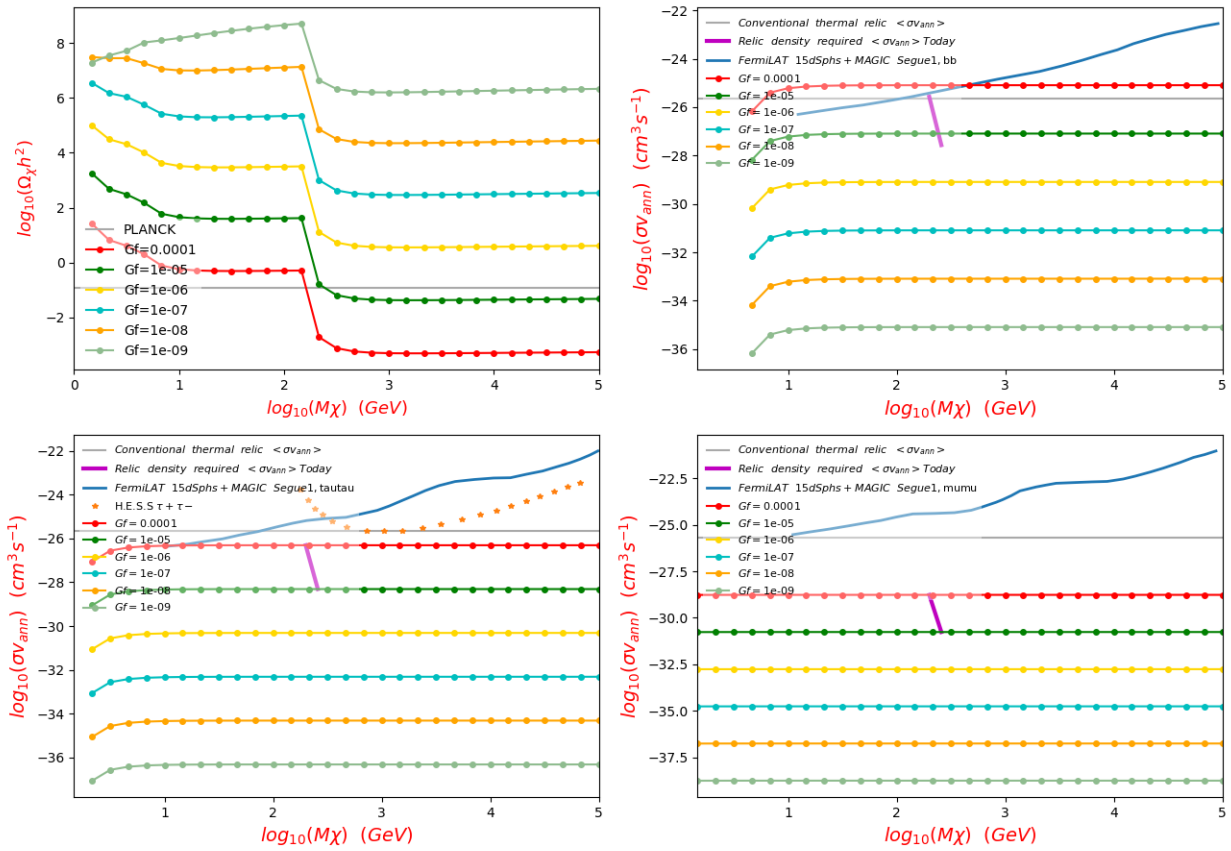

Vector DM annihilation
via a Scalar operator
with Yukawa like coupling

Fig. top left: $log_{10}(\Omega_\chi h^2)$ *VS* $log_{10}(M_\chi)$
Fig. top right: $b\bar{b}$ $log_{10}(\sigma v_{ann})$ *VS* $log_{10}(M_\chi)$
Fig. bottom left: $\tau^+\tau^-$ $log_{10}(\sigma v_{ann})$ *VS* $log_{10}(M_\chi)$
Fig. bottom right: $\mu^+\mu^-$ $log_{10}(\sigma v_{ann})$ *VS* $log_{10}(M_\chi)$

Figure 55: For vector Dark Matter annihilation via a scalar tensor operator with universal coupling, the relic density required Dark Matter mass m_χ and coupling constant G_f are shown on the top left panel. If Dark Matter annihilates purely to one final state, the maximal $\langle\sigma v\rangle_{anni}$ to 3 final state particles are respectively shown from top middle to bottom left: $\bar{b}b$, $\tau^+\tau^-$, $\mu^+\mu^-$. The constraints are from the observations of dSphs by FermiLAT and MAGIC [203], and the observation of the galactic halo with H.E.S.S [174]. The gray horizontal line is the conventional $\langle\sigma v\rangle_{anni} = 2.7 \cdot 10^{-26} cm^3 s^{-1}$ at the freeze-out moment, the $\langle\sigma v\rangle_{anni}$ it can produce today into each channel is shown as the violet curve (for $v = 220\, km/s$). See Table 12 for more explanation.

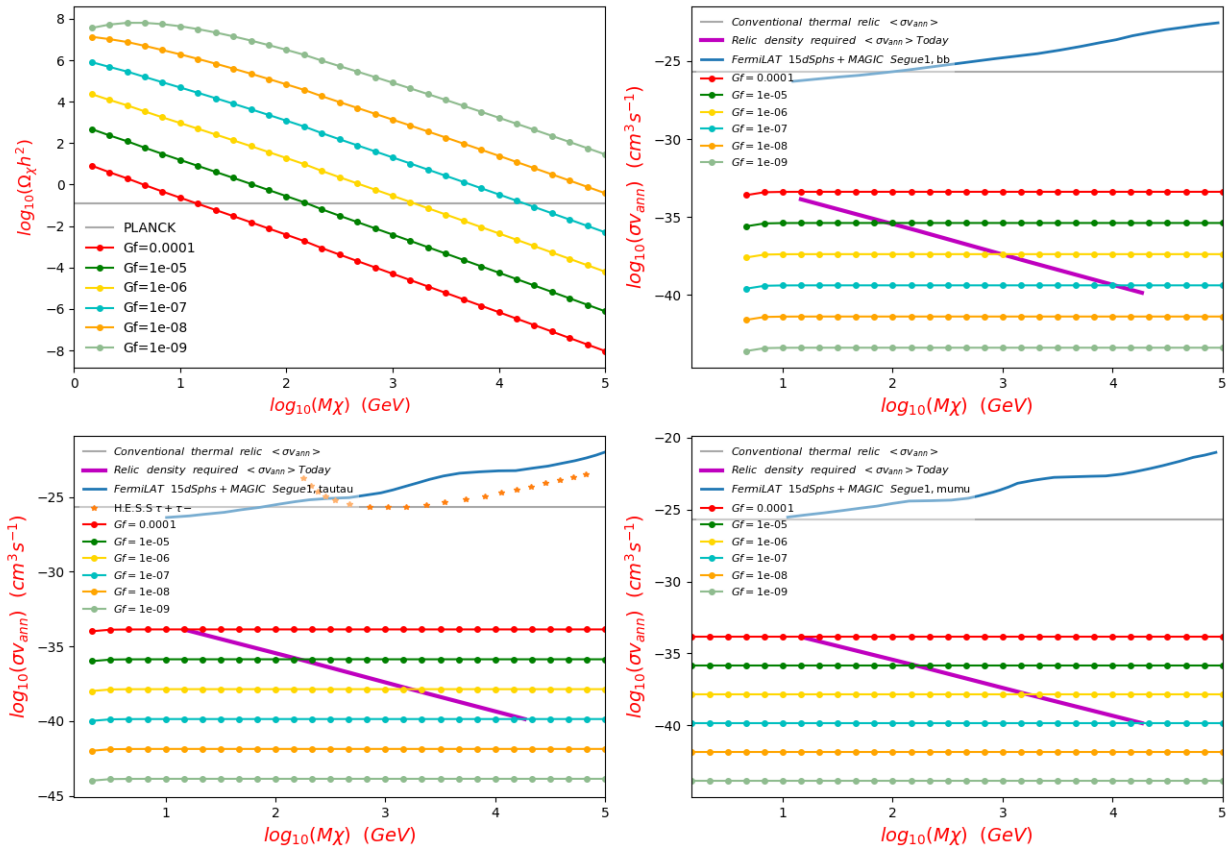

Vector DM annihilation
via a Vector operator
with universal coupling

Fig. top left: $log_{10}(\Omega_\chi h^2)$ *VS* $log_{10}(M_\chi)$
Fig. top right: $b\bar{b}$ $log_{10}(\sigma v_{ann})$ *VS* $log_{10}(M_\chi)$
Fig. bottom left: $\tau^+\tau^-$ $log_{10}(\sigma v_{ann})$ *VS* $log_{10}(M_\chi)$
Fig. bottom right: $\mu^+\mu^-$ $log_{10}(\sigma v_{ann})$ *VS* $log_{10}(M_\chi)$

Figure 56: For vector Dark Matter annihilation via a vector operator with universal coupling, the relic density required Dark Matter mass m_χ and coupling constant G_f are shown on the top left panel. If Dark Matter annihilates purely to one final state, the maximal $\langle\sigma v\rangle_{anni}$ to 3 final state particles are respectively shown from top middle to bottom left: $\bar{b}b$, $\tau^+\tau^-$, $\mu^+\mu^-$. The constraints are from the observations of dSphs by FermiLAT and MAGIC [203], and the observation of the galactic halo with H.E.S.S [174]. The gray horizontal line is the conventional $\langle\sigma v\rangle_{anni} = 2.7 \cdot 10^{-26}\, cm^3 s^{-1}$ at the freeze-out moment, the $\langle\sigma v\rangle_{anni}$ it can produce today into each channel is shown as the violet curve (for $v = 220\, km/s$). See Table 12 for more explanation.

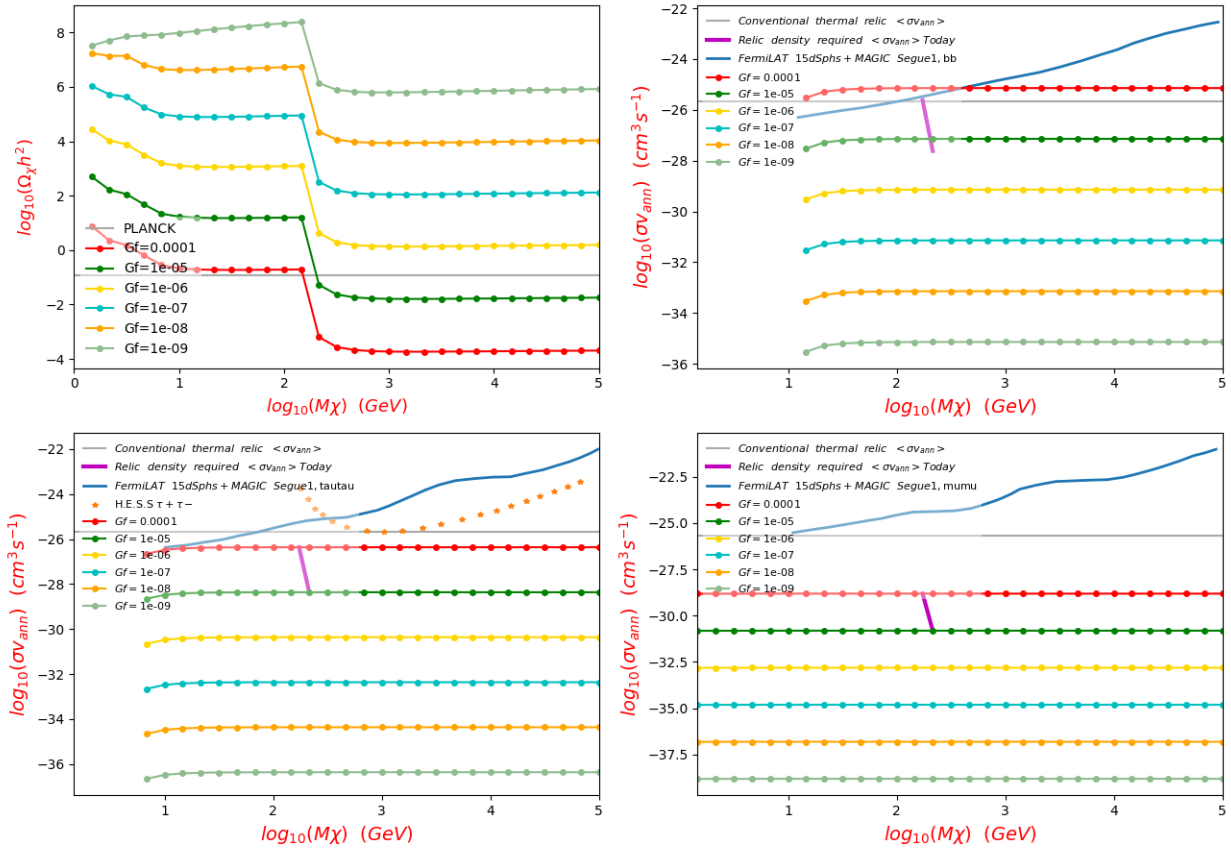

Vector DM annihilation
via a Tensor operator
with Yukawa like coupling

Fig. top left: $log_{10}(\Omega_\chi h^2)$ *VS* $log_{10}(M_\chi)$
Fig. top right: $b\bar{b}$ $log_{10}(\sigma v_{ann})$ *VS* $log_{10}(M_\chi)$
Fig. bottom left: $\tau^+\tau^-$ $log_{10}(\sigma v_{ann})$ *VS* $log_{10}(M_\chi)$
Fig. bottom right: $\mu^+\mu^-$ $log_{10}(\sigma v_{ann})$ *VS* $log_{10}(M_\chi)$

Figure 57: For vector Dark Matter annihilation via a tensor operator with universal coupling, the relic density required Dark Matter mass m_χ and coupling constant G_f are shown on the top left panel. If Dark Matter annihilates purely to one final state, the maximal $\langle\sigma v\rangle_{anni}$ to 3 final state particles are respectively shown from top middle to bottom left: $\bar{b}b$, $\tau^+\tau^-$, $\mu^+\mu^-$. The constraints are from the observations of dSphs by FermiLAT and MAGIC [203], and the observation of the galactic halo with H.E.S.S [174]. The gray horizontal line is the conventional $\langle\sigma v\rangle_{anni} = 2.7 \cdot 10^{-26}\, cm^3 s^{-1}$ at the freeze-out moment, the $\langle\sigma v\rangle_{anni}$ it can produce today into each channel is shown as the violet curve (for $v = 220\, km/s$). See Table 12 for more explanation.

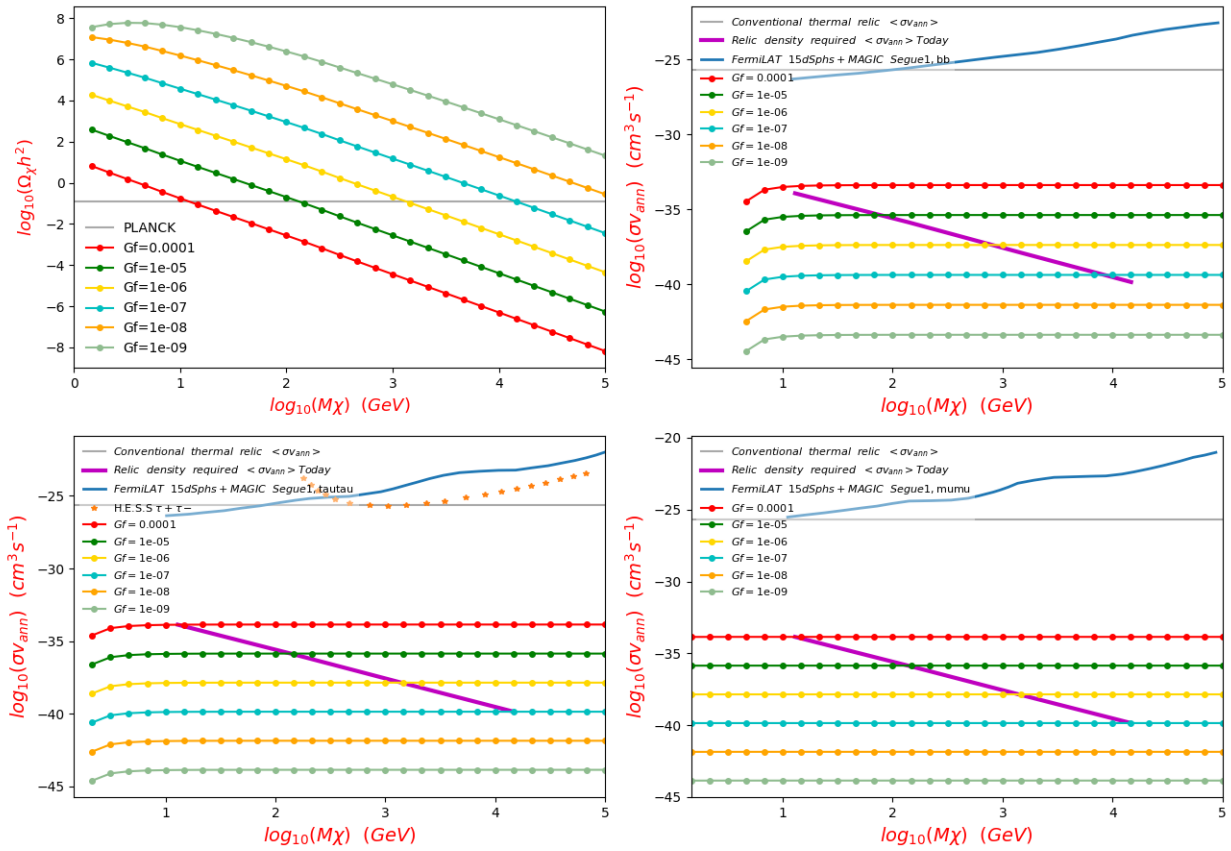

Vector DM annihilation
via a Vector-Axialvector operator
with universal coupling

Fig. top left: $log_{10}(\Omega_\chi h^2)$ *VS* $log_{10}(M_\chi)$
Fig. top right: $b\bar{b}$ $log_{10}(\sigma v_{ann})$ *VS* $log_{10}(M_\chi)$
Fig. bottom left: $\tau^+\tau^-$ $log_{10}(\sigma v_{ann})$ *VS* $log_{10}(M_\chi)$
Fig. bottom right: $\mu^+\mu^-$ $log_{10}(\sigma v_{ann})$ *VS* $log_{10}(M_\chi)$

Figure 58: For vector Dark Matter annihilation via a vector-axialvector operator with universal coupling, the relic density required Dark Matter mass m_χ and coupling constant G_f are shown on the top left panel. If Dark Matter annihilates purely to one final state, the maximal $\langle\sigma v\rangle_{anni}$ to 3 final state particles are respectively shown from top middle to bottom left: $\bar{b}b$, $\tau^+\tau^-$, $\mu^+\mu^-$. The constraints are from the observations of dSphs by FermiLAT and MAGIC [203], and the observation of the galactic halo with H.E.S.S [174]. The gray horizontal line is the conventional $\langle\sigma v\rangle_{anni} = 2.7 \cdot 10^{-26}\, cm^3 s^{-1}$ at the freeze-out moment, the $\langle\sigma v\rangle_{anni}$ it can produce today into each channel is shown as the violet curve (for $v = 220\, km/s$). See Table 12 for more explanation.

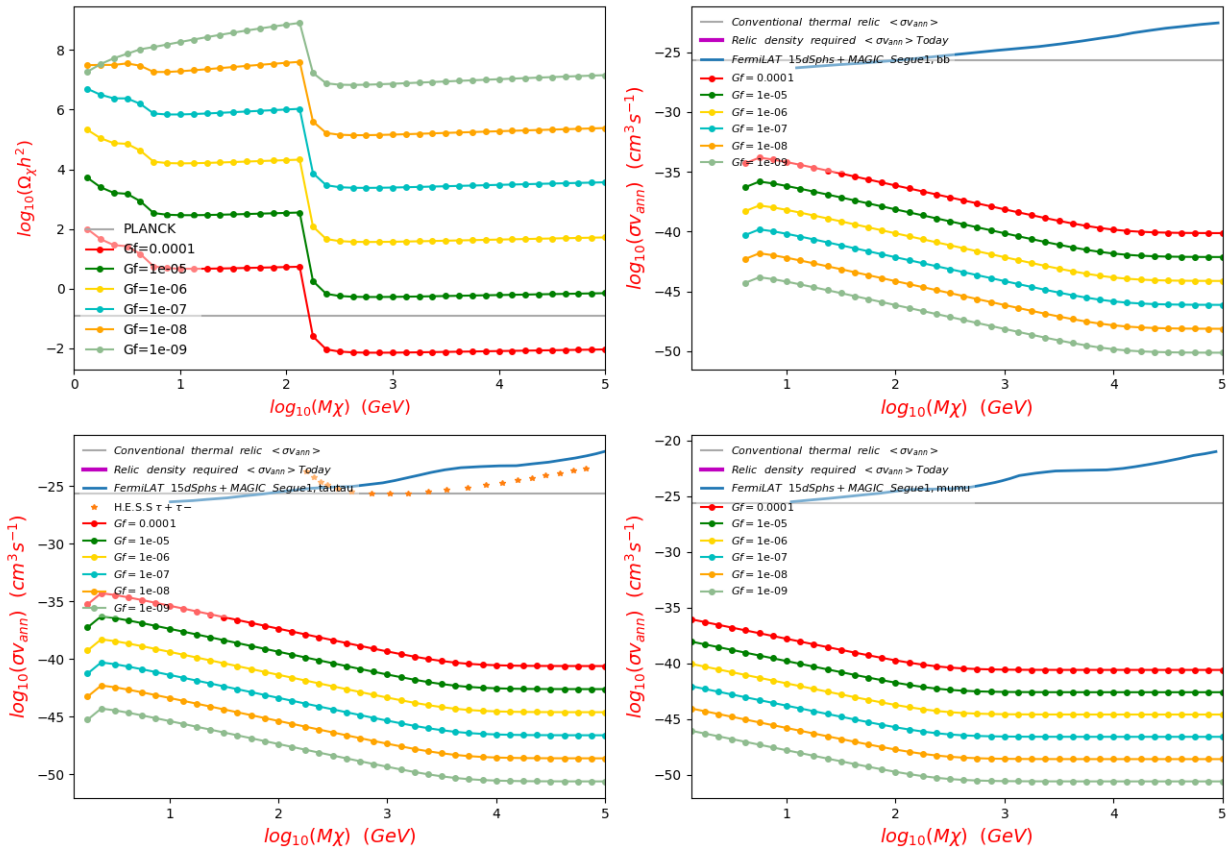

Vector DM annihilation
via an Alternative vector - Axialvector operator
with universal coupling

Fig. top left: $log_{10}(\Omega_\chi h^2)$ *VS* $log_{10}(M_\chi)$
Fig. top right: $b\bar{b}$ $log_{10}(\sigma v_{ann})$ *VS* $log_{10}(M_\chi)$
Fig. bottom left: $\tau^+\tau^-$ $log_{10}(\sigma v_{ann})$ *VS* $log_{10}(M_\chi)$
Fig. bottom right: $\mu^+\mu^-$ $log_{10}(\sigma v_{ann})$ *VS* $log_{10}(M_\chi)$

Figure 59: For vector Dark Matter annihilation via an alternative vector-axialvector operator with universal coupling, the relic density required Dark Matter mass m_χ and coupling constant G_f are shown on the top left panel. If Dark Matter annihilates purely to one final state, the maximal $\langle\sigma v\rangle_{anni}$ to 3 final state particles are respectively shown from top middle to bottom left: $\bar{b}b$, $\tau^+\tau^-$, $\mu^+\mu^-$. The constraints are from the observations of dSphs by FermiLAT and MAGIC [203], and the observation of the galactic halo with H.E.S.S [174]. The gray horizontal line is the conventional $\langle\sigma v\rangle_{anni} = 2.7 \cdot 10^{-26}\, cm^3 s^{-1}$ at the freeze-out moment, the $\langle\sigma v\rangle_{anni}$ it can produce today into each channel is shown as the violet curve (for $v = 220\, km/s$). See Table 12 for more explanation.

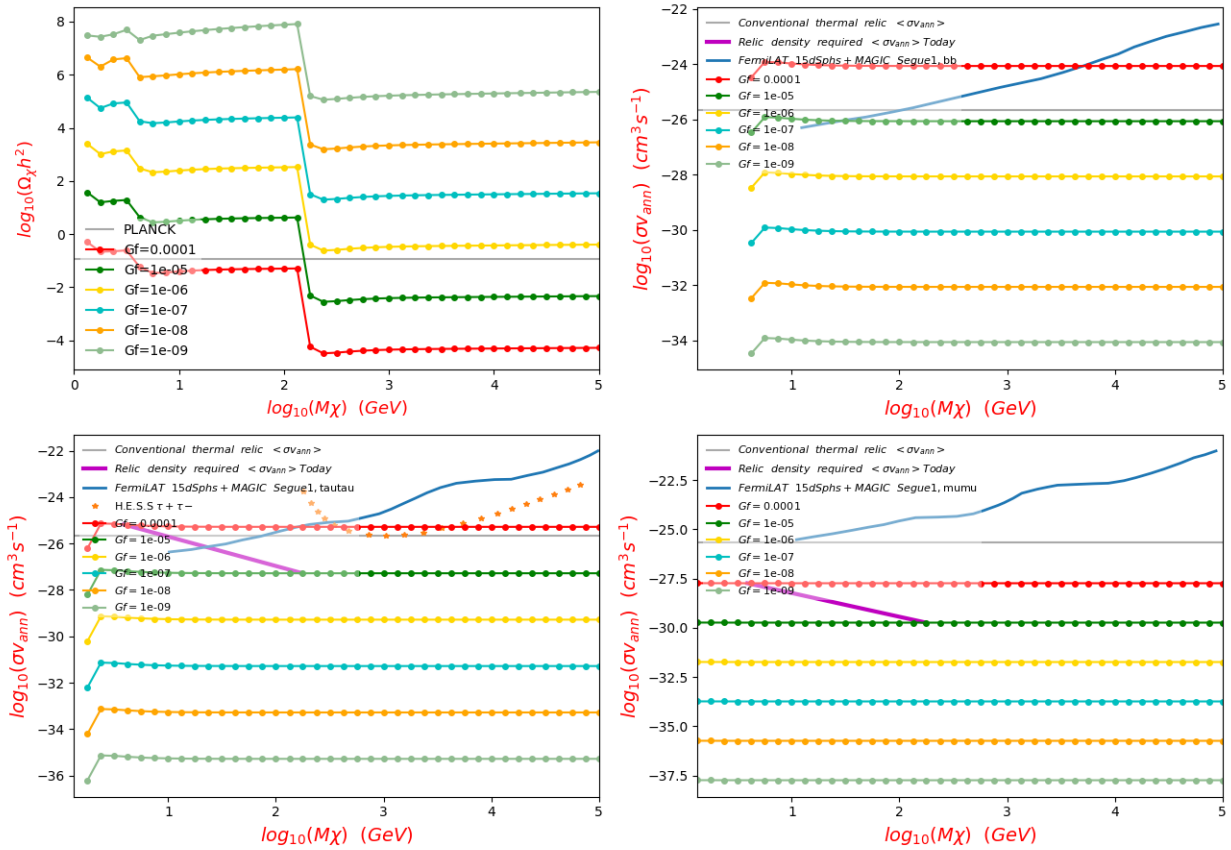

Vector DM annihilation
via an Alternative tensor operator
with Yukawa like coupling

Fig. top left: $log_{10}(\Omega_\chi h^2)$ *VS* $log_{10}(M_\chi)$
Fig. top right: $b\bar{b}$ $log_{10}(\sigma v_{ann})$ *VS* $log_{10}(M_\chi)$
Fig. bottom left: $\tau^+\tau^-$ $log_{10}(\sigma v_{ann})$ *VS* $log_{10}(M_\chi)$
Fig. bottom right: $\mu^+\mu^-$ $log_{10}(\sigma v_{ann})$ *VS* $log_{10}(M_\chi)$

Figure 60: For vector Dark Matter annihilation via an alternative tensor operator with universal coupling, the relic density required Dark Matter mass m_χ and coupling constant G_f are shown on the top left panel. If Dark Matter annihilates purely to one final state, the maximal $\langle\sigma v\rangle_{anni}$ to 3 final state particles are respectively shown from top middle to bottom left: $\bar{b}b$, $\tau^+\tau^-$, $\mu^+\mu^-$. The constraints are from the observations of dSphs by FermiLAT and MAGIC [203], and the observation of the galactic halo with H.E.S.S [174]. The gray horizontal line is the conventional $\langle\sigma v\rangle_{anni} = 2.7 \cdot 10^{-26}\, cm^3 s^{-1}$ at the freeze-out moment, the $\langle\sigma v\rangle_{anni}$ it can produce today into each channel is shown as the violet curve (for $v = 220\, km/s$). See Table 12 for more explanation.

Appendix C
Results and interpretations of the fit to the velocity dispersion data of the dSphs

$log_{10}(\rho_s)$	r_s[pc]	α	w	γ	r_a [pc]	δ	β_0	β_∞	χ^2
-1.968	1336.854	2.855	6.079	1.193	129.946	1.361	0.595	-2.792	26.206
-2.005	1486.827	3.000	6.011	1.244	129.946	1.361	0.595	-2.792	28.642
-2.074	1644.406	1.970	5.411	1.353	840.908	1.853	-1.856	-8.424	29.217
-1.526	931.379	1.055	3.679	1.362	823.639	1.227	-0.435	-5.961	29.784
-1.522	1070.139	2.215	6.817	0.984	999.339	1.068	-6.106	-4.502	30.948
-1.864	1292.984	1.124	5.794	1.476	798.711	0.628	-7.228	-2.781	31.266
-2.022	1436.807	1.429	4.904	1.501	105.199	1.347	-3.976	-3.406	32.878
-1.503	534.143	1.906	5.332	1.422	233.156	2.137	-1.369	-8.848	33.914
-0.855	1070.777	1.199	5.204	0.275	650.043	3.266	0.056	-6.134	34.989

Table 14: The best-fit parameters (d.o.f = 8) and χ^2 for the fit to the velocity dispersion data of the Draco dSph from Ref. [293]. Here the anisotropy profile is the Generalized Osipkov Merritt 3. It is obvious that γ is preferred to be larger than 1, so the Draco is more likely to be cuspy than cored.

$log_{10}(\rho_s)$	r_s[pc]	α	w	γ	r_a [pc]	δ	β_0	β_∞	χ^2
-1.901	1633.089	1.107	4.688	1.175	392.464	4.788	0.037	-1.839	6.910
-1.841	1633.049	1.752	3.685	1.178	629.995	4.215	-6.683	-3.411	9.311
-1.079	1548.446	1.522	3.082	0.420	294.873	3.951	-3.328	-0.219	10.348
-1.410	1224.484	1.132	4.846	0.885	479.488	4.932	-4.689	-5.861	12.474
-2.585	1549.947	2.092	6.166	1.837	281.025	2.828	-2.698	-4.689	13.474
-2.472	1215.701	2.912	4.132	1.553	152.569	3.769	0.004	-4.800	14.457
-2.241	1738.580	1.710	3.898	1.526	331.108	3.793	-8.230	-4.026	16.179
0.723	100.000	1.025	3.011	0.162	269.838	0.743	-0.667	-7.854	20.656
0.581	100.00	1.437	3.424	0.038	735.973	4.707	-5.089	-8.972	21.612

Table 15: The best-fit parameters (d.o.f = 6) and χ^2 for the fit to the velocity dispersion data of the Draco dSph from Ref. [117]. Here the anisotropy profile is the Generalized Osipkov Merritt 3. It is obvious that γ can be either very small or large, but the best fit is obtained for γ=1.175, which indicates a more cusp profile. γ=0.420 also pvovides a good fit, but it is also not cored.

$log_{10}(\rho_s)$	r_s[pc]	α	w	γ	r_a [pc]	δ	β_0	β_∞	χ^2
-0.665	474.354	1.873	4.153	0	282.093	2.111	0.271	-0.756	7.085
-0.700	1394.3	1.133	5.020	0	556.689	4.038	0.275	-0.368	7.661
-0.105	486.830	1.131	5.241	0	678.483	0.756	-4.643	-0.876	12.369
-0.155	699.102	1.075	6.378	0	265.851	1.303	-3.711	-7.138	14.102
1.346	100.0	0.534	3.098	0	381.190	3.594	-4.561	-5.287	14.899
0.063	1735.590	0.581	5.419	0	132.107	1.897	0.183	-0.301	16.113
-0.412	560.719	1.098	3.740	0	381.190	3.594	-4.561	-5.287	16.193
-0.762	2458.641	1.010	3.942	0	917.265	0.270	-2.009	-8.332	16.562

Table 16: The best-fit parameters and χ^2 for the fit to the velocity dispersion data of the Draco dSph from Ref. [293]. Here the anisotropy profile is the Generalized Osipkov Merritt 3, here d.o.f = 9 and since the inner slope γ is set to be 0.

$log_{10}(\rho_s)$	r_s[pc]	α	w	γ	r_a [pc]	δ	β_0	β_∞	χ^2
-1.229	611.645	1.851	3.045	1.0	635.588	1.359	-1.666	-1.676	5.763
-1.254	760.926	1.258	3.225	1.0	125.805	0.356	-2.022	-1.797	7.580
-1.773	2036.835	1.735	4.735	1.0	712.644	2.737	-0.796	-0.508	7.973
-1.424	905.417	2.474	3.387	1.0	743.826	2.063	-1.418	-0.368	8.498
-1.215	1500.984	2.216	3.636	1.0	104.789	0.256	-4.469	-8.810	8.765
-1.286	1114.243	0.756	3.542	1.0	462.797	3.397	-1.795	-7.730	8.962
-1.671	1663.010	1.706	4.159	1.0	610.331	0.308	-4.378	-5.519	9.040
-1.885	2422.825	1.406	3.354	1.0	610.331	0.308	-4.378	-5.519	9.394

Table 17: The best-fit parameters and χ^2 for the fit to the velocity dispersion data of the Draco dSph from Ref. [293]. Here the anisotropy profile is the Generalized Osipkov Merritt 3, here d.o.f = 9 and the inner slope γ is set to be 1.

$log_{10}(\rho_s)$	r_s[pc]	α	w	γ	r_a [pc]	δ	β_0	β_∞	χ^2
-0.712	394.310	2.591	5.163	0	498.249	3.718	-0.209	-6.673	22.722
-0.335	938.096	0.948	6.853	0	387.853	2.784	0.457	-4.523	25.909
0.005	818.858	0.739	4.829	0	222.439	0.893	-0.345	-0.899	27.295
0.356	1052.077	0.588	5.035	0	555.632	4.809	-2.576	-3.796	28.859
-0.325	357.453	1.573	4.677	0	347.845	2.760	0.776	-5.119	29.182
0.108	1020.939	0.726	5.614	0	566.555	1.656	-3.590	-7.736	30.665
0.365	578.156	0.699	4.765	0	829.379	4.964	-2.921	-6.871	32.864
0.675	2449.671	0.500	6.935	0	753.137	3.236	-6.640	-3.740	33.063

Table 18: The best-fit parameters and χ^2 for the fit to the velocity dispersion data of the Draco dSph from Ref. [117]. Here the anisotropy profile is the Generalized Osipkov Merritt 3, here d.o.f = 7 and the inner slope γ is set to be 0.

$log_{10}(\rho_s)$	r_s[pc]	α	w	γ	r_a [pc]	δ	β_0	β_∞	χ^2
-1.399	863.525	1.913	6.299	1.0	454.842	4.404	-0.786	-4.906	20.482
-1.783	1646.738	1.564	6.008	1.0	416.285	1.779	-0.014	-1.634	20.682
-1.735	1368.076	1.982	6.269	1.0	431.498	4.297	0.285	-2.859	21.292
0.232	100.000	2.678	4.283	1.0	341.647	2.881	0.391	-7.251	22.670
0.147	100.000	2.247	4.019	1.0	341.647	2.881	0.391	-7.251	23.609
-1.354	784.307	2.375	6.951	1.0	660.755	4.693	0.104	-8.524	24.065
-1.623	1110.411	2.340	6.546	1.0	444.950	1.569	-1.175	-8.046	26.706
-1.584	1283.040	1.697	5.124	1.0	806.270	2.837	-0.832	-1.621	26.726

Table 19: The best-fit parameters and χ^2 for the fit to the velocity dispersion data of the Draco dSph from Ref. [117]. Here the anisotropy profile is the Generalized Osipkov Merritt 3, here d.o.f = 7 and the inner slope γ is set to be 1.

$log_{10}(\rho_s)$	r_s[pc]	α	w	γ	r_a [pc]	δ	β_0	β_∞	χ^2
0.123	557.680	0.845	4.953	0	440.334	1.133	-0.499	-4.043	49.794
1.748	100.000	0.545	3.725	0	179.752	4.661	-5.225	-6.510	65.619
0.792	100.000	0.890	3.087	0	951.045	0.375	-6.661	-6.455	73.184
0.713	100.000	1.298	3.827	0	441.497	3.832	-5.131	-7.074	73.352
-0.025	491.440	0.940	5.160	0	942.906	1.595	-1.331	-7.069	81.832
0.019	605.653	0.676	3.673	0	181.536	0.998	-1.879	0.869	84.646
0.382	162.756	1.404	4.378	0	471.874	4.986	-3.527	-3.246	86.257
-0.932	931.018	0.914	3.024	0	175.045	4.016	0.413	-1.347	86.855

Table 20: The best-fit parameters and χ^2 for the fit to the velocity dispersion data of the Sculptor dSph from Ref. [293]. Here the anisotropy profile is the Generalized Osipkov Merritt 3, here d.o.f = 28 and the inner slope γ is set to be 0.

$log_{10}(\rho_s)$	r_s[pc]	α	w	γ	r_a [pc]	δ	β_0	β_∞	χ^2
-1.358	1146.117	1.213	6.699	1.0	999.609	1.704	-1.432	-6.729	51.111
-1.579	1093.059	2.376	5.459	1.0	596.526	2.926	-0.389	-0.300	52.338
-0.874	3000.000	0.500	7.000	1.0	609.684	2.434	-3.499	-7.959	53.361
-1.230	658.192	1.918	6.828	1.0	614.574	1.374	-0.537	-2.698	56.035
-2.095	2630.007	2.377	6.564	1.0	876.569	0.553	0.047	-3.168	58.213
-1.737	2416.393	1.348	6.087	1.0	212.765	1.627	-2.437	0.527	64.317
-1.426	1722.168	0.656	3.791	1.0	411.468	0.742	-0.543	-4.623	64.824
-1.062	645.261	1.505	3.448	1.0	555.125	0.407	-0.865	-4.906	64.961

Table 21: The best-fit parameters and χ^2 for the fit to the velocity dispersion data of the Sculptor dSph from Ref. [293]. Here the anisotropy profile is the Generalized Osipkov Merritt 3, here d.o.f = 28 and the inner slope γ is set to be 1.

$log_{10}(\rho_s)$	r_s[pc]	α	w	γ	r_a [pc]	δ	β_0	β_∞	χ^2
-0.022	1577.549	0.619	4.844	0	747.265	4.780	-0.140	0.303	36.943
-0.183	1012.148	0.958	6.893	0	531.597	1.006	0.724	-5.196	44.120
0.639	100	0.849	3.099	0	261.813	4.062	-0.985	-4.558	46.653
-0.421	709.657	1.126	3.780	0	223.661	3.083	-1.876	0.193	53.500
-0.647	1110.423	1.331	4.102	0	326.832	2.605	-2.239	0.580	54.448
0.015	452.937	1.469	5.782	0	154.292	4.520	-5.471	-1.745	54.573
0.203	100	2.508	3.061	0	371.991	2.007	-5.049	-5.398	59.908
0.195	1662.209	0.560	4.226	0	537.980	0.270	-2.916	-7.847	68.266

Table 22: The best-fit parameters and χ^2 for the fit to the velocity dispersion data of the Sculptor dSph from Ref. [117]. Here the anisotropy profile is the Generalized Osipkov Merritt 3, here d.o.f = 28 and the inner slope γ is set to be 0.

$log_{10}(\rho_s)$	r_s[pc]	α	w	γ	r_a [pc]	δ	β_0	β_∞	χ^2
-1.864	2345.055	1.517	4.797	1.0	206.478	2.048	-0.715	-0.101	40.706
-1.826	3000.000	0.990	6.931	1.0	133.003	0.998	-1.868	-0.387	41.303
-1.999	2733.492	2.155	3.359	1.0	665.877	1.935	-0.599	0.695	48.681
-1.511	842.937	2.685	5.229	1.0	725.092	3.757	-0.440	-3.511	49.944
-1.009	556.510	1.512	4.553	1.0	809.487	2.034	-0.285	-7.274	50.134
-1.651	1832.555	1.379	6.841	1.0	958.038	1.418	-1.436	-4.247	51.520
-1.329	821.612	1.798	4.540	1.0	853.737	1.494	-2.423	-0.763	51.566
0.278	173.874	0.962	4.426	1.0	342.908	2.889	-3.723	-8.288	55.151

Table 23: The best-fit parameters and χ^2 for the fit to the velocity dispersion data of the Sculptor dSph from Ref. [117]. Here the anisotropy profile is the Generalized Osipkov Merritt 3, here d.o.f = 28 and the inner slope γ is set to be 1.

$log_{10}(\rho_s)$	r_s[pc]	α	w	γ	r_a [pc]	δ	β_0	β_∞	χ^2
0.580	100.000	1.947	4.913	0	740.061	1.481	-5.773	-6.666	12.087
-1.617	2724.934	1.060	6.485	0	245.292	3.558	0.113	-0.253	12.854
0.484	100.000	1.956	4.235	0	675.595	3.784	-8.340	-8.955	12.899
0.368	100.000	2.635	4.576	0	184.411	3.041	-4.232	-3.982	13.096
0.263	100.000	2.635	3.879	0	184.411	3.041	-4.232	-3.982	13.415
0.486	100.000	2.635	5.369	0	184.411	3.041	-4.232	-3.982	15.403
0.299	100.000	2.597	4.013	0	516.079	1.159	-4.027	3.021	15.532
0.401	100.000	1.419	3.837	0	234.748	3.879	-6.910	-8.633	16.192

Table 24: The best-fit parameters and χ^2 for the fit to the velocity dispersion data of the Sextans dSph from Ref. [293]. Here the anisotropy profile is the Generalized Osipkov Merritt 3, here d.o.f = 7 and the inner slope γ is set to be 0.

$log_{10}(\rho_s)$	r_s[pc]	α	w	γ	r_a [pc]	δ	β_0	β_∞	χ^2
-0.134	100.000	2.572	3.064	10	912.112	2.468	-3.441	-8.107	10.569
0.029	100.000	2.035	3.403	1.0	726.779	4.819	-4.843	-3.998	10.675
0.323	100.000	1.643	4.282	1.0	631.704	3.407	-4.281	-6.852	11.060
-1.459	842.575	1.230	4.732	1.0	686.749	0.486	-1.446	-5.652	11.402
0.241	100.000	2.058	4.180	1.0	898.648	3.105	-5.179	-6.443	11.611
-1.227	100.000	2.342	3.309	1.0	296.627	2.299	-7.355	-8.224	11.870
0.266	100.000	1.932	5.062	1.0	359.639	1.868	-0.565	-7.829	12.356
-2.444	2624.216	2.539	5.339	1.0	385.720	2.363	-1.149	-0.061	12.411

Table 25: The best-fit parameters and χ^2 for the fit to the velocity dispersion data of the Sextans dSph from Ref. [293]. Here the anisotropy profile is the Generalized Osipkov Merritt 3, here d.o.f = 7 and the inner slope γ is set to be 1.

$log_{10}(\rho_s)$	r_s[pc]	α	w	γ	r_a [pc]	δ	β_0	β_∞	χ^2
-1.819	1676.251	2.496	5.868	0	870.658	4.938	0.167	-3.220	10.554
-0.478	550.185	0.849	3.977	0	736.003	2.390	-0.554	-1.677	13.634
1.551	100.000	0.983	5.761	0	401.740	1.541	-7.928	-7.496	13.737
0.399	100.000	2.588	5.036	0	514.437	0.551	-5.923	-3.069	13.741
0.715	100.000	1.850	5.649	0	568.372	4.555	-2.794	-3.748	13.833
0.971	100.000	1.515	5.700	0	790.854	1.216	-8.016	-3.886	14.251
-1.077	1486.802	0.817	4.455	0	843.414	3.356	0.156	-0.747	14.747
0.169	100.000	1.559	3.001	0	756.287	0.303	-1.154	-6.293	14.956

Table 26: The best-fit parameters and χ^2 for the fit to the velocity dispersion data of the Sextans dSph from Ref. [117]. Here the anisotropy profile is the Generalized Osipkov Merritt 3, here d.o.f = 7 and the inner slope γ is set to be 0.

$log_{10}(\rho_s)$	r_s[pc]	α	w	γ	r_a [pc]	δ	β_0	β_∞	χ^2
0.266	100.000	1.932	5.062	1.0	359.639	1.868	-0.565	-7.829	12.356
-0.018	100.000	2.670	3.460	1.0	595.940	0.706	-2.596	-5.592	13.375
-2.444	2624.216	2.539	5.339	1.0	385.720	2.363	-1.149	-0.061	12.411
-2.156	1281.572	2.065	6.616	1.0	953.063	3.557	0.064	-7.846	12.580
0.823	100.000	0.810	4.471	1.0	557.201	4.755	-2.001	-7.731	12.957
1.095	100.000	0.968	5.925	1.0	216.423	1.518	-3.701	-5.539	13.168
-0.009	100.000	1.095	3.061	1.0	561.156	3.204	-1.250	-2.926	13.173
0.417	100.000	1.359	6.373	1.0	178.613	3.491	0.329	-6.409	13.185

Table 27: The best-fit parameters and χ^2 for the fit to the velocity dispersion data of the Sextans dSph from Ref. [117]. Here the anisotropy profile is the Generalized Osipkov Merritt 3, here d.o.f = 7 and the inner slope γ is set to be 1.

$log_{10}(\rho_s)$	r_s[pc]	α	w	γ	r_a [pc]	δ	β_0	β_∞	χ^2
0.592	100.000	2.405	6.459	0	461.463	1.836	-3.160	-8.610	5.579
-0.240	187.846	2.207	4.606	0	657.431	3.035	-0.784	-3.707	6.154
2.602	100.000	0.607	6.212	0	768.417	4.973	-1.943	-7.819	6.185
-0.593	376.733	2.944	5.868	0	735.924	4.366	-0.018	-8.754	7.160
1.059	100.000	1.494	6.692	0	813.167	3.281	-8.479	-4.267	7.365
0.834	100.000	1.400	5.802	0	793.857	0.903	-7.871	-3.738	7.830
1.524	100.000	0.580	3.788	0	591.352	3.495	-6.109	-4.126	7.843
0.297	100.000	2.412	5.632	0	264.676	2.198	-2.244	-6.377	8.086

Table 28: The best-fit parameters and χ^2 for the fit to the velocity dispersion data of the LEO2 dSph from Ref. [293]. Here the anisotropy profile is the Generalized Osipkov Merritt 3, here d.o.f = 8 and the inner slope γ is set to be 0.

$log_{10}(\rho_s)$	r_s[pc]	α	w	γ	r_a [pc]	δ	β_0	β_∞	χ^2
-0.917	541.263	1.187	5.541	1	449.320	2.405	-0.103	0.149	3.366
0.038	137.533	1.005	3.471	1	364.382	0.712	-0.860	-6.735	3.502
0.807	108.147	0.655	3.998	1	156.774	0.494	-2.232	-2.503	4.312
-0.061	100.000	1.861	3.151	1	982.257	1.343	-0.391	-7.292	4.730
1.165	100.000	0.552	3.942	1	826.837	3.277	-8.952	-0.273	5.034
-1.857	1739.434	2.454	6.000	1	970.163	1.349	0.424	0.875	5.266
0.283	100.000	1.912	5.076	1	850.811	0.514	-3.133	-3.683	5.430
1.024	100.000	0.943	5.995	1	337.223	1.102	-6.428	-2.987	5.805

Table 29: The best-fit parameters and χ^2 for the fit to the velocity dispersion data of the LEO2 dSph from Ref. [293]. Here the anisotropy profile is the Generalized Osipkov Merritt 3, here d.o.f = 3 and the inner slope γ is set to be 1.

$log_{10}(\rho_s)$	r_s[pc]	α	w	γ	r_a [pc]	δ	β_0	β_∞	χ^2
2.531	100.000	0.688	6.672	0	888.749	0.342	-0.524	0.769	10.980
0.248	259.200	1.300	5.225	0	514.450	3.942	0.629	-1.386	11.175
1.205	1583.918	0.967	4.927	0	132.140	0.140	0.855	-7.675	11.857
0.729	100.000	2.020	6.160	0	388.463	3.164	-2.822	-6.732	13.365
-0.214	2057.838	0.675	5.640	0	868.113	4.711	0.692	0.076	13.816
0.682	100.000	2.408	6.667	0	329.175	3.152	-0.169	-5.045	14.535
0.744	100.000	2.040	6.151	0	619.300	1.397	-0.531	-8.754	15.478
0.830	100.000	1.101	4.070	0	988.889	4.716	-2.370	-1.513	17.173

Table 30: The best-fit parameters and χ^2 for the fit to the velocity dispersion data of the LEO2 dSph from Ref. [117]. Here the anisotropy profile is the Generalized Osipkov Merritt 3, here d.o.f = 2 and the inner slope γ is set to be 0.

$log_{10}(\rho_s)$	r_s[pc]	α	w	γ	r_a [pc]	δ	β_0	β_∞	χ^2
0.126	100.000	1.713	3.505	1	592.979	3.123	-0.848	-7.816	10.226
0.743	100.000	1.360	6.006	1	540.311	4.099	-0.693	-8.189	13.351
0.690	100.000	0.760	3.687	1	570.615	3.941	-2.239	-3.202	13.815
0.297	100.000	1.201	3.000	1	134.012	3.025	-7.599	-3.300	14.159
0.389	100.000	1.323	3.351	1	134.012	3.025	-7.599	-3.300	14.477
0.481	100.000	1.445	3.910	1	134.012	3.025	-7.599	-3.300	15.637
-0.494	1510.737	0.553	6.395	1	139.038	3.774	-5.327	-1.042	15.948
-1.521	938.525	2.341	4.321	1	777.403	4.147	0.123	-8.122	16.351

Table 31: The best-fit parameters and χ^2 for the fit to the velocity dispersion data of the LEO2 dSph from Ref. [117]. Here the anisotropy profile is the Generalized Osipkov Merritt 3, here d.o.f = 2 and the inner slope γ is set to be 1.

$log_{10}(\rho_s)$	r_s[pc]	α	w	γ	r_a [pc]	δ	β_0	β_∞	χ^2
0.632	100.000	1.126	3.071	0	561.022	0.295	-2.918	-2.689	10.893
1.792	100.000	0.500	3.487	0	322.555	0.862	-3.218	-1.458	12.591
0.515	100.000	1.596	3.322	0	826.974	3.196	-7.085	-7.478	13.004
0.233	100.000	2.981	3.321	0	328.705	4.623	-2.350	-6.600	14.202
1.536	680.955	0.537	6.777	0	849.289	3.608	-3.234	-2.163	14.450
-0.406	394.886	2.092	6.685	0	531.248	4.041	-2.503	-6.755	14.573
-0.320	437.557	1.083	3.463	0	484.264	1.568	-0.497	-2.306	14.684
-0.714	1718.927	1.262	5.174	0	321.453	4.018	-1.101	0.336	14.779

Table 32: The best-fit parameters and χ^2 for the fit to the velocity dispersion data of the LEO1 dSph from Ref. [293]. Here the anisotropy profile is the Generalized Osipkov Merritt 3, here d.o.f = 8 and the inner slope γ is set to be 0.

$log_{10}(\rho_s)$	r_s[pc]	α	w	γ	r_a [pc]	δ	β_0	β_∞	χ^2
-1.028	1518.303	0.720	4.961	1	207.787	3.956	-5.557	-3.230	9.568
-1.016	976.640	0.813	4.889	1	443.973	2.195	-1.791	-6.037	10.228
-0.686	2335.868	0.509	6.577	1	338.913	4.251	-7.011	-8.589	10.435
-0.935	2641.932	0.513	3.839	1	123.728	0.364	-0.045	-5.083	10.482
-0.717	2188.025	0.500	5.714	1	998.360	3.123	-6.669	-4.607	11.740
-2.055	1837.477	2.062	3.410	1	110.595	0.436	-0.069	0.306	12.425
-0.795	2611.000	0.500	6.161	1	338.913	4.251	-7.011	-8.589	12.500
0.339	100.000	1.512	3.310	1	371.836	1.336	-3.302	-6.755	12.842

Table 33: The best-fit parameters and χ^2 for the fit to the velocity dispersion data of the LEO1 dSph from Ref. [293]. Here the anisotropy profile is the Generalized Osipkov Merritt 3, here d.o.f = 8 and the inner slope γ is set to be 1.

$log_{10}(\rho_s)$	r_s[pc]	α	w	γ	r_a [pc]	δ	β_0	β_∞	χ^2
-0.399	1,607.628	0.757	5.067	0	868.797	1.315	-0.784	-3.630	28.751
0.985	870.704	0.564	6.252	0	554.568	1.691	-2.304	-4.304	29.829
-1.265	1,123.950	2.789	6.513	0	856.123	4.920	-0.005	-0.300	41.246
-0.584	1,675.037	1.494	6.914	0	809.162	0.252	-0.726	-8.932	41.553
-0.085	567.398	1.290	4.348	0	101.315	1.464	-6.071	-0.245	47.023
0.443	100.000	1.884	3.423	0	860.526	2.168	-3.929	-4.072	47.509
0.674	199.159	0.737	4.066	0	538.226	3.262	-2.994	-8.508	48.633
-0.455	649.777	1.459	4.768	0	354.400	1.680	-3.839	-1.022	48.746

Table 34: The best-fit parameters and χ^2 for the fit to the velocity dispersion data of the LEO1 dSph from Ref. [117]. Here the anisotropy profile is the Generalized Osipkov Merritt 3, here d.o.f = 8 and the inner slope γ is set to be 0.

$log_{10}(\rho_s)$	r_s[pc]	α	w	γ	r_a [pc]	δ	β_0	β_∞	χ^2
-1.194	779.017	1.284	5.445	1	618.705	3.689	-1.561	-4.511	22.473
-1.968	2251.938	2.458	4.074	1	423.261	0.621	0.242	-2.778	28.931
-1.568	890.464	2.863	3.822	1	723.570	1.468	-1.660	-1.181	29.010
-1.255	781.458	0.994	3.626	1	559.948	2.252	0.485	-3.230	29.360
-1.411	2169.524	0.644	4.756	1	926.875	4.529	-6.790	-8.063	30.264
-1.642	1911.250	1.513	6.179	1	258.562	4.801	-8.159	-4.712	30.504
-0.558	1225.918	0.559	5.761	1	510.808	2.152	-2.800	-7.184	30.829
-0.797	1000.539	0.719	5.595	1	377.407	2.255	-3.515	-7.293	31.517

Table 35: The best-fit parameters and χ^2 for the fit to the velocity dispersion data of the LEO1 dSph from Ref. [117]. Here the anisotropy profile is the Generalized Osipkov Merritt 3, here d.o.f = 8 and the inner slope γ is set to be 1.

$log_{10}(\rho_s)$	r_s[pc]	α	w	γ	r_a [pc]	δ	β_0	β_∞	χ^2
0.051	684.273	0.899	6.122	0	412.015	2.510	-2.404	-3.636	18.223
-1.051	766.680	2.547	6.144	0	345.935	1.350	-2.230	-0.596	19.740
0.255	2400.370	0.558	6.525	0	981.676	2.087	-5.386	-2.114	19.919
0.490	100.000	2.388	3.679	0	574.761	4.130	-1.370	-4.860	24.048
1.736	100.000	0.957	4.903	0	619.247	4.084	-6.456	-8.434	25.632
0.906	100.000	2.744	6.067	0	581.655	2.833	0.363	-8.404	27.233
1.115	100.000	2.312	6.571	0	569.581	3.682	-0.589	-7.608	28.970
1.647	100.000	1.318	5.699	0	945.138	2.249	-3.766	-6.767	30.731

Table 36: The best-fit parameters and χ^2 for the fit to the velocity dispersion data of the Fornax dSph from Ref. [293]. Here the anisotropy profile is the Generalized Osipkov Merritt 3, here d.o.f = 26 and the inner slope γ is set to be 0.

$log_{10}(\rho_s)$	r_s[pc]	α	w	γ	r_a [pc]	δ	β_0	β_∞	χ^2
-1.873	1687.489	1.543	5.077	1	985.041	3.759	-1.072	-0.368	17.732
-0.922	516.331	1.728	6.679	1	960.374	0.333	-2.341	-0.970	18.085
-1.621	1295.363	2.307	5.065	1	757.150	0.333	0.841	-0.986	19.527
-0.322	639.481	1.490	4.305	1	276.879	0.206	0.724	-3.304	20.230
0.528	100.000	1.702	3.314	1	976.727	3.384	-1.793	-3.426	20.806
0.792	100.000	0.930	3.416	1	594.155	1.627	0.742	-1.510	21.414
-1.380	867.776	1.780	5.161	1	945.074	1.437	-5.104	-2.214	21.332
-1.707	1039.287	2.455	5.436	1	520.660	1.002	-4.698	-1.285	22.142

Table 37: The best-fit parameters and χ^2 for the fit to the velocity dispersion data of the Fornax dSph from Ref. [293]. Here the anisotropy profile is the Generalized Osipkov Merritt 3, here d.o.f = 26 and the inner slope γ is set to be 1.

$log_{10}(\rho_s)$	r_s[pc]	α	w	γ	r_a [pc]	δ	β_0	β_∞	χ^2
-0.392	531.879	1.540	4.881	0	398.731	2.418	-6.259	-2.887	60.507
1.301	100.000	0.863	3.664	0	978.211	1.064	-2.959	-1.816	67.355
0.975	1302.854	0.512	6.240	0	168.262	1.157	-6.283	-6.451	69.162
0.901	351.743	0.744	4.587	0	396.097	4.104	-5.063	-1.777	72.217
0.784	100.000	1.049	3.745	0	195.642	2.748	-0.351	-8.175	78.484
3.997	100.000	0.514	6.573	0	683.728	1.952	-0.361	-8.493	82.374
-0.166	1427.417	0.769	6.260	0	295.106	1.073	-6.893	-1.758	87.317
0.683	100.000	1.624	3.298	0	959.139	2.279	-7.434	-2.952	90.505

Table 38: The best-fit parameters and χ^2 for the fit to the velocity dispersion data of the Fornax dSph from Ref. [117]. Here the anisotropy profile is the Generalized Osipkov Merritt 3, here d.o.f = 36 and the inner slope γ is set to be 0.

$log_{10}(\rho_s)$	r_s[pc]	α	w	γ	r_a [pc]	δ	β_0	β_∞	χ^2
-1.243	1637.533	0.927	6.405	1	566.431	0.454	-1.651	-2.833	45.200
-0.912	1388.846	0.799	6.478	1	867.816	1.357	-6.306	-2.782	52.856
0.371	368.634	0.540	4.065	1	877.319	1.279	-7.558	-3.241	55.067
-1.496	1395.772	1.302	6.070	1	940.075	1.794	-3.135	-1.229	56.699
-1.640	947.358	1.889	3.300	1	855.483	0.920	0.484	-0.827	57.457
-1.156	1454.280	0.789	4.170	1	522.311	2.274	-7.633	-1.855	58.343
-2.221	2747.476	1.872	5.158	1	700.675	3.552	-0.544	0.309	64.703
0.760	100.000	1.130	3.365	1	478.372	1.001	-6.219	-7.737	66.255

Table 39: The best-fit parameters and χ^2 for the fit to the velocity dispersion data of the Fornax dSph from Ref. [117]. Here the anisotropy profile is the Generalized Osipkov Merritt 3, here d.o.f = 36 and the inner slope γ is set to be 1.

$log_{10}(\rho_s)$	r_s[pc]	α	w	γ	r_a [pc]	δ	β_0	β_∞	χ^2
-0.684	657.142	1.217	5.941	0	802.134	2.452	0.032	-2.255	35.790
-0.157	680.622	0.850	5.770	0	417.377	0.754	0.687	-6.232	36.078
-0.999	1.530	1.530	6.157	0	417.377	4.693	0.305	-4.789	37.299
-0.772	271.407	2.700	3.993	0	203.937	0.970	0.683	-1.207	38.299
-0.797	994.603	0.989	5.202	0	839.534	2.155	0.388	-0.171	39.491
-0.374	1009.145	0.769	3.641	0	407.457	0.396	-0.381	-7.818	40.689
-0.120	702.807	0.699	4.846	0	604.452	1.045	0.537	-5.836	40.866
0.225	100.000	1.195	3.326	0	173.424	1.324	-2.242	-5.231	43.616

Table 40: The best-fit parameters and χ^2 for the fit to the velocity dispersion data of the Carina dSph from Ref. [293]. Here the anisotropy profile is the Generalized Osipkov Merritt 3, here d.o.f = 19 and the inner slope γ is set to be 0.

$log_{10}(\rho_s)$	r_s[pc]	α	w	γ	r_a [pc]	δ	β_0	β_∞	χ^2
-2.321	2972.939	1.359	6.406	1	845.153	0.470	-0.430	-0.480	35.422
-2.210	3000.000	1.851	5.013	1	254.536	3.586	-3.013	-0.426	38.092
-1.693	720.638	2.488	6.705	1	892.595	2.163	-0.589	-2.326	38.390
-2.124	1658.873	2.595	3.491	1	568.851	4.282	-0.369	-0.645	39.949
-1.692	1658.918	2.595	6.126	1	492.297	3.956	-1.694	-4.800	42.472
-1.689	1580.617	0.871	6.841	1	336.614	4.636	-0.780	-1.258	42.993
-2.070	2350.522	0.843	4.165	1	752.416	4.648	-1.532	-5.607	43.279
-2.282	3000.000	1.752	4.933	1	752.416	3.586	-3.013	-0.426	43.805

Table 41: The best-fit parameters and χ^2 for the fit to the velocity dispersion data of the Carina dSph from Ref. [293]. Here the anisotropy profile is the Generalized Osipkov Merritt 3, here d.o.f = 19 and the inner slope γ is set to be 1.

$log_{10}(\rho_s)$	r_s[pc]	α	w	γ	r_a [pc]	δ	β_0	β_∞	χ^2
1.588	262.720	0.536	3.804	0	106.554	4.353	-3.332	0.142	52.449
0.411	320.183	1.228	6.724	0	539.273	3.395	-1.249	-5.048	53.565
0.450	100.000	1.712	3.132	0	229.300	1.195	0.049	-5.334	58.680
1.116	403.928	0.782	6.961	0	436.890	4.634	-6.001	-8.673	62.720
-0.852	629.757	2.776	5.088	0	442.263	3.128	-4.081	-1.317	68.306
0.628	100.000	1.608	3.212	0	802.190	2.777	-2.370	-5.182	70.023
-0.977	622.664	2.466	4.970	0	650.787	1.110	-1.107	-2.339	71.015
1.926	192.591	0.609	4.946	0	406.242	3.715	-6.393	-6.337	71.527

Table 42: The best-fit parameters and χ^2 for the fit to the velocity dispersion data of the Carina dSph from Ref. [117]. Here the anisotropy profile is the Generalized Osipkov Merritt 3, here d.o.f = 16 and the inner slope γ is set to be 0.

$log_{10}(\rho_s)$	r_s[pc]	α	w	γ	r_a [pc]	δ	β_0	β_∞	χ^2
-2.431	2763.752	2.952	6.713	1	618.580	4.049	0.148	-0.248	30.137
-2.108	2982.212	1.796	3.562	1	284.769	4.613	-7.201	-1.669	30.281
-1.964	1503.726	1.842	4.189	1	706.065	2.508	-0.756	-1.006	31.984
-1.605	751.406	2.086	4.255	1	896.914	1.068	-0.931	-0.515	32.661
-1.356	601.158	2.949	4.495	1	251.059	2.670	-7.869	-2.136	35.201
-2.219	2993.383	0.853	4.156	1	295.153	0.933	-3.240	0.667	35.766
-1.324	872.575	0.689	3.331	1	983.675	2.899	-3.617	-0.421	36.060
-1.882	1839.786	0.924	6.162	1	492.589	1.369	-0.815	-2.458	36.117

Table 43: The best-fit parameters and χ^2 for the fit to the velocity dispersion data of the Carina dSph from Ref. [117]. Here the anisotropy profile is the Generalized Osipkov Merritt 3, here d.o.f = 16 and the inner slope γ is set to be 1.

$log_{10}(\rho_s)$	r_s[pc]	α	w	γ	r_a [pc]	δ	β_0	β_∞	χ^2
-0.487	2455.208	2.710	5.380	0	186.847	4.809	-7.025	0.844	16.064
1.160	100.000	0.736	3.426	0	947.291	3.647	-5.640	-3.827	19.232
1.056	100.000	1.210	4.658	0	749.268	2.160	-4.118	-7.301	19.300
0.245	100.000	2.481	3.153	0	877.391	4.254	-5.729	-6.803	19.607
1.532	100.000	0.898	3.865	0	165.064	0.133	-6.671	-8.542	20.339
0.573	1506.169	0.536	4.632	0	232.693	4.722	-6.295	0.059	20.539
-0.876	3000.000	2.187	5.088	0	263.232	3.553	-3.446	0.547	20.622
0.435	100.000	2.523	4.043	0	991.853	0.854	-3.929	-7.715	20.776

Table 44: The best-fit parameters and χ^2 for the fit to the velocity dispersion data of the UMi dSph from Ref. [293]. Here the anisotropy profile is the Generalized Osipkov Merritt 3, here d.o.f = 7 and the inner slope γ is set to be 0.

$log_{10}(\rho_s)$	r_s[pc]	α	w	γ	r_a [pc]	δ	β_0	β_∞	χ^2
-0.883	1011.968	0.587	4.162	1	517.340	1.990	-1.310	-2.086	15.721
-1.962	1675.848	2.064	4.810	1	696.347	3.504	-0.357	0.276	16.055
-0.929	641.88	1.240	5.831	1	645.109	1.432	-2.135	-8.421	16.145
-1.393	768.572	1.875	3.368	1	717.502	0.726	-0.771	-6.158	16.198
-0.887	816.340	0.717	4.138	1	517.340	1.990	-1.310	-2.086	16.385
-1.203	1011.782	2.058	6.685	1	195.199	2.233	-5.039	-0.093	16.598
-2.240	2581.866	2.325	3.290	1	741.229	2.356	-0.174	-1.568	17.635
1.135	100.000	0.500	3.282	1	957.591	3.757	-8.419	-1.002	17.773

Table 45: The best-fit parameters and χ^2 for the fit to the velocity dispersion data of the UMi dSph from Ref. [293]. Here the anisotropy profile is the Generalized Osipkov Merritt 3, here d.o.f = 7 and the inner slope γ is set to be 1.

$log_{10}(\rho_s)$	r_s[pc]	α	w	γ	r_a [pc]	δ	β_0	β_∞	χ^2
0.530	100.000	1.335	3.179	0	663.839	4.230	-2.657	-5.287	14.405
0.421	100.000	1.503	3.275	0	673.531	0.242	-4.106	-2.934	16.739
-0.037	1547.043	0.763	3.696	0	569.797	0.204	-0.854	-8.532	19.894
0.551	100.000	2.307	4.773	0	673.531	0.242	-4.106	-2.934	20.210
0.972	100.000	0.896	3.339	0	814.510	2.539	-5.087	-1.348	20.796
0.557	100.000	1.452	3.323	0	746.181	3.499	-2.587	-2.260	21.276
1.079	100.000	1.189	4.700	0	842.525	2.265	-3.925	-8.614	23.531
0.189	324.321	1.195	6.409	0	541.434	1.851	-0.646	-8.583	23.984

Table 46: The best-fit parameters and χ^2 for the fit to the velocity dispersion data of the UMi dSph from Ref. [117]. Here the anisotropy profile is the Generalized Osipkov Merritt 3, here d.o.f = 9 and the inner slope γ is set to be 0.

$log_{10}(\rho_s)$	r_s[pc]	α	w	γ	r_a [pc]	δ	β_0	β_∞	χ^2
-1.802	2438.616	1.092	5.811	1	548.531	0.411	-0.994	-1.798	15.441
-0.803	1443.067	0.637	5.916	1	654.866	2.573	-3.034	-5.188	15.661
1.201	100.000	0.500	3.338	1	894.551	3.632	-4.792	-5.905	17.096
-0.916	1376.269	0.811	4.738	1	131.144	2.581	-4.870	-0.405	17.718
-2.124	2574.617	1.636	5.929	1	883.620	4.003	-0.383	-0.617	17.834
-2.167	2405.882	1.945	4.330	1	935.605	1.318	-0.513	0.662	17.920
-1.012	1148.949	0.741	4.727	1	108.522	4.826	-4.415	-4.693	18.118
-1.624	1545.987	2.558	4.823	1	126.003	1.378	-6.233	0.434	19.373

Table 47: The best-fit parameters and χ^2 for the fit to the velocity dispersion data of the UMi dSph from Ref. [117]. Here the anisotropy profile is the Generalized Osipkov Merritt 3, here d.o.f = 9 and the inner slope γ is set to be 1.

$log_{10}(\rho_s)$	r_s[pc]	α	w	γ	r_a [pc]	δ	β_0	β_∞	χ^2
-0.895	556.499	2.234	5.082	0	870.178	0.744	0.886	-0.821	29.183
0.521	100.000	2.802	4.456	0	578.547	4.400	-1.451	-7.801	29.737
0.147	100.000	2.570	3.258	0	467.374	1.921	0.880	-1.647	32.267
0.731	100.000	1.384	4.038	0	882.926	4.053	-0.564	-6.832	32.446
-1.451	1315.776	2.136	5.515	0	940.140	3.076	0.732	0.097	32.845
1.902	100.000	0.895	5.539	0	238.169	0.402	-5.522	-6.656	35.515
0.566	100.000	2.654	4.329	0	582.790	2.618	-3.884	-7.652	35.553
0.876	383.130	0.628	4.906	0	759.894	0.520	-0.604	-3.637	37.831

Table 48: The best-fit parameters and χ^2 for the fit to the velocity dispersion data of the UMi dSph from Ref. [295]. Here the anisotropy profile is the Generalized Osipkov Merritt 3, here d.o.f = 18 and the inner slope γ is set to be 0.

$log_{10}(\rho_s)$	r_s[pc]	α	w	γ	r_a [pc]	δ	β_0	β_∞	χ^2
-1.367	2224.734	0.653	5.773	1	678.683	3.605	0.498	-1.990	29.611
0.753	100.000	1.245	4.228	1	755.590	1.982	0.707	-2.918	29.871
-0.323	243.455	2.883	5.467	1	973.033	1.761	0.512	-2.911	30.594
2.014	100.000	0.660	6.196	1	440.439	2.271	-0.128	-6.371	31.136
0.914	100.000	1.422	5.267	1	506.624	1.694	-1.693	-6.918	31.404
0.879	100.000	1.590	5.198	1	182.978	0.815	-0.456	-2.699	32.227
0.016	162.724	1.256	3.355	1	261.703	0.074	-0.791	-0.850	32.597
0.695	100.000	2.609	6.502	1	590.079	2.850	0.818	-2.353	33.247

Table 49: The best-fit parameters and χ^2 for the fit to the velocity dispersion data of the UMi dSph from Ref. [295]. Here the anisotropy profile is the Generalized Osipkov Merritt 3, here d.o.f = 18 and the inner slope γ is set to be 1.

Appendix D

IGRB constraints on the p-wave Dark Matter annihilation via a single or two mediators into the other fermion final states

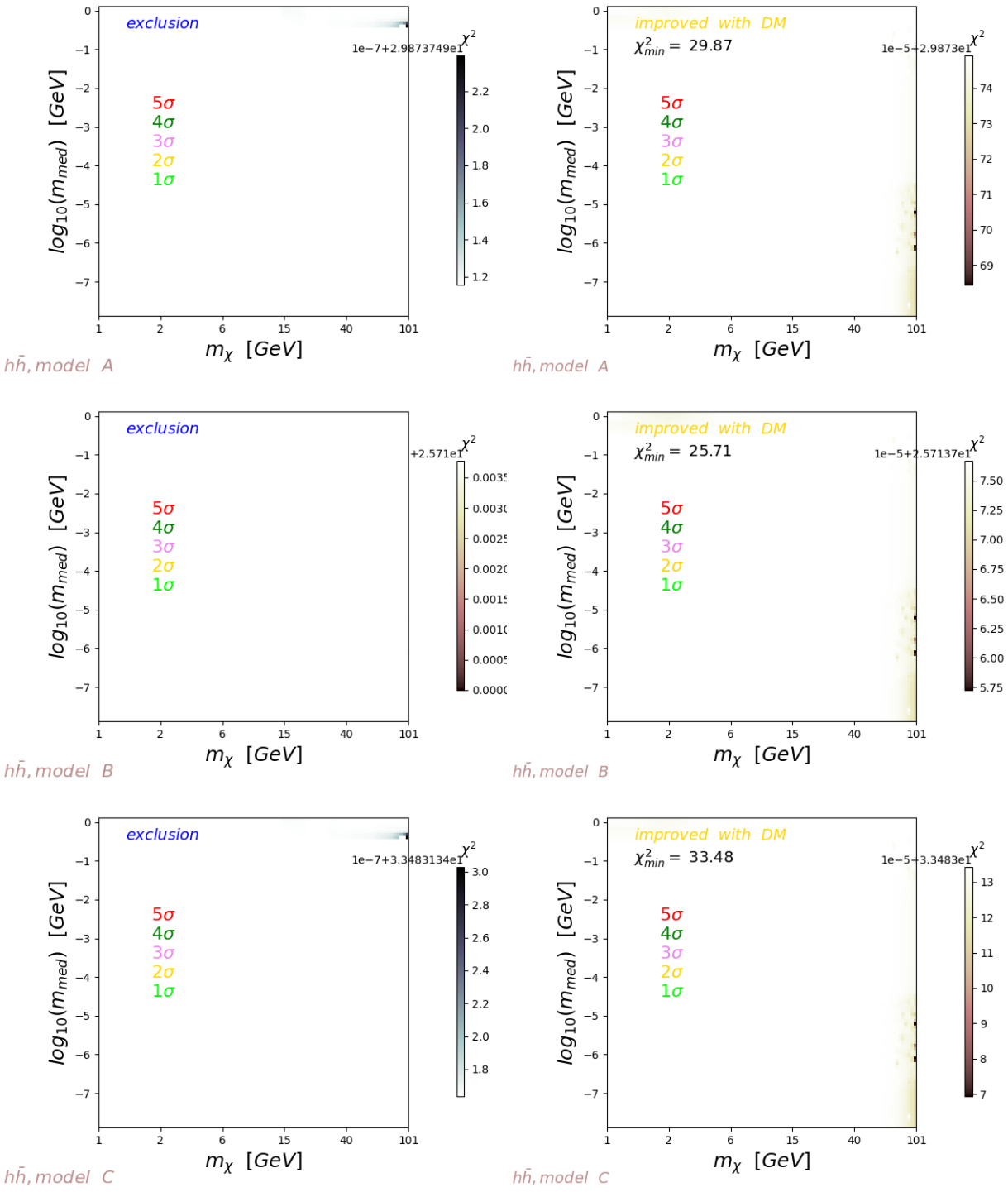

Figure 61: The distribution of χ^2 on the 2D map of m_χ and m_{med}.

$$\Phi_{tot,DM} = \Phi_2(\bar{\chi}\chi \to \phi\phi \to h\bar{h}), \tag{196}$$

The branching ratio of the $h\bar{h}$ channel is assumed to be $B(\bar{\chi}\chi \to h\bar{h}) = 100\%$. The annihilation of Dark Matter is Sommerfeld boosted. The extragalactic sources of IGRB are considered together with Dark Matter to fit the FermiLAT IGRB data [376]. The confidence contours are shown in different colors to enclose the best-fitting regions. The A, B, C models of the extragalactic sources are shown respectively on the top, middle, bottom panels. The exclusion fit and improved fit are respectively on the left and right side with colored contours.

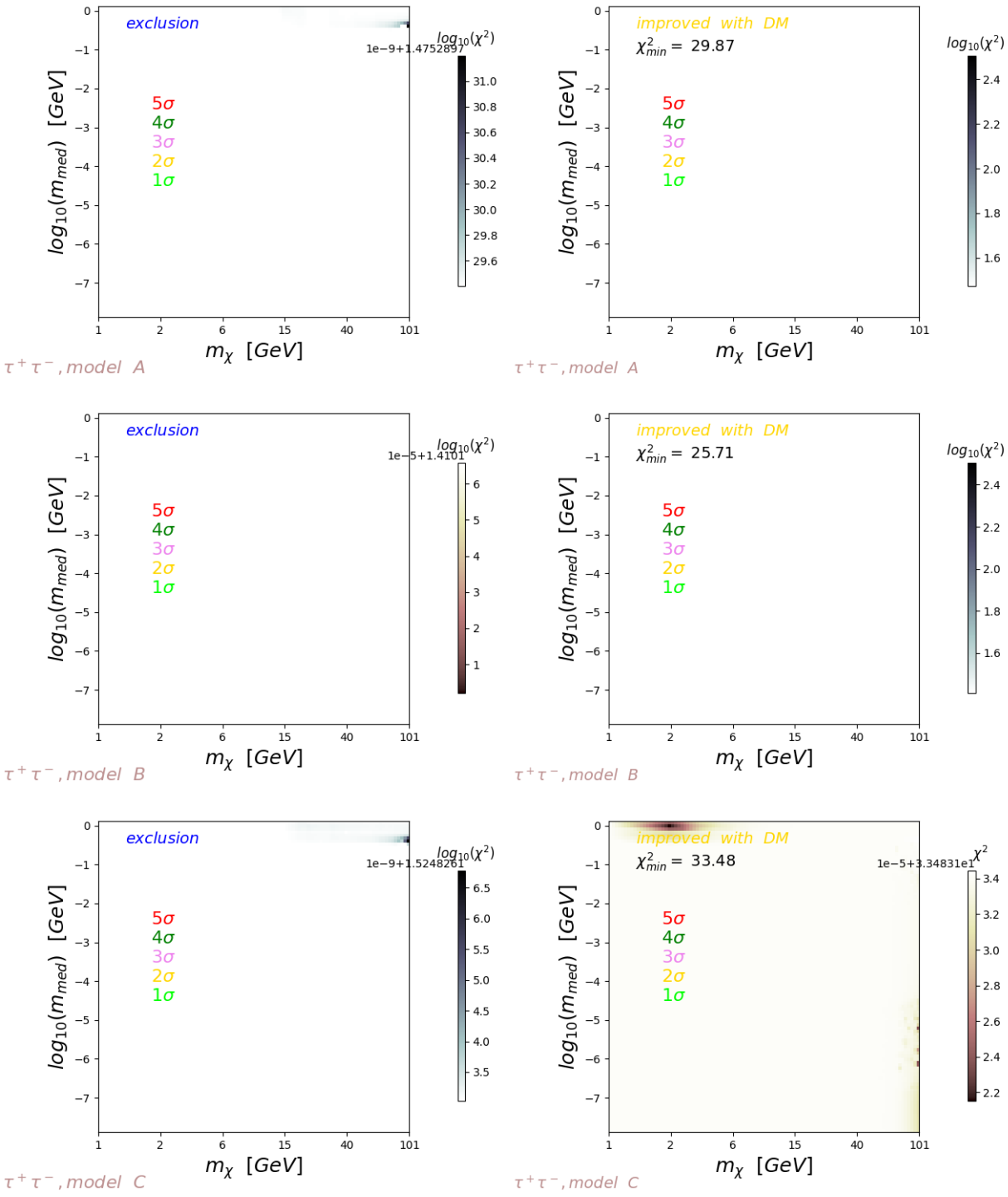

Figure 62: The distribution of χ^2 on the 2D map of m_χ and m_{med}.

$$\Phi_{tot,DM} = (1-\alpha)\cdot\Phi_1(\bar{\chi}\chi \to \phi \to \tau\bar{\tau}) + \alpha\cdot\Phi_2(\bar{\chi}\chi \to \phi\phi \to \tau\bar{\tau}), \tag{198}$$

with $\alpha = 1$. The branching ratio of the $\tau\bar{\tau}$ channel is assumed to be $B(\bar{\chi}\chi \to \tau\bar{\tau}) = 100\%$. And the annihilation of Dark Matter via a single mediator is Sommerfeld boosted. The extragalactic sources of IGRB are considered together with Dark Matter to fit the FermiLAT IGRB data [376]. The confidence contours are shown in different colors to enclose the best-fitting regions. The A, B, C models of the extragalactic sources are shown respectively on the top, middle, bottom panels. The exclusion fit and improved fit are respectively on the left and right side with colored contours.

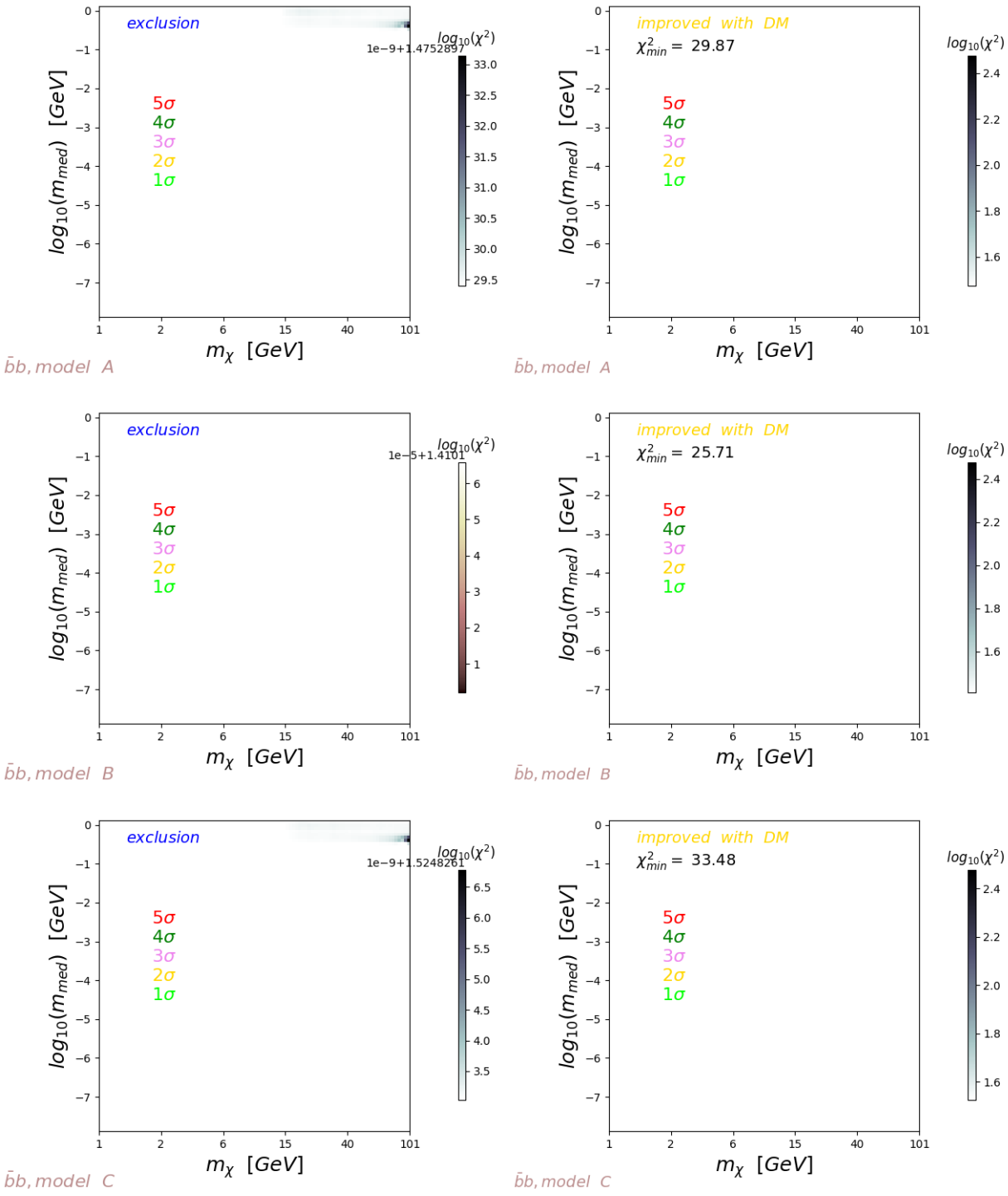

Figure 63: The distribution of χ^2 on the 2D map of m_χ and m_{med}.

$$\Phi_{tot,DM} = (1-\alpha)\cdot\Phi_1(\bar{\chi}\chi \to \phi \to b\bar{b}) + \alpha\cdot\Phi_2(\bar{\chi}\chi \to \phi\phi \to b\bar{b}), \tag{200}$$

with $\alpha = 1$. The branching ratio of the $b\bar{b}$ channel is assumed to be $B(\bar{\chi}\chi \to b\bar{b}) = 100\%$. And the annihilation of Dark Matter is Sommerfeld boosted. The extragalactic sources of IGRB are considered together with Dark Matter to fit the FermiLAT IGRB data [376]. The confidence contours are shown in different colors to enclose the best-fitting regions. The A, B, C models of the extragalactic sources are shown respectively on the top, middle, bottom panels. The exclusion fit and improved fit are respectively on the left and right side with colored contours.

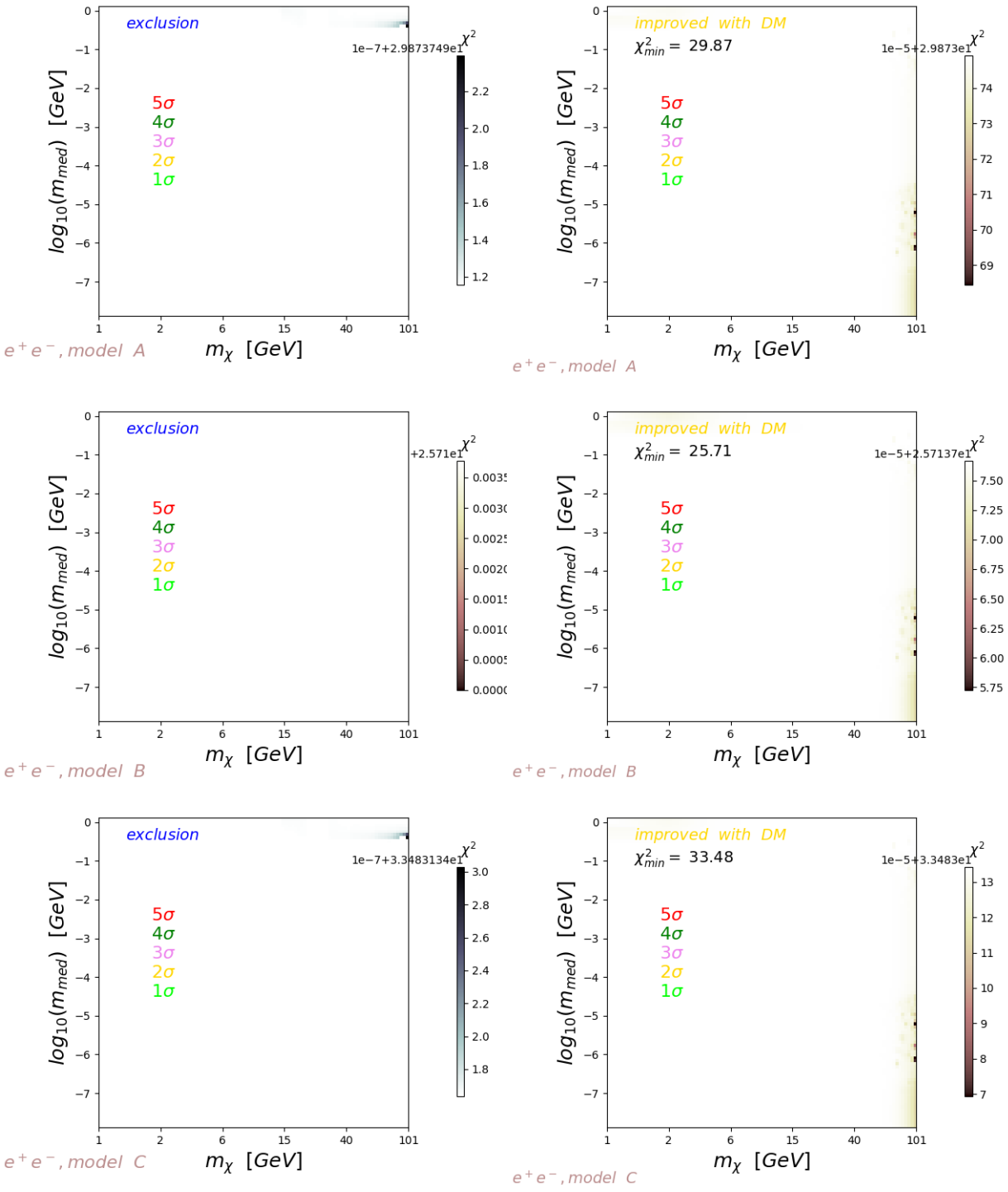

Figure 64: The distribution of χ^2 on the 2D map of m_χ and m_{med}.

$$\Phi_{tot,DM} = (1-\alpha)\cdot\Phi_1(\bar{\chi}\chi \to \phi \to e^+e^-) + \alpha\cdot\Phi_2(\bar{\chi}\chi \to \phi\phi \to e^+e^-), \tag{202}$$

with $\alpha = 1$. The branching ratio of the e^+e^- channel is assumed to be $B(\bar{\chi}\chi \to e^+e^-) = 100\%$. The annihilation of Dark Matter is Sommerfeld boosted. The extragalactic sources of IGRB are considered together with Dark Matter to fit the FermiLAT IGRB data [376]. The confidence contours are shown in different colors to enclose the best-fitting regions. The A, B, C models of the extragalactic sources are shown respectively on the top, middle, bottom panels. The exclusion fit and improved fit are respectively on the left and right side with colored contours.

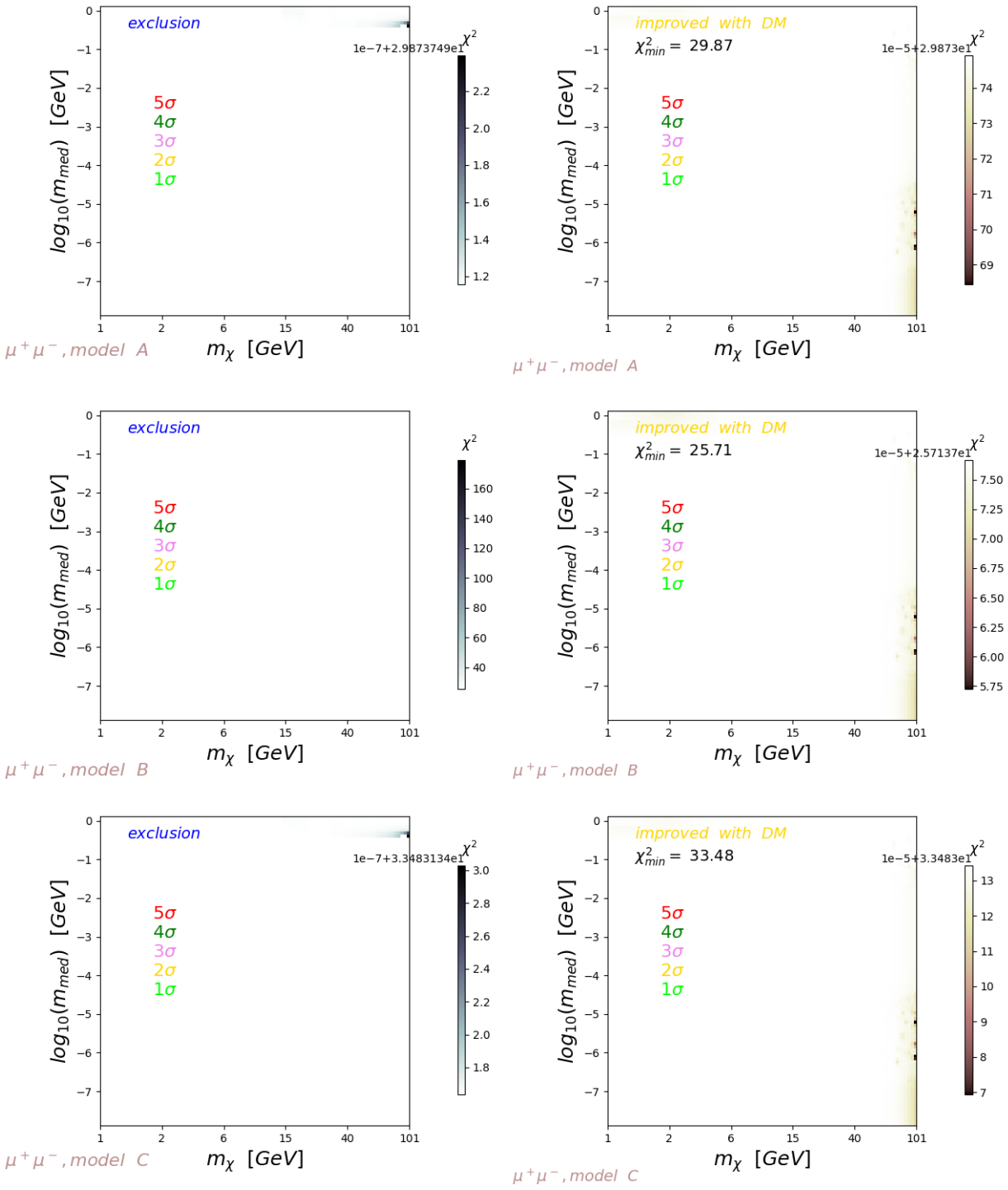

Figure 65: The distribution of χ^2 on the 2D map of m_χ and m_{med}.

$$\Phi_{tot,DM} = (1-\alpha)\cdot\Phi_1(\bar{\chi}\chi \to \phi \to \mu^+\mu^-) + \alpha\cdot\Phi_2(\bar{\chi}\chi \to \phi\phi \to \mu^+\mu^-), \tag{204}$$

with $\alpha = 1$. The branching ratio of the $\mu^+\mu^-$ channel is assumed to be $B(\bar{\chi}\chi \to \mu^+\mu^-) = 100\%$. The annihilation of Dark Matter is Sommerfeld boosted. The extragalactic sources of IGRB are considered together with Dark Matter to fit the FermiLAT IGRB data [376]. The confidence contours are shown in different colors to enclose the best-fitting regions. The A, B, C models of the extragalactic sources are shown respectively on the top, middle, bottom panels. The exclusion fit and improved fit are respectively on the left and right side with colored contours.

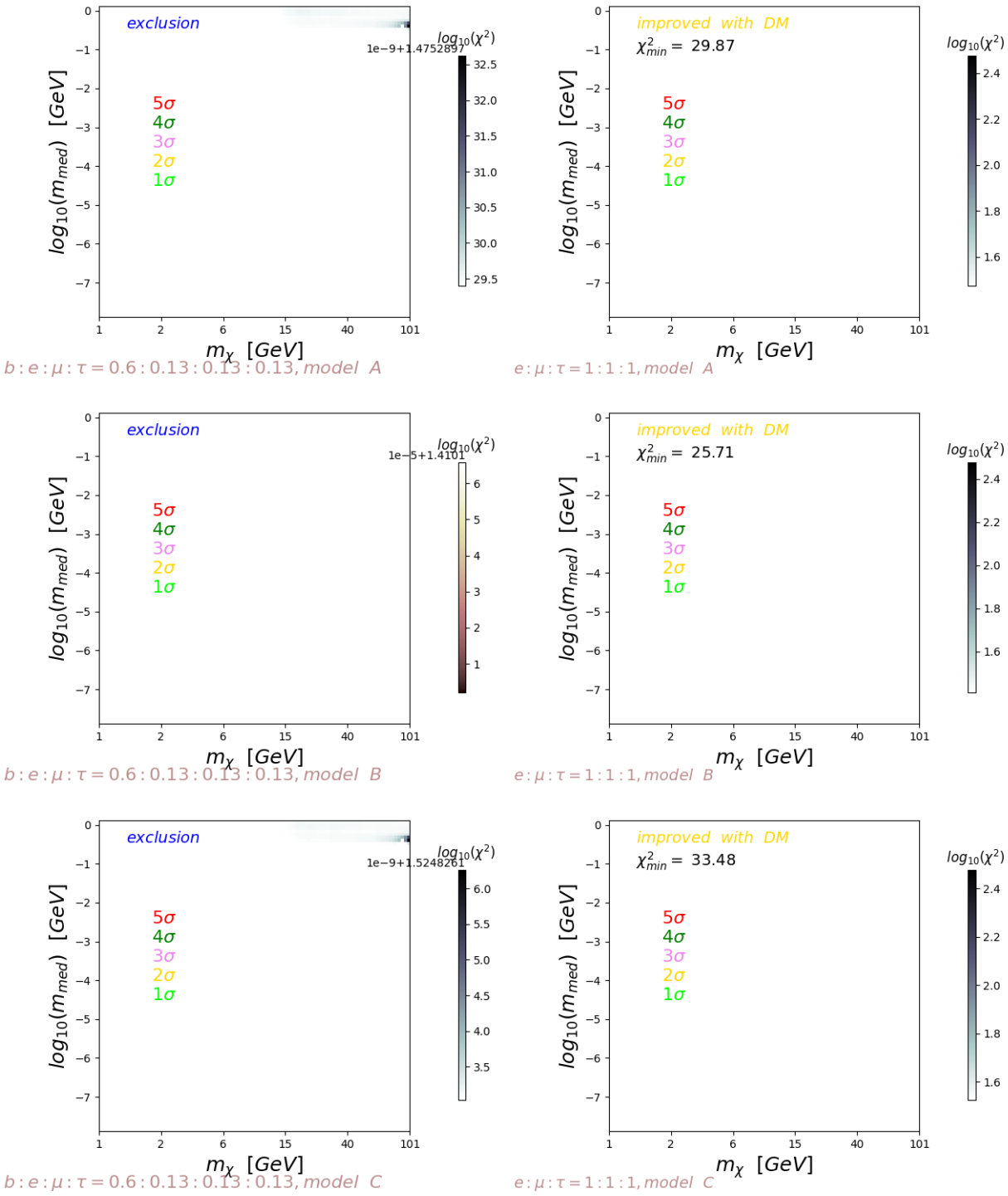

Figure 66: The distribution of χ^2 on the 2D map of m_χ and m_{med}.

$$\Phi_{tot,DM} = (1-\alpha)\cdot\Phi_1(\bar{\chi}\chi \to \phi \to e^+e^-, \mu^+\mu^-, \tau\bar{\tau}) + \alpha\cdot\Phi_2(\bar{\chi}\chi \to \phi\phi \to e^+e^-, \mu^+\mu^-, \tau\bar{\tau}), \quad (206)$$

with $\alpha = 1$. The branching ratio of the $e^+e^-, \mu^+\mu^-, \tau\bar{\tau}$ channels are assumed to be respectively 33.3%, 33.3%, 33.3%. The annihilation of Dark Matter is Sommerfeld boosted. The extragalactic sources of IGRB are considered together with Dark Matter to fit the FermiLAT IGRB data [376]. The confidence contours are shown in different colors to enclose the best-fitting regions. The A, B, C models of the extragalactic sources are shown respectively on the top, middle, bottom panels. The exclusion fit and improved fit are respectively on the left and right side with colored contours.

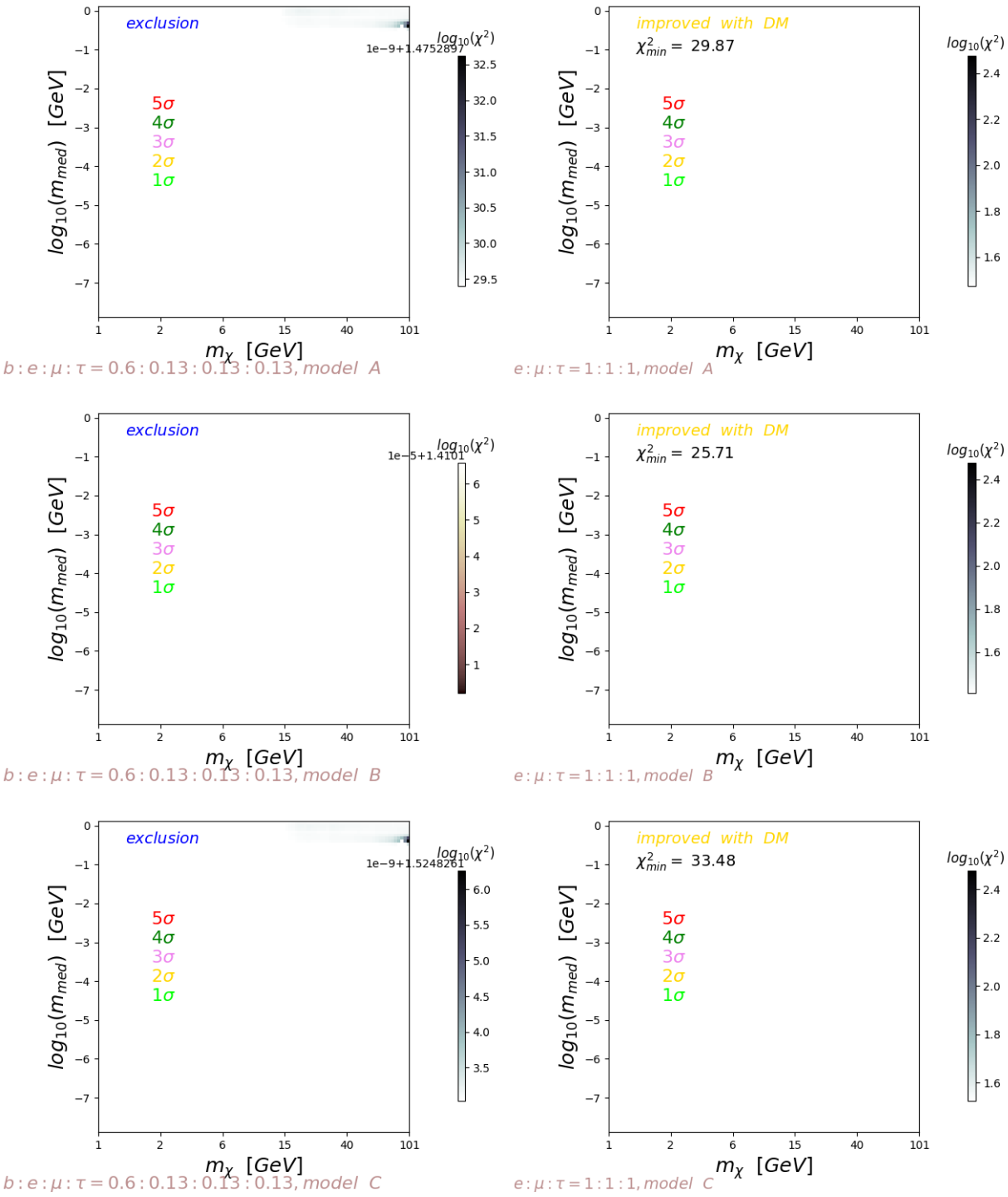

Figure 67: The distribution of χ^2 on the 2D map of m_χ and m_{med}.

$$\Phi_{tot,DM} = (1-\alpha)\cdot\Phi_1(\bar{\chi}\chi \to \phi \to b\bar{b}, e^+e^-, \mu^+\mu^-, \tau\bar{\tau}) + \alpha\cdot\Phi_2(\bar{\chi}\chi \to \phi\phi \to b\bar{b}, e^+e^-, \mu^+\mu^-, \tau\bar{\tau}), \quad (208)$$

with $\alpha = 1$. The branching ratio of the $b\bar{b}, e^+e^-, \mu^+\mu^-, \tau\bar{\tau}$ channels are assumed to be respectively 60%,13.3%, 13.3%, 13.3%. The annihilation of Dark Matter is Sommerfeld boosted. The extragalactic sources of IGRB are considered together with Dark Matter to fit the FermiLAT IGRB data [376]. The confidence contours are shown in different colors to enclose the best-fitting regions. The A, B, C models of the extragalactic sources are shown respectively on the top, middle, bottom panels. The exclusion fit and improved fit are respectively on the left and right side with colored contours.

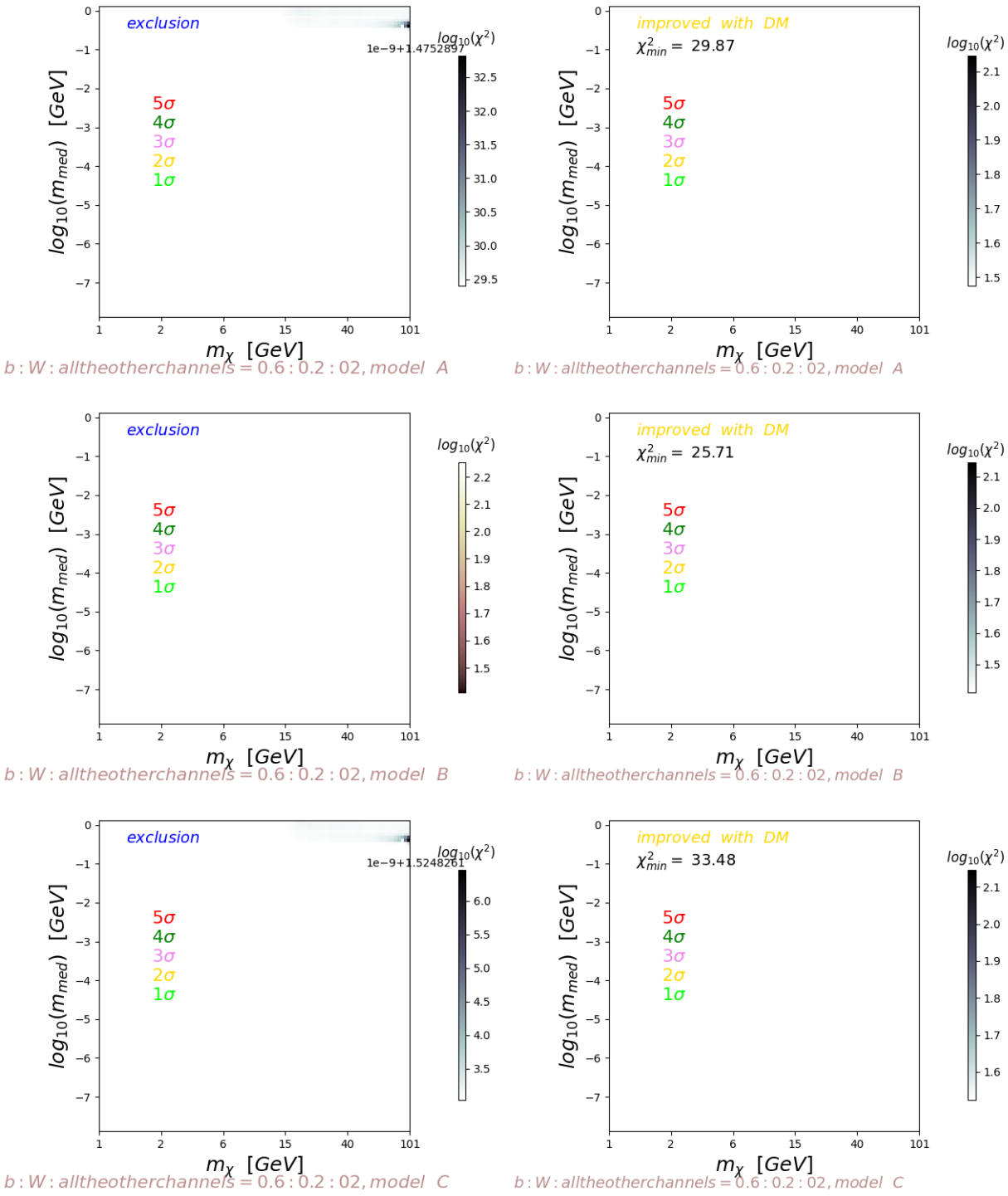

Figure 68: The distribution of χ^2 on the 2D map of m_χ and m_{med}.

$$\Phi_{tot,DM} = (1-\alpha)\cdot\Phi_1(\bar{\chi}\chi \to \phi \to b\bar{b}, W^+W^-, the\,others) + \alpha\cdot\Phi_2(\bar{\chi}\chi \to \phi\phi \to b\bar{b}, W^+W^-, the\,others), \quad (210)$$

with $\alpha = 1$. The branching ratio of the $b\bar{b}, W^+W^-$channels are assumed to be respectively 60%,20%, and 1/30 for each of the $\gamma\gamma$, $h\bar{h}$, $g\bar{g}$, $\tau^+\tau^-$, $\mu^+\mu^-$, e^+e^-channels. The annihilation of Dark Matter is Sommerfeld boosted. The extragalactic sources of IGRB are considered together with Dark Matter to fit the FermiLAT IGRB data [376]. The confidence contours are shown in different colors to enclose the best-fitting regions. The A, B, C models of the extragalactic sources are shown respectively on the top, middle, bottom panels. The exclusion fit and improved fit are respectively on the left and right side with colored contours.

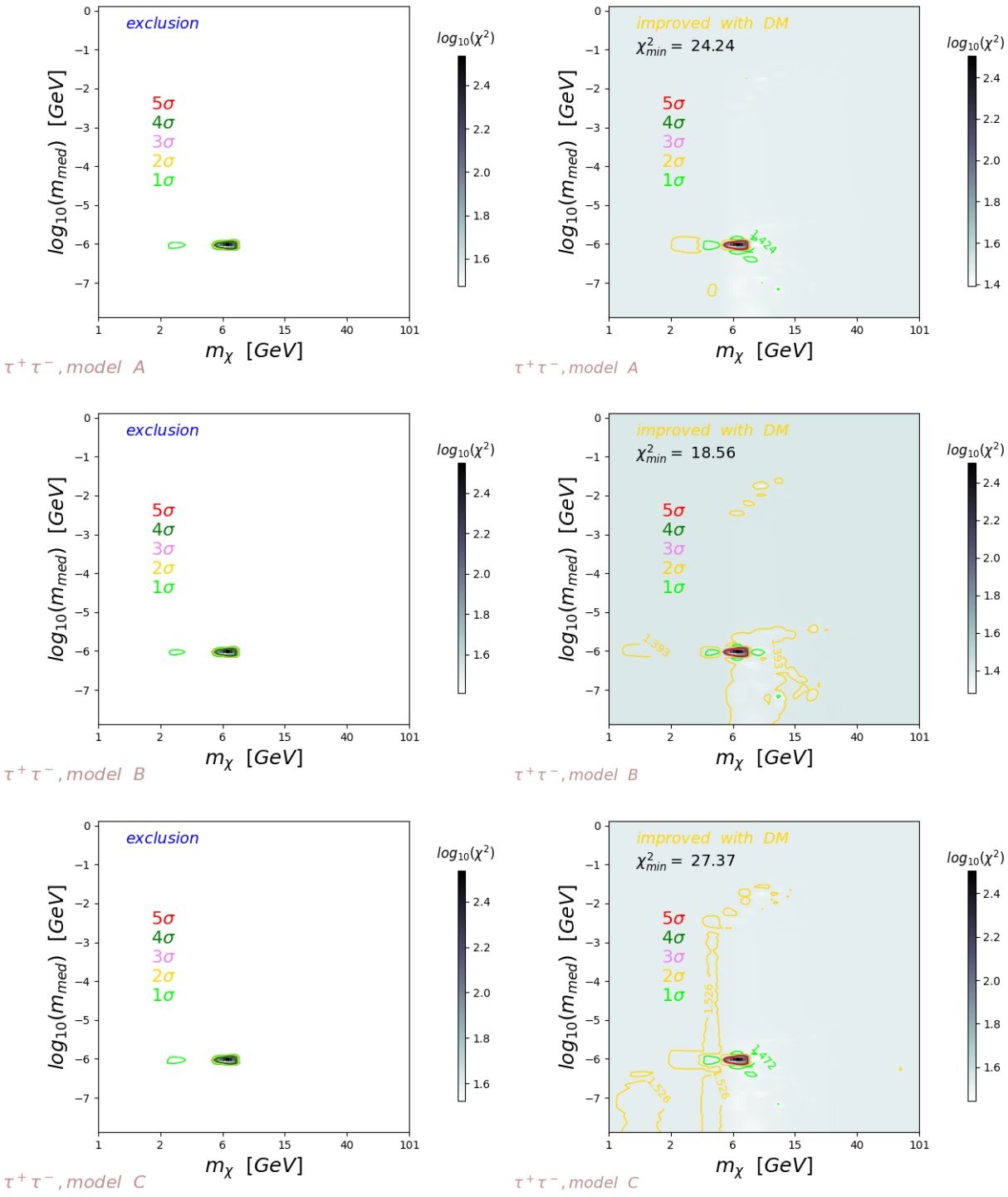

Figure 69: The distribution of χ^2 on the 2D map of m_χ and m_{med}.

$$\Phi_{tot,DM} = (1-\alpha)\cdot\Phi_1(\bar{\chi}\chi \to \phi \to \tau\bar{\tau}) + \alpha\cdot\Phi_2(\bar{\chi}\chi \to \phi\phi \to \tau\bar{\tau}), \tag{212}$$

with $\alpha = 0.9$. The branching ratio of the $\tau\bar{\tau}$ channel is assumed to be $B(\bar{\chi}\chi \to \tau\bar{\tau}) = 100\%$. And the annihilation of Dark Matter via a single mediator is Sommerfeld boosted. The extragalactic sources of IGRB are considered together with Dark Matter to fit the FermiLAT IGRB data [376]. The confidence contours are shown in different colors to enclose the best-fitting regions. The A, B, C models of the extragalactic sources are shown respectively on the top, middle, bottom panels. The exclusion fit and improved fit are respectively on the left and right side with colored contours.

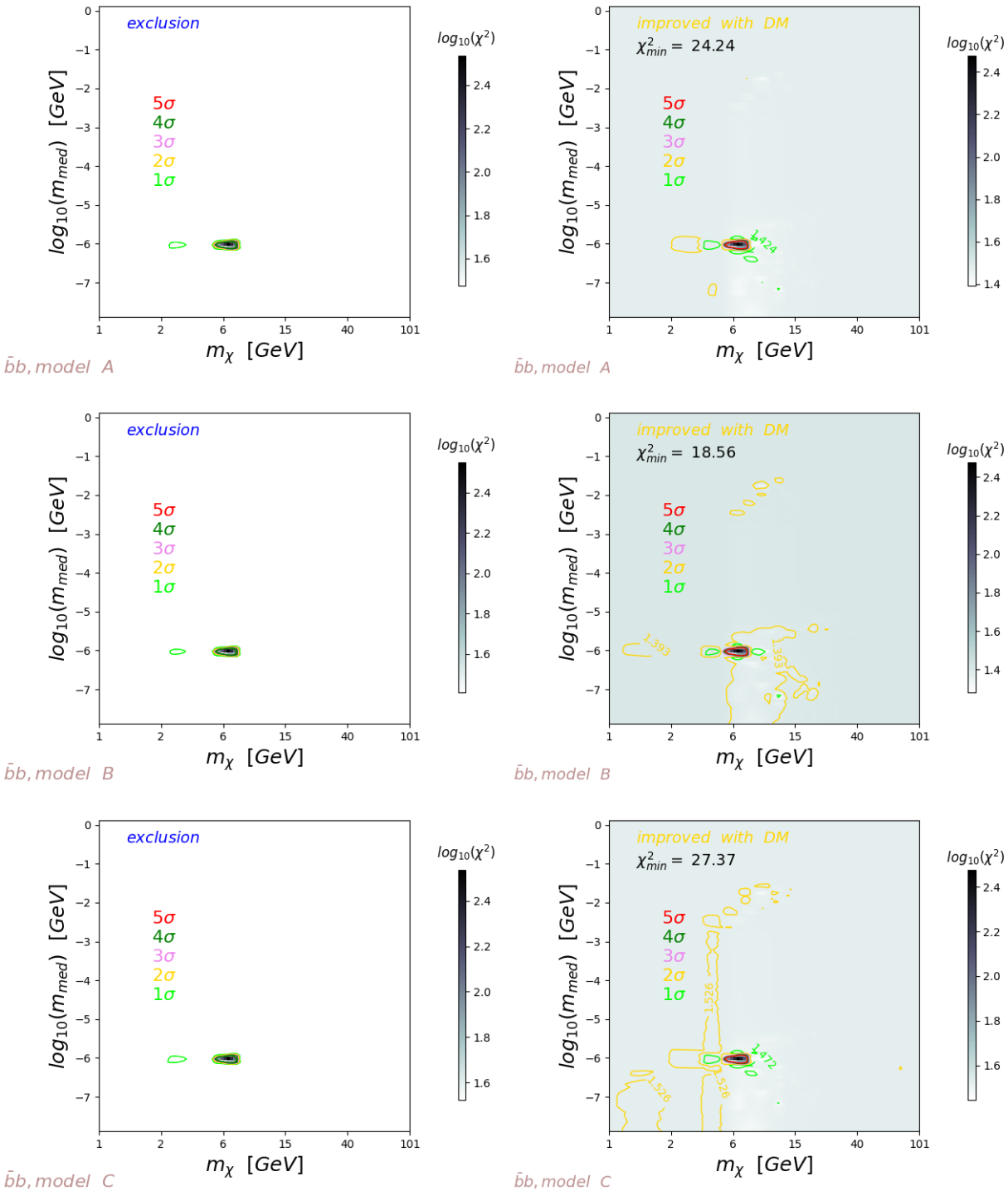

Figure 70: The distribution of χ^2 on the 2D map of m_χ and m_{med}.

$$\Phi_{tot,DM} = (1-\alpha)\cdot\Phi_1(\bar{\chi}\chi \to \phi \to b\bar{b}) + \alpha\cdot\Phi_2(\bar{\chi}\chi \to \phi\phi \to b\bar{b}), \tag{214}$$

with $\alpha = 0.9$. The branching ratio of the $b\bar{b}$ channel is assumed to be $B(\bar{\chi}\chi \to b\bar{b}) = 100\%$. And the annihilation of Dark Matter is Sommerfeld boosted. The extragalactic sources of IGRB are considered together with Dark Matter to fit the FermiLAT IGRB data [376]. The confidence contours are shown in different colors to enclose the best-fitting regions. The A, B, C models of the extragalactic sources are shown respectively on the top, middle, bottom panels. The exclusion fit and improved fit are respectively on the left and right side with colored contours.

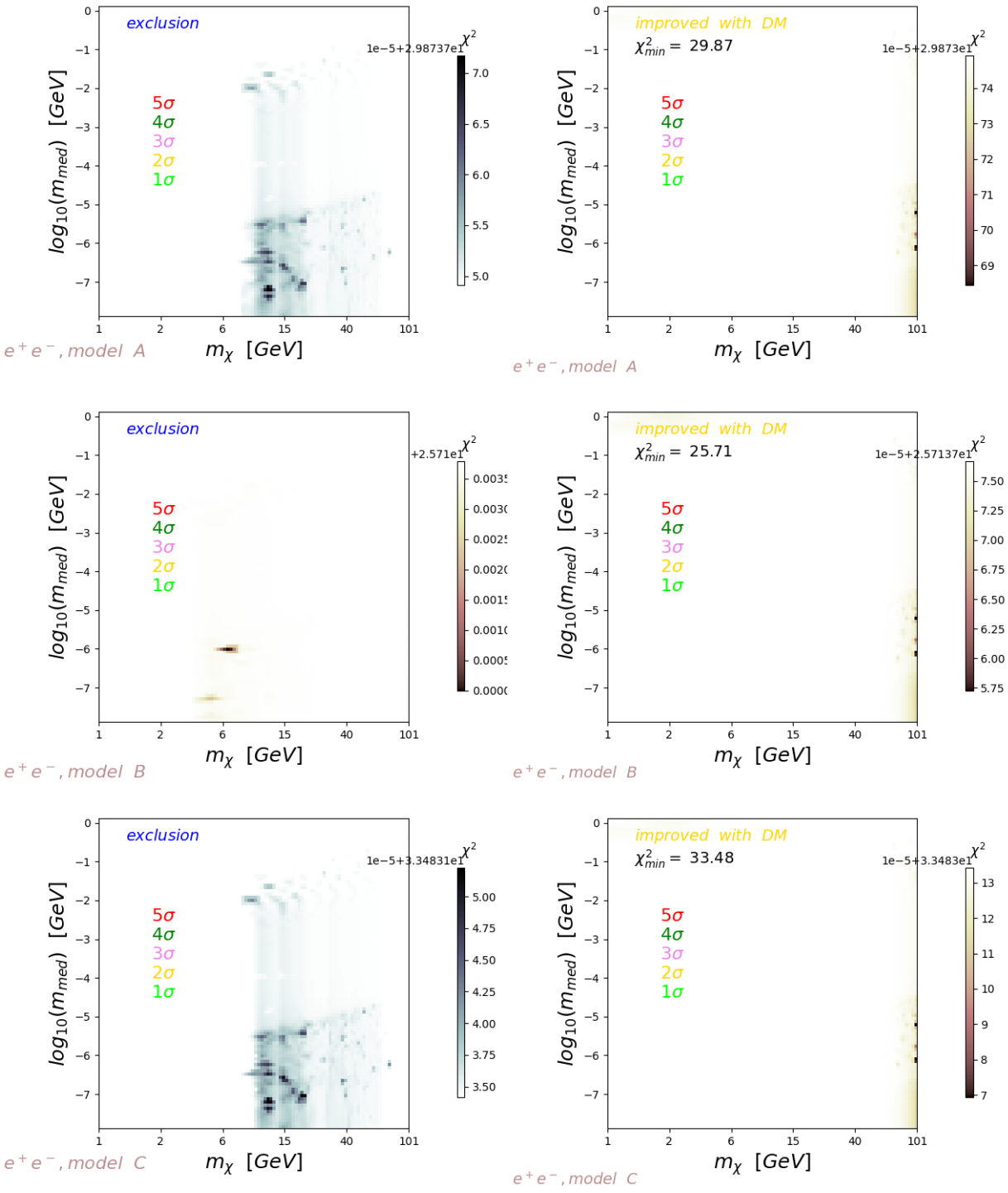

Figure 71: The distribution of χ^2 on the 2D map of m_χ and m_{med}.

$$\Phi_{tot,DM} = (1-\alpha)\cdot\Phi_1(\bar{\chi}\chi \to \phi \to e^+e^-) + \alpha\cdot\Phi_2(\bar{\chi}\chi \to \phi\phi \to e^+e^-), \tag{216}$$

with $\alpha = 0.9$. The branching ratio of the e^+e^- channel is assumed to be $B(\bar{\chi}\chi \to e^+e^-) = 100\%$. The annihilation of Dark Matter is Sommerfeld boosted. The extragalactic sources of IGRB are considered together with Dark Matter to fit the FermiLAT IGRB data [376]. The confidence contours are shown in different colors to enclose the best-fitting regions. The A, B, C models of the extragalactic sources are shown respectively on the top, middle, bottom panels. The exclusion fit and improved fit are respectively on the left and right side with colored contours.

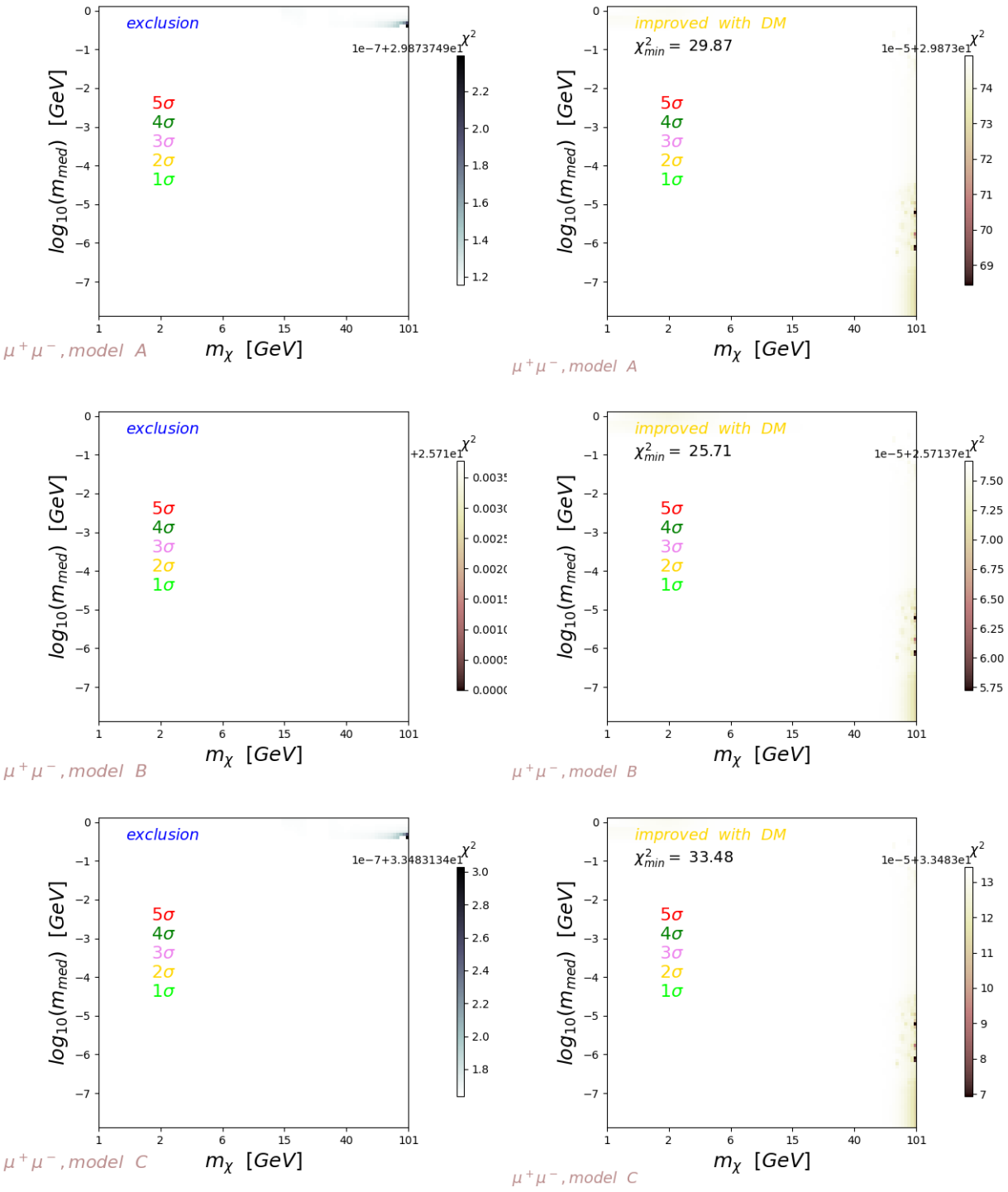

Figure 72: The distribution of χ^2 on the 2D map of m_χ and m_{med}.

$$\Phi_{tot,DM} = (1-\alpha)\cdot\Phi_1(\bar{\chi}\chi \to \phi \to \mu^+\mu^-) + \alpha\cdot\Phi_2(\bar{\chi}\chi \to \phi\phi \to \mu^+\mu^-), \tag{218}$$

with $\alpha = 0.9$. The branching ratio of the $\mu^+\mu^-$ channel is assumed to be $B(\bar{\chi}\chi \to \mu^+\mu^-) = 100\%$. The annihilation of Dark Matter is Sommerfeld boosted. The extragalactic sources of IGRB are considered together with Dark Matter to fit the FermiLAT IGRB data [376]. The confidence contours are shown in different colors to enclose the best-fitting regions. The A, B, C models of the extragalactic sources are shown respectively on the top, middle, bottom panels. The exclusion fit and improved fit are respectively on the left and right side with colored contours.

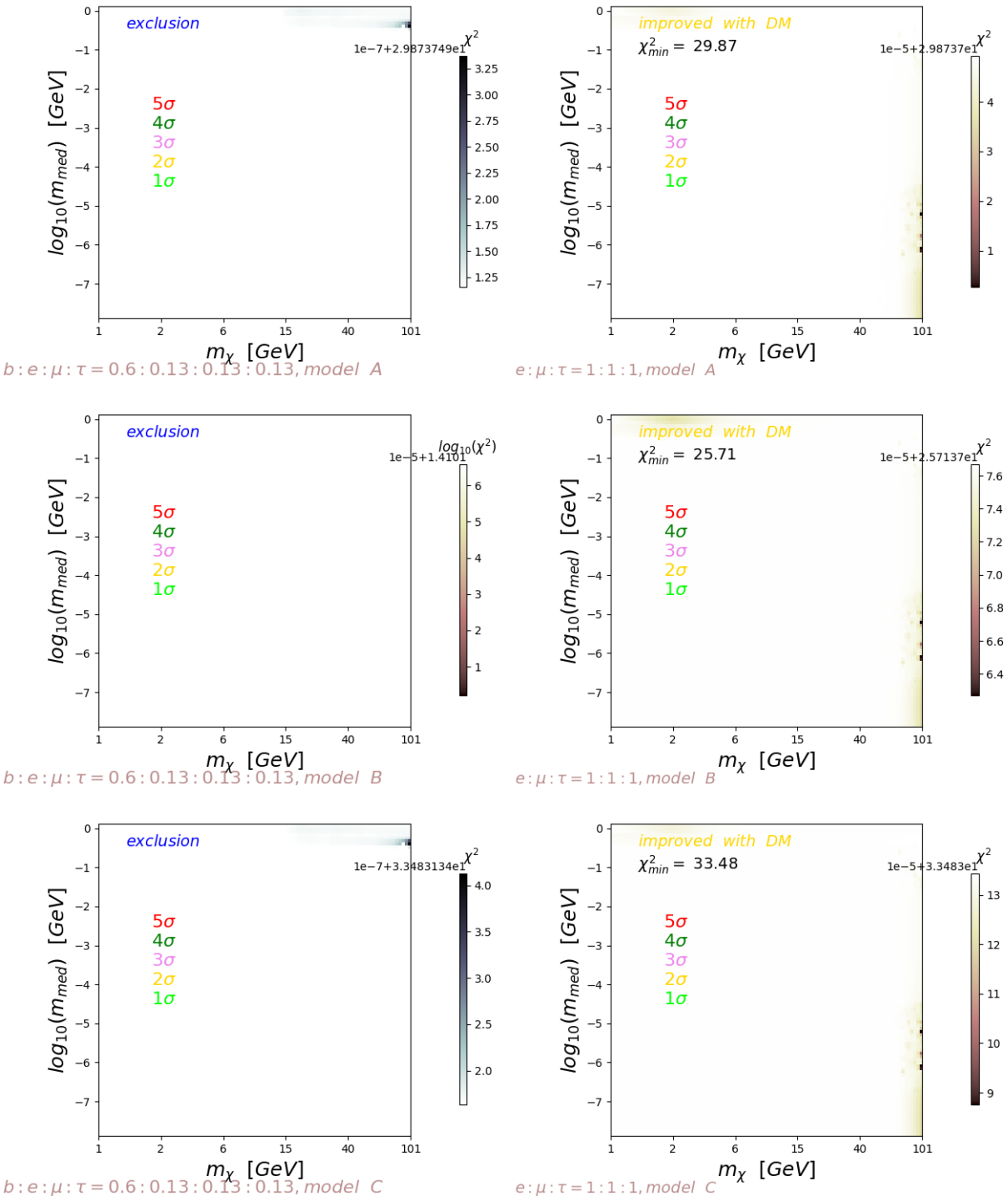

Figure 73: The distribution of χ^2 on the 2D map of m_χ and m_{med}.

$$\Phi_{tot,DM} = (1-\alpha)\cdot\Phi_1(\bar{\chi}\chi \to \phi \to e^+e^-, \mu^+\mu^-, \tau\bar{\tau}) + \alpha\cdot\Phi_2(\bar{\chi}\chi \to \phi\phi \to e^+e^-, \mu^+\mu^-, \tau\bar{\tau}), \quad (220)$$

with $\alpha = 0.9$. The branching ratio of the $e^+e^-, \mu^+\mu^-, \tau\bar{\tau}$ channels are assumed to be respectively 33.3%, 33.3%, 33.3%. The annihilation of Dark Matter is Sommerfeld boosted. The extragalactic sources of IGRB are considered together with Dark Matter to fit the FermiLAT IGRB data [376]. The confidence contours are shown in different colors to enclose the best-fitting regions. The A, B, C models of the extragalactic sources are shown respectively on the top, middle, bottom panels. The exclusion fit and improved fit are respectively on the left and right side with colored contours.

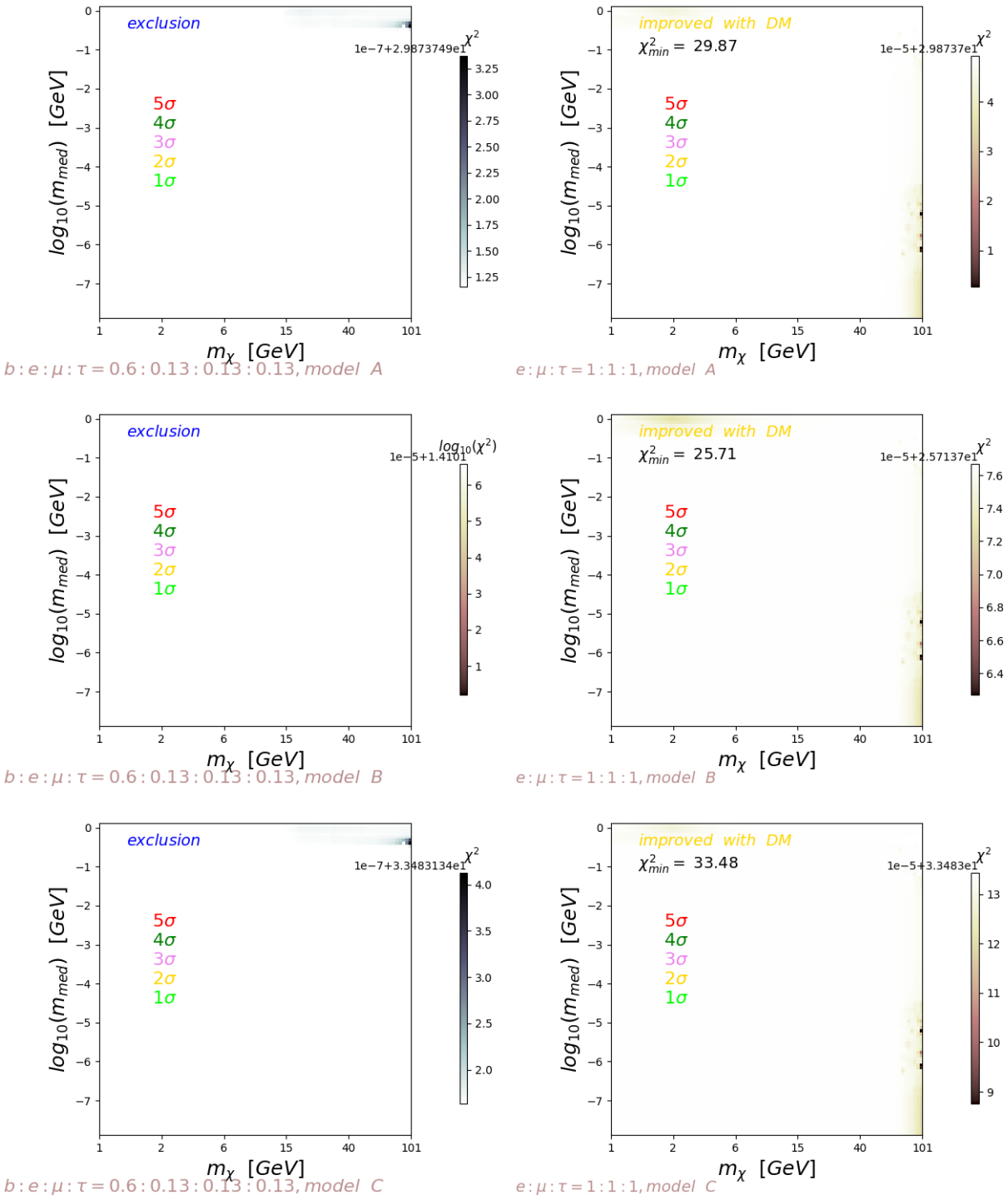

Figure 74: The distribution of χ^2 on the 2D map of m_χ and m_{med}.

$$\Phi_{tot,DM} = (1-\alpha)\cdot\Phi_1(\bar{\chi}\chi \to \phi \to b\bar{b}, e^+e^-, \mu^+\mu^-, \tau\bar{\tau}) + \alpha\cdot\Phi_2(\bar{\chi}\chi \to \phi\phi \to b\bar{b}, e^+e^-, \mu^+\mu^-, \tau\bar{\tau}), \quad (222)$$

with $\alpha = 0.9$. The branching ratio of the $b\bar{b}, e^+e^-, \mu^+\mu^-, \tau\bar{\tau}$ channels are assumed to be respectively 60%,13.3%, 13.3%, 13.3%. The annihilation of Dark Matter is Sommerfeld boosted. The extragalactic sources of IGRB are considered together with Dark Matter to fit the FermiLAT IGRB data [376]. The confidence contours are shown in different colors to enclose the best-fitting regions. The A, B, C models of the extragalactic sources are shown respectively on the top, middle, bottom panels. The exclusion fit and improved fit are respectively on the left and right side with colored contours.

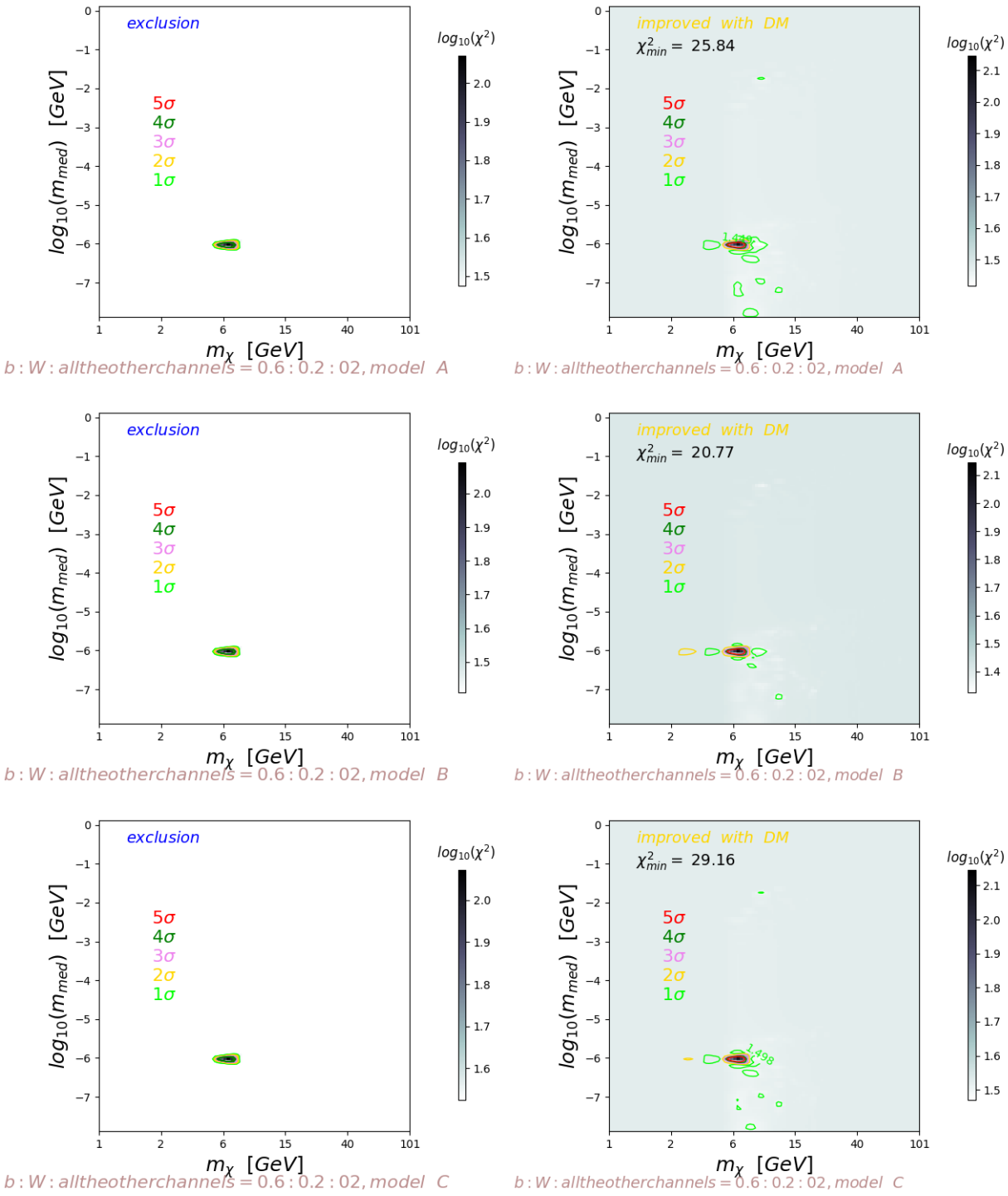

Figure 75: The distribution of χ^2 on the 2D map of m_χ and m_{med}.

$$\Phi_{tot,DM} = (1-\alpha)\cdot\Phi_1(\bar{\chi}\chi \to \phi \to b\bar{b}, W^+W^-, the\ others) + \alpha\cdot\Phi_2(\bar{\chi}\chi \to \phi\phi \to b\bar{b}, W^+W^-, the\ others), \quad (224)$$

with $\alpha = 0.9$. The branching ratio of the $b\bar{b}, W^+W^-$channels are assumed to be respectively 60%,20%, and 1/30 for each of the $\gamma\gamma$, $h\bar{h}$, $g\bar{g}$, $\tau^+\tau^-$, $\mu^+\mu^-$, e^+e^-channels. The annihilation of Dark Matter is Sommerfeld boosted. The extragalactic sources of IGRB are considered together with Dark Matter to fit the FermiLAT IGRB data [376]. The confidence contours are shown in different colors to enclose the best-fitting regions. The A, B, C models of the extragalactic sources are shown respectively on the top, middle, bottom panels. The exclusion fit and improved fit are respectively on the left and right side with colored contours.

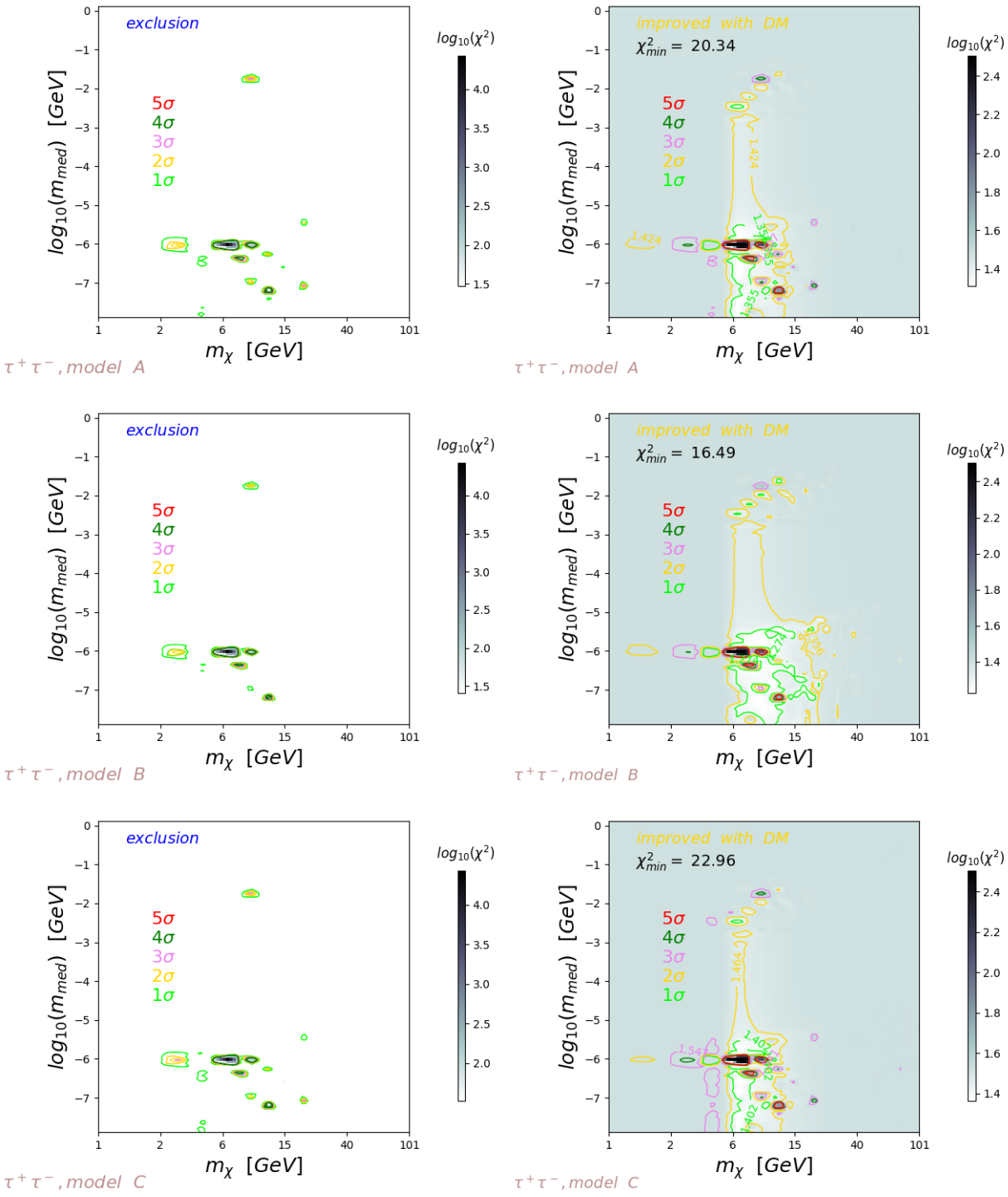

Figure 76: The distribution of χ^2 on the 2D map of m_χ and m_{med}.

$$\Phi_{tot,DM} = (1-\alpha)\cdot\Phi_1(\bar{\chi}\chi \to \phi \to \tau\bar{\tau}) + \alpha\cdot\Phi_2(\bar{\chi}\chi \to \phi\phi \to \tau\bar{\tau}), \tag{226}$$

with $\alpha = 0.1$. The branching ratio of the $\tau\bar{\tau}$ channel is assumed to be $B(\bar{\chi}\chi \to \tau\bar{\tau}) = 100\%$. And the annihilation of Dark Matter via a single mediator is Sommerfeld boosted. The extragalactic sources of IGRB are considered together with Dark Matter to fit the FermiLAT IGRB data [376]. The confidence contours are shown in different colors to enclose the best-fitting regions. The A, B, C models of the extragalactic sources are shown respectively on the top, middle, bottom panels. The exclusion fit and improved fit are respectively on the left and right side with colored contours.

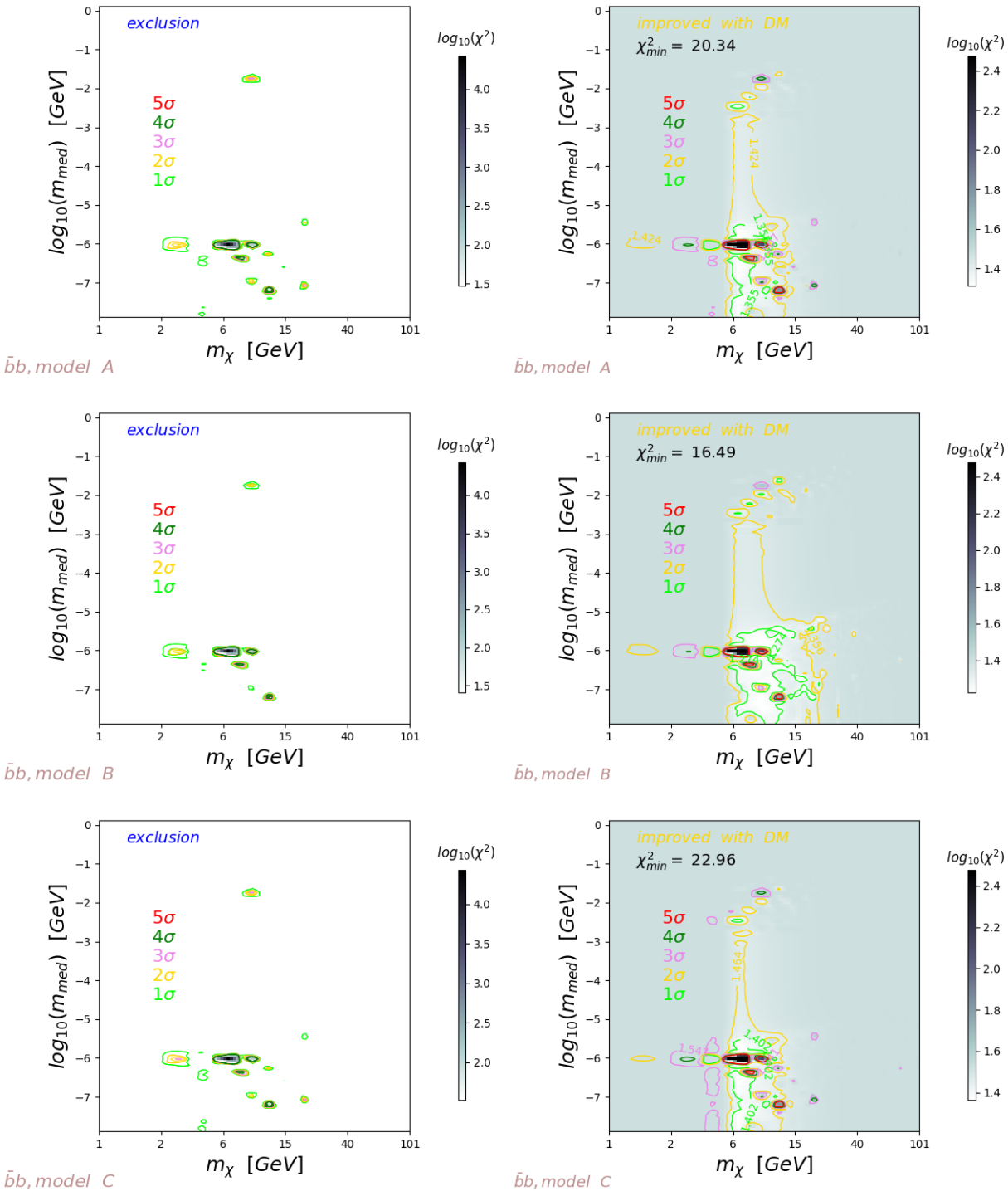

Figure 77: The distribution of χ^2 on the 2D map of m_χ and m_{med}.

$$\Phi_{tot,DM} = (1-\alpha)\cdot\Phi_1(\bar{\chi}\chi \to \phi \to b\bar{b}) + \alpha\cdot\Phi_2(\bar{\chi}\chi \to \phi\phi \to b\bar{b}), \tag{228}$$

with $\alpha = 0.1$. The branching ratio of the $b\bar{b}$ channel is assumed to be $B(\bar{\chi}\chi \to b\bar{b}) = 100\%$. And the annihilation of Dark Matter is Sommerfeld boosted. The extragalactic sources of IGRB are considered together with Dark Matter to fit the FermiLAT IGRB data [376]. The confidence contours are shown in different colors to enclose the best-fitting regions. The A, B, C models of the extragalactic sources are shown respectively on the top, middle, bottom panels. The exclusion fit and improved fit are respectively on the left and right side with colored contours.

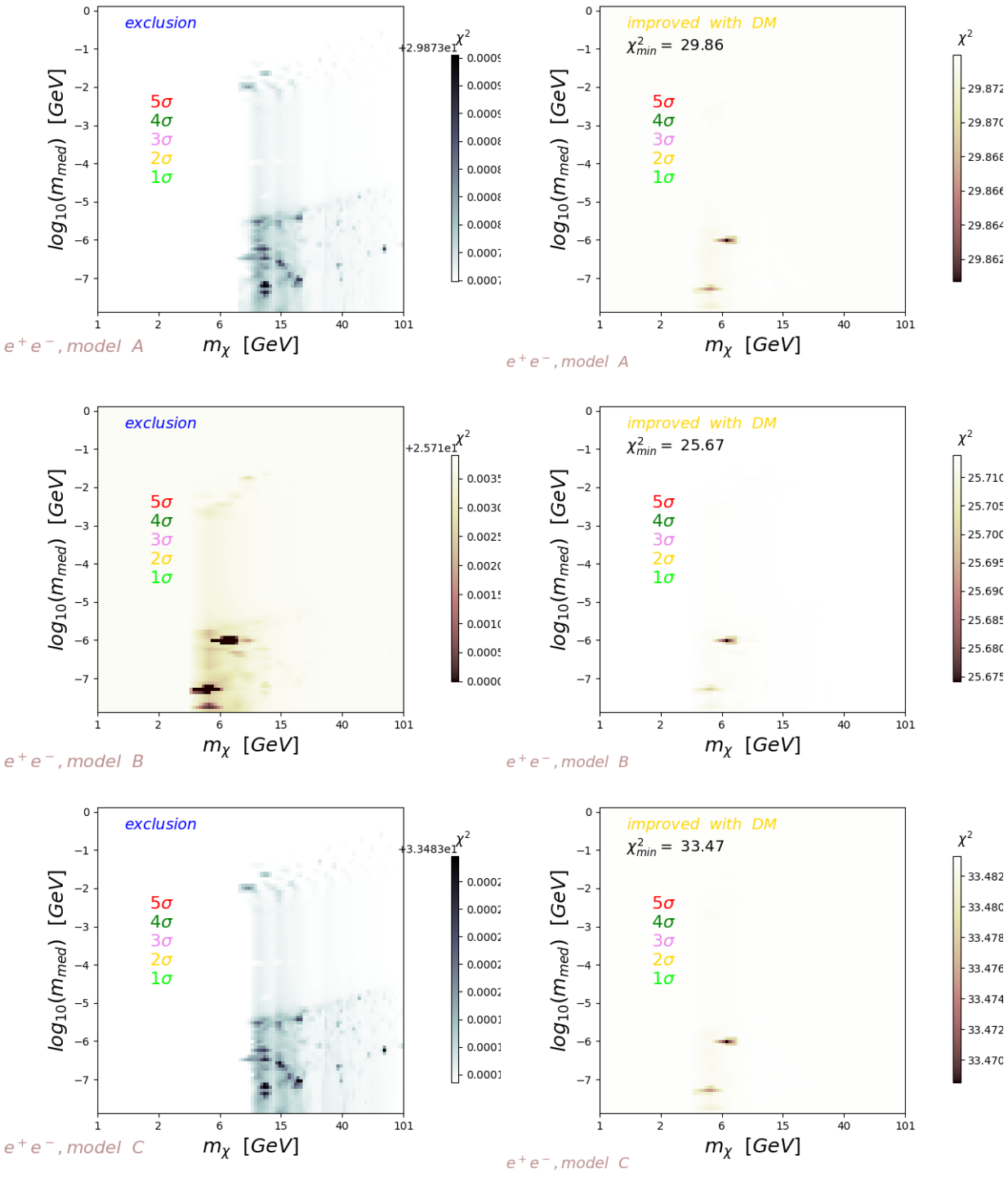

Figure 78: The distribution of χ^2 on the 2D map of m_χ and m_{med}.

$$\Phi_{tot,DM} = (1-\alpha)\cdot\Phi_1(\bar{\chi}\chi \to \phi \to e^+e^-) + \alpha\cdot\Phi_2(\bar{\chi}\chi \to \phi\phi \to e^+e^-), \tag{230}$$

with $\alpha = 0.1$. The branching ratio of the e^+e^- channel is assumed to be $B(\bar{\chi}\chi \to e^+e^-) = 100\%$. The annihilation of Dark Matter is Sommerfeld boosted. The extragalactic sources of IGRB are considered together with Dark Matter to fit the FermiLAT IGRB data [376]. The confidence contours are shown in different colors to enclose the best-fitting regions. The A, B, C models of the extragalactic sources are shown respectively on the top, middle, bottom panels. The exclusion fit and improved fit are respectively on the left and right side with colored contours.

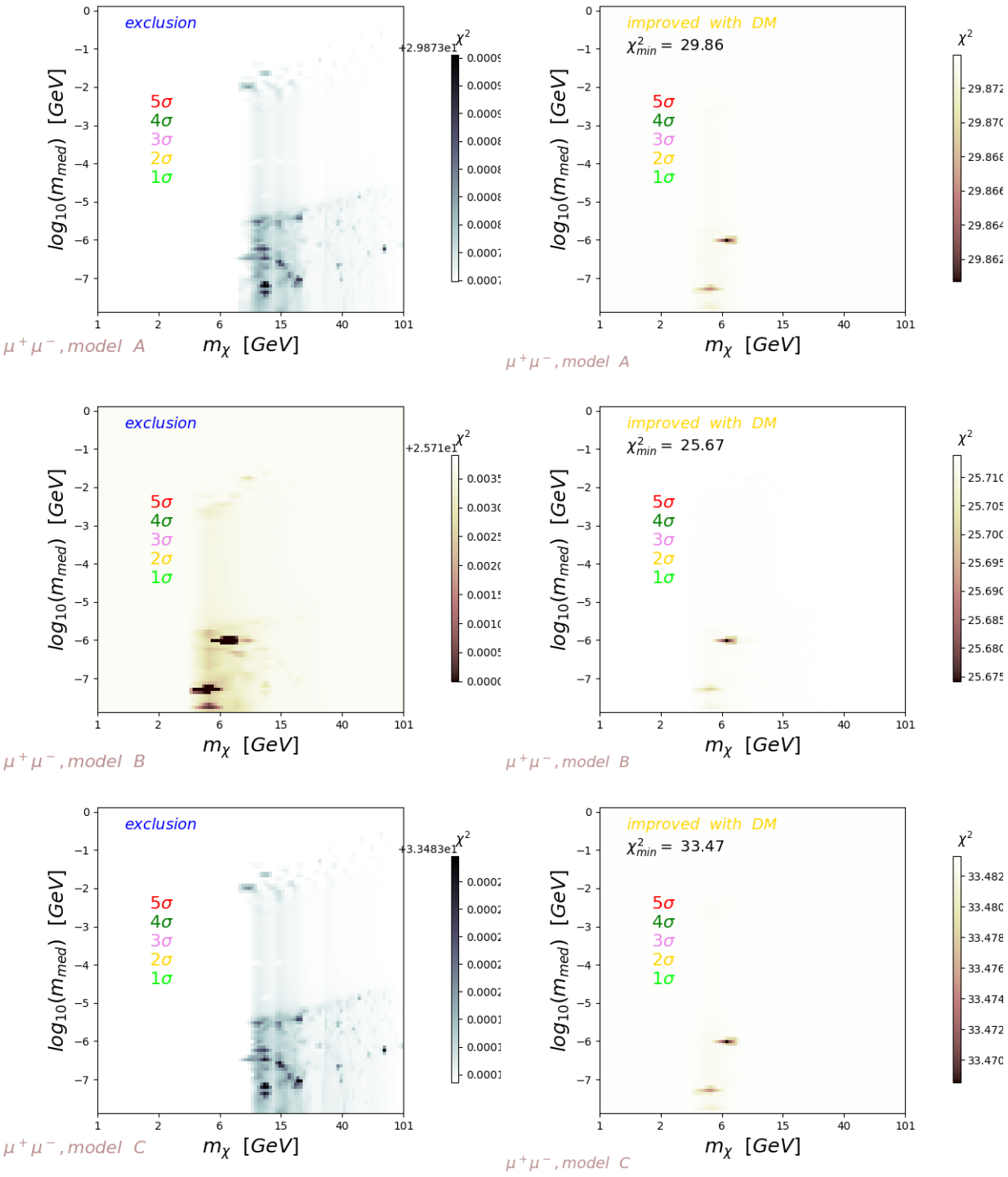

Figure 79: The distribution of χ^2 on the 2D map of m_χ and m_{med}.

$$\Phi_{tot,DM} = (1-\alpha)\cdot\Phi_1(\bar{\chi}\chi \to \phi \to \mu^+\mu^-) + \alpha\cdot\Phi_2(\bar{\chi}\chi \to \phi\phi \to \mu^+\mu^-), \tag{232}$$

with $\alpha = 0.1$. The branching ratio of the $\mu^+\mu^-$ channel is assumed to be $B(\bar{\chi}\chi \to \mu^+\mu^-) = 100\%$. The annihilation of Dark Matter is Sommerfeld boosted. The extragalactic sources of IGRB are considered together with Dark Matter to fit the FermiLAT IGRB data [376]. The confidence contours are shown in different colors to enclose the best-fitting regions. The A, B, C models of the extragalactic sources are shown respectively on the top, middle, bottom panels. The exclusion fit and improved fit are respectively on the left and right side with colored contours.

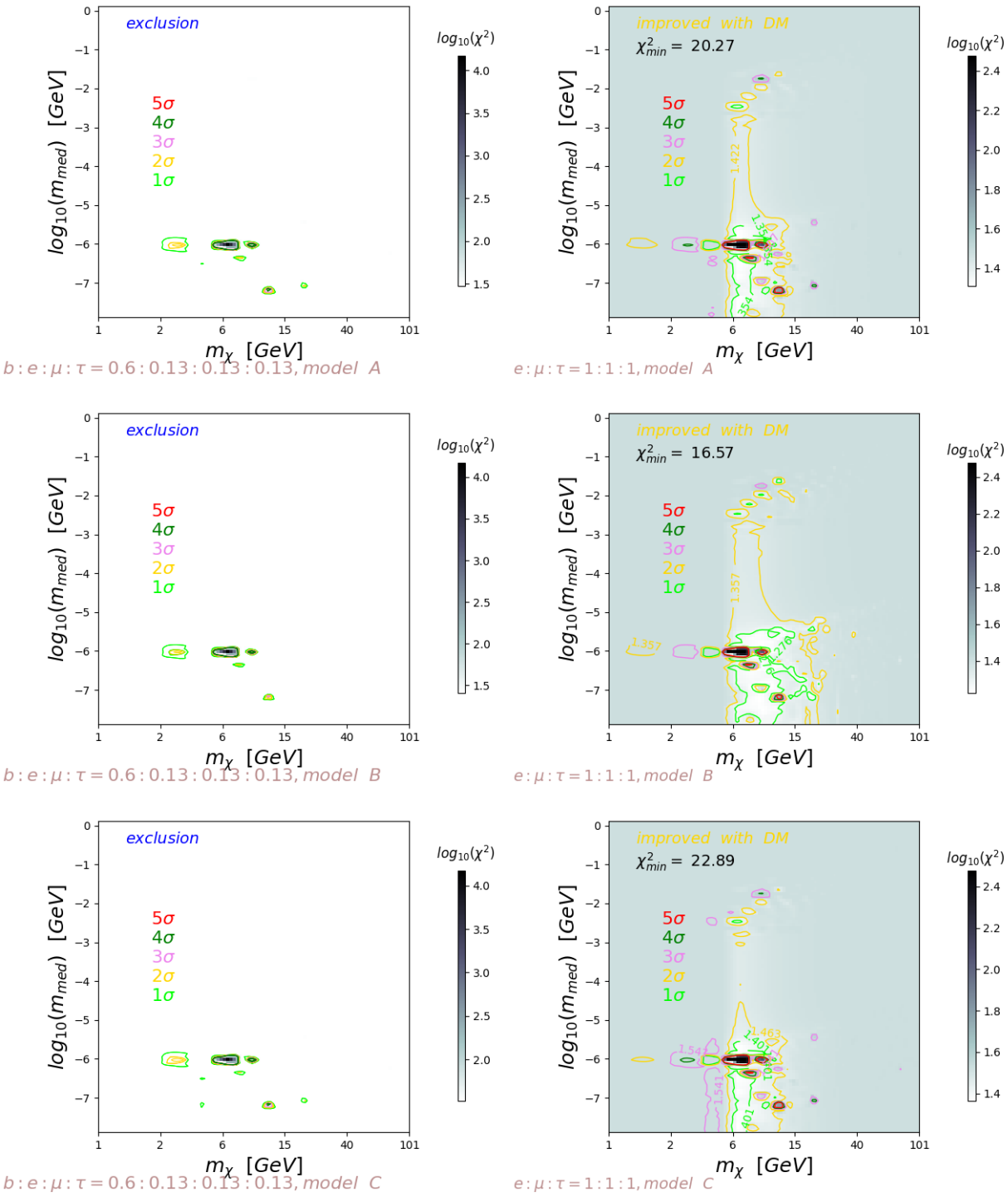

Figure 80: The distribution of χ^2 on the 2D map of m_χ and m_{med}.

$$\Phi_{tot,DM} = (1-\alpha)\cdot\Phi_1(\bar{\chi}\chi \to \phi \to e^+e^-, \mu^+\mu^-, \tau\bar{\tau}) + \alpha\cdot\Phi_2(\bar{\chi}\chi \to \phi\phi \to e^+e^-, \mu^+\mu^-, \tau\bar{\tau}), \quad (234)$$

with $\alpha = 0.1$. The branching ratio of the $e^+e^-, \mu^+\mu^-, \tau\bar{\tau}$ channels are assumed to be respectively 33.3%, 33.3%, 33.3%. The annihilation of Dark Matter is Sommerfeld boosted. The extragalactic sources of IGRB are considered together with Dark Matter to fit the FermiLAT IGRB data [376]. The confidence contours are shown in different colors to enclose the best-fitting regions. The A, B, C models of the extragalactic sources are shown respectively on the top, middle, bottom panels. The exclusion fit and improved fit are respectively on the left and right side with colored contours.

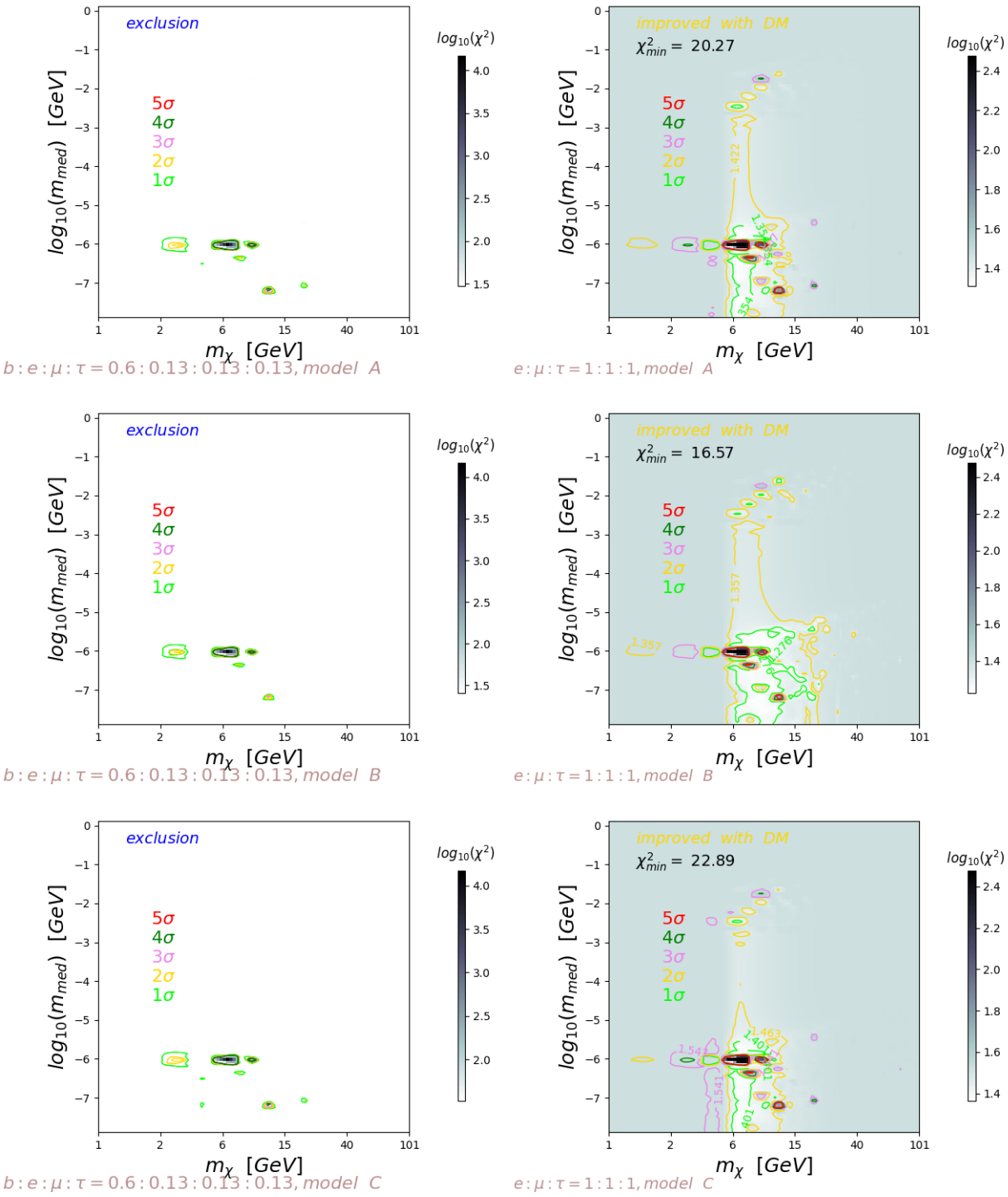

Figure 81: The distribution of χ^2 on the 2D map of m_χ and m_{med}.

$$\Phi_{tot,DM} = (1-\alpha)\cdot\Phi_1(\bar{\chi}\chi \to \phi \to b\bar{b}, e^+e^-, \mu^+\mu^-, \tau\bar{\tau}) + \alpha\cdot\Phi_2(\bar{\chi}\chi \to \phi\phi \to b\bar{b}, e^+e^-, \mu^+\mu^-, \tau\bar{\tau}), \quad (236)$$

with $\alpha = 0.1$. The branching ratio of the $b\bar{b}, e^+e^-, \mu^+\mu^-, \tau\bar{\tau}$ channels are assumed to be respectively 60%,13.3%, 13.3%, 13.3%. The annihilation of Dark Matter is Sommerfeld boosted. The extragalactic sources of IGRB are considered together with Dark Matter to fit the FermiLAT IGRB data [376]. The confidence contours are shown in different colors to enclose the best-fitting regions. The A, B, C models of the extragalactic sources are shown respectively on the top, middle, bottom panels. The exclusion fit and improved fit are respectively on the left and right side with colored contours.

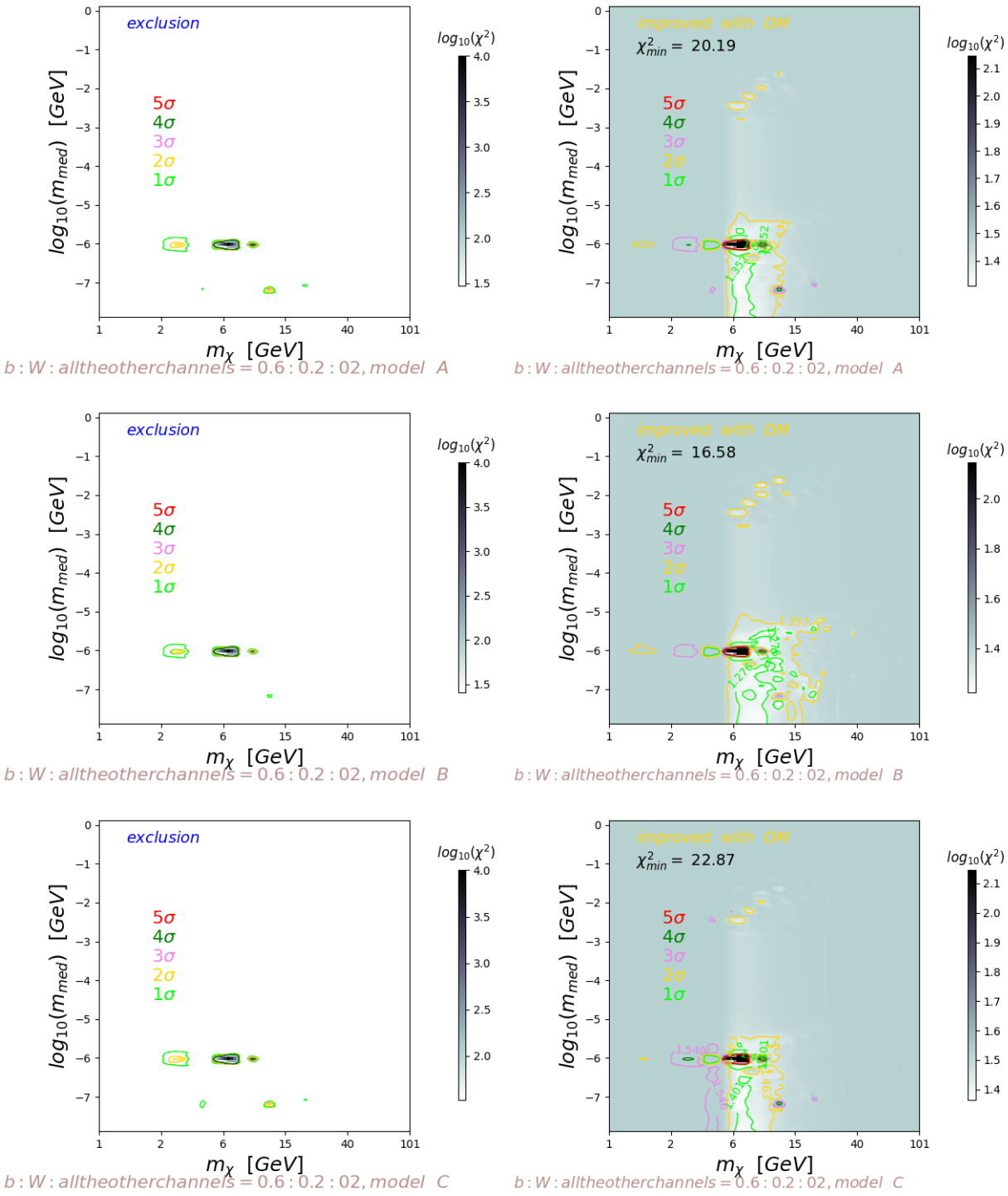

Figure 82: The distribution of χ^2 on the 2D map of m_χ and m_{med}.

$$\Phi_{tot,DM} = (1-\alpha)\cdot\Phi_1(\bar{\chi}\chi \to \phi \to b\bar{b}, W^+W^-, the\,others) + \alpha\cdot\Phi_2(\bar{\chi}\chi \to \phi\phi \to b\bar{b}, W^+W^-, the\,others), \quad (238)$$

with $\alpha = 0.1$. The branching ratio of the $b\bar{b}, W^+W^-$channels are assumed to be respectively 60%,20%, and 1/30 for each of the $\gamma\gamma$, $h\bar{h}$, $g\bar{g}$, $\tau^+\tau^-$, $\mu^+\mu^-$, e^+e^-channels. The annihilation of Dark Matter is Sommerfeld boosted. The extragalactic sources of IGRB are considered together with Dark Matter to fit the FermiLAT IGRB data [376]. The confidence contours are shown in different colors to enclose the best-fitting regions. The A, B, C models of the extragalactic sources are shown respectively on the top, middle, bottom panels. The exclusion fit and improved fit are respectively on the left and right side with colored contours.

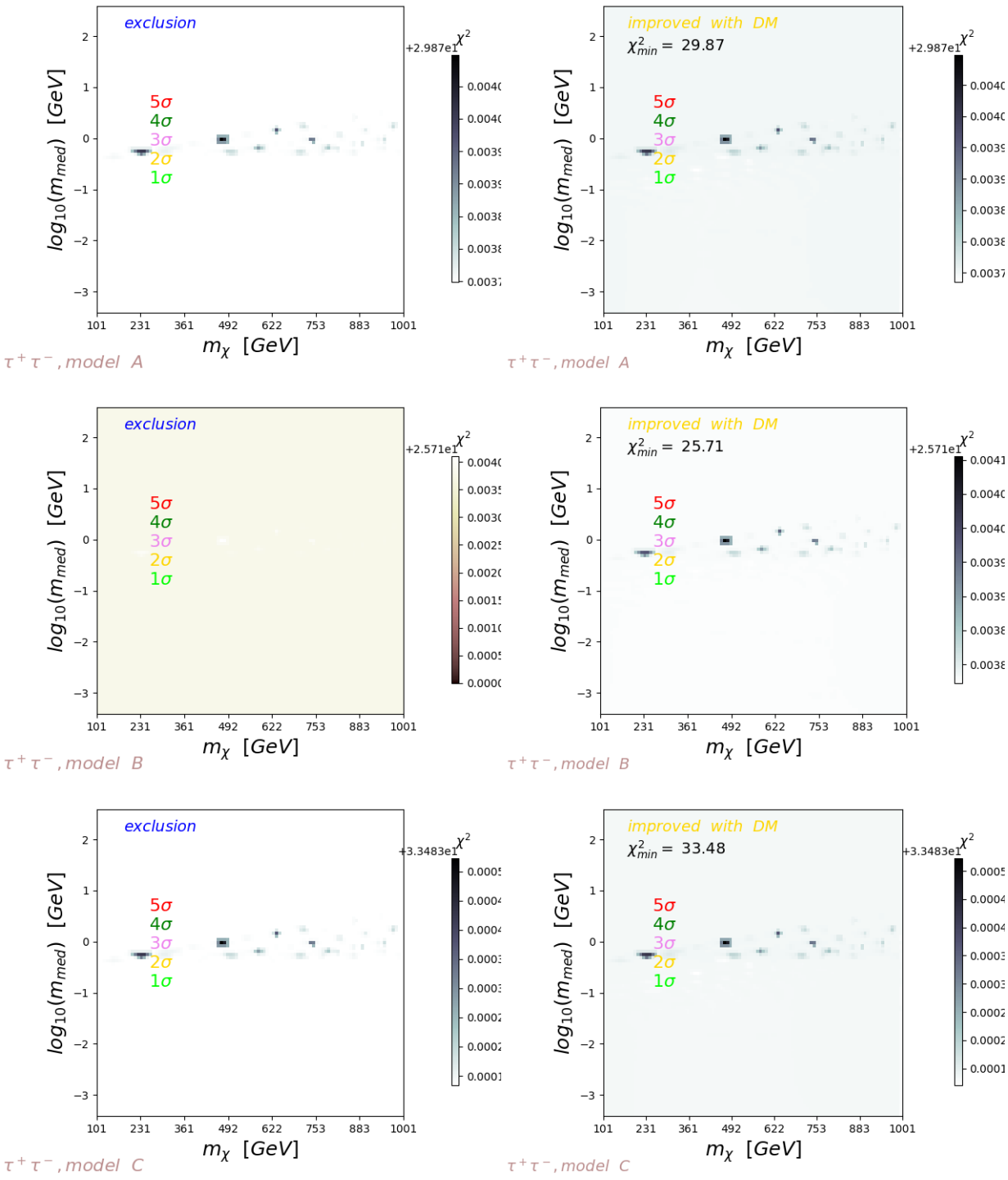

Figure 83: The distribution of χ^2 on the 2D map of m_χ and m_{med}.

$$\Phi_{tot,DM} = (1-\alpha)\cdot\Phi_1(\bar{\chi}\chi \to \phi \to \tau\bar{\tau}) + \alpha\cdot\Phi_2(\bar{\chi}\chi \to \phi\phi \to \tau\bar{\tau}), \tag{240}$$

with $\alpha = 1$. The branching ratio of the $\tau\bar{\tau}$ channel is assumed to be $B(\bar{\chi}\chi \to \tau\bar{\tau}) = 100\%$. And the annihilation of Dark Matter via a single mediator is Sommerfeld boosted. The extragalactic sources of IGRB are considered together with Dark Matter to fit the FermiLAT IGRB data [376]. The confidence contours are shown in different colors to enclose the best-fitting regions. The A, B, C models of the extragalactic sources are shown respectively on the top, middle, bottom panels. The exclusion fit and improved fit are respectively on the left and right side with colored contours.

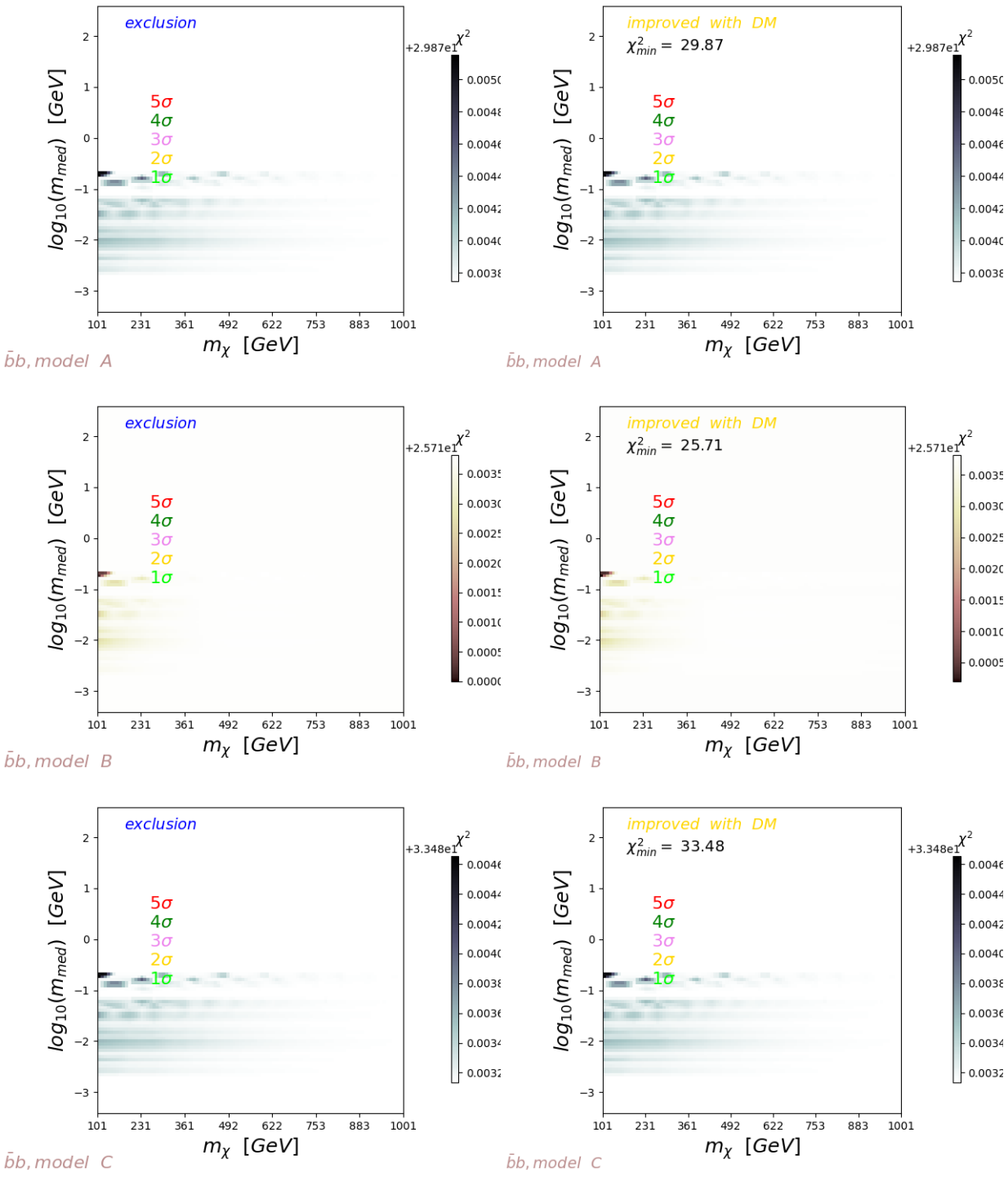

Figure 84: The distribution of χ^2 on the 2D map of m_χ and m_{med}.

$$\Phi_{tot,DM} = (1-\alpha)\cdot\Phi_1(\bar{\chi}\chi \to \phi \to b\bar{b}) + \alpha\cdot\Phi_2(\bar{\chi}\chi \to \phi\phi \to b\bar{b}), \tag{242}$$

with $\alpha = 1$. The branching ratio of the $b\bar{b}$ channel is assumed to be $B(\bar{\chi}\chi \to b\bar{b}) = 100\%$. And the annihilation of Dark Matter is Sommerfeld boosted. The extragalactic sources of IGRB are considered together with Dark Matter to fit the FermiLAT IGRB data [376]. The confidence contours are shown in different colors to enclose the best-fitting regions. The models A,C of the extragalactic sources are shown respectively on the top, middle, bottom panels. The exclusion fit and improved fit are respectively on the left and right side with colored contours.

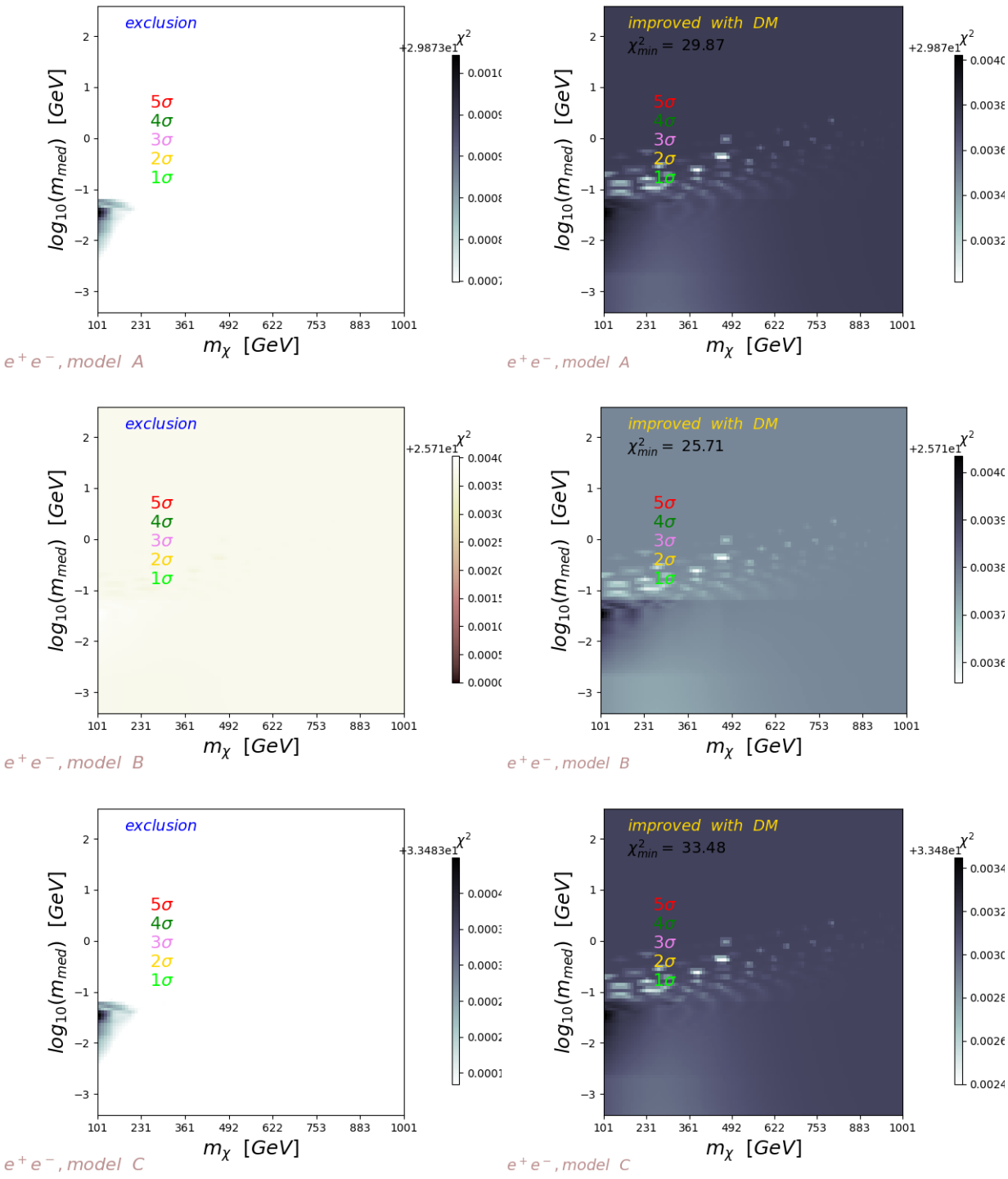

Figure 85: The distribution of χ^2 on the 2D map of m_χ and m_{med}.

$$\Phi_{tot,DM} = (1-\alpha)\cdot\Phi_1(\bar{\chi}\chi \to \phi \to e^+e^-) + \alpha\cdot\Phi_2(\bar{\chi}\chi \to \phi\phi \to e^+e^-), \tag{244}$$

with $\alpha = 1$. The branching ratio of the e^+e^- channel is assumed to be $B(\bar{\chi}\chi \to e^+e^-) = 100\%$. The annihilation of Dark Matter is Sommerfeld boosted. The extragalactic sources of IGRB are considered together with Dark Matter to fit the FermiLAT IGRB data [376]. The confidence contours are shown in different colors to enclose the best-fitting regions. The models A, C of the extragalactic sources are shown respectively on the top, middle, bottom panels. The exclusion fit and improved fit are respectively on the left and right side with colored contours.

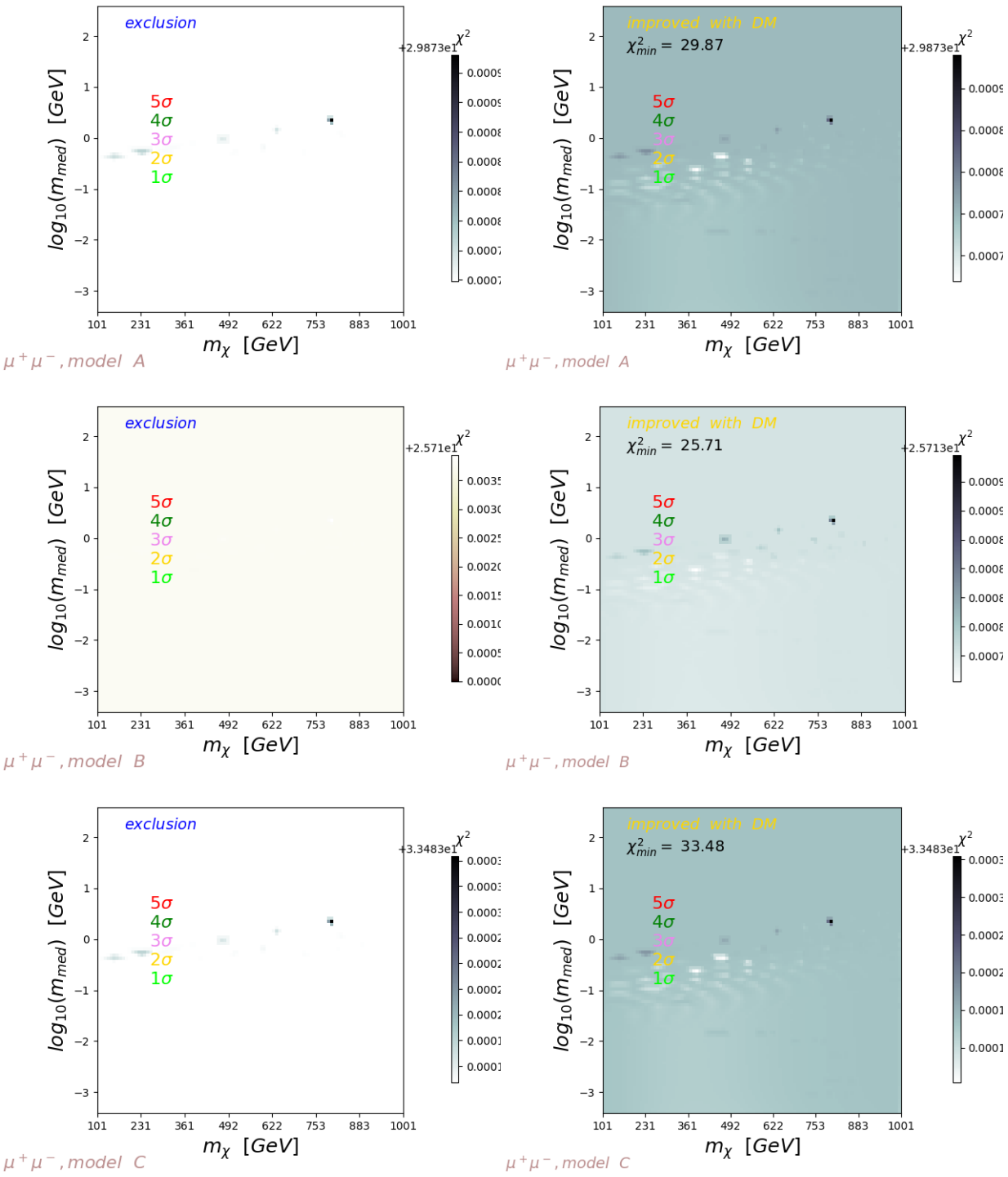

Figure 86: The distribution of χ^2 on the 2D map of m_χ and m_{med}.

$$\Phi_{tot,DM} = (1-\alpha)\cdot\Phi_1(\bar{\chi}\chi \to \phi \to \mu^+\mu^-) + \alpha\cdot\Phi_2(\bar{\chi}\chi \to \phi\phi \to \mu^+\mu^-), \tag{246}$$

with $\alpha = 1$. The branching ratio of the $\mu^+\mu^-$ channel is assumed to be $B(\bar{\chi}\chi \to \mu^+\mu^-) = 100\%$. The annihilation of Dark Matter is Sommerfeld boosted. The extragalactic sources of IGRB are considered together with Dark Matter to fit the FermiLAT IGRB data [376]. The confidence contours are shown in different colors to enclose the best-fitting regions. The models A, C of the extragalactic sources are shown respectively on the top, middle, bottom panels. The exclusion fit and improved fit are respectively on the left and right side with colored contours.

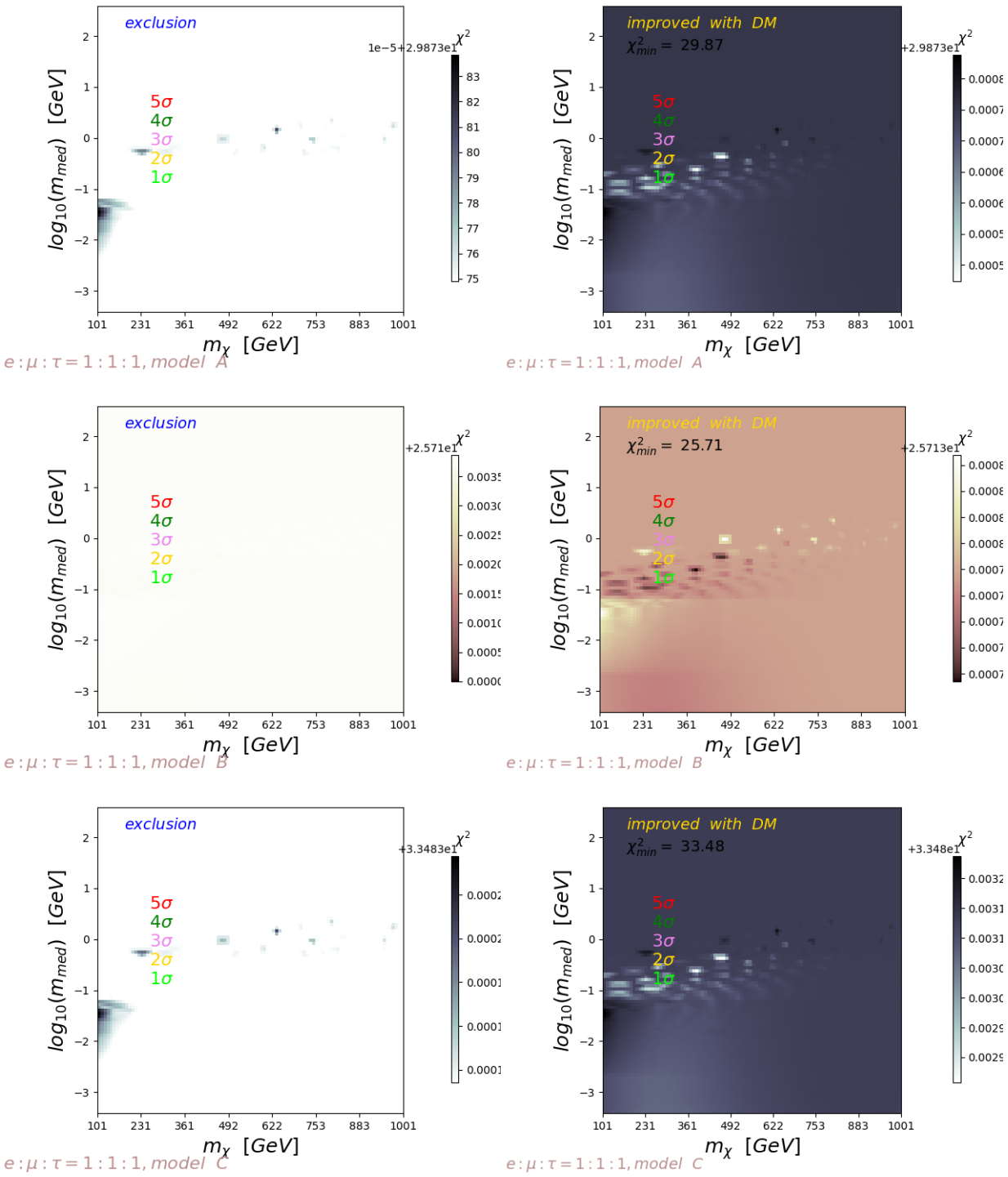

Figure 87: The distribution of χ^2 on the 2D map of m_χ and m_{med}.

$$\Phi_{tot,DM} = (1-\alpha)\cdot\Phi_1(\bar{\chi}\chi \to \phi \to e^+e^-, \mu^+\mu^-, \tau\bar{\tau}) + \alpha\cdot\Phi_2(\bar{\chi}\chi \to \phi\phi \to e^+e^-, \mu^+\mu^-, \tau\bar{\tau}), \quad (248)$$

with $\alpha = 1$. The branching ratio of the $e^+e^-, \mu^+\mu^-, \tau\bar{\tau}$ channels are assumed to be respectively 33.3%, 33.3%, 33.3%. The annihilation of Dark Matter is Sommerfeld boosted. The extragalactic sources of IGRB are considered together with Dark Matter to fit the FermiLAT IGRB data [376]. The confidence contours are shown in different colors to enclose the best-fitting regions. The A, B, C models of the extragalactic sources are shown respectively on the top, middle, bottom panels. The exclusion fit and improved fit are respectively on the left and right side with colored contours.

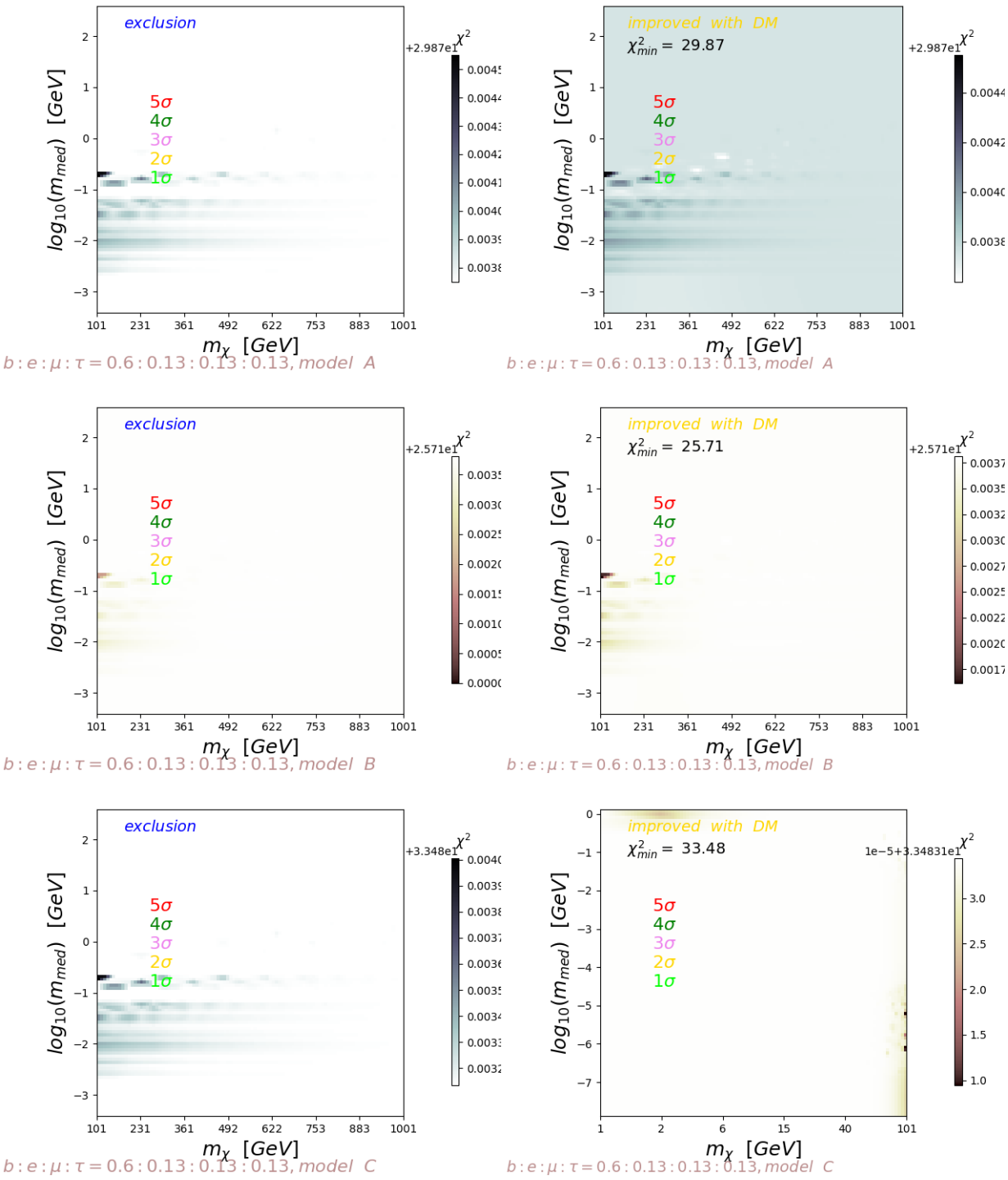

Figure 88: The distribution of χ^2 on the 2D map of m_χ and m_{med}.

$$\Phi_{tot,DM} = (1-\alpha)\cdot\Phi_1(\bar{\chi}\chi \to \phi \to b\bar{b}, e^+e^-, \mu^+\mu^-, \tau\bar{\tau}) + \alpha\cdot\Phi_2(\bar{\chi}\chi \to \phi\phi \to b\bar{b}, e^+e^-, \mu^+\mu^-, \tau\bar{\tau}), \quad (250)$$

with $\alpha = 1$. The branching ratio of the $b\bar{b}, e^+e^-, \mu^+\mu^-, \tau\bar{\tau}$ channels are assumed to be respectively 60%,13.3%, 13.3%, 13.3%. The annihilation of Dark Matter is Sommerfeld boosted. The extragalactic sources of IGRB are considered together with Dark Matter to fit the FermiLAT IGRB data [376]. The confidence contours are shown in different colors to enclose the best-fitting regions. The A, B, C models of the extragalactic sources are shown respectively on the top, middle, bottom panels. The exclusion fit and improved fit are respectively on the left and right side with colored contours.

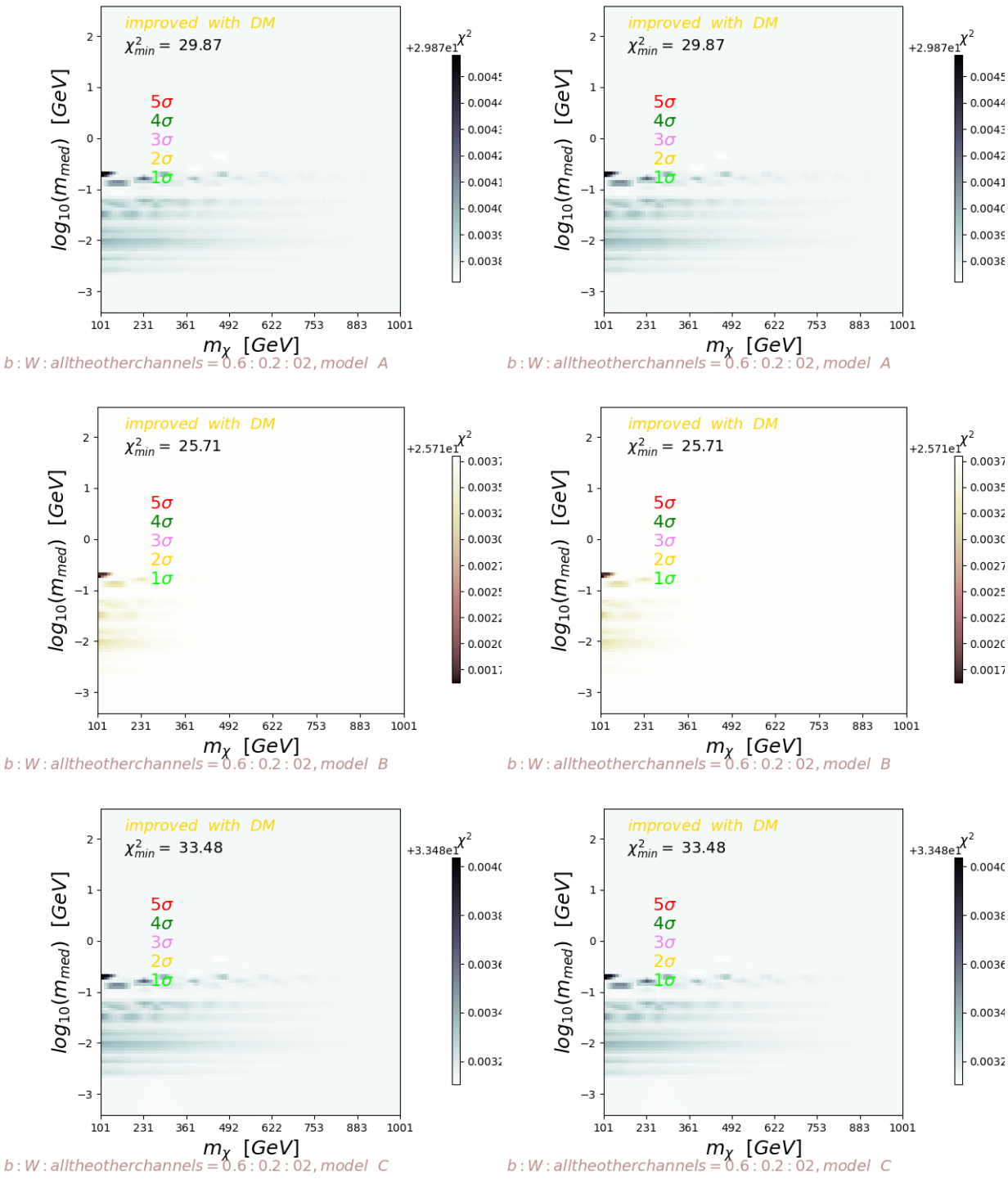

Figure 89: The distribution of χ^2 on the 2D map of m_χ and m_{med}.

$$\Phi_{tot,DM} = (1-\alpha)\cdot\Phi_1(\bar{\chi}\chi \to \phi \to b\bar{b}, W^+W^-, the\,others) + \alpha\cdot\Phi_2(\bar{\chi}\chi \to \phi\phi \to b\bar{b}, W^+W^-, the\,others), \quad (252)$$

with $\alpha = 1$. The branching ratio of the $b\bar{b}, W^+W^-$channels are assumed to be respectively 60%,20%, and 1/30 for each of the $\gamma\gamma$, $h\bar{h}$, $g\bar{g}$, $\tau^+\tau^-$, $\mu^+\mu^-$, e^+e^-channels. The annihilation of Dark Matter is Sommerfeld boosted. The extragalactic sources of IGRB are considered together with Dark Matter to fit the FermiLAT IGRB data [376]. The confidence contours are shown in different colors to enclose the best-fitting regions. The A, B, C models of the extragalactic sources are shown respectively on the top, middle, bottom panels. The exclusion fit and improved fit are respectively on the left and right side with colored contours.

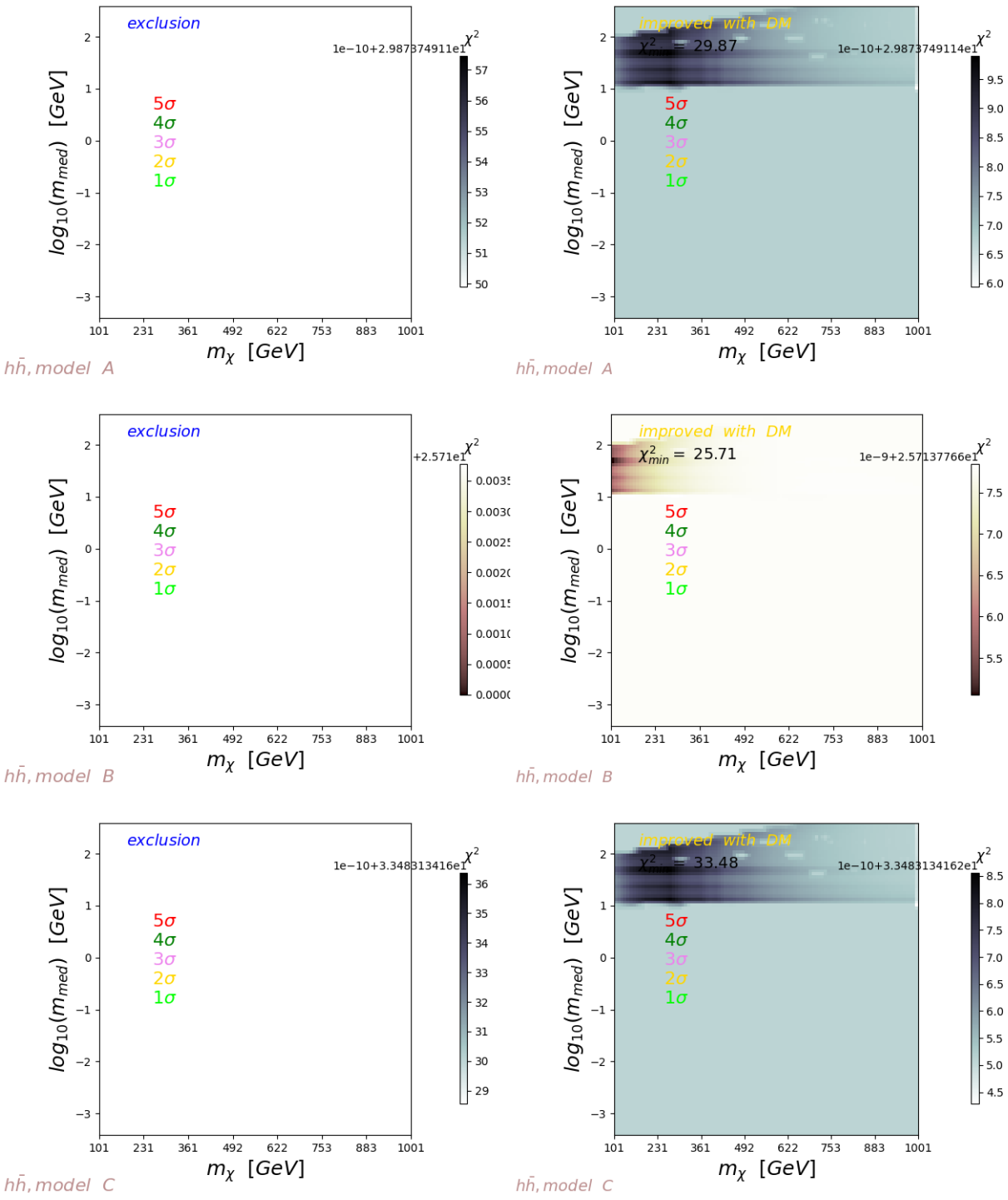

Figure 90: The distribution of χ^2 on the 2D map of m_χ and m_{med}.

$$\Phi_{tot,DM} = \Phi_2(\bar{\chi}\chi \to \phi\phi \to h\bar{h}), \tag{254}$$

with $\alpha = 0.9$. The branching ratio of the $h\bar{h}$ channel is assumed to be $B(\bar{\chi}\chi \to h\bar{h}) = 100\%$. The annihilation of Dark Matter is Sommerfeld boosted. The extragalactic sources of IGRB are considered together with Dark Matter to fit the FermiLAT IGRB data [376]. The confidence contours are shown in different colors to enclose the best-fitting regions. The models A, ,C of the extragalactic sources are shown respectively on the top, middle, bottom panels. The exclusion fit and improved fit are respectively on the left and right side with colored contours.

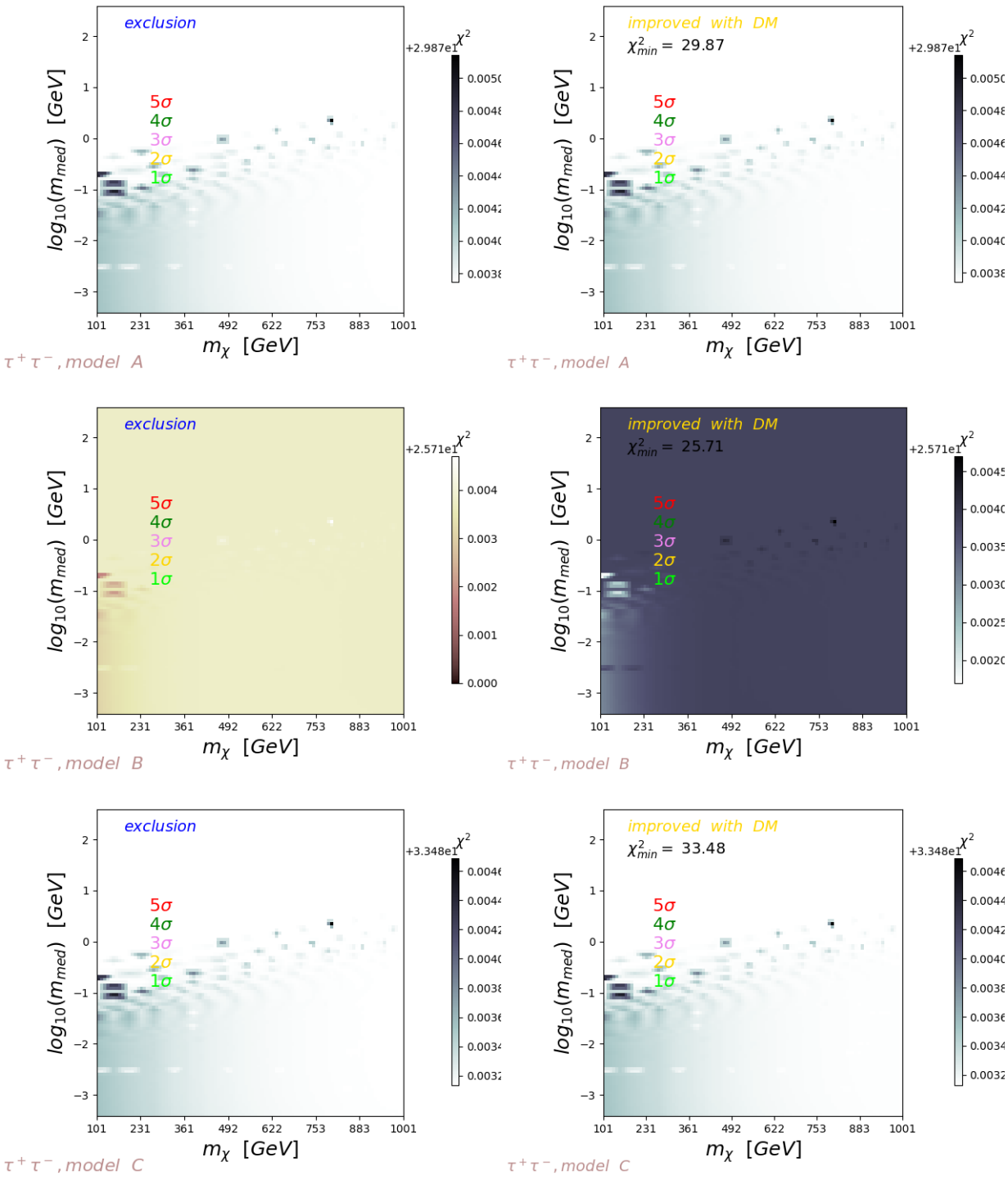

Figure 91: The distribution of χ^2 on the 2D map of m_χ and m_{med}.

$$\Phi_{tot,DM} = (1-\alpha)\cdot\Phi_1(\bar{\chi}\chi \to \phi \to \tau\bar{\tau}) + \alpha\cdot\Phi_2(\bar{\chi}\chi \to \phi\phi \to \tau\bar{\tau}), \tag{256}$$

with $\alpha = 0.9$. The branching ratio of the $\tau\bar{\tau}$ channel is assumed to be $B(\bar{\chi}\chi \to \tau\bar{\tau}) = 100\%$. And the annihilation of Dark Matter via a single mediator is Sommerfeld boosted. The extragalactic sources of IGRB are considered together with Dark Matter to fit the FermiLAT IGRB data [376]. The confidence contours are shown in different colors to enclose the best-fitting regions. The A, B, C models of the extragalactic sources are shown respectively on the top, middle, bottom panels. The exclusion fit and improved fit are respectively on the left and right side with colored contours.

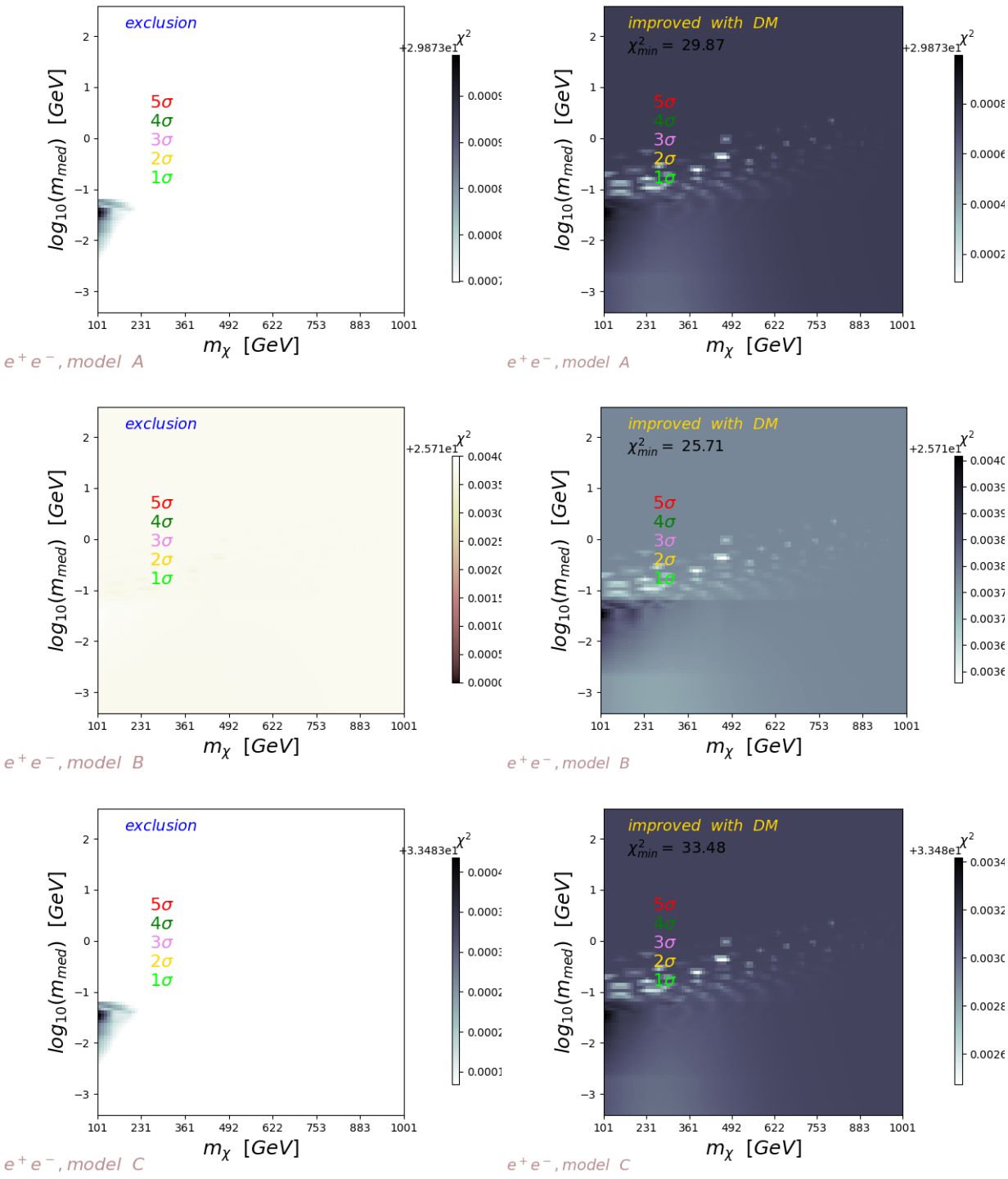

Figure 92: The distribution of χ^2 on the 2D map of m_χ and m_{med}.

$$\Phi_{tot,DM} = (1-\alpha)\cdot\Phi_1(\bar{\chi}\chi \to \phi \to e^+e^-) + \alpha\cdot\Phi_2(\bar{\chi}\chi \to \phi\phi \to e^+e^-), \tag{258}$$

with $\alpha = 0.9$. The branching ratio of the e^+e^- channel is assumed to be $B(\bar{\chi}\chi \to e^+e^-) = 100\%$. The annihilation of Dark Matter is Sommerfeld boosted. The extragalactic sources of IGRB are considered together with Dark Matter to fit the FermiLAT IGRB data [376]. The confidence contours are shown in different colors to enclose the best-fitting regions. The A, B, C models of the extragalactic sources are shown respectively on the top, middle, bottom panels. The exclusion fit and improved fit are respectively on the left and right side with colored contours.

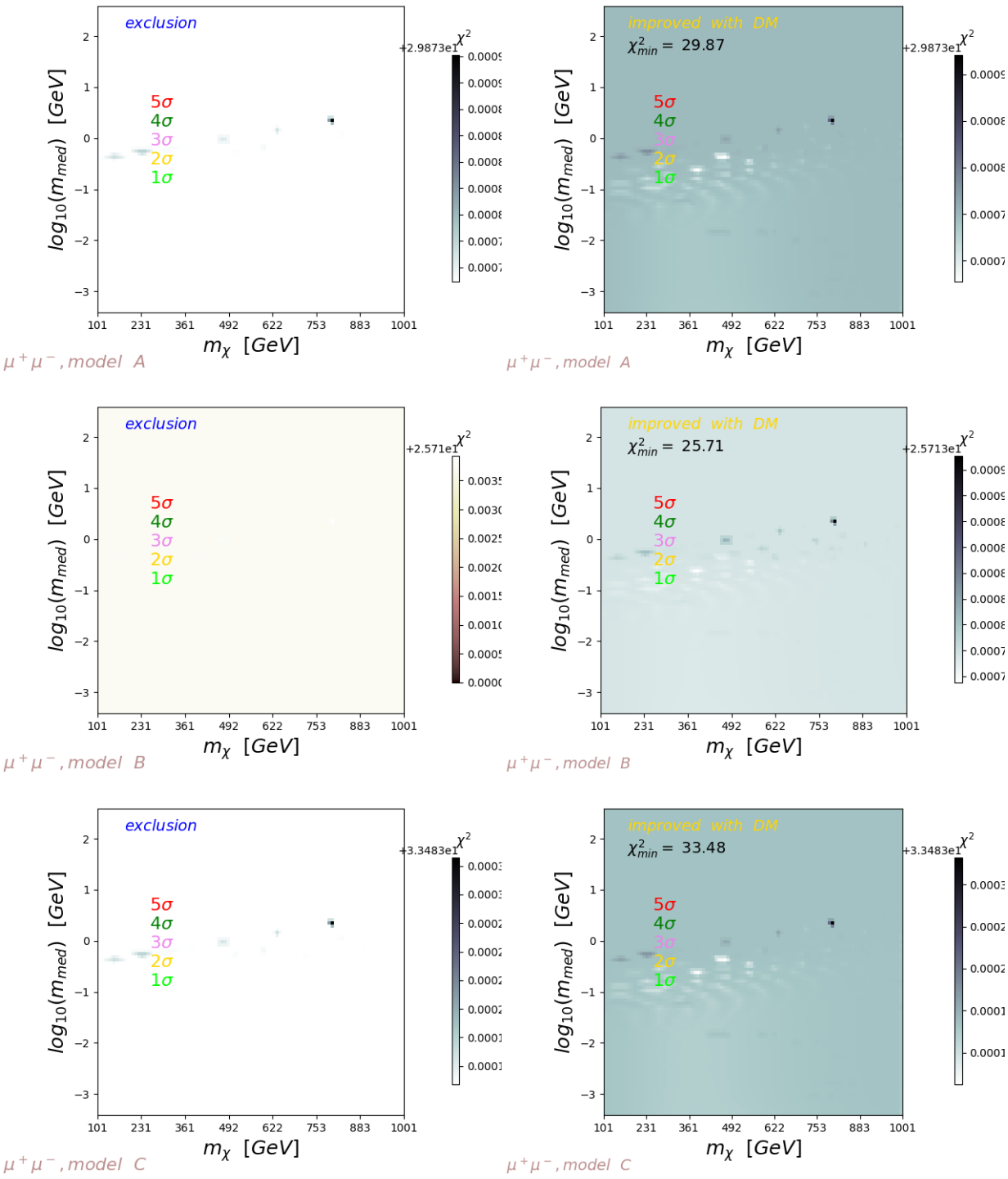

Figure 93: The distribution of χ^2 on the 2D map of m_χ and m_{med}.

$$\Phi_{tot,DM} = (1-\alpha)\cdot\Phi_1(\bar{\chi}\chi \to \phi \to \mu^+\mu^-) + \alpha\cdot\Phi_2(\bar{\chi}\chi \to \phi\phi \to \mu^+\mu^-), \tag{260}$$

with $\alpha = 0.9$. The branching ratio of the $\mu^+\mu^-$ channel is assumed to be $B(\bar{\chi}\chi \to \mu^+\mu^-) = 100\%$. The annihilation of Dark Matter is Sommerfeld boosted. The extragalactic sources of IGRB are considered together with Dark Matter to fit the FermiLAT IGRB data [376]. The confidence contours are shown in different colors to enclose the best-fitting regions. The A, B, C models of the extragalactic sources are shown respectively on the top, middle, bottom panels. The exclusion fit and improved fit are respectively on the left and right side with colored contours.

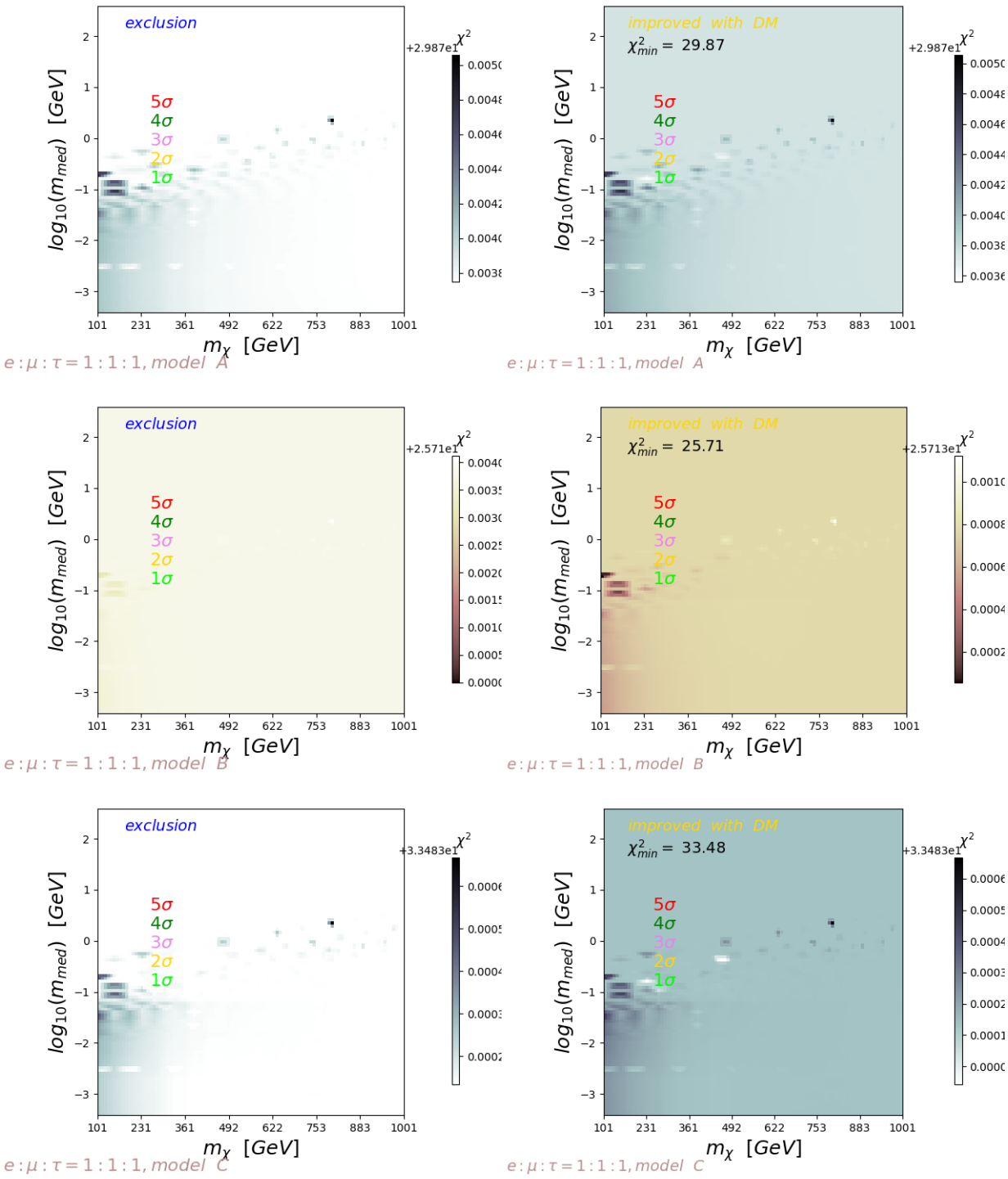

Figure 94: The distribution of χ^2 on the 2D map of m_χ and m_{med}.

$$\Phi_{tot,DM} = (1-\alpha)\cdot\Phi_1(\bar{\chi}\chi \to \phi \to e^+e^-, \mu^+\mu^-, \tau\bar{\tau}) + \alpha\cdot\Phi_2(\bar{\chi}\chi \to \phi\phi \to e^+e^-, \mu^+\mu^-, \tau\bar{\tau}), \quad (262)$$

with $\alpha = 0.9$. The branching ratio of the $e^+e^-, \mu^+\mu^-, \tau\bar{\tau}$ channels are assumed to be respectively 33.3%, 33.3%, 33.3%. The annihilation of Dark Matter is Sommerfeld boosted. The extragalactic sources of IGRB are considered together with Dark Matter to fit the FermiLAT IGRB data [376]. The confidence contours are shown in different colors to enclose the best-fitting regions. The A, B, C models of the extragalactic sources are shown respectively on the top, middle, bottom panels. The exclusion fit and improved fit are respectively on the left and right side with colored contours.

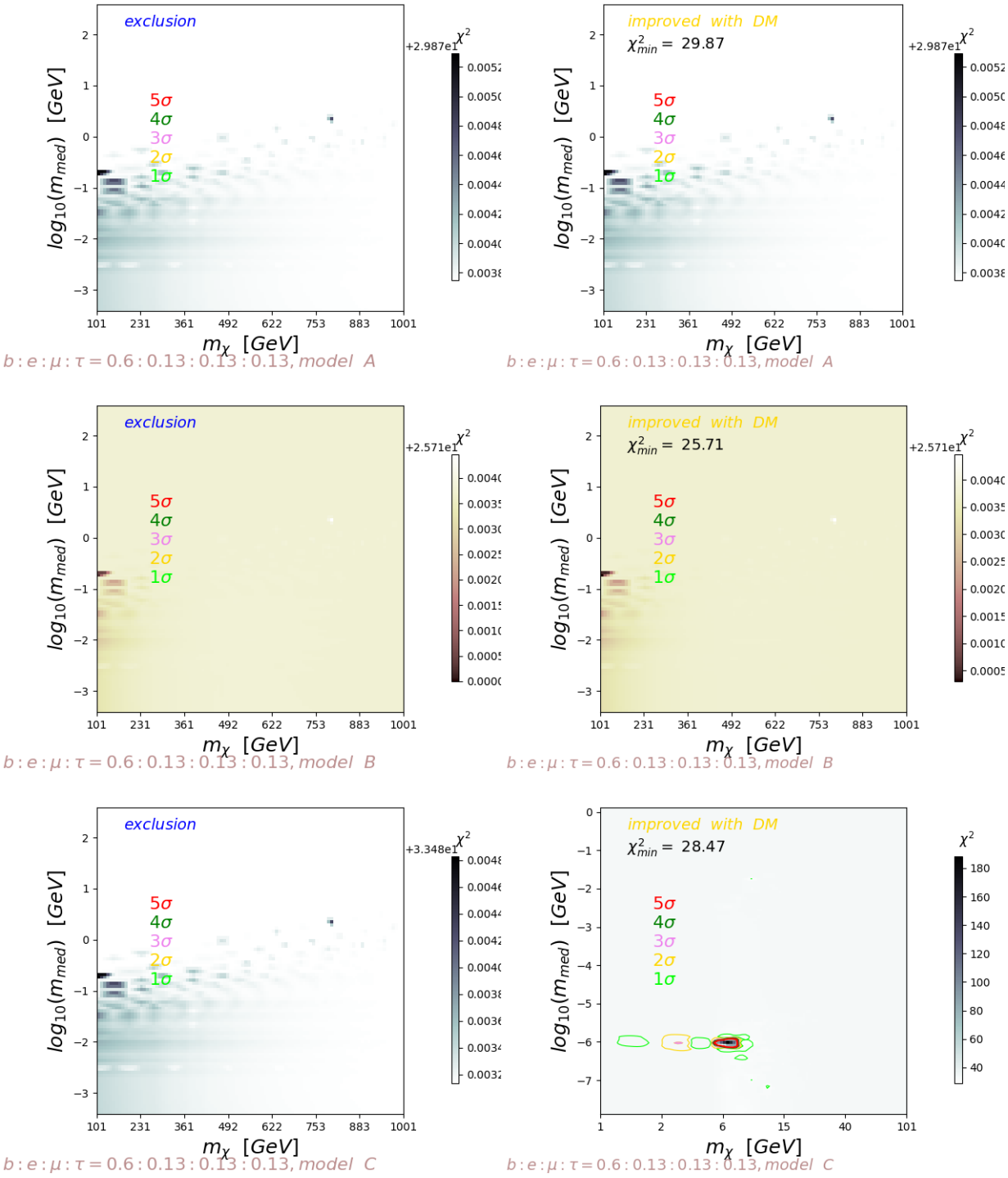

Figure 95: The distribution of χ^2 on the 2D map of m_χ and m_{med}.

$$\Phi_{tot,DM} = (1-\alpha)\cdot\Phi_1(\bar{\chi}\chi \to \phi \to b\bar{b}, e^+e^-, \mu^+\mu^-, \tau\bar{\tau}) + \alpha\cdot\Phi_2(\bar{\chi}\chi \to \phi\phi \to b\bar{b}, e^+e^-, \mu^+\mu^-, \tau\bar{\tau}), \quad (264)$$

with $\alpha = 0.9$. The branching ratio of the $b\bar{b}, e^+e^-, \mu^+\mu^-, \tau\bar{\tau}$ channels are assumed to be respectively 60%,13.3%, 13.3%, 13.3%. The annihilation of Dark Matter is Sommerfeld boosted. The extragalactic sources of IGRB are considered together with Dark Matter to fit the FermiLAT IGRB data [376]. The confidence contours are shown in different colors to enclose the best-fitting regions. The A, B, C models of the extragalactic sources are shown respectively on the top, middle, bottom panels. The exclusion fit and improved fit are respectively on the left and right side with colored contours.

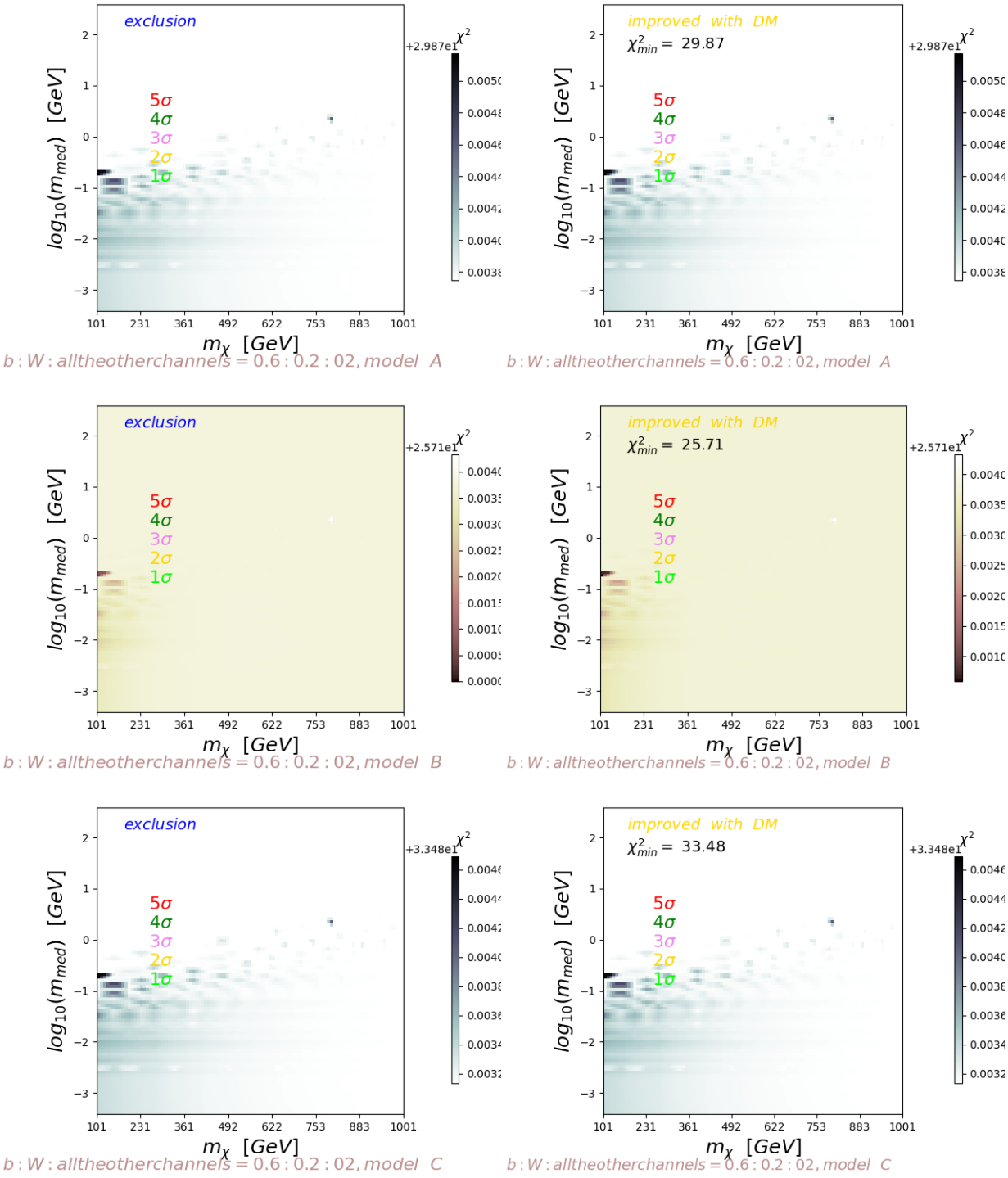

Figure 96: The distribution of χ^2 on the 2D map of m_χ and m_{med}.

$$\Phi_{tot,DM} = (1-\alpha)\cdot\Phi_1(\bar{\chi}\chi \to \phi \to b\bar{b}, W^+W^-, the\,others) + \alpha\cdot\Phi_2(\bar{\chi}\chi \to \phi\phi \to b\bar{b}, W^+W^-, the\,others), \quad (266)$$

with $\alpha = 0.9$. The branching ratio of the $b\bar{b}, W^+W^-$channels are assumed to be respectively 60%,20%, and 1/30 for each of the $\gamma\gamma$, $h\bar{h}$, $g\bar{g}$, $\tau^+\tau^-$, $\mu^+\mu^-$, e^+e^-channels. The annihilation of Dark Matter is Sommerfeld boosted. The extragalactic sources of IGRB are considered together with Dark Matter to fit the FermiLAT IGRB data [376]. The confidence contours are shown in different colors to enclose the best-fitting regions. The A, B, C models of the extragalactic sources are shown respectively on the top, middle, bottom panels. The exclusion fit and improved fit are respectively on the left and right side with colored contours.

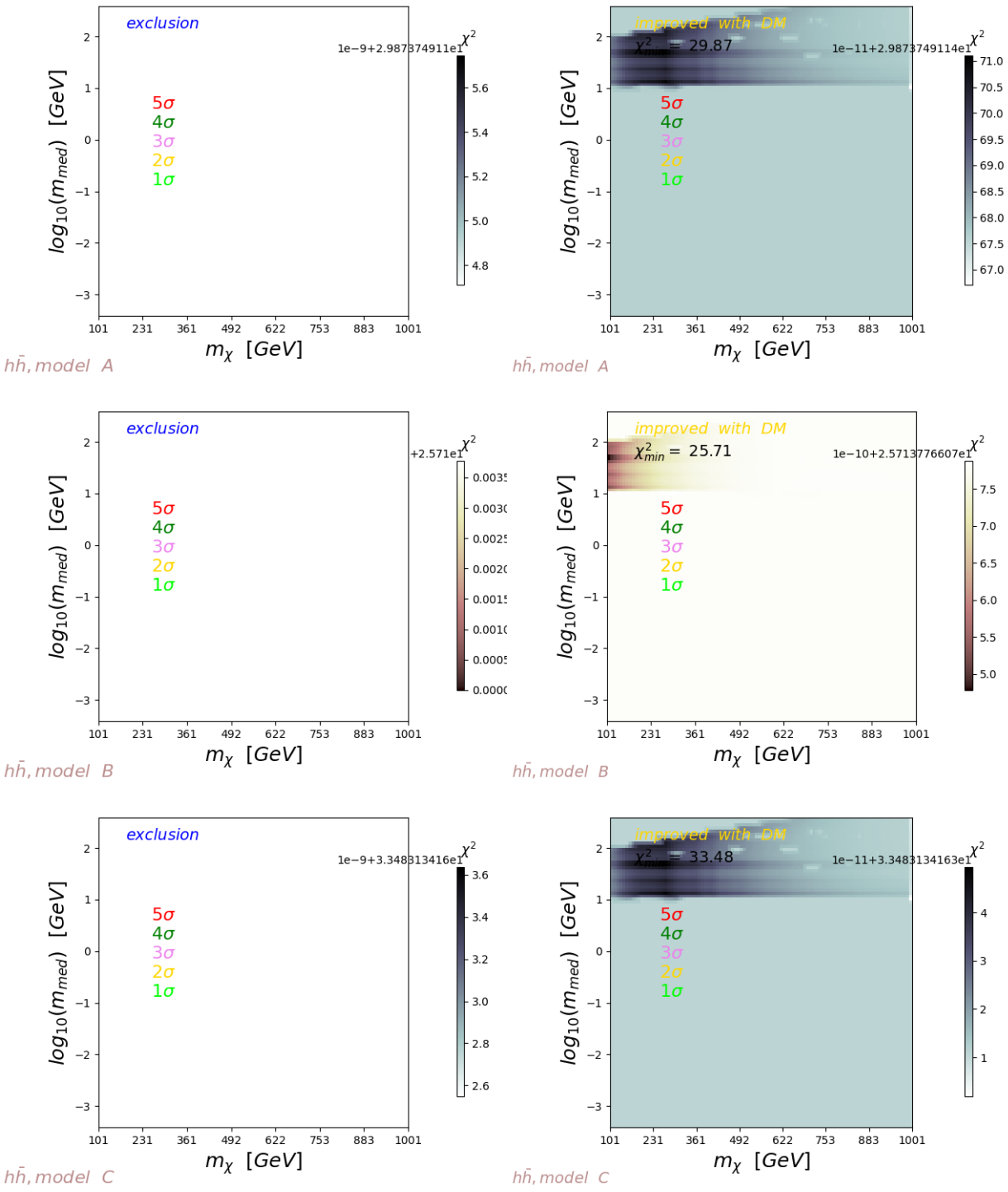

Figure 97: The distribution of χ^2 on the 2D map of m_χ and m_{med}.

$$\Phi_{tot,DM} = \Phi_2(\bar{\chi}\chi \to \phi\phi \to h\bar{h}), \tag{268}$$

with $\alpha = 0.1$. The branching ratio of the $h\bar{h}$ channel is assumed to be $B(\bar{\chi}\chi \to h\bar{h}) = 100\%$. The annihilation of Dark Matter is Sommerfeld boosted. The extragalactic sources of IGRB are considered together with Dark Matter to fit the FermiLAT IGRB data [376]. The confidence contours are shown in different colors to enclose the best-fitting regions. The A, B, C models of the extragalactic sources are shown respectively on the top, middle, bottom panels. The exclusion fit and improved fit are respectively on the left and right side with colored contours.

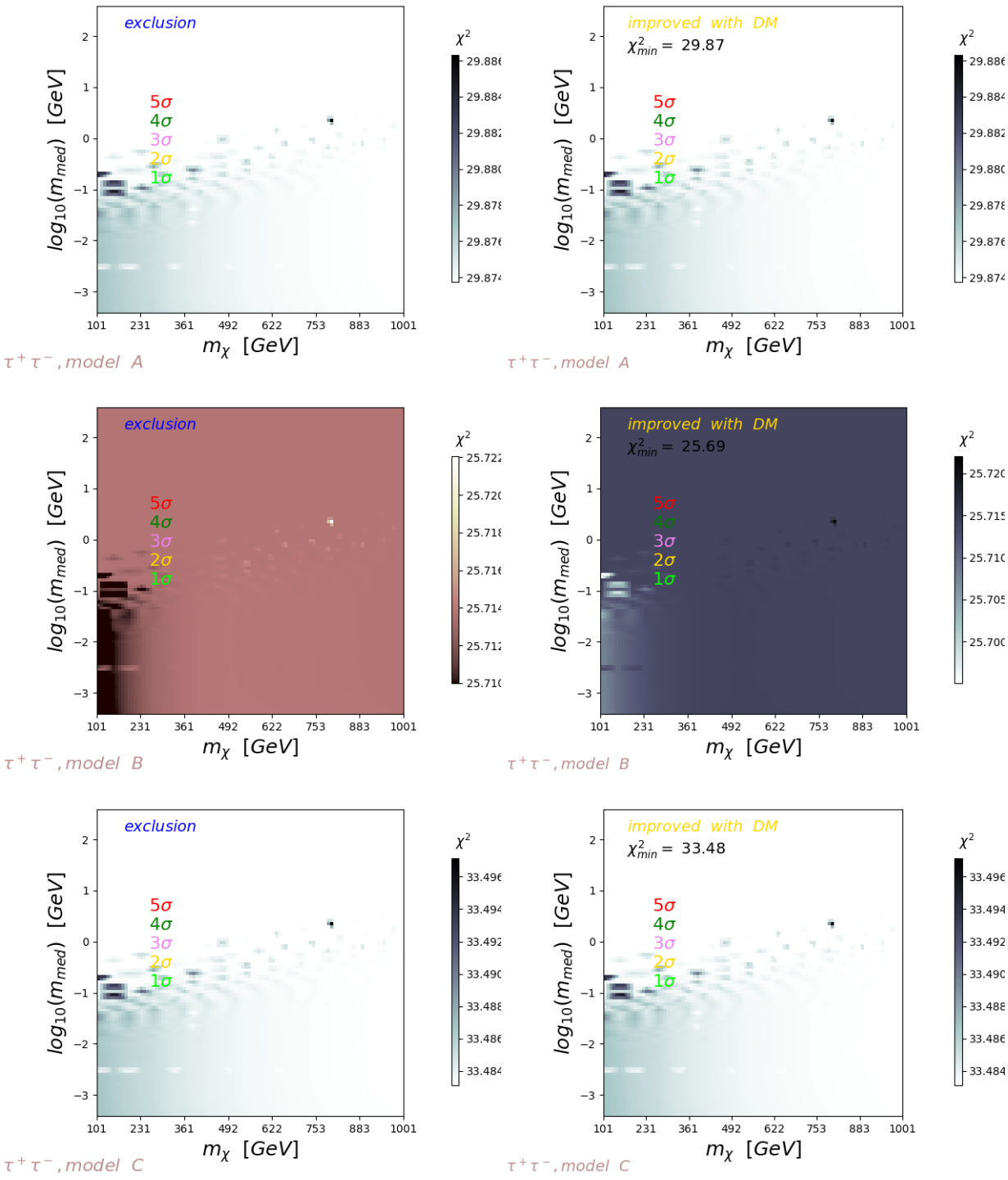

Figure 98: The distribution of χ^2 on the 2D map of m_χ and m_{med}.

$$\Phi_{tot,DM} = (1-\alpha)\cdot\Phi_1(\bar{\chi}\chi \to \phi \to \tau\bar{\tau}) + \alpha\cdot\Phi_2(\bar{\chi}\chi \to \phi\phi \to \tau\bar{\tau}), \tag{270}$$

with $\alpha = 0.1$. The branching ratio of the $\tau\bar{\tau}$ channel is assumed to be $B(\bar{\chi}\chi \to \tau\bar{\tau}) = 100\%$. And the annihilation of Dark Matter via a single mediator is Sommerfeld boosted. The extragalactic sources of IGRB are considered together with Dark Matter to fit the FermiLAT IGRB data [376]. The confidence contours are shown in different colors to enclose the best-fitting regions. The A, B, C models of the extragalactic sources are shown respectively on the top, middle, bottom panels. The exclusion fit and improved fit are respectively on the left and right side with colored contours.

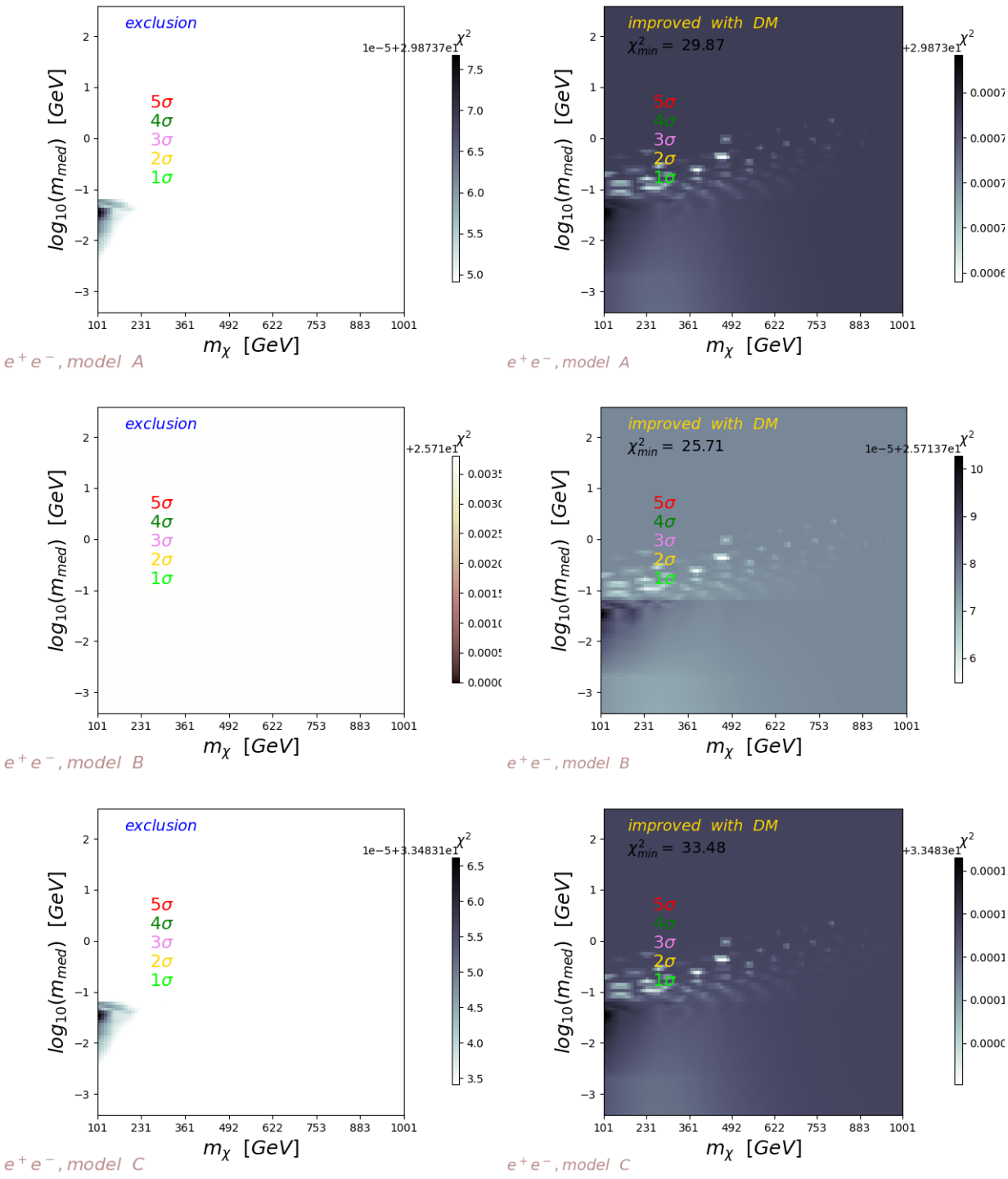

Figure 99: The distribution of χ^2 on the 2D map of m_χ and m_{med}.

$$\Phi_{tot,DM} = (1-\alpha)\cdot\Phi_1(\bar{\chi}\chi \to \phi \to e^+e^-) + \alpha\cdot\Phi_2(\bar{\chi}\chi \to \phi\phi \to e^+e^-), \tag{272}$$

with $\alpha = 0.1$. The branching ratio of the e^+e^- channel is assumed to be $B(\bar{\chi}\chi \to e^+e^-) = 100\%$. The annihilation of Dark Matter is Sommerfeld boosted. The extragalactic sources of IGRB are considered together with Dark Matter to fit the FermiLAT IGRB data [376]. The confidence contours are shown in different colors to enclose the best-fitting regions. The A, B, C models of the extragalactic sources are shown respectively on the top, middle, bottom panels. The exclusion fit and improved fit are respectively on the left and right side with colored contours.

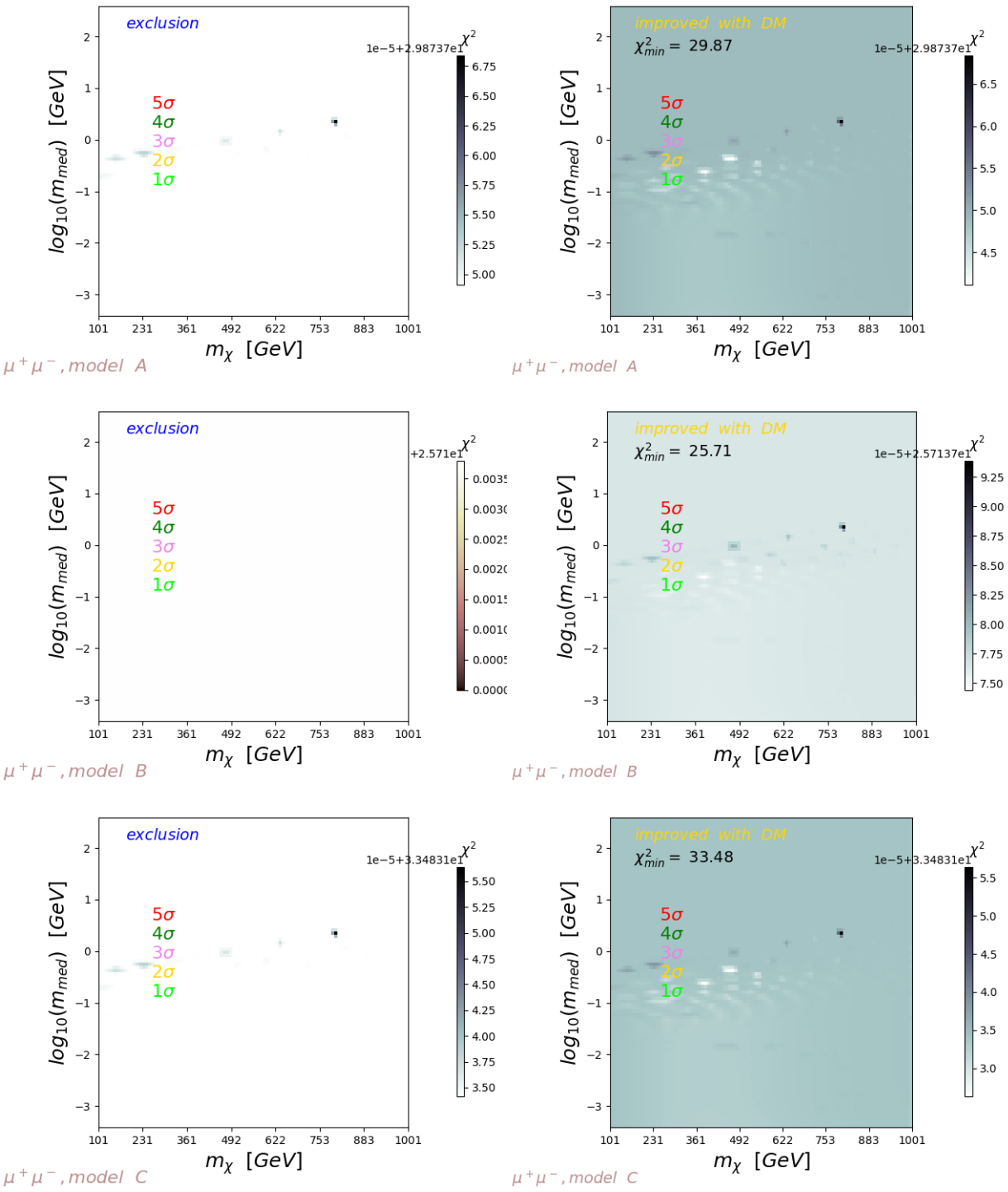

Figure 100: The distribution of χ^2 on the 2D map of m_χ and m_{med}.

$$\Phi_{tot,DM} = (1-\alpha)\cdot\Phi_1(\bar{\chi}\chi \to \phi \to \mu^+\mu^-) + \alpha\cdot\Phi_2(\bar{\chi}\chi \to \phi\phi \to \mu^+\mu^-), \tag{274}$$

with $\alpha = 0.1$. The branching ratio of the $\mu^+\mu^-$ channel is assumed to be $B(\bar{\chi}\chi \to \mu^+\mu^-) = 100\%$. The annihilation of Dark Matter is Sommerfeld boosted. The extragalactic sources of IGRB are considered together with Dark Matter to fit the FermiLAT IGRB data [376]. The confidence contours are shown in different colors to enclose the best-fitting regions. The A, B, C models of the extragalactic sources are shown respectively on the top, middle, bottom panels. The exclusion fit and improved fit are respectively on the left and right side with colored contours.

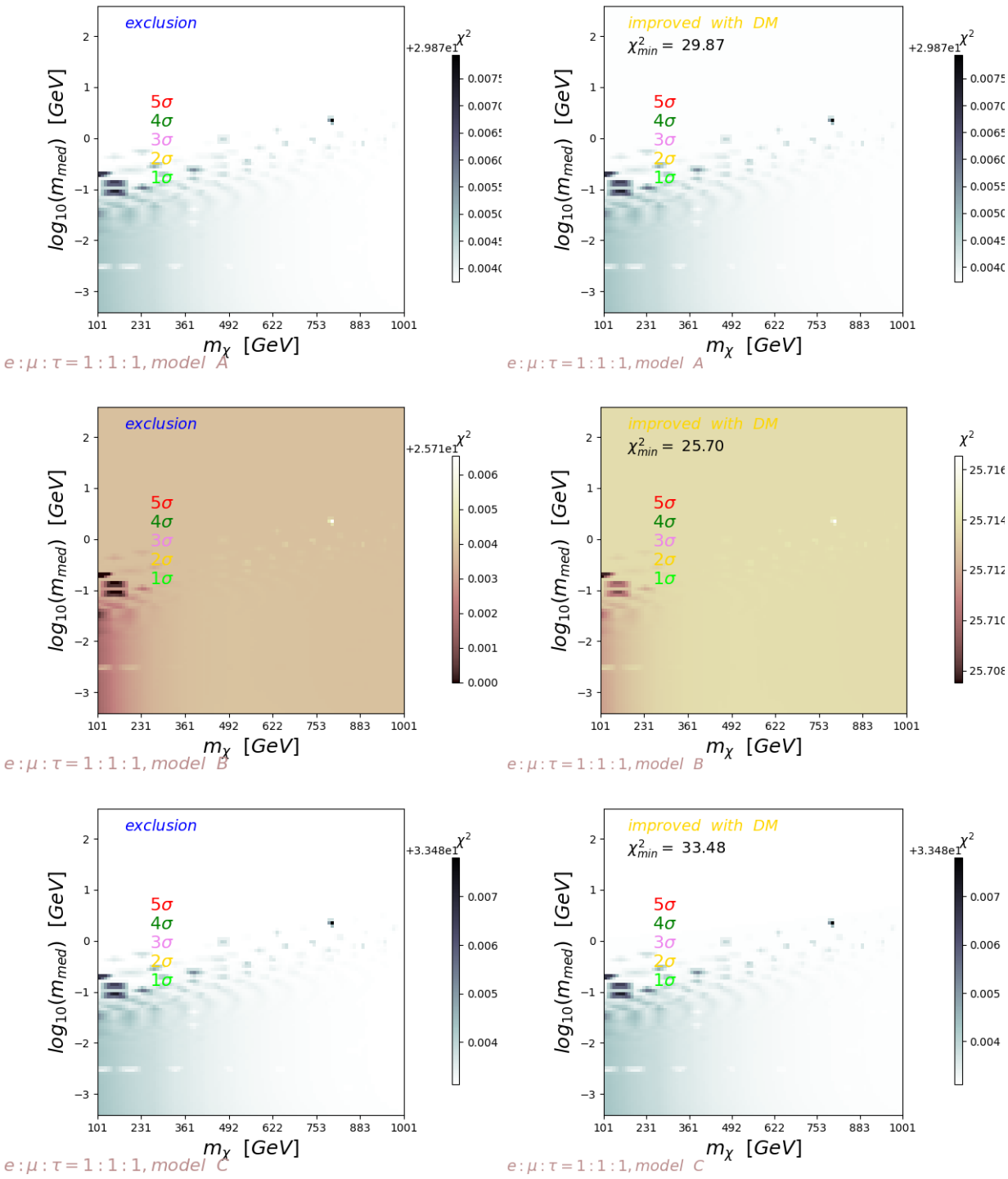

Figure 101: The distribution of χ^2 on the 2D map of m_χ and m_{med}.

$$\Phi_{tot,DM} = (1-\alpha)\cdot\Phi_1(\bar{\chi}\chi \to \phi \to e^+e^-, \mu^+\mu^-, \tau\bar{\tau}) + \alpha\cdot\Phi_2(\bar{\chi}\chi \to \phi\phi \to e^+e^-, \mu^+\mu^-, \tau\bar{\tau}), \quad (276)$$

with $\alpha = 0.1$. The branching ratio of the $e^+e^-, \mu^+\mu^-, \tau\bar{\tau}$ channels are assumed to be respectively 33.3%, 33.3%, 33.3%. The annihilation of Dark Matter is Sommerfeld boosted. The extragalactic sources of IGRB are considered together with Dark Matter to fit the FermiLAT IGRB data [376]. The confidence contours are shown in different colors to enclose the best-fitting regions. The A, B, C models of the extragalactic sources are shown respectively on the top, middle, bottom panels. The exclusion fit and improved fit are respectively on the left and right side with colored contours.

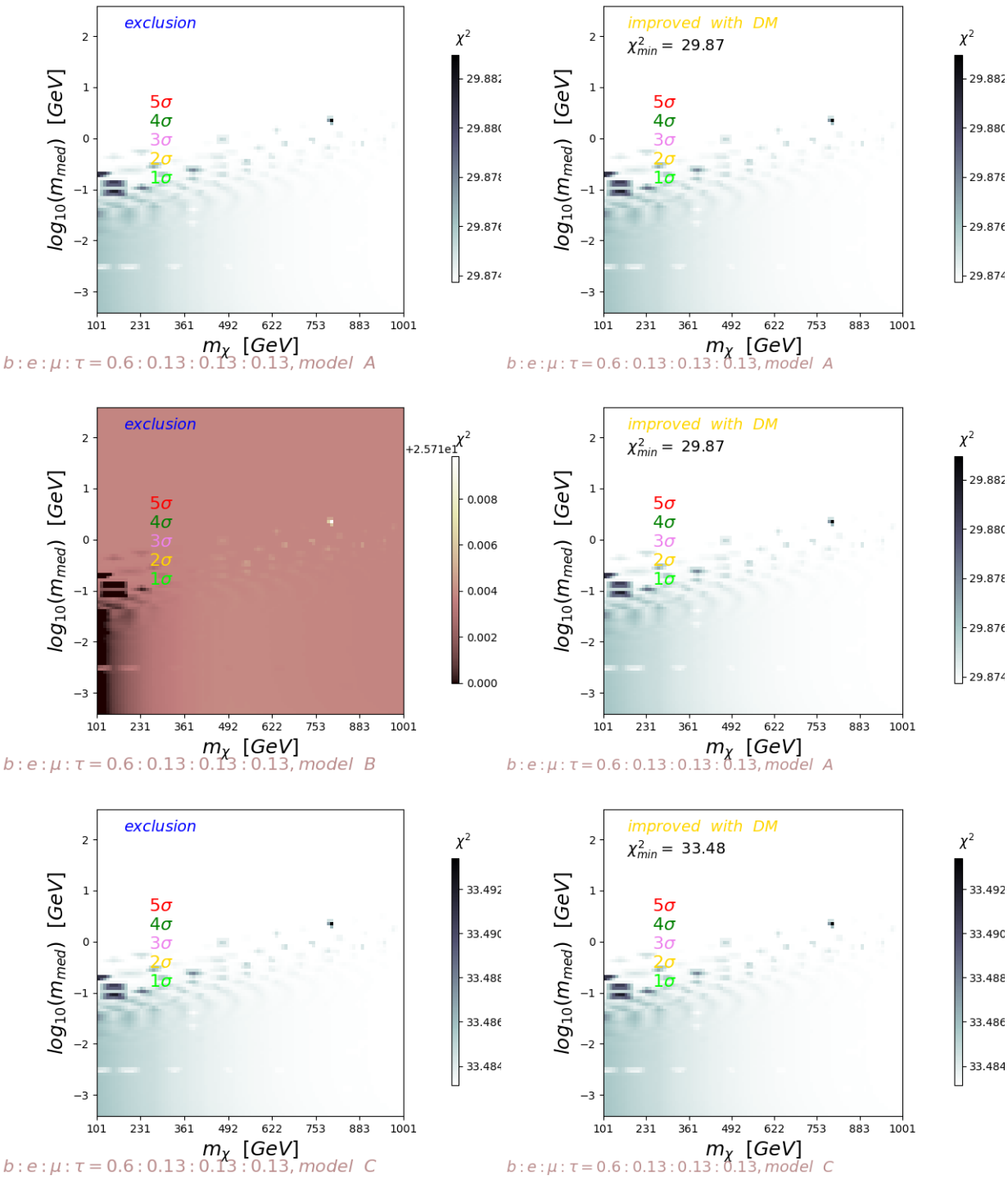

Figure 102: The distribution of χ^2 on the 2D map of m_χ and m_{med}.

$$\Phi_{tot,DM} = (1-\alpha)\cdot\Phi_1(\bar{\chi}\chi \to \phi \to b\bar{b}, e^+e^-, \mu^+\mu^-, \tau\bar{\tau}) + \alpha\cdot\Phi_2(\bar{\chi}\chi \to \phi\phi \to b\bar{b}, e^+e^-, \mu^+\mu^-, \tau\bar{\tau}), \quad (278)$$

with $\alpha = 0.1$. The branching ratio of the $b\bar{b}, e^+e^-, \mu^+\mu^-, \tau\bar{\tau}$ channels are assumed to be respectively 60%,13.3%, 13.3%, 13.3%. The annihilation of Dark Matter is Sommerfeld boosted. The extragalactic sources of IGRB are considered together with Dark Matter to fit the FermiLAT IGRB data [376]. The confidence contours are shown in different colors to enclose the best-fitting regions. The A, B, C models of the extragalactic sources are shown respectively on the top, middle, bottom panels. The exclusion fit and improved fit are respectively on the left and right side with colored contours.

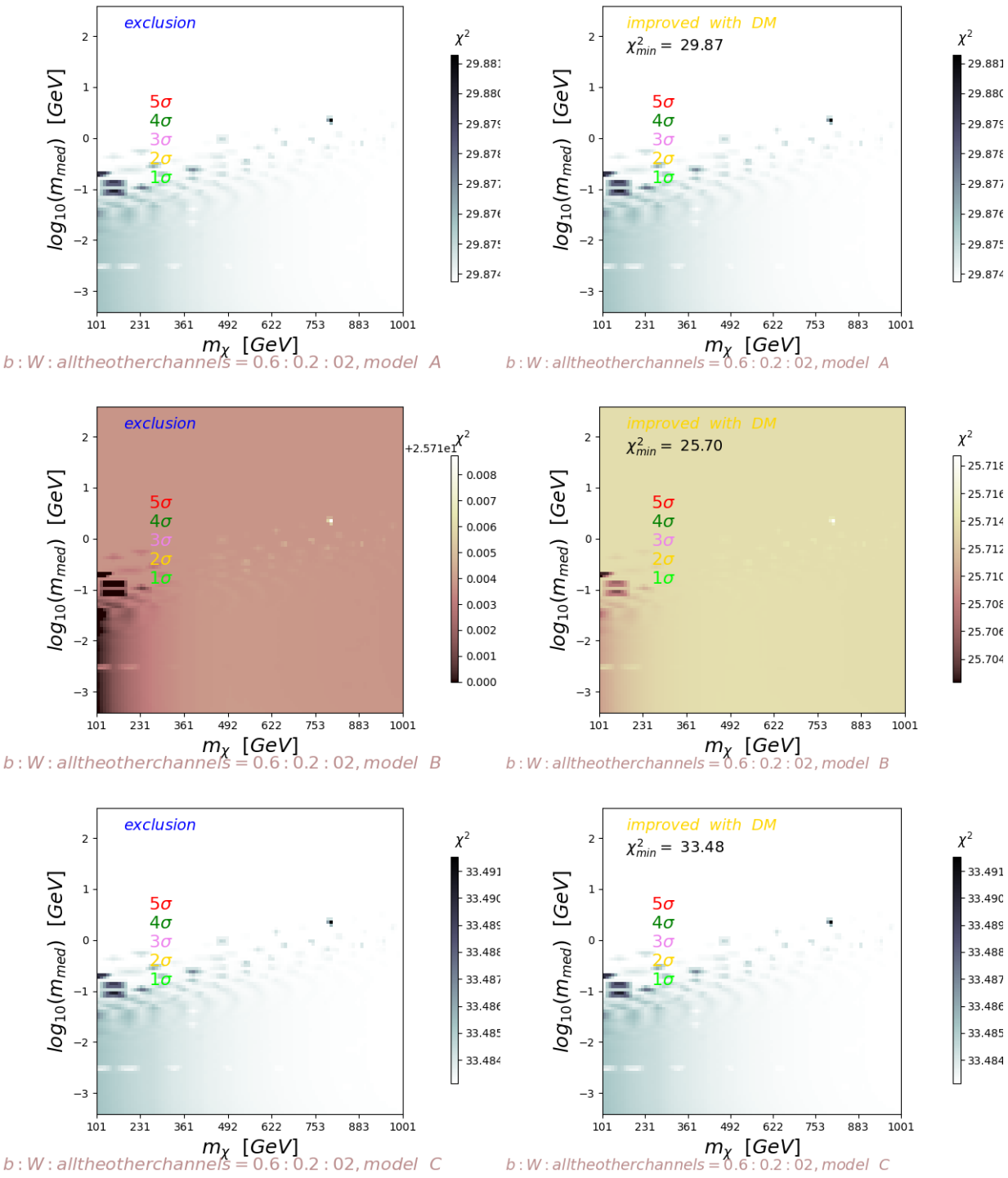

Figure 103: The distribution of χ^2 on the 2D map of m_χ and m_{med}.

$$\Phi_{tot,DM} = (1-\alpha)\cdot\Phi_1(\bar{\chi}\chi \to \phi \to b\bar{b}, W^+W^-, the\ others) + \alpha\cdot\Phi_2(\bar{\chi}\chi \to \phi\phi \to b\bar{b}, W^+W^-, the\ others), \quad (280)$$

with $\alpha = 0.1$. The branching ratio of the $b\bar{b}, W^+W^-$channels are assumed to be respectively 60%,20%, and 1/30 for each of the $\gamma\gamma$, $h\bar{h}$, $g\bar{g}$, $\tau^+\tau^-$, $\mu^+\mu^-$, e^+e^-channels. The annihilation of Dark Matter is Sommerfeld boosted. The extragalactic sources of IGRB are considered together with Dark Matter to fit the FermiLAT IGRB data [376]. The confidence contours are shown in different colors to enclose the best-fitting regions. The A, B, C models of the extragalactic sources are shown respectively on the top, middle, bottom panels. The exclusion fit and improved fit are respectively on the left and right side with colored contours.

References

[1] Dodelson, S., 2003. Modern cosmology. Elsevier.

[2] Smoot, G.F., Bennett, C.L., Kogut, A., Wright, E.L., Aymon, J., Boggess, N.W., Cheng, E.S., De Amici, G., Gulkis, S., Hauser, M.G. and Hinshaw, G., 1992. Structure in the COBE differential microwave radiometer first-year maps. The Astrophysical Journal, 396, pp.L1-L5.

[3] Miller, A., Beach, J., Bradley, S., Caldwell, R., Chapman, H., Devlin, M.J., Dorwart, W.B., Herbig, T., Jones, D., Monnelly, G. and Netterfield, C.B., 2002. The QMAP and MAT/TOCO experiments for measuring anisotropy in the cosmic microwave background. The Astrophysical Journal Supplement Series, 140(2), p.115.

[4] Tegmark, M., de Oliveira-Costa, A. and Hamilton, A.J., 2003. High resolution foreground cleaned CMB map from WMAP. Physical Review D, 68(12), p.123523.

[5] Wang, X., Tegmark, M., Jain, B. and Zaldarriaga, M., 2003. Last stand before WMAP: Cosmological parameters from lensing, CMB, and galaxy clustering. Physical Review D, 68(12), p.123001.

[6] Aghanim, N., Akrami, Y., Ashdown, M., Aumont, J., Baccigalupi, C., Ballardini, M., ... & Battye, R. (2018). Planck 2018 results. VI. Cosmological parameters. arXiv preprint arXiv:1807.06209.

[7] Riess, A. G., Macri, L. M., Hoffmann, S. L., Scolnic, D., Casertano, S., Filippenko, A. V., ... & Chornock, R. (2016). A 2.4% determination of the local value of the Hubble constant. The Astrophysical Journal, 826(1), 56.

[8] Poincare, H. (1906a), L' Astronomie, 158.

[9] Zwicky, F. (1937). On the Masses of Nebulae and of Clusters of Nebulae. The Astrophysical Journal, 86, 217.

[10] Babcock, H. W. (1939). The rotation of the Andromeda Nebula. Lick Observatory Bulletin, 19, 41-51.

[11] Markevitch, M., 2005. Chandra observation of the most interesting cluster in the universe. arXiv preprint astro-ph/0511345.

[12] Rubin, V.C. and Ford Jr, W.K., 1970. Rotation of the Andromeda nebula from a spectroscopic survey of emission regions. The Astrophysical Journal, 159, p.379.]

[13] Rubin, V.C., Ford Jr, W.K. and Thonnard, N., 1980. Rotational properties of 21 SC galaxies with a large range of luminosities and radii, from NGC 4605/R= 4kpc/to UGC 2885/R= 122 kpc. The Astrophysical Journal, 238, pp.471-487.

[14] Rubin, V.C., 1979. Rotation curves of high-luminosity spiral galaxies and the rotation curve of our Galaxy. In Symposium-International Astronomical Union (Vol. 84, pp. 211-220). Cambridge University Press.

[15] Douglas Clowe, Marusă Bradač, Anthony H. Gonzalez, Maxim Markevitch, Scott W. Randall, Christine Jones, et al. A direct empirical proof of the existence of dark matter. Astrophys. J., 648:L109–L113, 2006.

[16] NASA, STScIand ESO WFI, et al. 1e 0657-56: Nasa finds direct proof of dark matter. http://chandra.harvard.edu/photo/2006/1e0657/index.html.

[17] Del Popolo, A., 2013, July. Non-baryonic dark matter in cosmology. In AIP Conference Proceedings (Vol. 1548, No. 1, pp. 2-63). AIP.

[18] Newton, I., 1952. Opticks, or, a treatise of the reflections, refractions, inflections & colours of light. Courier Corporation.

[19] Dyson F. W., Eddington A. S.& Davidson C.. 1920A determination of the deflection of light by the Sun's gravitational field, from observations made at the total eclipse of May 29, 1919. Phil. Trans. R. Soc. Lond. A 220, 291-333(doi:10.1098/rsta.1920.0009).

[20] Massey, R., Kitching, T., & Richard, J. (2010). The dark matter of gravitational lensing. Reports on Progress in Physics, 73(8), 086901.

[21] Bartelmann, M., 2010. Gravitational lensing. Classical and Quantum Gravity, 27(23), p.233001.

[22] Kneib J P, Hudelot P, Ellis R S, et al. A Wide-Field Hubble Space Telescope Study of the Cluster Cl 0024+ 1654 at z= 0.4. II. The Cluster Mass Distribution[J]. The Astrophysical Journal, 2003, 598(2): 804.

[23] Jee, M. J., Ford, H. C., Illingworth, G. D., White, R. L., Broadhurst, T. J., Coe, D. A., ... & Bouwens, R. J. (2007). Discovery of a ringlike dark matter structure in the core of the galaxy cluster Cl 0024+ 17. The Astrophysical Journal, 661(2), 728.

[24] Cowsik, R., & McClelland, J. (1972). An upper limit on the neutrino rest mass. Physical Review Letters, 29(10), 669.

[25] Ostriker, J. P., & Peebles, P. J. (1973). A numerical study of the stability of flattened galaxies: or, can cold galaxies survive?. The Astrophysical Journal, 186, 467-480.

[26] Ostriker, J. P., Peebles, P. J. E., & Yahil, A. (1974). The size and mass of galaxies, and the mass of the universe. The Astrophysical Journal, 193, L1-L4.

[27] Einasto, J., Saar, E., Kaasik, A., & Chernin, A. D. (1974). Missing mass around galaxies: morphological evidence. Nature, 252(5479), 111.

[28] White, S. D., & Rees, M. J. (1978). Core condensation in heavy halos: a two-stage theory for galaxy formation and clustering. Monthly Notices of the Royal Astronomical Society, 183(3), 341-358.

[29] Press, W. H., & Schechter, P. (1974). Formation of galaxies and clusters of galaxies by self-similar gravitational condensation. The Astrophysical Journal, 187, 425-438.

[30] Greengard, L. (1990). The numerical solution of the n-body problem. Computers in physics, 4(2), 142-152.

[31] Frenk, C. S., & White, S. D. (2012). Dark matter and cosmic structure. Annalen der Physik, 524(9-10), 507-534.

[32] Lovell, Mark R., et al. "The haloes of bright satellite galaxies in a warm dark matter universe." Monthly Notices of the Royal Astronomical Society 420.3 (2012): 2318-2324.

[33] White, S. D., Frenk, C. S., & Davis, M. (1983). Clustering in a neutrino-dominated universe. The Astrophysical Journal, 274, L1-L5.

[34] Albareti, F. D., Prieto, C. A., Almeida, A., Anders, F., Anderson, S., Andrews, B. H., ... & Avila-Reese, V. (2017). The 13th data release of the Sloan Digital Sky Survey: first spectroscopic data from the SDSS-IV survey mapping nearby galaxies at Apache point observatory. The Astrophysical Journal Supplement Series, 233(2), 25.

[35] Springel, V., White, S.D., Jenkins, A., Frenk, C.S., Yoshida, N., Gao, L., Navarro, J., Thacker, R., Croton, D., Helly, J. and Peacock, J.A., 2005. Simulations of the formation, evolution and clustering of galaxies and quasars. nature, 435(7042), p.629.

[36] Croton, D.J., Springel, V., White, S.D., De Lucia, G., Frenk, C.S., Gao, L., Jenkins, A., Kauffmann, G., Navarro, J.F. and Yoshida, N., 2006. The many lives of active galactic nuclei: cooling flows, black holes and the luminosities and colours of galaxies. Monthly Notices of the Royal Astronomical Society, 365(1), pp.11-28.

[37] Kuhlen, Michael, Mark Vogelsberger, and Raul Angulo. "Numerical simulations of the dark universe: State of the art and the next decade." Physics of the Dark Universe 1.1-2 (2012): 50-93.

[38] Springel, V., Frenk, C.S. and White, S.D., 2006. The large-scale structure of the Universe. nature, 440(7088), p.1137.

[39] Vogelsberger, M., Genel, S., Springel, V., Torrey, P., Sijacki, D., Xu, D., ... & Hernquist, L. (2014). Properties of galaxies reproduced by a hydrodynamic simulation. Nature, 509(7499), 177.e

[40] Sijacki, D., Vogelsberger, M., Genel, S., Springel, V., Torrey, P., Snyder, G. F., ... & Hernquist, L. (2015). The Illustris simulation: the evolving population of black holes across cosmic time. Monthly Notices of the Royal Astronomical Society, 452(1), 575-596.

[41] Lewis, A. and Challinor, A., 2006. Weak gravitational lensing of the CMB. Physics Reports, 429(1), pp.1-65.

[42] Ade, P.A., Aghanim, N., Armitage-Caplan, C., Arnaud, M., Ashdown, M., Atrio-Barandela, F., Aumont, J., Baccigalupi, C., Banday, A.J., Barreiro, R.B. and Bartlett, J.G., 2014. Planck 2013 results. XVI. Cosmological parameters. Astronomy & Astrophysics, 571, p.A16.

[43] Madhavacheril, M.S., Sehgal, N. and Slatyer, T.R., 2014. Current dark matter annihilation constraints from CMB and low-redshift data. Physical Review D, 89(10), p.103508.

[44] Ade, P.A., Aghanim, N., Arnaud, M., Ashdown, M., Aumont, J., Baccigalupi, C., Banday, A.J., Barreiro, R.B., Bartlett, J.G., Bartolo, N. and Battaner, E., 2016. Planck 2015 results-xiii. cosmological parameters. Astronomy & Astrophysics, 594, p.A13.

[45] Milgrom, M. (1983). A modification of the Newtonian dynamics as a possible alternative to the hidden mass hypothesis. The Astrophysical Journal, 270, 365-370.

[46] Hodson, A. O., & Zhao, H. (2017). Generalizing MOND to explain the missing mass in galaxy clusters. Astronomy & Astrophysics, 598, A127.

[47] [47] J. Dubinski and R. G. Carlberg, Astrophys. J.378, 496 (1991).

[48] [48] J. F. Navarro, C. S. Frenk, and S. D. M. White, Astrophys. J.462, 563 (1996), astro-ph/9508025.

[49] [49] J. F. Navarro, C. S. Frenk, and S. D. M. White, Astrophys. J.490, 493 (1997), astro-ph/9611107.

[50] B. Moore, S. Ghigna, F. Governato, G. Lake, T. R. Quinn, J. Stadel, and P. Tozzi, Astrophys. J.524,L19 (1999), astro-ph/9907411.

[51] M. Boylan-Kolchin, J. S. Bullock, and M. Kaplinghat, Mon. Not. Roy. Astron. Soc.415, L40 (2011),1103.0007.

[52] M. Boylan-Kolchin, J. S. Bullock, and M. Kaplinghat, Mon. Not. Roy. Astron. Soc.422, 1203 (2012),1111.2048.

[53] E. Papastergis, R. Giovanelli, M. P. Haynes, and F. Shankar, Astron. Astrophys.574, A113 (2015),1407.4665.

[54] S. Garrison-Kimmel, M. Boylan-Kolchin, J. S. Bullock, and E. N. Kirby, Mon. Not. Roy. Astron.Soc.444, 222 (2014), 1404.5313.

[55] Falck, B., Koyama, K., Zhao, G.B. and Li, B., 2014. The Vainshtein mechanism in the cosmic web. Journal of Cosmology and Astroparticle Physics, 2014(07), p.058.

[56] Platscher, M., Smirnov, J., Meyer, S. and Bartelmann, M., 2018. Long range effects in gravity theories with Vainshtein screening. Journal of Cosmology and Astroparticle Physics, 2018(12), p.009.

[57] Jungman, G., Kamionkowski, M., & Griest, K. (1996). Supersymmetric dark matter. Physics Reports, 267(5-6), 195-373.

[58] Bertone, G., Hooper, D. and Silk, J., 2005. Particle dark matter: Evidence, candidates and constraints. Physics reports, 405(5-6), pp.279-390.

[59] Boyarsky, A., Drewes, M., Lasserre, T., Mertens, S., & Ruchayskiy, O. (2019). Sterile neutrino dark matter. Progress in Particle and Nuclear Physics, 104, 1-45.

[60] McCarthy, I.G., Bird, S., Schaye, J., Harnois-Deraps, J., Font, A.S. and Van Waerbeke, L., 2018. The BAHAMAS project: the CMB–large-scale structure tension and the roles of massive neutrinos and galaxy formation. Monthly Notices of the Royal Astronomical Society, 476(3), pp.2999-3030.

[61] R. Bähre, B. Döbrich, J. Dreyling-Eschweiler, S. Ghazaryan, R. Hodajerdi, D. Horns,F. Januschek, E.-A. Knabbe, A. Lindner, D. Notz,et al., J. Instrum.8, T09001 (2013).

[62] E. Armengaud, F. Avignone, M. Betz, P. Brax, P. Brun, G. Cantatore, J. Carmona, G. Carosi,F. Caspers, S. Caspi,et al., J. Instrum.9, T05002 (2014)

[63] Collaboration, X.E.N.O.N., Aprile, E., Aalbers, J., Agostini, F., Alfonsi, M., Althueser, L., Amaro, F.D., Anthony, M., Arneodo, F., Baudis, L. and Bauermeister, B., 2018. Dark matter search results from a one ton-year exposure of XENON1T. Physical Review Letters, 121(11), p.111302.

[64] Cui, X., Abdukerim, A., Chen, W., Chen, X., Chen, Y., Dong, B., Fang, D., Fu, C., Giboni, K., Giuliani, F. and Gu, L., 2017. Dark matter results from 54-ton-day exposure of PandaX-II experiment. Physical review letters, 119(18), p.181302.

[65] Kudryavtsev, V.A., 2019. Recent Results from LUX and Prospects for Dark Matter Searches with LZ. Universe, 5(3), p.73.

[66] Aad, G., Abbott, B., Abdallah, J., Abdinov, O., Abeloos, B., Aben, R., Abolins, M., AbouZeid, O.S., Abramowicz, H., Abreu, H. and Abreu, R., 2016. Search for supersymmetry at $\sqrt{s} = 13$ TeV in final states with jets and two same-sign leptons or three leptons with the ATLAS detector. The European Physical Journal C, 76(5), p.259.

[67] Sirunyan, A.M., Tumasyan, A., Adam, W., Ambrogi, F., Asilar, E., Bergauer, T., Brandstetter, J., Brondolin, E., Dragicevic, M., Erö, J. and Del Valle, A.E., 2018. Search for supersymmetry in proton-proton collisions at 13 TeV using identified top quarks. Physical Review D, 97(1), p.012007.

[68] Bertone, G., 2010. The moment of truth for WIMP dark matter. Nature, 468(7322), p.389.

[69] Kolb, E.W. and Long, A.J., 2017. Superheavy dark matter through Higgs portal operators. Physical Review D, 96(10), p.103540.

[70] Pospelov, M., Ritz, A. and Voloshin, M., 2008. Secluded WIMP dark matter. Physics Letters B, 662(1), pp.53-61.

[71] Horns, D., Jaeckel, J., Lindner, A., Redondo, J. and Ringwald, A., 2013. Searching for WISPy cold dark matter with a dish antenna. Journal of Cosmology and Astroparticle Physics, 2013(04), p.016.

[72] Horns, D., Lindner, A., Lobanov, A. and Ringwald, A., 2013. WISPers from the dark side: radio probes of axions and hidden photons. arXiv preprint arXiv:1309.4170.

[73] G. Grilli di Cortona, E. Hardy, J. Pardo Vega, and G.Villadoro,J. High Energy Phys. 01 (2016) 034

[74] Horns, D., Ringwald, A. and Le Hoang Nguyen, A.L., 2018. Axions and other WISPs. PARTICLES, STRINGS AND THE EARLY UNIVERSE, p.285.

[75] Tulin, S. and Yu, H.B., 2018. Dark matter self-interactions and small scale structure. Physics Reports, 730, pp.1-57.

[76] Rocha, M., Peter, A.H., Bullock, J.S., Kaplinghat, M., Garrison-Kimmel, S., Onorbe, J. and Moustakas, L.A., 2013. Cosmological simulations with self-interacting dark matter–I. Constant-density cores and substructure. Monthly Notices of the Royal Astronomical Society, 430(1), pp.81-104.

[77] Peiris, H.V., Komatsu, E., Verde, L., Spergel, D.N., Bennett, C.L., Halpern, M., Hinshaw, G., Jarosik, N., Kogut, A., Limon, M. and Meyer, S.S., 2003. First-year Wilkinson microwave anisotropy probe (WMAP)* observations: implications for inflation. The Astrophysical Journal Supplement Series, 148(1), p.213.

[78] Itoh, Y., Yahata, K. and Takada, M., 2010. Dipole anisotropy of galaxy distribution: Does the CMB rest frame exist in the local universe?. Physical Review D, 82(4), p.043530.

[79] Peter, A.H., Rocha, M., Bullock, J.S. and Kaplinghat, M., 2013. Cosmological simulations with self-interacting dark matter–II. Halo shapes versus observations. Monthly Notices of the Royal Astronomical Society, 430(1), pp.105-120.

[80] M. Kaplinghat, S. Tulin, and H.-B. Yu, Phys. Rev.D89, 035009 (2014), 1310.7945

[81] R. Essig, A. Manalaysay, J. Mardon, P. Sorensen, and T. Volansky, Phys.Rev.Lett.109, 021301(2012), 1206.2644.

[82] Hufnagel, M., Schmidt-Hoberg, K. and Wild, S., 2018. BBN constraints on MeV-scale dark sectors. Part II: electromagnetic decays. Journal of Cosmology and Astroparticle Physics, 2018(11), p.032.

[83] Montero, J.C., Castellanos, A.R.R. and Sánchez-Vega, B.L., 2018. Axion dark matter in a 3– 3– 1 model. Physical Review D, 97(6), p.063015.

[84] Majumdar, J., Calore, F. and Horns, D., 2018. Gamma-ray spectral modulations of Galactic pulsars caused by photon-ALPs mixing. arXiv preprint arXiv:1801.08813.

[85] Majorovits, B., 2017. MADMAX: A new road to axion dark matter detection. arXiv preprint arXiv:1712.01062.

[86] Zhang, J., Tsai, Y.L.S., Kuo, J.L., Cheung, K. and Chu, M.C., 2018. Ultralight Axion Dark Matter and Its Impact on Dark Halo Structure in N-body Simulations. The Astrophysical Journal, 853(1), p.51.

[87] Aoki, A. and Soda, J., 2017. Detecting ultralight axion dark matter wind with laser interferometers. International Journal of Modern Physics D, 26(07), p.1750063.

[88] Blas, D., Nacir, D.L. and Sibiryakov, S., 2017. Ultralight dark matter resonates with binary pulsars. Physical review letters, 118(26), p.261102.

[89] Chaudhuri, S., Graham, P.W., Irwin, K., Mardon, J., Rajendran, S. and Zhao, Y., 2015. Radio for hidden-photon dark matter detection. Physical Review D, 92(7), p.075012.

[90] Arias, P., Cadamuro, D., Goodsell, M., Jaeckel, J., Redondo, J. and Ringwald, A., 2012. WISPy cold dark matter. Journal of Cosmology and Astroparticle Physics, 2012(06), p.013.

[91] Nguyen, L.H., Lobanov, A. and Horns, D., 2019. First results from the WISPDMX radio frequency cavity searches for hidden photon dark matter. arXiv preprint arXiv:1907.12449.

[92] Neronov, A., Malyshev, D., & Eckert, D. (2016). Decaying dark matter search with NuSTAR deep sky observations. Physical Review D, 94(12), 123504.

[93] Brandt, T. D. (2016). Constraints on MACHO dark matter from compact stellar systems in ultra-faint dwarf galaxies. The Astrophysical Journal Letters, 824(2), L31.

[94] Bartolo, N., De Luca, V., Franciolini, G., Lewis, A., Peloso, M. and Riotto, A., 2019. Primordial Black Hole Dark Matter: LISA Serendipity. Physical Review Letters, 122(21), p.211301.

[95] Bringmann, T., Depta, P.F., Domcke, V. and Schmidt-Hoberg, K., 2019. Towards closing the window of primordial black holes as dark matter: The case of large clustering. Physical Review D, 99(6), p.063532.

[96] Manshanden, J., Gaggero, D., Bertone, G., Connors, R.M. and Ricotti, M., 2019. Multi-wavelength astronomical searches for primordial black holes. Journal of Cosmology and Astroparticle Physics, 2019(06), p.026.

[97] Kusenko, A., & Rosenberg, L. J. (2013). Snowmass-2013 Cosmic Frontier 3 (CF3) working group summary: non-WIMP dark matter. arXiv preprint arXiv:1310.8642.

[98] Poulin, V., Boddy, K.K., Bird, S. and Kamionkowski, M., 2018. Implications of an extended dark energy cosmology with massive neutrinos for cosmological tensions. Physical Review D, 97(12), p.123504.

[99] Battaglieri, M., Belloni, A., Chou, A., Cushman, P., Echenard, B., Essig, R., ... & Graham, P. (2017). US cosmic visions: new ideas in dark matter 2017: community report. arXiv preprint arXiv:1707.04591.

[100] Nguyen, N., Horns, D. and Bringmann, T., 2012. AstroFit: an interface program for exploring complementarity in dark matter research. In Astroparticle, Particle, Space Physics and Detectors for Physics Applications (pp. 1025-1030).

[101] Sirunyan, A.M., Tumasyan, A., Adam, W., Ambrogi, F., Asilar, E., Bergauer, T., Brandstetter, J., Brondolin, E., Dragicevic, M., Erö, J. and Del Valle, A.E., 2018. Search for supersymmetry in proton-proton collisions at 13 TeV using identified top quarks. Physical Review D, 97(1), p.012007.

[102] Aad, G., Abbott, B., Abdallah, J., Abdinov, O., Abeloos, B., Aben, R., Abolins, M., AbouZeid, O.S., Abramowicz, H., Abreu, H. and Abreu, R., 2016. Search for supersymmetry at $\sqrt{s} = 13$ TeV in final states with jets and two same-sign leptons or three leptons with the ATLAS detector. The European Physical Journal C, 76(5), p.259.

[103] Zheng, J.M., Yu, Z.H., Shao, J.W., Bi, X.J., Li, Z. and Zhang, H.H., 2012. Constraining the interaction strength between dark matter and visible matter: I. fermionic dark matter. Nuclear Physics B, 854(2), pp.350-374.

[104] Yu, Z.H., Zheng, J.M., Bi, X.J., Li, Z., Yao, D.X. and Zhang, H.H., 2012. Constraining the interaction strength between dark matter and visible matter: II. scalar, vector and spin-3/2 dark matter. Nuclear Physics B, 860(1), pp.115-151.

[105] Dreiner, H.K., Huck, M., Krämer, M., Schmeier, D. and Tattersall, J., 2013. Illuminating dark matter at the ILC. Physical Review D, 87(7), p.075015.

[106] De Simone, A., Monin, A., Thamm, A. and Urbano, A., 2013. On the effective operators for Dark Matter annihilations. Journal of Cosmology and Astroparticle Physics, 2013(02), p.039.

[107] Balázs, C., Conrad, J., Farmer, B., Jacques, T., Li, T., Meyer, M., Queiroz, F.S. and Sánchez-Conde, M.A., 2017. Sensitivity of the Cherenkov Telescope Array to the detection of a Dark Matter signal in comparison to direct detection and collider experiments. Physical Review D, 96(8), p.083002.

[108] Zhang, S., Jin, J. and Crandall, R.E., 1997. Computation of special functions. American Journal of Physics, 65, pp.355-355.

[109] De Simone, A. and Jacques, T., 2016. Simplified models vs. effective field theory approaches in Dark Matter searches. The European Physical Journal C, 76(7), p.367.

[110] Petruk, O. (2009). Approximation of the radiation power of CCC electrons due to the inverse-Compton process in the black-body photon CCC field. Astronomy & Astrophysics, 499(3), 643-648.

[111] Fermi-LAT collaboration and Di Mauro, M., 2015, July. The origin of the Fermi-LAT γ-ray background. In 14th Marcel Grossmann Meeting on Recent Developments in Theoretical and Experimental General Relativity, Astrophysics, and Relativistic Field Theories (MG14) Rome, Italy (Vol. 2016, pp. 1601-04323).

[112] PPPC4DMID - A Poor Particle Physicist Cookbook for Dark Matter Indirect Detection. http://www.marcocirelli.net/PPPC4DMID.html).

[113] Cirelli, M., Corcella, G., Hektor, A., Hütsi, G., Kadastik, M., Panci, P., Raidal, M., Sala, F. and Strumia, A., 2011. PPPC 4 DM ID: a poor particle physicist cookbook for Dark Matter indirect detection. Journal of Cosmology and Astroparticle Physics, 2011(03), p.051.

[114] PPPC4DMID website: hqqp://www.marcocirelli.net/PPPC4DMID.html

[115] Iengo, R., 2009. Sommerfeld enhancement: general results from field theory diagrams. Journal of High Energy Physics, 2009(05), p.024.

[116] Iengo, R., 2009. Sommerfeld enhancement for a Yukawa potential. arXiv preprint arXiv:0903.0317.

[117] Charbonnier, A., Combet, C., Daniel, M., Funk, S., Hinton, J.A., Maurin, D., Power, C., Read, J.I., Sarkar, S., Walker, M.G. and Wilkinson, M.I., 2011. Dark matter profiles and annihilation in dwarf spheroidal galaxies: prospectives for present and future γ-ray observatories–I. The classical dwarf spheroidal galaxies. Monthly Notices of the Royal Astronomical Society, 418(3), pp.1526-1556.

[118] Griest, K. and Seckel, D., 1991. Three exceptions in the calculation of relic abundances. Physical Review D, 43(10), p.3191.

[119] Perrin, C.L., 1997. Numerical Recipes in Fortran 90: The Art of Scientific Computing, Volume 2 (3 CD-ROMs and Manual) By William H. Press, Saul A. Teukolsky, William T. Vetterling, and Brian P. Flannery. Cambridge University Press: New York, 1996.

[120] https://people.sc.fsu.edu/~jburkardt/f_src/jacobi_polynomial/jacobi_polynomial.html

[121] http://people.sc.fsu.edu/~jburkardt/f_src/special_functions/special_functions.html

[122] http://people.sc.fsu.edu/~jburkardt/f_src/special_functions/special_functions.f90

[123] Cowan, G., 2015. Statistics for Searches at the LHC. In LHC Phenomenology (pp. 321-355). Springer, Cham.

[124] http://pdg.lbl.gov/2014/reviews/rpp2014-rev-statistics.pdf

[125] H.E.S.S. Collaboration, H. Abdallah et al., Search for dark matter annihilations towards the inner Galactic halo from 10 years of observations with H.E.S.S, Phys. Rev. Lett. 117 (2016) 111301, [1607.08142].

[126] Pierre, M., Siegal-Gaskins, J.M. and Scott, P., 2014. Sensitivity of CTA to dark matter signals from the Galactic Center. Journal of Cosmology and Astroparticle Physics, 2014(06), p.024.

[127] MAGIC collaboration, 2016. Limits to dark matter annihilation cross-section from a combined analysis of MAGIC and Fermi-LAT observations of dwarf satellite galaxies. Journal of Cosmology and Astroparticle Physics, 2016(02), p.039.

[128] Aartsen, M.G., Ackermann, M., Adams, J., Aguilar, J.A., Ahlers, M., Ahrens, M., Al Samarai, I., Altmann, D., Andeen, K., Anderson, T. and Ansseau, I., 2017. Search for Neutrinos from Dark Matter Self-Annihilations in the center of the Milky Way with 3 years of IceCube/DeepCore. The European Physical Journal C, 77(9), p.627.

[129] B.-Q. Lu and H.-S. Zong, Limits on dark matter from AMS-02 antiproton and positron fraction data, Phys. Rev. D93 (2016) 103517, [1510.04032].

[130] HAWC Collaboration, A. U. Abeysekara et al., A Search for Dark Matter in the Galactic Halo with HAWC, JCAP 1802 (2018) 049, [1710.10288]

[131] Cui, X., Abdukerim, A., Chen, W., Chen, X., Chen, Y., Dong, B., Fang, D., Fu, C., Giboni, K., Giuliani, F. and Gu, L., 2017. Dark matter results from 54-ton-day exposure of PandaX-II experiment. Physical review letters, 119(18), p.181302.

[132] Xia, J., Abdukerim, A., Chen, W., Chen, X., Chen, Y., Cui, X., Fang, D., Fu, C., Giboni, K., Giuliani, F. and Gu, L., 2019. PandaX-II constraints on spin-dependent WIMP-nucleon effective interactions. Physics Letters B, 792, pp.193-198.

[133] Zhang, H., Abdukerim, A., Chen, W., Chen, X., Chen, Y., Cui, X., Dong, B., Fang, D., Fu, C., Giboni, K. and Giuliani, F., 2019. Dark matter direct search sensitivity of the PandaX-4T experiment. SCIENCE CHINA Physics, Mechanics & Astronomy, 62(3), p.31011.

[134] Akerib, D.S., Alsum, S., Araújo, H.M., Bai, X., Bailey, A.J., Balajthy, J., Beltrame, P., Bernard, E.P., Bernstein, A., Biesiadzinski, T.P. and Boulton, E.M., 2017. Results from a search for dark matter in the complete LUX exposure. Physical review letters, 118(2), p.021303.

[135] Amole, C., Ardid, M., Arnquist, I.J., Asner, D.M., Baxter, D., Behnke, E., Bressler, M., Broerman, B., Cao, G., Chen, C.J. and Chowdhury, U., 2019. Dark matter search results from the complete exposure of the PICO-60 C_3F_8 bubble chamber. Physical Review D, 100(2), p.022001.

[136] Behnke, E., Behnke, J., Brice, S.J., Broemmelsiek, D., Collar, J.I., Conner, A., Cooper, P.S., Crisler, M., Dahl, C.E., Fustin, D. and Grace, E., 2012. First dark matter search results from a 4-kg CF_3I bubble chamber operated in a deep underground site. Physical Review D, 86(5), p.052001.

[137] Attisha, M.J., 2006. Cryogenic dark matter search (CDMS II): Application of neural networks and wavelets to event analysis (No. UMI-32-27793; FERMILAB-THESIS-2006-87). Fermi National Accelerator Lab.(FNAL), Batavia, IL (United States).

[138] CDMS II Collaboration, 2010. Dark matter search results from the CDMS II experiment. Science, 327(5973), pp.1619-1621.

[139] Schneck, Kristiana. Search for Low-Mass Dark Matter wtih SuperCDMS Soudan and Study of Shorted Electric Field Configurations in CDMS Detectors. No. FERMILAB-THESIS-2015-41. 2015.

[140] Undagoitia, T.M. and Rauch, L., 2015. Dark matter direct-detection experiments. Journal of Physics G: Nuclear and Particle Physics, 43(1), p.013001.

[141] Barklow, T., Brau, J., Fujii, K., Gao, J., List, J., Walker, N. and Yokoya, K., 2015. ILC operating scenarios. arXiv preprint arXiv:1506.07830.

[142] Habermehl, M., 2018. Dark Matter at the International Linear Collider (No. DESY-THESIS-2018-039). Verlag Deutsches Elektronen-Synchrotron.

[143] S. A. Malik, C. McCabe, H. Araujo, A. Belyaev, C. Bœhm, J. Brooke et al., Interplay and characterization of dark matter searches at colliders and in direct detection experiments, Physics of the Dark Universe 9 (2015) 51–58.

[144] Planck Collaboration, P. A. R. Ade et al., Planck 2015 results. XIII. Cosmological parameters, Astron. Astrophys. 594 (2016) A13, [1502.01589].

[145] Kennedy, J. (2011). Particle swarm optimization. In Encyclopedia of machine learning (pp. 760-766). Springer, Boston, MA.

[146] Schutte, J. F., Groenwold, A. A. (2005). A study of global optimization using particle swarms. Journal of global optimization, 31(1), 93-108.

[147] Abazajian, K.N., Blanchet, S. and Harding, J.P., 2012. Current and future constraints on Dark Matter from prompt and inverse-Compton photon emission in the isotropic diffuse gamma-ray background. Physical Review D, 85(4), p.043509.

[148] Charbonnier, A., Combet, C. and Maurin, D., 2012. CLUMPY: A code for $\gamma-$ray signals from dark matter structures. Computer Physics Communications, 183(3), pp.656-668.

[149] Zhao, H. (1996). Analytical models for galactic nuclei. Monthly Notices of the Royal Astronomical Society, 278(2), 488-496.

[150] Gondolo, P., Edsjö, J., Bergström, L., Ullio, P. and Baltz, E.A., 2001. DARKSUSY–A NUMERICAL PACKAGE FOR DARK MATTER CALCULATIONS IN THE MSSM. In The Identification Of Dark Matter (pp. 318-323).

[151] Bringmann, T., Edsjö, J., Gondolo, P., Ullio, P. and Bergström, L., 2018. DarkSUSY 6: an advanced tool to compute dark matter properties numerically. Journal of Cosmology and Astroparticle Physics, 2018(07), p.033.

[152] Belanger, G., Boudjema, F., Pukhov, A. and Semenov, A., 2014. micrOMEGAs_3: A program for calculating dark matter observables. Computer Physics Communications, 185(3), pp.960-985.

[153] Athron, P., Balazs, C., Bringmann, T., Buckley, A., Chrząszcz, M., Conrad, J., Cornell, J.M., Dal, L.A., Dickinson, H., Edsjö, J. and Farmer, B., 2018. GAMBIT: the global and modular beyond-the-standard-model inference tool. The European Physical Journal C, 78(2), p.98.

[154] Matsumoto, S., Mukhopadhyay, S. and Tsai, Y.L.S., 2016. Effective theory of WIMP dark matter supplemented by simplified models: singlet-like Majorana fermion case. Physical Review D, 94(6), p.065034.

[155] Falkowski, Adam. Higgs basis: proposal for an EFT basis choice for LHC HXSWG. No. LHCHXSWG-INT-2015-001. 2015.

[156] Brivio, I. and Trott, M., 2018. The Standard Model as an effective field theory. Physics Reports.

[157] Kahlhoefer, F., 2017. Review of LHC dark matter searches. International Journal of Modern Physics A, 32(13), p.1730006.

[158] Abdallah, J., Araujo, H., Arbey, A., Ashkenazi, A., Belyaev, A., Berger, J., Boehm, C., Boveia, A., Brennan, A., Brooke, J. and Buchmueller, O., 2015. Simplified models for dark matter searches at the LHC. Physics of the Dark Universe, 9, pp.8-23.

[159] Beltran, M., Hooper, D., Kolb, E.W. and Krusberg, Z.A., 2009. Deducing the nature of dark matter from direct and indirect detection experiments in the absence of collider signatures of new physics. Physical Review D, 80(4), p.043509.

[160] Alanne, T. and Goertz, F., 2017. Extended dark matter EFT. arXiv preprint arXiv:1712.07626.

[161] Morgante, E., 2018. Simplified dark matter models. Advances in High Energy Physics, 2018.

[162] Bell, N.F., Cai, Y., Dent, J.B., Leane, R.K. and Weiler, T.J., 2015. Dark matter at the LHC: Effective field theories and gauge invariance. Physical Review D, 92(5), p.053008.

[163] Albert, A., Backovic, M., Boveia, A., Buchmueller, O., Busoni, G., De Roeck, A., Doglioni, C., DuPree, T., Fairbairn, M., Genest, M.H. and Gori, S., 2017. Recommendations of the LHC Dark Matter Working Group: Comparing LHC searches for heavy mediators of dark matter production in visible and invisible decay channels. arXiv preprint arXiv:1703.05703.

[164] Zheng, J.M., Yu, Z.H., Shao, J.W., Bi, X.J., Li, Z. and Zhang, H.H., 2012. Constraining the interaction strength between dark matter and visible matter: I. fermionic dark matter. Nuclear Physics B, 854(2), pp.350-374.

[165] Yu, Z.H., Zheng, J.M., Bi, X.J., Li, Z., Yao, D.X. and Zhang, H.H., 2012. Constraining the interaction strength between dark matter and visible matter: II. scalar, vector and spin-3/2 dark matter. Nuclear Physics B, 860(1), pp.115-151.

[166] Liem, S., Bertone, G., Calore, F., de Austri, R.R., Tait, T.M., Trotta, R. and Weniger, C., 2016. Effective field theory of dark matter: a global analysis. Journal of High Energy Physics, 2016(9), p.77.

[167] De Simone, A., Monin, A., Thamm, A. and Urbano, A., 2013. On the effective operators for Dark Matter annihilations. Journal of Cosmology and Astroparticle Physics, 2013(02), p.039.

[168] De Simone, A. and Jacques, T., 2016. Simplified models vs. effective field theory approaches in dark matter searches. The European Physical Journal C, 76(7), p.367.

[169] Belyaev, A., Panizzi, L., Pukhov, A. and Thomas, M., 2017. Dark Matter characterization at the LHC in the Effective Field Theory approach. Journal of High Energy Physics, 2017(4), p.110.

[170] Belyaev, A., Bertuzzo, E., Barros, C.C., Eboli, O., di Cortona, G.G., Iocco, F. and Pukhov, A., 2019. Interplay of the LHC and non-LHC dark matter searches in the effective field theory approach. Physical Review D, 99(1), p.015006.

[171] Griest, K. and Seckel, D., 1991. Three exceptions in the calculation of relic abundances. Physical Review D, 43(10), p.3191.

[172] Husdal, L., 2016. On effective degrees of freedom in the early universe. Galaxies, 4(4), p.78.

[173] Goodman, J., Ibe, M., Rajaraman, A., Shepherd, W., Tait, T.M. and Yu, H.B., 2010. Constraints on dark matter from colliders. Physical Review D, 82(11), p.116010.

[174] H.E.S.S. Collaboration, H. Abdallah et al., Search for dark matter annihilations towards the inner Galactic halo from 10 years of observations with H.E.S.S, Phys. Rev. Lett. 117 (2016) 111301, [1607.08142].

[175] Queiroz, F.S., 2016. Dark matter overview: collider, direct and indirect detection searches. arXiv preprint arXiv:1605.08788.

[176] Busoni, G., De Simone, A., Gramling, J., Morgante, E. and Riotto, A., 2014. On the validity of the effective field theory for dark matter searches at the LHC, part II: complete analysis for the s-channel. Journal of Cosmology and Astroparticle Physics, 2014(06), p.060.

[177] Buchmüller, O., Dolan, M.J. and McCabe, C., 2014. Beyond effective field theory for dark matter searches at the LHC. Journal of High Energy Physics, 2014(1), p.25.

[178] Albert, A., Anderson, B., Bechtol, K., Drlica-Wagner, A., Meyer, M., Sánchez-Conde, M., Strigari, L., Wood, M., Abbott, T.M.C., Abdalla, F.B. and Benoit-Lévy, A., 2017. Searching for dark matter annihilation in recently discovered Milky Way satellites with Fermi-LAT. The Astrophysical Journal, 834(2), p.110.

[179] Balázs, C., Conrad, J., Farmer, B., Jacques, T., Li, T., Meyer, M., Queiroz, F.S. and Sánchez-Conde, M.A., 2017. Sensitivity of the Cherenkov Telescope Array to the detection of a dark matter signal in comparison to direct detection and collider experiments. Physical Review D, 96(8), p.083002.

[180] Funk, S., 2015. Indirect detection of dark matter with γ rays. Proceedings of the National Academy of Sciences, 112(40), pp.12264-12271.

[181] Collaboration, X.E.N.O.N., Aprile, E., Aalbers, J., Agostini, F., Alfonsi, M., Althueser, L., Amaro, F.D., Anthony, M., Arneodo, F., Baudis, L. and Bauermeister, B., 2018. Dark matter search results from a one ton-year exposure of XENON1T. Physical Review Letters, 121(11), p.111302.

[182] Aprile, E., Aalbers, J., Agostini, F., Alfonsi, M., Amaro, F.D., Anthony, M., Antunes, B., Arneodo, F., Balata, M., Barrow, P. and Baudis, L., 2017. The XENON1T dark matter experiment. The European Physical Journal C, 77(12), p.881.

[183] Bauer, D., Buckley, J., Cahill-Rowley, M., Cotta, R., Drlica-Wagner, A., Feng, J.L., Funk, S., Hewett, J., Hooper, D., Ismail, A. and Kaplinghat, M., 2015. Dark matter in the coming decade: Complementary paths to discovery and beyond. Physics of the Dark Universe, 7, pp.16-23.

[184] Anand, N., Fitzpatrick, A.L. and Haxton, W.C., 2014. Weakly interacting massive particle-nucleus elastic scattering response. Physical Review C, 89(6), p.065501.

[185] Schneck, K., Cabrera, B., Cerdeño, D.G., Mandic, V., Rogers, H.E., Agnese, R., Anderson, A.J., Asai, M., Balakishiyeva, D., Barker, D. and Thakur, R.B., 2015. Dark matter effective field theory scattering in direct detection experiments. Physical Review D, 91(9), p.092004.

[186] Catena, R., Ibarra, A., Rappelt, A. and Wild, S., 2018. Halo-independent comparison of direct detection experiments in the effective theory of dark matter-nucleon interactions. Journal of Cosmology and Astroparticle Physics, 2018(07), p.028.

[187] Fitzpatrick, A.L., Haxton, W., Katz, E., Lubbers, N. and Xu, Y., 2013. The effective field theory of dark matter direct detection. Journal of Cosmology and Astroparticle Physics, 2013(02), p.004.

[188] Jochen Schieck, Holger Kluck, 2017, Dark Matter, Vienna University of Technology.

[189] Cannoni, M., Vergados, J.D. and Gomez, M.E., 2011. Scheme for the extraction of WIMP-nucleon scattering cross sections from total event rates. Physical Review D, 83(7), p.075010.

[190] Fan, J., Reece, M. and Wang, L.T., 2010. Non-relativistic effective theory of dark matter direct detection. Journal of Cosmology and Astroparticle Physics, 2010(11), p.042.

[191] Dent, J.B., Krauss, L.M., Newstead, J.L. and Sabharwal, S., 2015. General analysis of direct dark matter detection: From microphysics to observational signatures. Physical Review D, 92(6), p.063515.

[192] Ellis, J., Ferstl, A. and Olive, K.A., 2000. Re-evaluation of the elastic scattering of supersymmetric dark matter. Physics Letters B, 481(2-4), pp.304-314.

[193] Airapetian, A., Akopov, N., Akopov, Z., Andrus, A., Aschenauer, E.C., Augustyniak, W., Avakian, R., Avetissian, A., Avetissian, E., Belostotski, S. and Bianchi, N., 2007. Precise determination of the spin structure function g 1 of the proton, deuteron, and neutron. Physical Review D, 75(1), p.012007.

[194] C. Amole, M. Ardid, I. J. Arnquist, D. M. Asner, D. Baxter, E. Behnke et al., Dark matter search results from the PICO-60 C 3 F 8 bubble chamber, Physical review letters 118 (2017) 251301.

[195] Bell, N.F., Cai, Y. and Medina, A.D., 2014. Co-annihilating dark matter: effective operator analysis and collider phenomenology. Physical Review D, 89(11), p.115001.

[196] D'Agnolo, R.T., Mondino, C., Ruderman, J.T. and Wang, P.J., 2018. Exponentially light dark matter from coannihilation. Journal of High Energy Physics, 2018(8), p.79.

[197] Matsumoto, S. and Senami, M., 2006. Efficient coannihilation process through strong Higgs self-coupling in LKP dark matter annihilation. Physics Letters B, 633(6), pp.671-674.

[198] Edsjö, J. and Gondolo, P., 1997. Neutralino relic density including coannihilations. Physical Review D, 56(4), p.1879.

[199] Nihei, T., Roszkowski, L. and de Austri, R.R., 2002. Exact cross sections for the neutralino-slepton coannihilation. Journal of High Energy Physics, 2002(07), p.024.

[200] G. Steigman, B. Dasgupta and J. F. Beacom, Precise Relic WIMP Abundance and its Impact on Searches for Dark Matter Annihilation, Phys. Rev. D86 (2012) 023506, [1204.3622].

[201] Fermi-LAT Collaborations, M. Ackermann et al., Searching for Dark Matter Annihilation from Milky Way Dwarf Spheroidal Galaxies with Six Years of Fermi Large Area Telescope Data, Phys. Rev. Lett. 115 (2015) 231301, [1503.02641].

[202] Fermi-LAT Collaborations, M. Di Mauro, Isotropic diffuse and extragalactic γ-ray background: emission from extragalactic sources vs dark matter annihilating particles, J. Phys. Conf. Ser. 718 (2016) 042019, [1601.04322]

[203] Fermi-LAT, MAGIC Collaborations, M. L. Ahnen et al., Limits to dark matter annihilation cross-section from a combined analysis of MAGIC and Fermi-LAT observations of dwarf satellite galaxies, JCAP 1602 (2016) 039, [1601.06590].

[204] VERITAS Collaboration, S. Archambault et al., Dark Matter Constraints from a Joint Analysis of Dwarf Spheroidal Galaxy Observations with VERITAS, Phys. Rev. D95 (2017) 082001, [1703.04937]

[205] B. Opitz, Searches for dark matter self-annihilation signals from dwarf spheroidal galaxies and the Fornax galaxy cluster with imaging air Cherenkov telescopes, Ph.D. thesis, University of Hamburg, 2014.

[206] Brüggen, Marcus "Dark Matter Searches" in Particles, Strings and the Early Universe : The Structure of Matter and Space-Time / Haller, Johannes, Grefe, Michael (eds.), Verlag Deutsches Elektronen-Synchrotron : 2018

[207] H. Edler, "Indirect searches for gamma rays from self annihilation of heavy dark matter particles with the taiga experiment." Bachelor thesis at the University of Hamburg 4, 2018. updated in internal note (TAIGA).

[208] Petricca, F., Angloher, G., Bento, A., Bucci, C., Canonica, L., Defay, X., Erb, A., v Feilitzsch, F., Iachellini, N.F., Gorla, P. and Gütlein, A., 2016, May. New results on low-mass dark matter from the CRESST-II experiment. In Journal of Physics: Conference Series (Vol. 718, No. 4, p. 042044). IOP Publishing.

[209] Walker, M.G., Mateo, M., Olszewski, E.W., Gnedin, O.Y., Wang, X., Sen, B. and Woodroofe, M., 2007. Velocity dispersion profiles of seven dwarf spheroidal galaxies. The Astrophysical Journal Letters, 667(1), p.L53.

[210] Baushev, A.N., 2011. Principal properties of the velocity distribution of dark matter particles on the outskirts of the Solar system. Monthly Notices of the Royal Astronomical Society: Letters, 417(1), pp.L83-L87.

[211] Chae, Y.J. and Perelstein, M., 2013. Dark matter search at a linear collider: effective operator approach. Journal of High Energy Physics, 2013(5), p.138.

[212] B. P. Abbott, R. Abbott, T. Abbott, M. Abernathy, F. Acernese, K. Ackley et al., Observation of gravitational waves from a binary black hole merger, Physical review letters 116 (2016) 061102.

[213] J. Liu, X. Chen and X. Ji, Current status of direct dark matter detection experiments, Nature Physics 13 (2017) 212.

[214] Aalbers, J., Agostini, F., Alfonsi, M., Amaro, F.D., Amsler, C., Aprile, E., Arazi, L., Arneodo, F., Barrow, P., Baudis, L. and Benabderrahmane, M.L., 2016. DARWIN: towards the ultimate dark matter detector. Journal of Cosmology and Astroparticle Physics, 2016(11), p.017.

[215] Ren, X., Zhao, L., Abdukerim, A., Chen, X., Chen, Y., Cui, X., Fang, D., Fu, C., Giboni, K., Giuliani, F. and Gu, L., 2018. Constraining dark matter models with a light mediator at the PandaX-II experiment. Physical review letters, 121(2), p.021304.

[216] Das, A. and Dasgupta, B., 2017. Selection rule for enhanced Dark Matter annihilation. Physical review letters,118(25), p.251101.

[217] Diamanti, R., Lopez-Honorez, L., Mena, O., Palomares-Ruiz, S., & Vincent, A. C. (2014). Constraining Dark Matterlate-time energy injection: decays and p-wave annihilations. Journal of Cosmology and Astroparticle Physics, 2014(02),017.

[218] An, Haipeng, Mark B. Wise, and Yue Zhang. "Strong CMB constraint on P-wave annihilating Dark Matter." PhysicsLetters B 773 (2017): 121-124.

[219] Aaboud, Morad, et al. "Search for resonances in the mass distribution of jet pairs with one or two jets identified as b-jets in proton-proton collisions at s= 13 TeV with the ATLAS detector." Physical Review D 98.3 (2018): 032016.

[220] Aprile, E., Aalbers, J., Agostini, F., Alfonsi, M., Althueser, L., Amaro, F. D., ...& Benabderrahmane, M. L. (2018). Dark Matter Search Results from a One Tonne × Year Exposure of XENON1T. arXiv preprint arXiv:1805.12562.

[221] Francesca Calore, TeVPA 2018, Inidrect Dark Matter searches. *https* : *//indico.desy.de/indico/event*/18204/*session*/6/*contribution*/356/*material*/*slides*/0.*pdf*

[222] J. Coronado-Blazquez et al. TeVPA 2018, 'UNIDENTIFIED GAMMA-RAY SOURCES AS TARGETS FOR INDIRECT Dark Matter DETECTION WITH FERMI-LAT', https://indico.desy.de/indico/event/18204/session/12/contribution/27/material/slides/0.pdf

[223] Horns, D. (2016, May). Gamma-Ray Astronomy from the Ground. In Journal of Physics: Conference Series (Vol. 718, No. 2, p. 022010). IOP Publishing.

[224] Borah, D., Dasgupta, A., Dey, U. K., Patra, S., & Tomar, G. (2017). Multi-component fermionic Dark Matter and IceCube PeV scale neutrinos in left-right model with gauge unification. Journal of High Energy Physics, 2017(9), 5.

[225] Zornoza, J. D., & Toennis, C. (2017, September). Results of Dark Matter searches with the ANTARES neutrino telescope. In Journal of Physics: Conference Series (Vol. 888, No. 1, p. 012206). IOP Publishing.

[226] Bartels, R., Storm, E., Weniger, C., Calore, F. (2018). The Fermi-LAT GeV excess as a tracer of stellar mass in the Galactic bulge. Nature Astronomy, 1.

[227] Funk, S., 2015. Indirect detection of Dark Matter with γ rays. Proceedings of the National Academy of Sciences, 112(40), pp.12264-12271.

[228] Calore, F., Serpico, P.D. and Zaldivar, B., 2018. Dark Matter constraints from dwarf galaxies: a data-driven analysis. arXiv preprint arXiv:1803.05508.

[229] Osipkov, L.P., 1979. Spherical systems of gravitating bodies with an ellipsoidal velocity distribution. Pisma v Astronomicheskii Zhurnal, 5, pp.77-80.

[230] Hernquist, L., 1990. An analytical model for spherical galaxies and bulges. The Astrophysical Journal, 356, pp.359-364.

[231] An, J., Zhao, H. (2012). Fitting functions for Dark Matter density profiles. Monthly Notices of the Royal Astronomical Society, 428(4), 2805-2811.

[232] Mamon, G.A. and Lokas, E.L., 2005. Dark Matter in elliptical galaxies -II. Estimating the mass within the virial radius. Monthly Notices of the Royal Astronomical Society, 363(3), pp.705-722.

[233] Baes, M. and Van Hese, E., 2007. Dynamical models with a general anisotropy profile. Astronomy & Astrophysics, 471(2), pp.419-432.

[234] Binney, J., Tremaine, S. (2011). Galactic dynamics (Vol. 20). Princeton university press.

[235] H. C. Plummer, On the problem of distribution in globular star clusters,MNRAS71(Mar., 1911)460–470.

[236] I. King,The structure of star clusters. I. an empirical density law,Astronomic. J.67(Oct., 1962) 471.

[237] J. L. Sersic,Atlas de galaxias australes. 1968.

[238] Kowalczyk, K., Lokas, E. L., Valluri, M. (2018). The effect of non-sphericity on mass and anisotropy measurements in dSph galaxies with Schwarzschild method. Monthly Notices of the Royal Astronomical Society, 476(3), 2918-2930.

[239] Baes, M. and Van Hese, E., 2007. Dynamical models with a general anisotropy profile. Astronomy & Astrophysics, 471(2), pp. 419-432.

[240] Walker, Matthew G., and Jorge Penarrubia. "A method for measuring (slopes of) the mass profiles of dwarf spheroidal galaxies." The Astrophysical Journal 742.1 (2011): 20.

[241] Mamon, G.A. and Lokas, E.L., 2005. Dark Matter in elliptical galaxies I. Is the total mass density profile of the NFW form or even steeper?. Monthly Notices of the Royal Astronomical Society, 362(1), pp.95-109.

[242] Binney, J. and Mamon, G.A., 1982. M/L and velocity anisotropy from observations of spherical galaxies, or must M87 have a massive black hole?. Monthly Notices of the Royal Astronomical Society, 200(2), pp.361-375.

[243] Walker, M.G., Mateo, M., Olszewski, E.W., Penarrubia, J., Evans, N.W. and Gilmore, G., 2009. A universal mass profile for dwarf spheroidal galaxies?. The Astrophysical Journal, 704(2), p.1274.

[244] Wolf, J., Martinez, G.D., Bullock, J.S., Kaplinghat, M., Geha, M., Munoz, R.R., Simon, J.D. and Avedo, F.F., 2010. Accurate masses for dispersion-supported galaxies. Monthly Notices of the Royal Astronomical Society, 406(2), pp.1220-1237.

[245] Bonnivard, V., Hutten, M., Nezri, E., Charbonnier, A., Combet, C. and Maurin, D., 2016. CLUMPY: Jeans analysis, γ-ray and ν fluxes from Dark Matter (sub-) structures. Computer physics communications, 200, pp.336-349.

[246] Zhao, Y., Bi, X. J., Yin, P. F., Zhang, X. (2018). Constraint on the velocity dependent Dark Matter annihilation cross section from gamma-ray and kinematic observations of ultrafaint dwarf galaxies. Physical Review D, 97(6), 063013.

[247] https://conservancy.umn.edu/bitstream/handle/11299/158173/maurin.pdf?sequence=1

[248] $http://www.physics.ntua.gr/corfu2017/Talks/moritz_huetten@desy_de_01.pdf$

[249] Edsjo, J., Gondolo, P. (1997). Neutralino relic density including coannihilations. Physical Review D, 56(4), 1879.

[250] Cannoni, M. (2017). Lorentz invariant relative velocity and relativistic binary collisions. International Journal of Modern Physics A, 32(02n03), 1730002.

[251] De Zeeuw, P. T., Evans, N. W., Schwarzschild, M. (1995). Jeans and Boltzmann solutions for oblate galaxies with flat rotation curves. arXiv preprint astro-ph/9512082.

[252] Jalali, M. A., Tremaine, S. (2011). Generalized Schwarzschild's method. Monthly Notices of the Royal Astronomical Society, 410(3), 2003-2015.

[253] Tempel, E., Tenjes, P. (2006). Line-of-sight velocity dispersions and a mass-distribution model of the Sa galaxy NGC 4594. Monthly Notices of the Royal Astronomical Society, 371(3), 1269-1279.

[254] Kipper, R. (2016). Galaxy modelling: dynamical methods and applications (Doctoral dissertation).

[255] Bonnivard, V., Combet, C., Daniel, M., Funk, S., Geringer-Sameth, A., Hinton, J.A., Maurin, D., Read, J.I., Sarkar, S., Walker, M.G. and Wilkinson, M.I., 2015. Dark Matter annihilation and decay in dwarf spheroidal galaxies: The classical and ultrafaint dSphs. Monthly Notices of the Royal Astronomical Society, 453(1), pp.849-867.

[256] Ichikawa, K., Ishigaki, M. N., Matsumoto, S., Ibe, M., Sugai, H., Hayashi, K., Horigome, S. I. (2017). Foreground effect on the J-factor estimation of classical dwarf spheroidal galaxies. Monthly Notices of the Royal Astronomical Society, 468(3), 2884-2896.

[257] Freedman, W. L., Ho, L. C. (Eds.). (2004). Measuring and Modeling the Universe: Volume 2, Carnegie Observatories Astrophysics Series (Vol. 2). Cambridge University Press.

[258] Diemand, J., Kuhlen, M., Madau, P., Zemp, M., Moore, B., Potter, D., Stadel, J. (2008). Clumps and streams in the local Dark Matter distribution. Nature, 454(7205), 735.

[259] Lavalle, J., Yuan, Q., Maurin, D., Bi, X. J. (2008). Full calculation of clumpiness boost factors for antimatter cosmic rays in the light of Λ CDM N-body simulation results-Abandoning hope in clumpiness enhancement ?. Astronomy Astrophysics, 479(2), 427-452.

[260] Shin'ichiro ANDO, TeVPA 2018, Modeling evolution of Dark Matter substructure and annihilation boost. https://indico.desy.de/indico/event/18204/session/12/contribution/194/material/slides/0.pdf

[261] Ludlow, A. D., Navarro, J. F., Angulo, R. E., Boylan-Kolchin, M., Springel, V., Frenk, C.,& White, S. D. (2014). The mass-concentration-redshift relation of cold Dark Matter haloes. Monthly Notices of the Royal Astronomical Society, 441(1), 378-388.

[262] Anderhalden, D., & Diemand, J. (2013). Density profiles of CDM microhalos and their implications for annihilation boost factors. Journal of Cosmology and Astroparticle Physics, 2013(04), 009.

[263] Lisanti, M., Mishra-Sharma, S., Rodd, N. L., & Safdi, B. R. (2018). Search for Dark Matter Annihilation in Galaxy Groups. Physical review letters, 120(10), 101101.

[264] Gao, L., Navarro, J. F., Frenk, C. S., Jenkins, A., Springel, V., & White, S. D. (2012). The Phoenix Project: the dark side of rich Galaxy clusters. Monthly Notices of the Royal Astronomical Society, 425(3), 2169-2186.

[265] Hayashi, K., Ichikawa, K., Matsumoto, S., Ibe, M., Ishigaki, M. N., & Sugai, H. (2016). Dark Matter annihilation and decay from non-spherical dark halos in galactic dwarf satellites. Monthly Notices of the Royal Astronomical Society, 461(3), 2914-2928.

[266] Ando, S. I., & Nagai, D. (2012). Fermi-LAT constraints on Dark Matter annihilation cross section from observations of the Fornax cluster. Journal of Cosmology and Astroparticle Physics, 2012(07), 017.

[267] Prada, F., Klypin, A., Flix, J., Martinez, M., & Simonneau, E. (2004). Astrophysical inputs on the SUSY Dark Matter annihilation detectability. arXiv preprint astro-ph/0401512.

[268] G.R. Blumenthal, S. Faber, R. Flores and J.R. Primack, Contraction of Dark Matter galactic halos due to baryonic infall, Astrophys. J. 301 (1986) 27 [INSPIRE].

[269] Gustafsson, M., Fairbairn, M., & Sommer-Larsen, J. (2006). Baryonic pinching of galactic Dark Matter halos. Physical Review D, 74(12), 123522.

[270] Lacroix, T., Boehm, C., & Silk, J. (2015). Ruling out thermal Dark Matter with a black hole induced spiky profile in the M87 galaxy. Physical Review D, 92(4), 043510.

[271] Siegal-Gaskins, J.M., 2015. Separating astrophysical sources from indirect Dark Matter signals. Proceedings of the National Academy of Sciences, 112(40), pp.12272-12277.

[272] Cardone, V.F., Piedipalumbo, E. and Tortora, C., 2005. Spherical galaxy models with power-law logarithmic slope. Monthly Notices of the Royal Astronomical Society, 358(4), pp.1325-1336.

[273] Fattahi, A., Navarro, J.F., Sawala, T., Frenk, C.S., Sales, L.V., Oman, K., Schaller, M. and Wang, J., 2016. The cold Dark Matter content of Galactic dwarf spheroidals: no cores, no failures, no problem. arXiv preprint arXiv:1607.06479.

[274] Kumar, Jason, and Danny Marfatia. "Matrix element analyses of Dark Matter scattering and annihilation." Physical Review D 88.1 (2013): 014035.

[275] Yu, Z.H., Zheng, J.M., Bi, X.J., Li, Z., Yao, D.X. and Zhang, H.H., 2012. Constraining the interaction strength between Dark Matter and visible matter: II. scalar, vector and spin-3/2 Dark Matter. Nuclear Physics B, 860(1), pp.115-151.

[276] Blumenthal, J., Gretskov, P., Kramer, M. and Wiebusch, C., 2015. Effective field theory interpretation of searches for Dark Matter annihilation in the Sun with the IceCube Neutrino Observatory. Physical Review D, 91(3), p.035002.

[277] Felix Kahlhoefer. Complementarity of Searches for Dark Matter. PHD thesis at the University of Oxford, Trinity Term 2014.

[278] Fox, P.J., Harnik, R., Kopp, J. and Tsai, Y., 2012. Missing energy signatures of Dark Matter at the LHC. Physical Review D, 85(5), p.056011.

[279] Harnik, R. and Kribs, G.D., 2009. Effective theory of Dirac Dark Matter. Physical Review D, 79(9), p.095007.

[280] Dreiner, H.K., Huck, M., KrÃ¤mer, M., Schmeier, D. and Tattersall, J., 2013. Illuminating Dark Matter at the ILC. Physical Review D, 87(7), p.075015.

[281] Malik, S.A., McCabe, C., Araujo, H., Belyaev, A., Boehm, C., Brooke, J., Buchmueller, O., Davies, G., De Roeck, A., de Vries, K. and Dolan, M.J., 2015. Interplay and characterization of Dark Matter searches at colliders and in direct detection experiments. Physics of the Dark Universe, 9, pp.51-58.

[282] Gilmore, G., Wilkinson, M.I., Wyse, R.F., Kleyna, J.T., Koch, A., Evans, N.W. and Grebel, E.K., 2007. The observed properties of Dark Matter on small spatial scales. The Astrophysical Journal, 663(2), p.948.

[283] Katz, H., Lelli, F., McGaugh, S.S., Di Cintio, A., Brook, C.B. and Schombert, J.M., 2016. Testing feedback-modified Dark Matter haloes with galaxy rotation curves: estimation of halo parameters and consistency with ΛCDM scaling relations. Monthly Notices of the Royal Astronomical Society, 466(2), pp.1648-1668.

[284] Genina, A., Benítez-Llambay, A., Frenk, C.S., Cole, S., Fattahi, A., Navarro, J.F., Oman, K.A., Sawala, T. and Theuns, T., 2017. The core–cusp problem: a matter of perspective. Monthly Notices of the Royal Astronomical Society, 474(1), pp.1398-1411.

[285] Tollerud, E.J., Bullock, J.S., Graves, G.J. and Wolf, J., 2010. From galaxy clusters to ultra-faint dwarf spheroidals: a fundamental curve connecting dispersion-supported galaxies to their dark matter halos. The Astrophysical Journal, 726(2), p.108.

[286] Navarro, Julio F. "The structure of cold dark matter halos." Symposium-international astronomical union. Vol. 171. Cambridge University Press, 1996.

[287] J. Einasto (1965), Kinematics and dynamics of stellar systems, Trudy Inst. Astrofiz. Alma-Ata 5, 87

[288] Burkert, Andreas, and Joseph Silk. "On the structure and nature of dark matter halos." arXiv preprint astro-ph/9904159 (1999).

[289] Massari, D., Breddels, M.A., Helmi, A., Posti, L., Brown, A.G.A. and Tolstoy, E., 2018. Three-dimensional motions in the Sculptor dwarf galaxy as a glimpse of a new era. Nature Astronomy, 2(2), p.156.

[290] Opitz, B. and HESS collaboration, 2010, March. Dark matter searches with HESS. In AIP Conference Proceedings (Vol. 1223, No. 1, pp. 140-148). AIP.

[291] Albert, A., Alfaro, R., Alvarez, C., Álvarez, J.D., Arceo, R., Arteaga-Velázquez, J.C., Rojas, D.A., Solares, H.A., Bautista-Elivar, N., Becerril, A. and Belmont-Moreno, E., 2018. Dark matter limits from dwarf spheroidal galaxies with the HAWC gamma-ray observatory. The Astrophysical Journal, 853(2), p.154.

[292] Łokas, E.L., 2009. The mass and velocity anisotropy of the Carina, Fornax, Sculptor and Sextans dwarf spheroidal galaxies. Monthly Notices of the Royal Astronomical Society: Letters, 394(1), pp.L102-L106.

[293] Salucci, P., Wilkinson, M.I., Walker, M.G., Gilmore, G.F., Grebel, E.K., Koch, A., Frigerio Martins, C. and Wyse, R.F., 2012. Dwarf spheroidal galaxy kinematics and spiral galaxy scaling laws. Monthly Notices of the Royal Astronomical Society, 420(3), pp.2034-2041.

[294] Mateo, M., Olszewski, E.W. and Walker, M.G., 2008. The velocity dispersion profile of the remote dwarf spheroidal galaxy Leo I: A tidal hit and run?. The Astrophysical Journal, 675(1), p.201.

[295] Munoz, R.R., Frinchaboy, P.M., Majewski, S.R., Kuhn, J.R., Chou, M.Y., Palma, C., Sohn, S.T., Patterson, R.J. and Siegel, M.H., 2005. Exploring halo substructure with giant stars: the velocity dispersion profiles of the Ursa Minor and Draco Dwarf spheroidal galaxies at large angular separations. The Astrophysical Journal Letters, 631(2), p.L137.

[296] Tyler, C., 2002. Particle Dark Matter constraints from the Draco dwarf galaxy. Physical Review D, 66(2), p.023509.

[297] Koch, A., Kleyna, J.T., Wilkinson, M.I., Grebel, E.K., Gilmore, G.F., Evans, N.W., Wyse, R.F. and Harbeck, D.R., 2007. Stellar kinematics in the remote Leo II dwarf spheroidal galaxy—Another brick in the wall. The Astronomical Journal, 134(2), p.566.

[298] Battaglia, Giuseppina, Amina Helmi, and Maarten Breddels. "Internal kinematics and dynamical models of dwarf spheroidal galaxies around the Milky Way." New Astronomy Reviews 57.3-4 (2013): 52-79.

[299] Schwarzschild, Martin. "Mass distribution and mass-luminosity ratio in galaxies." The Astronomical Journal 59 (1954): 273.

[300] Battaglia, G., Tolstoy, E., Helmi, A., Irwin, M., Parisi, P., Hill, V. and Jablonka, P., 2011. Study of the Sextans dwarf spheroidal galaxy from the DART Ca II triplet survey. Monthly Notices of the Royal Astronomical Society, 411(2), pp.1013-1034.

[301] Strigari, L.E., Frenk, C.S. and White, S.D., 2018. Dynamical constraints on the Dark Matter distribution of the Sculptor dwarf spheroidal from stellar proper motions. The Astrophysical Journal, 860(1), p.56.

[302] Bringmann, T., Hofmann, S. (2007). Thermal decoupling of WIMPs from first principles. Journal of Cosmology and Astroparticle Physics, 2007(04), 016.

[303] van den Aarssen, L. G., Bringmann, T., Goedecke, Y. C. (2012). Thermal decoupling and the smallest subhalo mass in Dark Matter models with Sommerfeld-enhanced annihilation rates. Physical Review D, 85(12), 123512.

[304] Bringmann, T., Hofmann, S. (2007). Thermal decoupling of WIMPs from first principles. Journal of Cosmology and Astroparticle Physics, 2007(04), 016.

[305] Binder, T., Bringmann, T., Gustafsson, M. and Hryczuk, A., 2017. Early kinetic decoupling of dark matter: when the standard way of calculating the thermal relic density fails. Physical Review D, 96(11), p.115010.

[306] Gelmini, G. B. (2015). TASI 2014 lectures: the hunt for Dark Matter. arXiv preprint arXiv:1502.01320.

[307] Arina, C. (2018). Impact of cosmological and astrophysical constraints on Dark Matter simplified models. arXiv preprint arXiv:1805.04290.

[308] Feng, J. L., Kaplinghat, M., Yu, H. B. (2010). Sommerfeld enhancements for thermal relic Dark Matter. Physical Review D, 82(8), 083525.

[309] Berezinsky, V.S., Dokuchaev, V.I. and Eroshenko, Y.N., 2014. Small-scale clumps of dark matter. Physics-Uspekhi, 57(1), p.1.

[310] Johnson, C., Caputo, R., Karwin, C., Murgia, S., Ritz, S., Shelton, J. and Fermi-LAT Collaboration, 2019. Search for gamma-ray emission from p-wave Dark Matter annihilation in the Galactic Center. Physical Review D, 99(10), p.103007.

[311] Oman, K.A., Navarro, J.F., Fattahi, A., Frenk, C.S., Sawala, T., White, S.D., Bower, R., Crain, R.A., Furlong, M., Schaller, M. and Schaye, J., 2015. The unexpected diversity of dwarf galaxy rotation curves. Monthly Notices of the Royal Astronomical Society, 452(4), pp.3650-3665.

[312] Fermi LAT Collaboration, Anisotropies in the diffuse gamma-ray background measured by the Fermi LAT, Physical Review D 85 (2012) 083007, [arXiv:1202.2856]

[313] Felcini, M., 2018. Searches for Dark Matter Particles at the LHC. arXiv preprint arXiv:1809.06341.

[314] Okoli, C., Taylor, J.E. and Afshordi, N., 2018. Searching for Dark Matter annihilation from individual halos: uncertainties, scatter and signal-to-noise ratios. Journal of Cosmology and Astroparticle Physics, 2018(08), p.019.

[315] Aprile, E., Aalbers, J., Agostini, F., Alfonsi, M., Althueser, L., Amaro, F.D., Antochi, V.C., Angelino, E., Arneodo, F., Barge, D. and Baudis, L., 2019. A Search for Light Dark Matter Interactions Enhanced by the Migdal effect or Bremsstrahlung in XENON1T. arXiv preprint arXiv:1907.12771.

[316] Ackermann, M., Ajello, M., Albert, A.T., Atwood, W.B., Baldini, L., Ballet, J., Barbiellini, G., Bastieri, D., Bechtol, K., Bellazzini, R. and Berenji, B., 2011. Constraining Dark Matter models from a combined analysis of Milky Way satellites with the Fermi Large Area Telescope. Physical Review Letters, 107(24), p.241302.

[317] Horns, D., 2005. TeV γ-radiation from Dark Matter annihilation in the Galactic center. Physics Letters B, 607(3-4), pp.225-232.

[318] Karwin, C., Murgia, S., Tait, T.M., Porter, T.A. and Tanedo, P., 2017. Dark Matter interpretation of the Fermi-LAT observation toward the galactic center. Physical Review D, 95(10), p.103005.

[319] Yuan, Q. and Feng, L., 2018. Dark Matter Particle Explorer observations of high-energy cosmic ray electrons plus positrons and their physical implications. SCIENCE CHINA Physics, Mechanics & Astronomy, 61(10), p.101002.

[320] Knödlseder, J., 2016. The future of gamma-ray astronomy. Comptes Rendus Physique, 17(6), pp.663-678.

[321] Acciari, V.A., Ansoldi, S., Antonelli, L.A., Engels, A.A., Arcaro, C., Baack, D., Babić, A., Banerjee, B., Bangale, P., de Almeida, U.B. and Barrio, J.A., 2018. Constraining Dark Matter lifetime with a deep gamma-ray survey of the Perseus Galaxy Cluster with MAGIC. Physics of the Dark Universe, 22, pp.38-47.

[322] Aartsen, M.G., Ackermann, M., Adams, J., Aguilar, J.A., Ahlers, M., Ahrens, M., Al Samarai, I., Altmann, D., Andeen, K., Anderson, T. and Ansseau, I., 2018. Search for neutrinos from decaying Dark Matter with IceCube. The European Physical Journal C, 78(10), p.831.

[323] Ibe, M., Murayama, H. and Yanagida, T.T., 2009. Breit-Wigner enhancement of Dark Matter annihilation. Physical Review D, 79(9), p.095009.

[324] Bi, X.J., Yin, P.F. and Yuan, Q., 2012. Breit-Wigner enhancement considering the Dark Matter kinetic decoupling. Physical Review D, 85(4), p.043526.

[325] Cuesta, A.J., Prada, F., Klypin, A. and Moles, M., 2008. The virialized mass of Dark Matter haloes. Monthly Notices of the Royal Astronomical Society, 389(1), pp.385-397.

[326] Kravtsov, A., 2010. Dark Matter substructure and dwarf galactic satellites. Advances in Astronomy, 2010.

[327] Cassel, S., 2010. Sommerfeld factor for arbitrary partial wave processes. Journal of Physics G: Nuclear and Particle Physics, 37(10), p.105009.

[328] Slatyer, Tracy R. "The Sommerfeld enhancement for Dark Matter with an excited state." Journal of Cosmology and Astroparticle Physics 2010.02 (2010): 028.

[329] Das, Anirban, and Basudeb Dasgupta. "Selection rule for enhanced Dark Matter annihilation." Physical review letters 118.25 (2017): 251101.

[330] An, H., Wise, M.B. and Zhang, Y., 2017. Strong CMB constraint on P-wave annihilating Dark Matter. Physics Letters B, 773, pp.121-124.

[331] Tulin, Sean, Hai-Bo Yu, and Kathryn M. Zurek. "Beyond collisionless dark matter: particle physics dynamics for dark matter halo structure." physical Review D 87.11 (2013): 115007.

[332] Kahlhoefer, Felix, Kai Schmidt-Hoberg, and Sebastian Wild. "Dark matter self-interactions from a general spin-0 mediator." Journal of Cosmology and Astroparticle Physics 2017.08 (2017): 003.

[333] Bringmann, Torsten, et al. "Strong constraints on self-interacting dark matter with light mediators." Physical review letters 118.14 (2017): 141802.

[334] Blum, K., Sato, R., & Slatyer, T. R. (2016). Self-consistent calculation of the Sommerfeld enhancement. Journal of Cosmology and Astroparticle Physics, 2016(06), 021.

[335] Profumo, S., 2005. TeV γ-rays and the largest masses and annihilation cross sections of neutralino Dark Matter. Physical Review D, 72(10), p.103521.

[336] Lattanzi, M. and Silk, J., 2009. Can the WIMP annihilation boost factor be boosted by the Sommerfeld enhancement?. Physical Review D, 79(8), p.083523.

[337] Choquette, J., Cline, J.M. and Cornell, J.M., 2016. p-wave annihilating Dark Matter from a decaying predecessor and the Galactic Center excess. Physical Review D, 94(1), p.015018.

[338] Hooper, D., Linden, T. and Lopez, A., 2016. Radio galaxies dominate the high-energy diffuse gamma-ray background. Journal of Cosmology and Astroparticle Physics, 2016(08), p.019.

[339] Campbell, S., Dutta, B. and Komatsu, E., 2010. Effects of velocity-dependent Dark Matter annihilation on the energy spectrum of the extragalactic gamma-ray background. Physical Review D, 82(9), p.095007.

[340] Charles, E., Sanchez-Conde, M., Anderson, B., Caputo, R., Cuoco, A., Di Mauro, M., Drlica-Wagner, A., Gomez-Vargas, G.A., Meyer, M., Tibaldo, L. and Wood, M., 2016. Sensitivity projections for Dark Matter searches with the Fermi large area telescope. Physics Reports, 636, pp.1-46.

[341] Barger, V., Keung, W.Y., Marfatia, D. and Shaughnessy, G., 2009. PAMELA and Dark Matter. Physics Letters B, 672(2), pp.141-146.

[342] Donato, F., Maurin, D., Brun, P., Delahaye, T. and Salati, P., 2009. Constraints on WIMP Dark Matter from the High Energy PAMELA p/p data. Physical review letters, 102(7), p.071301.

[343] Feng, L., Yang, R.Z., He, H.N., Dong, T.K., Fan, Y.Z. and Chang, J., 2014. AMS-02 positron excess: new bounds on Dark Matter models and hint for primary electron spectrum hardening. Physics Letters B, 728, pp.250-255.

[344] Jin, H.B., Wu, Y.L. and Zhou, Y.F., 2017. Astrophysical background and Dark Matter implication based on latest AMS-02 data. arXiv preprint arXiv:1701.02213.

[345] Calore, F., Cholis, I., McCabe, C. and Weniger, C., 2015. A tale of tails: Dark Matter interpretations of the Fermi GeV excess in light of background model systematics. Physical Review D, 91(6), p.063003.

[346] Liu, X. and Liu, Z., 2018. TeV Dark Matter and the DAMPE electron excess. Physical Review D, 98(3), p.035025.

[347] Ackermann, M., Ajello, M., Albert, A., Atwood, W.B., Baldini, L., Ballet, J., Barbiellini, G., Bastieri, D., Bechtol, K., Bellazzini, R. and Bissaldi, E., 2015. The spectrum of isotropic diffuse gamma-ray emission between 100 MeV and 820 GeV. The Astrophysical Journal, 799(1), p.86.

[348] Lu, B.Q., Wu, Y.L., Zhang, W.H. and Zhou, Y.F., 2018. Constraints on the Sommerfeld-enhanced Dark Matter annihilation from the gamma rays of subhalos and dwarf galaxies. Journal of Cosmology and Astroparticle Physics, 2018(04), p.035.

[349] Elor, Gilly, et al. "Model-independent indirect detection constraints on hidden sector dark matter." Journal of Cosmology and Astroparticle Physics 2016.06 (2016): 024.

[350] Ciafaloni, P., Comelli, D., Riotto, A., Sala, F., Strumia, A. and Urbano, A., 2011. Weak corrections are relevant for Dark Matter indirect detection. Journal of Cosmology and Astroparticle Physics, 2011(03), p.019.

[351] Jenkins, A., Frenk, C.S., White, S.D., Colberg, J.M., Cole, S., Evrard, A.E., Couchman, H.M.P. and Yoshida, N., 2001. The mass function of Dark Matter haloes. Monthly Notices of the Royal Astronomical Society, 321(2), pp.372-384.

[352] Warren, M.S., Abazajian, K., Holz, D.E. and Teodoro, L., 2006. Precision determination of the mass function of Dark Matter halos. The Astrophysical Journal, 646(2), p.881.

[353] Tinker, J., Kravtsov, A.V., Klypin, A., Abazajian, K., Warren, M., Yepes, G., Gottlöber, S. and Holz, D.E., 2008. Toward a halo mass function for precision cosmology: the limits of universality. The Astrophysical Journal, 688(2), p.709.

[354] Sheth R., Tormen G., 1999, MNRAS, 308, 119

[355] Press W. H., Schechter P., 1974, ApJ, 187, 425

[356] Pillepich, A., Porciani, C. and Hahn, O., 2010. Halo mass function and scale-dependent bias from N-body simulations with non-Gaussian initial conditions. Monthly Notices of the Royal Astronomical Society, 402(1), pp.191-206.

[357] Geng, C.Q., Lee, C.C. and Shen, J.L., 2015. Matter power spectra in viable f (R) gravity models with massive neutrinos. Physics Letters B, 740, pp.285-290.

[358] Mo, H., Van den Bosch, F. and White, S., 2010. Galaxy formation and evolution. Cambridge University Press.

[359] Profumo, S. and Jeltema, T.E., 2009. Extragalactic inverse Compton light from Dark Matter annihilation and the Pamela positron excess. Journal of Cosmology and Astroparticle Physics, 2009(07), p.020.

[360] Delahaye, T., Bœhm, C. and Silk, J., 2012. Can Planck constrain indirect detection of Dark Matter in our Galaxy?. Monthly Notices of the Royal Astronomical Society: Letters, 422(1), pp.L16-L20.

[361] Pandey, K.L., Karwal, T. and Das, S., 2019. Alleviating the $ H_0 $ and $\sigma_8 $ anomalies with a decaying Dark Matter modelAlleviating the $ H_0 $ and $\sigma_8 $ anomalies with a decaying Dark Matter model. arXiv preprint arXiv:1902.10636.

[362] Natarajan, A., Zhu, N. and Yoshida, N., 2015. Probing the Small Scale Matter Power Spectrum through Dark Matter Annihilation in the Early Universe. arXiv preprint arXiv:1503.03480.

[363] Voit, G.M., 2005. Tracing cosmic evolution with clusters of galaxies. Reviews of Modern Physics, 77(1), p.207.

[364] Rodríguez-Puebla, A., Behroozi, P., Primack, J., Klypin, A., Lee, C. and Hellinger, D., 2016. Halo and subhalo demographics with Planck cosmological parameters: Bolshoi–Planck and MultiDark–Planck simulations. Monthly Notices of the Royal Astronomical Society, 462(1), pp.893-916.

[365] Meyer, M., 2013. The Opacity of the Universe for High and Very High Energy gamma-Rays (No. DESY-THESIS-2013-033).

[366] Liu, W., Bi, X.J., Lin, S.J. and Yin, P.F., 2017. Constraints on Dark Matter annihilation and decay from the isotropic gamma-ray background. Chinese Physics C, 41(4), p.045104.

[367] Zdziarski, A.A. and Svensson, R., 1989. Absorption of X-rays and gamma rays at cosmological distances. The Astrophysical Journal, 344, pp.551-566.

[368] Hütten, M., Combet, C. and Maurin, D., 2018. Extragalactic diffuse γ-rays from Dark Matter annihilation: revised prediction and full modelling uncertainties. Journal of Cosmology and Astroparticle Physics, 2018(02), p.005.

[369] Kumar, J. and Marfatia, D., 2013. Matrix element analyses of Dark Matter scattering and annihilation. Physical Review D, 88(1), p.014035.

[370] Boveia, A., Buchmueller, O., Busoni, G., D'Eramo, F., De Roeck, A., De Simone, A., Doglioni, C., Dolan, M.J., Genest, M.H., Hahn, K. and Haisch, U., 2019. Recommendations on presenting LHC searches for missing transverse energy signals using simplified s-channel models of dark matter. Physics of the Dark Universe, p.100365.

[371] O. Mattelaer, E. Vryonidou, "Dark Matter production through loop-induced processes at the LHC: the s-channel mediator case" (EPJC75(2015)436).

[372] Arina, C., Backović, M., Heisig, J. and Lucente, M., 2017. Solar γ rays as a complementary probe of Dark Matter. Physical Review D, 96(6), p.063010.

[373] Schmidt-Hoberg, Kai, Florian Staub, and Martin Wolfgang Winkler. "Constraints on light mediators: confronting dark matter searches with B physics." Physics Letters B 727.4-5 (2013): 506-510.

[374] Abercrombie, D., Akchurin, N., Akilli, E., Maestre, J.A., Allen, B., Gonzalez, B.A., Andrea, J., Arbey, A., Azuelos, G., Azzi, P. and Backović, M., 2019. Dark Matter benchmark models for early LHC run-2 searches: report of the ATLAS/CMS Dark Matter forum. Physics of the Dark Universe, p.100371.

[375] Bernal, N. and Palomares-Ruiz, S., 2012. Constraining dark matter properties with gamma-rays from the Galactic Center with Fermi–LAT. Nuclear Physics B, 857(3), pp.380-410.

[376] Di Mauro, M. and Donato, F., 2015. Composition of the Fermi-LAT isotropic gamma-ray background intensity: Emission from extragalactic point sources and dark matter annihilations. Physical Review D, 91(12), p.123001.

[377] Wyithe, J.B., Turner, E.L. and Spergel, D.N., 2001. Gravitational lens statistics for generalized NFW profiles: Parameter degeneracy and implications for self-interacting cold Dark Matter. The Astrophysical Journal, 555(1), p.504.

[378] Dehnen, Walter, and Dean E. McLaughlin. "Dynamical insight into dark matter haloes." Monthly Notices of the Royal Astronomical Society 363.4 (2005): 1057-1068.

[379] Zechlin, H.S., Fernandes, M.V., Elsaesser, D. and Horns, D., 2012. Dark Matter subhaloes as gamma-ray sources and candidates in the first Fermi-LAT catalogue. Astronomy & Astrophysics, 538, p.A93.

[380] CMS collaboration. (2017). Measurements of properties of the Higgs boson decaying into the four-lepton final state in pp collisions at sqrt (s)= 13 TeV. arXiv preprint arXiv:1706.09936.

[381] Zechlin, H.S. and Horns, D., 2012. Unidentified sources in the Fermi-LAT second source catalog: the case for DM subhalos. Journal of Cosmology and Astroparticle Physics, 2012(11), p.050.

[382] Abazajian, K., Zheng, Z., Zehavi, I., Weinberg, D.H., Frieman, J.A., Berlind, A.A., Blanton, M.R., Bahcall, N.A., Brinkmann, J., Schneider, D.P. and Tegmark, M., 2005. Cosmology and the halo occupation distribution from small-scale galaxy clustering in the Sloan Digital Sky Survey. The Astrophysical Journal, 625(2), p.613.

[383] Ninković, S., 1985. On the structure and mass of the galactic halo. Astrophysics and space science, 110(2), pp.379-391.

[384] Boylan-Kolchin, M., 2017. The globular cluster–Dark Matter halo connection. Monthly Notices of the Royal Astronomical Society, 472(3), pp.3120-3130.

[385] Sánchez-Conde, Miguel A., and Francisco Prada. "The flattening of the concentration–mass relation towards low halo masses and its implications for the annihilation signal boost." Monthly Notices of the Royal Astronomical Society 442.3 (2014): 2271-2277.

[386] Macciò, Andrea V., et al. "The inner structure of haloes in Cold+ Warm dark matter models." Monthly Notices of the Royal Astronomical Society 428.1 (2013): 882-890.

[387] Hennawi, Joseph F., et al. "Characterizing the cluster lens population." The Astrophysical Journal 654.2 (2007): 714.

[388] Aaron D. Ludlow, Sownak Bose, Raúl E. Angulo, Lan Wang, Wojciech A. Hellwing, Julio F. Navarro, Shaun Cole, Carlos S. Frenk, The mass–concentration–redshift relation of cold and warm dark matter haloes, Monthly Notices of the Royal Astronomical Society, Volume 460, Issue 2, 01 August 2016, Pages 1214–1232, https://doi.org/10.1093/mnras/stw1046

[389] Falco, Martina, et al. "Dynamical signatures of infall around galaxy clusters: a generalized Jeans equation." Monthly Notices of the Royal Astronomical Society 436.3 (2013): 2639-2649.

[390]

[391] Colafrancesco, S., Profumo, S. and Ullio, P., 2006. Multi-frequency analysis of neutralino Dark Matter annihilations in the Coma cluster. Astronomy & Astrophysics, 455(1), pp.21-43.

[392] Zhang, L., Miniati, F. and Sigl, G., 2010. Inverse Compton gamma-rays from Galactic Dark Matter annihilation: Anisotropy signatures. arXiv preprint arXiv:1008.1801.

[393] Chen, Bin, and Timothy S. Bastian. "The role of inverse Compton scattering in solar coronal hard X-ray and γ-ray sources." The Astrophysical Journal 750, no. 1 (2012): 35.

[394] Regis, M. and Ullio, P., 2008. Multiwavelength signals of Dark Matter annihilations at the Galactic center. Physical Review D, 78(4), p.043505.

[395] Schlickeiser, R., 2013. Cosmic ray astrophysics. Springer Science & Business Media.

[396] Tsang, O. and Kirk, J.G., 2007. The inverse Compton catastrophe and high brightness temperature radio sources. Astronomy & Astrophysics, 463(1), pp.145-152.

[397] Lyutikov, M., 2013. Inverse Compton model of pulsar high-energy emission. Monthly Notices of the Royal Astronomical Society, 431(3), pp.2580-2589.

[398] Vannoni, G., Gabici, S. and Aharonian, F.A., 2009. Diffusive shock acceleration in radiation-dominated environments. Astronomy & Astrophysics, 497(1), pp.17-26.

[399] Sari, R.E. and Esin, A.A., 2001. On the synchrotron self-Compton emission from relativistic shocks and its implications for gamma-ray burst afterglows. The Astrophysical Journal, 548(2), p.787.

[400] Sigl, G., 2017. Astroparticle Physics: Theory and Phenomenology.

[401] Petruk, O., 2009. Approximation of the radiation power of electrons due to the inverse-Compton process in the black-body photon field. Astronomy & Astrophysics, 499(3), pp.643-648.

[402] Manolakou, K., Horns, D. and Kirk, J.G., 2007. Spectral evolution of non-thermal electron distributions in intense radiation fields. Astronomy & Astrophysics, 474(3), pp.689-700.

[403] Pinzke, A., Pfrommer, C. and Bergström, L., 2011. Prospects of detecting gamma-ray emission from galaxy clusters: cosmic rays and Dark Matter annihilations. Physical Review D, 84(12), p.123509.

[404] Jones, F.C., 1968. Calculated spectrum of inverse-Compton-scattered photons. Physical Review, 167(5), p.1159.

[405] Blumenthal, G.R. and Gould, R.J., 1970. Bremsstrahlung, synchrotron radiation, and compton scattering of high-energy electrons traversing dilute gases. Reviews of Modern Physics, 42(2), p.237.

[406] Jamil, M., 2011. High Energy Radiation from Black Holes: Gamma Rays, Cosmic Rays, and Neutrinos, by Charles D. Dermer and Govind Menon: Scope: monograph. Level: graduate students and advanced researchers.

[407] Meyer, M., Raue, M., Mazin, D. and Horns, D., 2012. Limits on the extragalactic background light in the Fermi era. Astronomy & Astrophysics, 542, p.A59.

[408] Cirelli, M. and Panci, P., 2009. Inverse Compton constraints on the Dark Matter e±excesses. Nuclear Physics B, 821(1-2), pp.399-416.

[409] "2018 CODATA Value". The NIST Reference on Constants, Units, and Uncertainty. NIST. 20 May 2019. Retrieved 2019-05-20.

[410] J. Hisano, S. Matsumoto and M. M. Nojiri, Phys. Rev. Lett.92, 031303 (2004)

[411] J. Hisano, S. Matsumoto, M. M. Nojiri and O. Saito, Phys. Rev. D71, 063528(2005).

[412] Hisano, J., Matsumot, S., Nagai, M., Saito, O. and Senami, M., 2007. Non-perturbative effect on thermal relic abundance of Dark Matter. Physics Letters B, 646(1), pp.34-38.

[413] Liu, Z.P., Wu, Y.L. and Zhou, Y.F., 2013. Sommerfeld enhancements with vector, scalar, and pseudoscalar force carriers. Physical Review D, 88(9), p.096008.

[414] Lu, B.Q., Wu, Y.L., Zhang, W.H. and Zhou, Y.F., 2018. Constraints on the Sommerfeld-enhanced Dark Matter annihilation from the gamma rays of subhalos and dwarf galaxies. Journal of Cosmology and Astroparticle Physics, 2018(04), p.035.

[415] Shelton, J., Shapiro, S.L. and Fields, B.D., 2015. Black hole window into p-wave dark matter annihilation. Physical review letters, 115(23), p.231302.

[416] An, H., Wise, M.B. and Zhang, Y., 2016. Effects of bound states on Dark Matter annihilation. Physical Review D, 93(11), p.115020.

[417] Petraki, K., Postma, M. and De Vries, J., 2017. Radiative bound-state-formation cross-sections for Dark Matter interacting via a Yukawa potential. Journal of High Energy Physics, 2017(4), p.77.

[418] Robertson, D.S. and Albuquerque, I.F., 2018. Probing velocity dependent self-interacting Dark Matter with neutrino telescopes. Journal of Cosmology and Astroparticle Physics, 2018(02), p.056.

[419] Zurek, K.M., 2009. Multicomponent Dark Matter. Physical Review D, 79(11), p.115002.

[420] Jia, Lian-Bao. "Velocity-dependent self-interacting dark matter from thermal freeze-out and tests in direct detections." The European Physical Journal C 80.2 (2020): 1-9.

[421] Denner, A., Heinemeyer, S., Puljak, I., Rebuzzi, D., Spira, M., & LHC Higgs Cross Section Working Group. (2011). Standard model Higgs-boson branching ratios with uncertainties. The European Physical Journal C, 71(9), 1753.

[422] Aad, Georges, et al. "Measurements of the Higgs boson production and decay rates and coupling strengths using pp collision data at $\sqrt{s}$ =7 and 8 TeV in the ATLAS experiment." The European Physical Journal C 76.1 (2016): 1-5

[423] P.A. Zyla et al. (Particle Data Group), Prog. Theor. Exp. Phys. 2020, 083C01 (2020).

Acknowledgments

I would like to thank all the people who have oered love and support to me during the ve years of PhD. This is a long journey with joy and obstacles, with out you, this journey must be very dicult. Many thanks!

A tutor for a day is a father for a lifetime (a Chinese proverb). Then how about a tutor for ve years? My supervisor, Prof. Dr. Dieter Horns, he has opened the door and led me to the world of Dark Matter searches, and has taught me to enjoy working on specic topics. He has shown great patience and oered continous support to me not only in physics but also in life. He has oered continous support to help me to move forward and armed me with new tools. The discussions with him have inspired and activated me a lot of times, he is keen to every topic I have worked on, and his passion for work and strictness in dealing with technical details have inuenced me a lot. I am not good at expressing my emotion, but I have waited long time to express my everlasting feeling of gratefulness and thanksfulness to him. I wish also I would have chance to become a researcher like him in the future.

I would like to thank Dr. Martin Tluczykont, he is always open to my questions and has oered a lot of support to my work, I have learned a lot from him, and I really enjoyed the discussion with him. There are some moments he has impressived me a lot when he was helping me or the others in the group. He has a good sense of humor, I will never forget the jokes he has shared with us.

With a special mention to Jhilik Majumdar, Ludmilla Dirson, Le Hoang Nguyen, Andrei Lobanov, Rayk Nachtigall, Bjrn Optiz, Maike Kunnas, Gu Yikun, Kin Hang Yeung, Junghoon Lee, Ali , Henric Edler, Padam Ghimire, Robert Stein, Harita Retnakaran, Atila Abramowski, etc. It was fantastic to have the opportunity to work with you. What a cracking place to work! I will always miss the time with you, and I wish to have chance to meet and collaborate with you in the future. I would especially thank Ludmilla Dirson and Yikun Gu for their help to correct my grammar in the thesis. They have oered a lot of help to improve the phrases in this dissertation. I am also grateful to the following university sta: Rainer Peter Feller, for his unfailing IT support and assistance.

I am grateful to Dr. Kai Schmidt-Hoberg for referring this thesis and Prof.Dr. Günter Sigl, Dr. Andrei Lobanov, and Prof. Dr. Caren I. Hagner for refereeing my defense.

I am grateful to everyone family members and friends, who have provided me through moral and emotional support in my life. Especially I want to thank Misss Jouhua Liao for helping me to pass the tough days during my PhD time.

A very special gratitude goes out to all down at SFB676 and Excellent Cluster of Quantum Universe in Hamburg for providing the funding of this work. And nally, last but by no means least, also to everyone who I may have forgot to mention here. It was great sharing the time with all of you during last five years.

Thank you!